Application of a phase-field model to ferroelectrics

Ananya Renuka Balakrishna

Brasenose College
Doctor of Philosophy in Engineering Science
University of Oxford

Hilary Term 2016

To Ammamma,

my grandmother and my best friend,

who has encouraged and inspired me throughout my life.

Application of a phase-field model to ferroelectrics

Ananya Renuka Balakrishna, Brasenose College, University of Oxford

For the degree of D.Phil. in Engineering Science, Hilary Term 2016

Abstract

The current work uses a phase-field model to design nanoscale ferroelectric device concepts and to explore nanoscale ferroelectric behaviour. The results are expected to serve initial steps for nanoscale experimentation and to assist in the industrial application of ferroelectrics.

The use of ferroelectrics in nanoscale devices such as sensors or energy harvesters has increased in recent times. This has advanced research interests in nanoscale ferroelectric properties. In the current study, a phase-field model is used as a research tool to explore nanoscale behaviour of barium titanate. The model is first used to design and optimize nano-actuator concepts that generate actuation strains ~0.45%. This strain is four times as large as the strain offered by piezoceramic actuators in market. Next, the model is used to describe how scaling and surface conditions affect the formation of nanoscale polarization patterns, such as vortices. The results demonstrate the dominant effect of surface conditions and explain experimental observations of phase, tetragonality and polarization patterns in ferroelectric nanoparticles. The phase-field model is next extended to three dimensions and is used to test the stability of nanoscale periodic polarization patterns. The results describe the internal stress and electric fields developed in these patterns, and illustrate a mechanism of how complex polarization patterns can be formed under external strain or electric fields. Here, a conceptual design of an energy harvester is also explored.

The current work explores the application of a phase-field model as a design tool to develop nano-actuator and energy harvester concepts. The results on actuation/harvester cycle and the design parameter optimization would assist in developing device prototypes and eventually benefit in industrial fabrication. The phase-field model extended to three dimensions contributes to the study of domain patterns with out-of-plane polarizations and will assist in engineering a more realistic ferroelectric device. The results on the effects of scaling, surface energy and external loads on nanoscale polarization patterns, explains prior experimental observations of polarization patterns and provide useful insights on how to engineer domain configurations for nanoscale applications. Finally, the results motivate research towards developing prospective nanoscale applications from other smart materials, such as relaxors and ferromagnets.

Acknowledgements

I am immensely grateful to my supervisor, Professor John Huber, for giving me the best guidance, support and encouragement in every aspect of my life at Oxford. He is an excellent researcher and a great teacher – an example I hope to emulate in my future career. I would like to thank him for investing generous amounts of time and efforts in helping me grow intellectually from a clueless undergrad, and teaching me the invaluable skills of hard work and patience in pursuing research. I am deeply indebted to his supervision (and reference letters) without which completing my thesis would not have been possible.

I am very thankful to many generous and inspiring people who have helped me complete this work and grow as a researcher – to Professor Chad Landis and Dr. Dorinamaria Carka in UT Austin, for their generosity in sharing finite element codes to start my DPhil research; to Dr. Ingo Münch in Karlsruhe Institute of Technology, for introducing me to ferroelectrics (cocktails and even songs) and helping me in finite element coding which has been important to my DPhil; to the Felix Scholarship Trust, which made it possible for me to study at Oxford and introduced me to new cultures and experiences; to ARC Oxford, for letting me use the supercomputing facility; to Nils Reimer for reading my applications. I am very thankful to have had all this support during my DPhil.

I thank all the members in the SMME Group for creating an excellent research environment – to Professor Antoine Jérusalem and Professor Jin-Chong Tan for giving constructive inputs on my research during the transfer viva; to Kurien and Kwanlae for the lively (non-)academic everyday discussions; to Rob, Tuncay, Mehmet, Jianan, Prashant for application advice; to Sukarni, Amanda, Jon, Hisham for the administrative and IT support.

I am very grateful to be a part of Brasenose College, which has supported me in a myriad of activities that range from attending conferences to playing basketball tournaments. I have enjoyed the lively social life at Brasenose and am pleased to have made some great friends at Oxford – Sophie, Dhruti, Vikranth and Huma, who have enriched my DPhil life with lots of movie nights, truck food, beer, desi-jokes and laughter. I also very much appreciate the well wishes from Kalammajji et al., Ashu maama et al. and the care from my uncle and family in Liverpool – Madhu maama et al. have given me a home away from home during my stay in the UK.

Finally, I would like to thank the people that I love most and who with one way or another have taken this journey with me: to my parents Renu and Balu, who have always given me their best support and unconditional love, which has kept me going all this time; to my brother Shashank, who continues to motivate and inspire me endlessly to pursue a career in research; to my boyfriend Nils, whose presence, love and support makes each day a happy one; and to my most treasured friend Vasan, who has been a great strength of support and a laughter drug during all the ups-downs of my life. I am very lucky to have you all!

Contents

1

Introduction and literature review

1.1 Motivation

Ferroelectrics are materials that possess spontaneous polarization which can be reoriented by the application of an external electric field or through mechanical forces. Such reorientation is typically accompanied by a change in crystal geometry and surface charge distribution, which gives rise to a strong electro-mechanical coupling. This coupling in ferroelectrics finds applications in many devices [1], such as transducers [2], energy harvesters [3] and memory elements [4]. For example, a commercially available ferroelectric product is the ferroelectric random access memory (FeRAM), see Fig. 1.1(a-b) [5], [6]. FeRAMs store data in binary form on a ferroelectric thin film, with '1' and '0' corresponding to 'up' and 'down' polarization states respectively. Advantages of FeRAM over other conventional RAMs available in market include low power usage and faster switching rates. The key working element is a ferroelectric layer of thickness ~ 200nm, so for this device, the nanoscale material behaviour is of great importance.

Another application of ferroelectrics today is in the many commercially available transducers that employ the piezoelectric effect of the active material. For example, the diesel injection valve developed by Siemens, Bosch and Toyota [7] employs the piezoelectric effect of a multi-layered actuator made from lead zirconate

(a) (b)

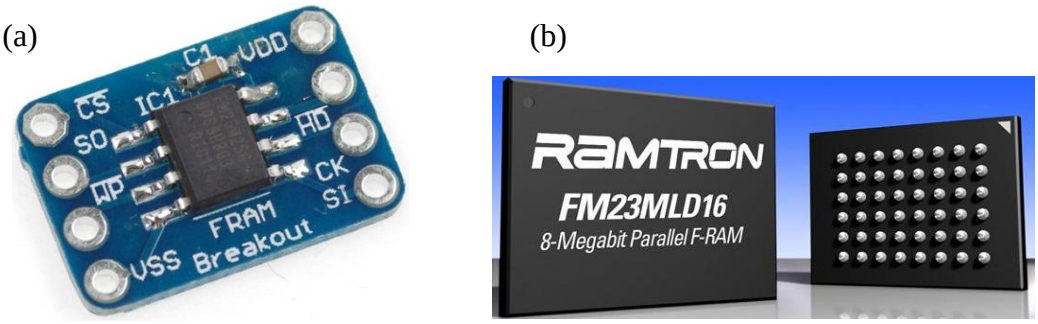

Figure 1.1: Ferroelectric non-volatile RAM devices developed by (a) Switch Science [5] (b) Ramtron International Corporation for commercial use [6]. Reprinted with permission from Cypress and Digitimes, respectively.

titanate (PZT), see Fig. 1.2(a). These actuators offer high fuel pressure, quick injection control and hence minimize the exhaust gases. While the actuators use bulk ferroelectric elements, tens of mm in size, their design is reliant on an understanding of material behaviour at the grain size (μm) and sub-grain scale (nm). Ferroelectrics have also been used in combination with other active materials, for example in a magnetic noise sensor, see Fig. 1.2(b). Here a layered composite of barium titanate (ferroelectric) and cobalt ferrite (magnetostrictive) is used. On exposing the sensor to a magnetic field, the cobalt ferrite generates magnetostriction, which is transferred to the barium titanate layer as stress. This results in the generation of charge/voltage on the ferroelectric layer from the piezoelectric effect. Piezoelectric materials have been widely applied in devices since their discovery and the study of microscale or nanoscale material behaviour is well established [8], [9]. However, the use of ferroelectrics in truly nanoscale devices is a recent development [10].

Nanoscale ferroelectric devices for electro-mechanical applications in sensing and energy harvesting have been developed in laboratory demonstrations [11], see Fig. 1.3(a-c). In the study by Koka et al. [11], a voltage of 345mV was generated from an array of barium titanate nanowires of diameter ~600nm, in response to a vibrating

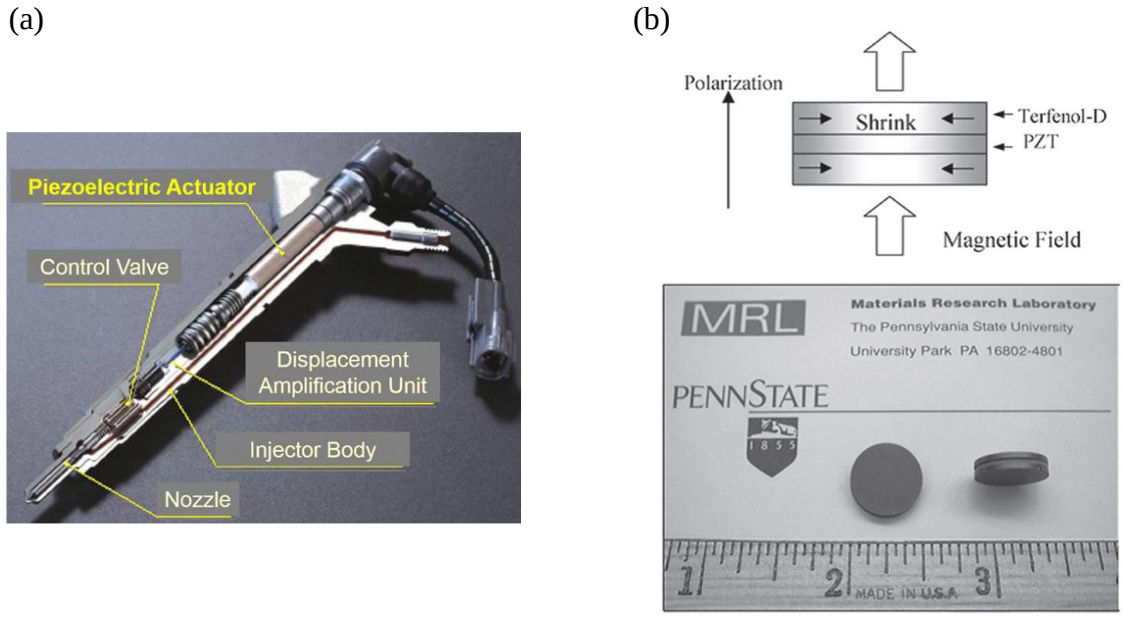

Figure 1.2: (a) Diesel injection valve with multi-layered piezoelectric actuator [7] (b) Magnetic noise sensor with a ferroelectric-magnetostrictive composite [12]. Copyright 2019 The Japan Society of Applied Physics.

mass of 30g placed on the top surface, see Fig. 1.3(a-b). The effect of the nanowire aspect ratio on the voltage generated was investigated in this study.

Fig. 1.3 illustrates an example of a traditional approach to the design of ferroelectric devices – a laboratory based incremental approach where new inventions are tested through experimental methods. In experiments, the device ideas are typically based on qualitative assumptions and the investigations can be time consuming and expensive. On the other hand, modelling methods are gaining recognition as a way to predict realistic ferroelectric behaviour and therefore possess potential as a design tool to assist the development of nanoscale device concepts. The aim of this thesis is to apply modelling methods to develop nanoscale device concepts and to explore ferroelectric properties at the nanoscale.

Advances in synthesis and fabrication of nanoscale structures [13] – [14], and progress in modelling techniques has broadened the scope of ferroelectric

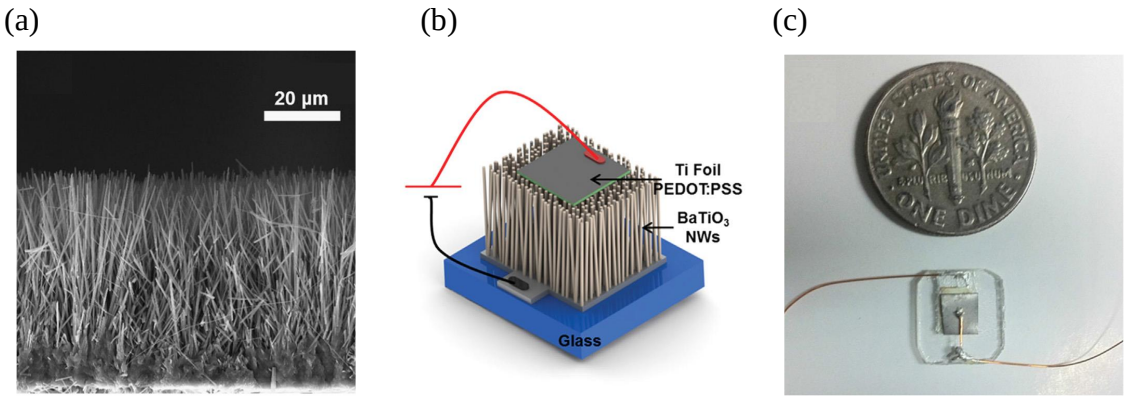

Figure 1.3: Array of barium titanate nanowires employed in sensing and energy harvesting applications [11]. (a) $BaTiO_3$ nanowire array (b) schematic of the energy harvester design (c) fabricated energy harvester device. © IOP Publishing. Reproduced with permission. All rights reserved.

applications [15]. The prospects of ferroelectrics in nanoscale industry can be explored through modelling techniques in a time and money efficient approach. At the nanoscale, it is important to note that the local inhomogeneous fields due to stress and electric field become significant and could potentially affect the working of nanoscale devices [16], [17]. For example, if designing a bulk scale piezoelectric actuator, although the stresses in individual grains may matter to some degree, it is typically sufficient to assume a bulk-scale piezoelectric response. But if designing a nanoscale ferroelectric actuator, the stresses present can greatly affect the device operation. Therefore a modelling method is required to account for local fields in order to accurately describe nanoscale ferroelectric behaviour. Additionally, modelling methods can provide insight into nanoscale ferroelectric properties [18], [19], which enable the engineering of nanoscale devices such as actuators and memory elements [20].

The phase-field method is currently regarded as one of the more powerful tools available to study nanoscale ferroelectric properties [21]–[23], in comparison to modelling techniques based on the micromechanics approach [24], [25]. This is because

the phase-field model does not make any a priori assumptions on the initial microstructural or nanoscale arrangement of the material and the structural evolution is a natural process arising from energy minimization in the material system. The phase field models when used as a bottom-up approach to design devices, allow us to explore the device performance before fabrication. For example, in the work by Muench et al. [26], [27] a phase-field model was employed to explore the working concept of an energy harvester [26], and subsequently the harvester performance on coupling with a rectifier and a capacitor was studied [27]. The effect of boundary conditions, such as substrate strain [22], [28], electric field [29] or surface energy [30], on nanoscale ferroelectric properties can be explored using phase-field methods.

The use of a phase-field model in a bottom-up approach to develop nanoscale ferroelectric devices is a relatively new concept. This provides an opportunity to explore the use of a phase-field model as a design tool. The potential applications of ferroelectrics coupled with the advancements in modelling methods serve as a motivation for the current study. In the following chapters, I apply a phase-field model:

- to explore conceptual device designs in ferroelectrics, such as nano-actuator and energy harvester concepts based on ferroelectric switching;
- to study the effects of scaling and surface energy on the formation of certain polarization patterns, which possess a potential to enhance storage density in memory devices;
- to explore the stability of periodic polarization patterns at the nanoscale that are predicted to form in tetragonal ferroelectrics.

Overall, the thesis demonstrates a numerical approach to invent and explore nanoscale ferroelectric devices, and contributes to the understanding of ferroelectric behaviour observed in nanoscale experiments. It is hoped that the modelling approach

could serve as an important initial step before nanoscale experimentation and be of benefit to the industrial application of ferroelectrics.

1.2 Key concepts

A ferroelectric is characterised by the presence of non-zero electrical polarization in the absence of an external electric field. Specifically, a ferroelectric has more than one stable state of polarization and can be switched by electric field. Ferroelectricity is observed in certain hydrogen-bonded materials [31], in oxides with a perovskite structure [32] and in structural families with intergrowth of perovskite layers and other oxides [33]. Of the above structures, ferroelectrics of the perovskite oxide family are most widely explored due to the strong electromechanical coupling, and hence usefulness in practical applications.

Barium Titanate ($BaTiO_3$) is a well-known example of a ferroelectric crystal which possesses a simple perovskite structure [34], [35]. The properties of $BaTiO_3$ are well established [36]–[40], leading to the development of reliable material models [29], [41], [42]. These material models encourage device design of memory elements, energy harvesters, and so forth with $BaTiO_3$ as the working material [43], [44]. Further, the semiconductor industry has initiated device exploration in $BaTiO_3$ and is motivated to use environmentally friendly materials that are free of lead [1]. These features motivate the choice of $BaTiO_3$ as the ferroelectric material to explore in the present work. However, some of the design concepts explored could be relevant for other materials. This section describes the key concepts in ferroelectrics and the associated definitions, using $BaTiO_3$ as the reference material.

The barium titanate unit cell comprises of one barium ion, Ba^{2+} three oxygen

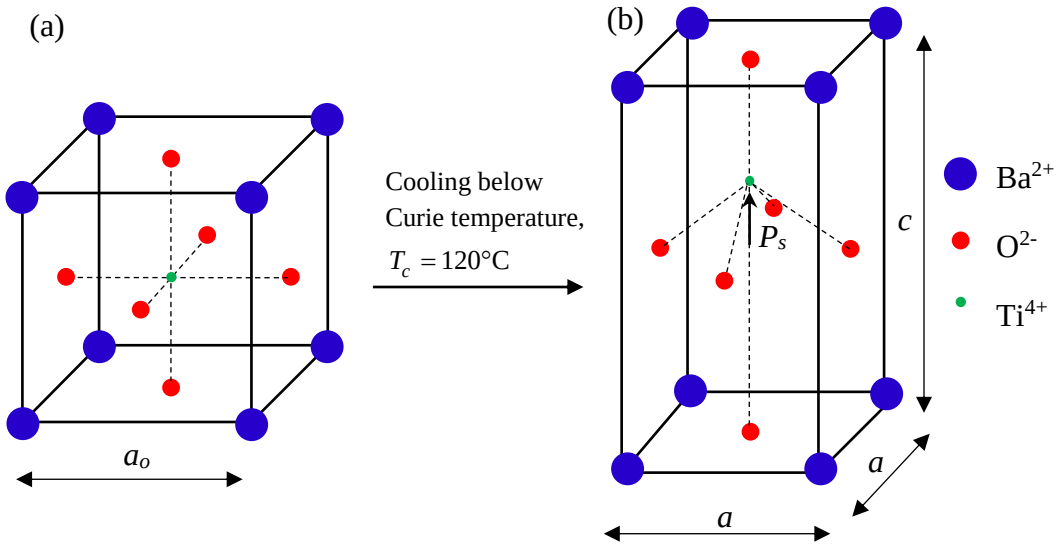

Figure 1.4: Lattice structure of barium titanate, $BaTiO_3$ in (a) paraelectric phase (b) ferroelectric phase. Note that the ion displacements are greatly exaggerated here, $(c - a_0)/a_0 \sim 0.0082$.

ions, O^{2-} and one titanium ion, Ti^{4+} arranged as shown in Fig. 1.4(a-b). At high temperatures ($>120°C$), $BaTiO_3$ exists in a **paraelectric** state with a centrosymmetric cubic geometry and zero dipole moment in the unit cell, Fig. 1.4(a). On cooling barium titanate below the **Curie temperature**, $T_c = 120°C$, the titanium ion, Ti^{4+} shifts from its central position resulting in a net dipole moment in the unit cell, Fig. 1.4(b). This non-centrosymmetric structure of $BaTiO_3$ gives rise to **spontaneous polarization**, P_s transforming the material from the paraelectric phase with cubic structure to a ferroelectric phase with tetragonal structure. Further cooling of tetragonal $BaTiO_3$ to $0°C$ results in an orthorhombic structure, and cooling below $-90°C$ transforms barium titanate into a rhombohedral structure. During the phase transition at T_c, the appearance of spontaneous polarization in ferroelectrics is accompanied by **spontaneous strain**, as the lattice parameter of the unit cells changes from a cubic geometry with side a_0 to a

tetragonal structure with sides c and a as shown in Fig. 1.4(a-b). In $BaTiO_3$ the lattice parameters are related as $c > a_0$ and $a < a_0$, giving rise to spontaneous strains of 0.0082 and -0.0027 respectively.

The ferroelectric behaviour arises because the off centre Ti^{4+} ion can be switched into any of six symmetrical positions – in each case it is offset towards the centre of one face of the unit cell, see Fig. 1.5(a). This Ti^{4+} can be moved from its offset position by the application of an external electric field or stress as shown in Fig. 1.5(b). The displacement of the Ti^{4+} by electric field or stresses is known as ferroelectric or ferroelastic switching respectively. Reorientation of the spontaneous polarization through $90°$ or $180°$, by the application of electric field or stress is referred to as $90°$ switching or $180°$ switching respectively, see Fig. 1.5(b). $90°$ switching is accompanied by mechanical strains due to the change in crystal *c*-axis orientation, and in $BaTiO_3$ these strains are of the order of $\sim 1\%$ [45].

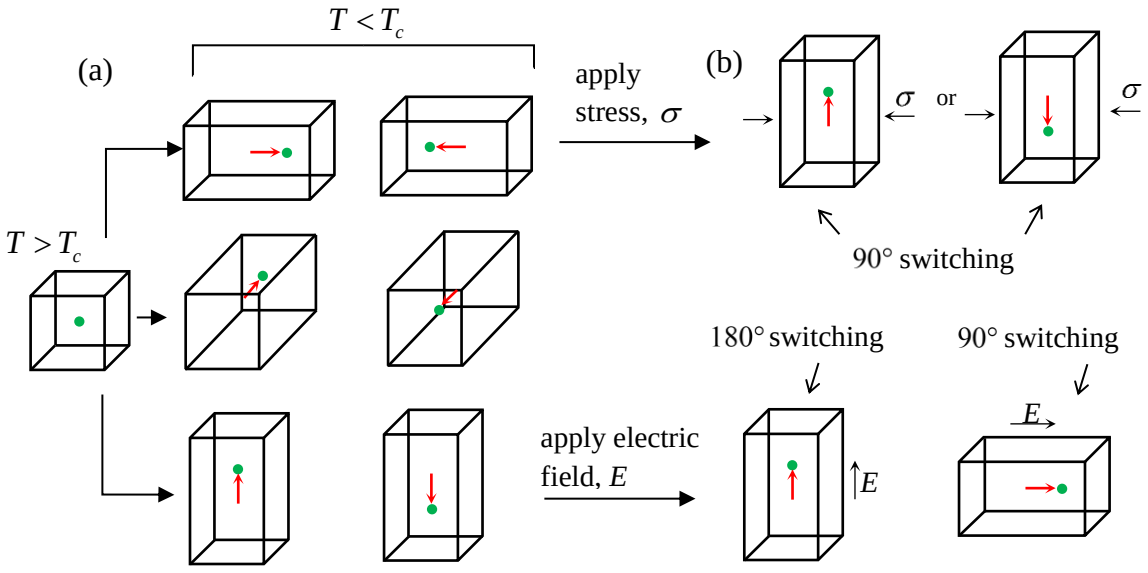

Figure 1.5: Schematic diagram indicating (a) orientation of spontaneous polarization in $BaTiO_3$ unit cells along six crystallographic directions (b) ferroelectric switching under the presence of electric fields and stresses.

Up to now, ferroelectric properties were described with reference to a unit cell of $BaTiO_3$. However, in a typical ferroelectric, unit cells group together to form regions with uniform polarization, referred to as **domains**, see Fig. 1.6(a). These domains are separated from their neighbours through **domain walls**, which are thin regions that collectively represent a polarization gradient between the neighbouring domains as shown by the schematic in Fig. 1.6(b-c). In tetragonal ferroelectrics, the 180° and 90° domain walls are commonly observed, see Fig. 1.6(b-c). At the 180° domain wall the spontaneous polarization in unit cells approaches near zero values, changing the local crystal structure of unit cells from tetragonal to cubic. The 90° wall bridges domains with mismatched lattice parameters and rotates the neighbouring domains through an

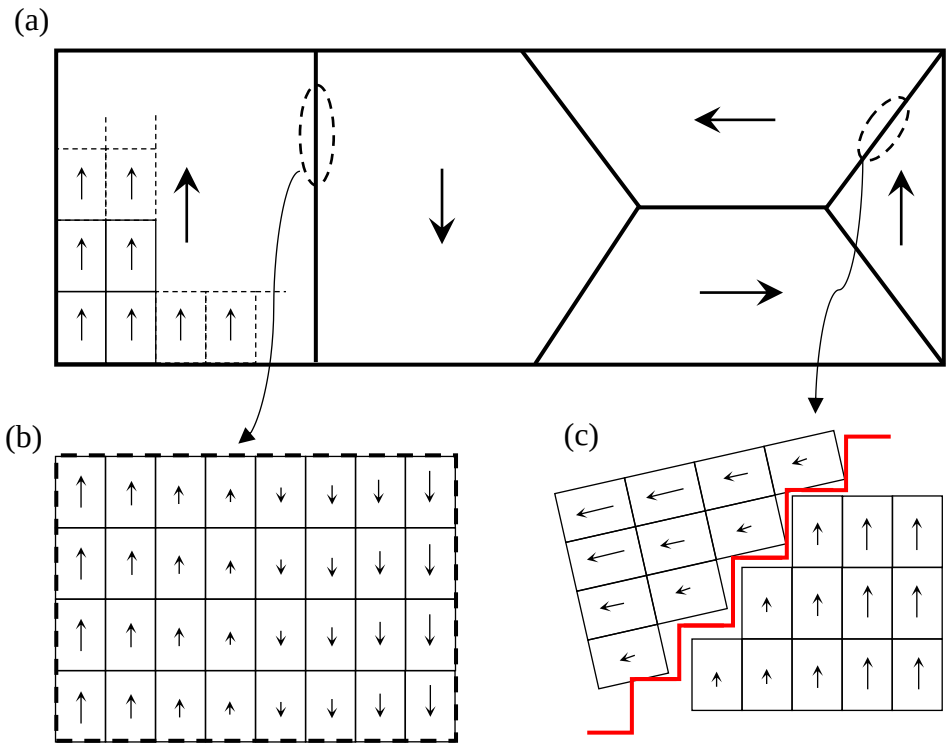

Figure 1.6: Schematic representation of (a) a uniformly polarized regions - domains (b) 180° domain wall (c) 90° domain wall in a typical ferroelectric specimen. The red line indicates lattice mismatch at the 90° domain wall.

angle as indicated by the red-line in Fig. 1.6(c). The 180° and 90° domain walls typically possess misfit stresses or/and local electric fields, and are discussed in detail in chapter 2.

In a typical ferroelectric specimen polarized domains arrange themselves in compatible format, such as head to tail or tail to head polarization vector arrangements, to form a polarization pattern, see Fig. 1.7. Such an arrangement eliminates net charge on the domain walls that would contribute to an increase in domain wall energy [46], [47]. Polarization patterns are important to the working of nanoscale devices, where the device size is comparable to the polarized domain size. In such cases, the type of polarization patterns, and the position/movement of individual domain walls [48], [49] affects the working of nanoscale ferroelectric devices, such as actuators [18]. The evolution/rearrangement of the polarized domains under electric fields or stresses [50], [51], is important to engineering nanoscale devices and can be predicted using modelling methods. Some of the polarization patterns that are predicted to form in tetragonal ferroelectrics are shown schematically in Fig. 1.7.

The band-like and stripe-like domain patterns, see Fig. 1.7(a-b) consist of alternate bands of 180° and 90° domains respectively. These patterns are widely observed in tetragonal ferroelectrics [46], [52], [53]. The stripe-like features in Fig. 1.7(b) are known to relieve misfit stresses. However, the vortex-like patterns in

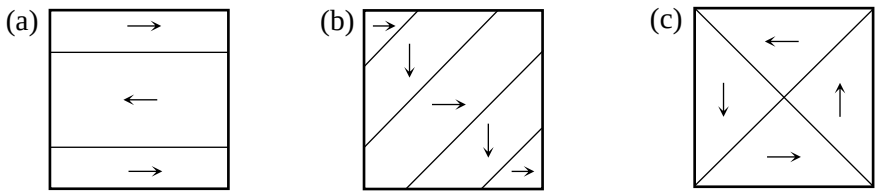

Figure 1.7: Schematic representation of domain arrangements in polarization patterns with (a) band-like (b) stripe-like (c) vortex-like features.

Fig. 1.7(c) where polarized domains fit together to form a flux-closure are rarely observed in experiments. These vortex polarization patterns have the potential to enhance storage density in memory devices [20], and their elusive nature in ferroelectrics is studied in chapter 4 of this thesis.

A ferroelectric crystal with non-zero net (or average) polarization exhibits the piezoelectric effect that is often employed for electro-mechanical energy conversion in transducers and energy harvesters. The linear **direct and converse piezoelectric effects** of a ferroelectric crystal can be described by [54]:

$$D_i = d_{ikl}\sigma_{kl} + \kappa_{ik}^{\sigma} E_k \tag{1.1}$$

$$\varepsilon_{ij} = s_{ijkl}^{E}\sigma_{kl} + d_{kij}E_k. \tag{1.2}$$

In Eq. (1.1), the electric displacement D_i, piezoelectric coefficient tensor d_{ikl} and stress σ_{kl} describe the direct piezoelectric effect. That is, application of stresses generates electric displacement and is employed in devices such as sensors or energy harvesters. The dielectric constant under constant stress, κ_{ik}^{σ} and electric field, E_k describe the **dielectric effect**, where application of electric field induces polarization in a dielectric material. In Eq. (1.2) the converse piezoelectric effect is described by the strain, ε_{ij}, converse piezoelectric coefficient tensor d_{kij} and electric field E_k. Here, the application of an electric field generates mechanical strain; this is commonly employed in actuators or motors. The compliance under constant electric field s_{ijkl}^{E} and stress σ_{kl} contributes to the **elastic effect** that induces strain in a material. The direct and converse piezoelectric effects can also be derived from a free energy expression, with stress and electric fields as derivatives of free energy – this is discussed in the context of material models in section 1.3.

At the macroscopic scale (typically a few micrometres in size upwards), application of an electric field across a ferroelectric specimen with multiple domains, can cause the polarization in each domain to align with the applied field. This process is known as **poling**; the net polarization increases with the applied electric field, until complete polarization reorientation is achieved, see Fig. 1.8(a). The net polarization value reaches a maximum and is referred to as the **saturation polarization,** P_{sat} . On removal of the electric field, the material retains a net polarization called the **remnant polarization**, P_{rem} and the corresponding strain is the **remnant strain**, ε_{rem} as shown in Fig. 1.8(a-b).

On applying a reverse electric field, the net polarization in the ferroelectric specimen decreases and at the **coercive electric field**, E_c that is characteristic of the ferroelectric, the polarization reduces to zero. Further decrease in the electric field causes domains polarized along the reverse electric field to grow, switching the net

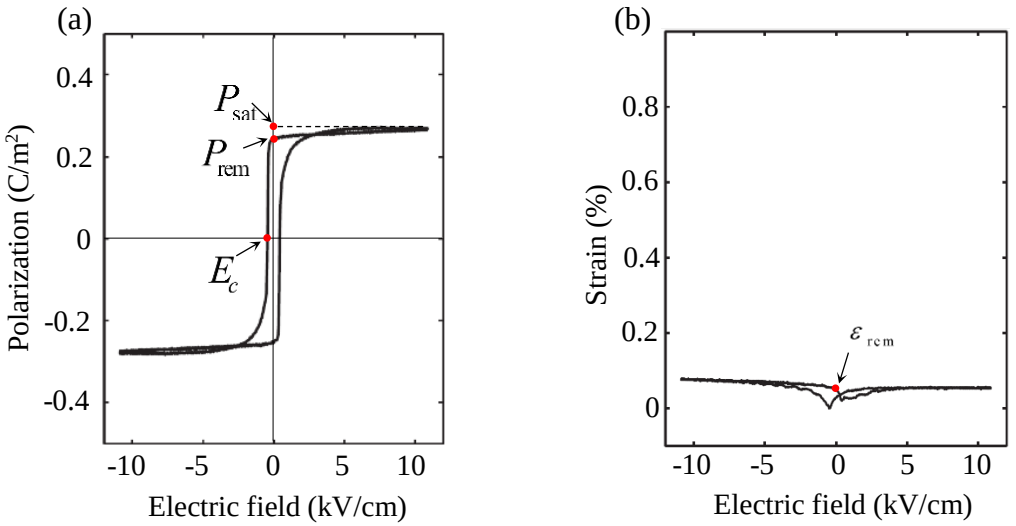

Figure 1.8: (a) Polarization vs. electric field loop for single crystal barium titanate showing hysteresis (b) The corresponding strain vs. electric field loop for $BaTiO_3$ [45]. Reprinted from Ref. [45], with permission from Elsevier.

polarization through 180° in-plane. Note that small values of strains, <0.1%, are observed during 180° ferroelectric switching, see Fig. 1.8(b). Increase in magnitude of the reverse electric field causes polarization to reach saturation. The electric field cycle is repeated and the polarization versus electric field curve forms a closed loop referred to as the **hysteresis loop**, Fig. 1.8(a). Hence, a ferroelectric can be polarized into at least two distinct stable states, such as those observed at the tips of the hysteresis loops and can retain the net polarization even after the removal of the electric field. This ferroelectric property is employed by non-volatile memories, where the ferroelectric polarization states represent binary numbers '0' and '1' [55].

An ideal hysteresis loop is symmetric while the shape of the loop, coercive field and spontaneous polarization values can be affected by the presence of mechanical stresses, as shown in Fig. 1.9 [45]. For example in Fig. 1.9, under compressive stresses,

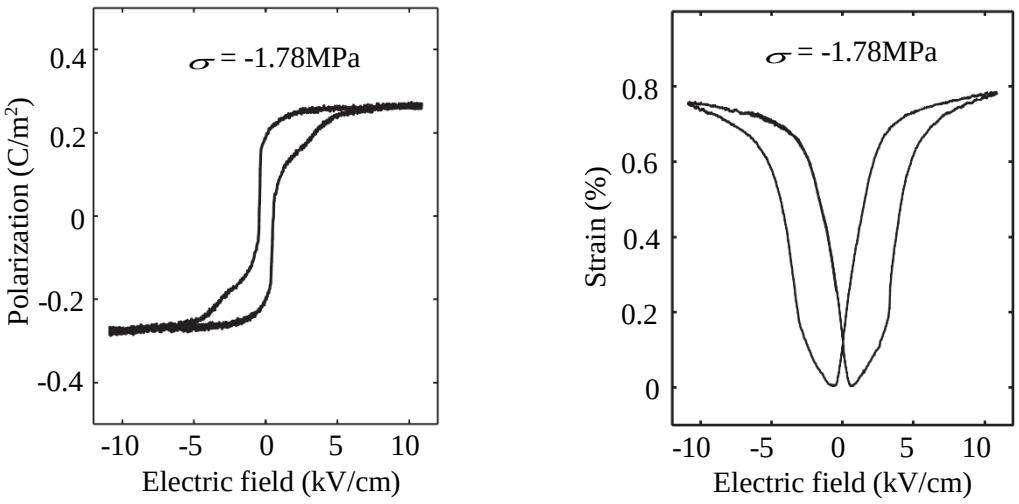

Figure 1.9: Polarization vs. electric field and strain vs. electric field loops for single crystal barium titanate showing deviation from Fig. 1.8(a-b) under compressive mechanical stresses, $\sigma = -1.78\text{MPa}$ [45]. Reprinted from Ref. [45], with permission from Elsevier.

$\sigma = -1.78\text{MPa}$, the applied electric field forced an out-of-plane **polarization switching**, i.e., a $90°$ switching, which was accompanied by mechanical strains of ~0.8% in single crystal $BaTiO_3$. These values are several times greater than the strains attained through $180°$ switching, see Fig. 1.8(b), or through the piezoelectric effect alone. The strains achieved on $90°$ switching are greater than the values typical piezoceramics can offer, and thereby enable potential applications in actuators. This concept of enhanced strain from ferroelectric switching is explored in chapter 3, to design nanoscale actuator concepts.

The electrical and mechanical properties of ferroelectrics can also be described using modelling methods which are based on phenomenological theories, for example the phase-field method. These modelling methods commonly derive their input material parameters from experiments and can predict the ferroelectric material response under a variety of loading conditions. In the next section, material models are introduced and the different types of theoretical models are discussed.

1.3 Material models

Macroscopic phenomenology

Phenomenological theories of ferroelectrics typically treat the material as a continuum and postulate fields that describe the elastic, dielectric and thermal properties of the ferroelectric system [54]. These material models can then describe ferroelectric devices through simulations, and help to connect theoretical understanding with experimental observations.

In general, the classical laws of mechanics and the laws of thermodynamics are used to obtain relationships between the elastic, dielectric and thermal properties of the

ferroelectric system. For example, the work done over volume V, when subjected to an infinitesimal change in strain, $\mathrm{d}\varepsilon_{ij}$ and electric displacement, $\mathrm{d}D_i$ in the presence of constant stress, σ_{ij} and electric field, E_i is given by:

$$W = \int_V (\sigma_{ij}\mathrm{d}\varepsilon_{ij} + E_i \mathrm{d}D_i)\mathrm{d}V\,. \tag{1.3}$$

(Note: Indicial notation with summation over repeated indices will be used for Cartesian coefficients throughout.) Now, having described an expression for the work done, W, the internal energy per unit volume of the system is next considered. Here, $\mathrm{d}Q$ is defined as an infinitesimal quantity of heat added to the system, and the change in internal energy per unit volume, $\mathrm{d}U$, is given by the first law of thermodynamics as:

$$\mathrm{d}U = \mathrm{d}Q + \mathrm{d}W \tag{1.4}$$

Assuming reversibility, from the second law of thermodynamics, the heat added to the system, $\mathrm{d}Q$, can be described as a product of the temperature, T, and the change in entropy, $\mathrm{d}S$. Next, on substituting Eq. (1.3) in Eq. (1.4), the increment of internal energy of the system is given by,

$$\mathrm{d}U = T\mathrm{d}S + \sigma_{ij}\mathrm{d}\varepsilon_{ij} + E_k \mathrm{d}D_k\,. \tag{1.5a}$$

The stress, σ_{ij} and strain, ε_{ij} tensors are symmetric, that is $\sigma_{ij} = \sigma_{ji}$. The indicial notation can be reduced using the Voigt notation, for σ_{ij}: $\sigma_1 = \sigma_{11}$, $\sigma_2 = \sigma_{22}$, $\sigma_3 = \sigma_{33}$, $\sigma_4 = \sigma_{23} = \sigma_{32}$, $\sigma_5 = \sigma_{13} = \sigma_{31}$, and $\sigma_6 = \sigma_{12} = \sigma_{21}$, and similarly for strain, but with $\varepsilon_4 = \varepsilon_{23} + \varepsilon_{32}$, $\varepsilon_5 = \varepsilon_{13} + \varepsilon_{31}$, and $\varepsilon_6 = \varepsilon_{12} + \varepsilon_{21}$. Then Eq. (1.5a) becomes,

$$\mathrm{d}U = T\mathrm{d}S + \sigma_i \mathrm{d}\varepsilon_i + E_k \mathrm{d}D_k \qquad i = 1\ldots 6,\ k = 1\ldots 3. \tag{1.5b}$$

Eq. (1.5b) describes the thermal, elastic and electric properties of a material with S, ε_i and D_k as independent variables. However, in order to describe the ferroelectric behaviour it is convenient to treat temperature T, strain ε_i, and electric displacement D_k, as independent variables. This is done by transforming Eq. (1.5b) to an appropriate thermodynamic potential [54], such as the Helmholtz free energy, ψ,

$$\psi = U - TS . \tag{1.6}$$

The differential form of the Helmholtz free energy, ψ, in Eq. (1.6), considering an infinitesimal change in the independent variables is given by,

$$\mathrm{d}\psi = -S\mathrm{d}T + \sigma_i \mathrm{d}\varepsilon_i + E_i \mathrm{d}D_i . \tag{1.7}$$

Eq. (1.7) demonstrates that the entropy S, the stress σ_i, and the electric field E_i, are related to the Helmholtz free energy as:

$$S = -\left(\frac{\partial \psi}{\partial T}\right)_{\boldsymbol{\varepsilon},\mathbf{D}}, \qquad \sigma_i = \left(\frac{\partial \psi}{\partial \varepsilon_i}\right)_{T,\mathbf{D}}, \qquad E_i = \left(\frac{\partial \psi}{\partial D_i}\right)_{T,\boldsymbol{\varepsilon}} . \tag{1.8}$$

In Eq. (1.8), the entropy, S, is a partial derivative of the free energy, ψ, with respect to temperature, T, at constant strain, $\boldsymbol{\varepsilon}$, and constant electric displacement, $\mathbf{D}$. Likewise, the stresses σ_i, and electric fields E_i, are defined as partial derivatives of free energy with respect to strain and electric displacement respectively. The expressions for the stresses σ_i and electric fields E_i in Eq. (1.8), can be written in the linear differential form,

$$\mathrm{d}\sigma_i = \left(\frac{\partial \sigma_i}{\partial T}\right)_{\mathbf{D},\boldsymbol{\varepsilon}} \mathrm{d}T + \left(\frac{\partial \sigma_i}{\partial \varepsilon_j}\right)_{\mathbf{D},T} \mathrm{d}\varepsilon_j + \left(\frac{\partial \sigma_i}{\partial D_j}\right)_{\boldsymbol{\varepsilon},T} \mathrm{d}D_j \tag{1.9}$$

$$\mathrm{d}E_i = \left(\frac{\partial E_i}{\partial T}\right)_{\mathbf{D},\boldsymbol{\varepsilon}} \mathrm{d}T + \left(\frac{\partial E_i}{\partial \varepsilon_j}\right)_{\mathbf{D},T} \mathrm{d}\varepsilon_j + \left(\frac{\partial E_i}{\partial D_j}\right)_{\boldsymbol{\varepsilon},T} \mathrm{d}D_j \tag{1.10}$$

The coefficients in Eq. (1.9) and Eq. (1.10) are known as compliances and are functions of the independent variables. These compliances provide a measure of the coupling between electrical, thermal and mechanical fields, and can be experimentally measured. For example, under isothermal conditions Eq. (1.9) and Eq. (1.10) reduce to:

$$\mathrm{d}\sigma_i = c_{ij}^{D,T}\mathrm{d}\varepsilon_j - h_{ij}^{T}\mathrm{d}D_j \tag{1.11}$$

$$\mathrm{d}E_i = -h_{ij}^{T}\mathrm{d}\varepsilon_j + \kappa_{ij}^{\varepsilon,T}\mathrm{d}D_j \tag{1.12}$$

where $c_{ij}^{D,T} = \left(\partial\sigma_i/\partial\varepsilon_j\right)_{\mathbf{D},T}$, is the isothermal elastic compliance at constant electric displacement, $h_{ij}^{T} = -\left(\partial E_j/\partial\varepsilon_i\right)_{\mathbf{D},T}$, is the isothermal linear piezoelectric compliance and $\kappa_{ij}^{\varepsilon,T} = \left(\partial E_i/\partial D_j\right)_{\boldsymbol{\varepsilon},T}$, is the inverse isothermal permittivity at constant strain. Similarly the relations in section 1.2, Eq. (1.1) and Eq. (1.2) that describe the linear direct and converse piezoelectric effect can be derived from the energy equation, Eq. (1.5), when transformed to a Gibbs thermodynamic potential [54].

Up to this point, only linear differential equations of state were considered, i.e., from Eq. (1.7) and Eq. (1.8) the free energy was expressed in terms of the first order derivatives,

$$\psi = \psi_{\mathrm{T}} + \left(\frac{\partial\psi}{\partial\varepsilon_i}\right)\varepsilon_i + \left(\frac{\partial\psi}{\partial D_i}\right)D_i \tag{1.13}$$

where ψ_{T} is a function of temperature alone. However in ferroelectrics, some of the important characteristics, such as hysteresis, are non-linear. To describe the non-linear ferroelectric characteristics, the free energy ψ in Eq. (1.13) is expanded as a Taylor series in electric displacement, D_i, and strain, ε_i:

$$\psi = \psi_{\mathrm{T}} + \left(\frac{\partial \psi}{\partial \varepsilon_i}\right)\varepsilon_i + \left(\frac{\partial \psi}{\partial D_i}\right)D_i + \frac{1}{2}\left(\frac{\partial^2 \psi}{\partial \varepsilon_i \partial \varepsilon_j}\right)\varepsilon_i \varepsilon_j + \frac{1}{2}\left(\frac{\partial^2 \psi}{\partial D_i \partial D_j}\right)D_i D_j + \left(\frac{\partial^2 \psi}{\partial \varepsilon_i \partial D_j}\right)\varepsilon_i D_j + \ldots \tag{1.14}$$

The derivatives in Eq. (1.14) are taken at $D_i = 0$, $\varepsilon_i = 0$. This free energy expression can describe both the polar (tetragonal) and non-polar (centrosymmetric) states of a ferroelectric crystal, provided the odd-rank tensor coefficients in Eq. (1.14) are zero. Assuming that the strains are small, that is involving the terms in Eq. (1.14) with $\varepsilon_i \prod_j D_j$ and $\varepsilon_i \varepsilon_j$ only, and neglecting the other higher order strain terms, the free energy expansion up to sixth order derivatives is [54]:

$$\psi = \psi_{\mathrm{T}} + \frac{1}{2}c_{ij}^{D,T}\varepsilon_i \varepsilon_j + \frac{1}{2}\kappa_{ij}^{\varepsilon,T} D_i D_j + \frac{1}{2}q_{ijk}^{T} D_i D_j \varepsilon_k + \frac{1}{4}\xi_{ijkl}^{\varepsilon,T} D_i D_j D_k D_l + \frac{1}{6}\gamma_{ijklmn}^{\varepsilon,T} D_i D_j D_k D_l D_m D_n \tag{1.15}$$

where, q_{ijk}^{T}, $\xi_{ijkl}^{\varepsilon,T}$, $\gamma_{ijklmn}^{\varepsilon,T}$ are the associated tensorial coefficients for the higher order terms. The free energy of a ferroelectric system is conveniently described by expressing Eq. (1.15) in terms of its order parameter, polarization. The polarization, P_i, in a ferroelectric crystal is related to the electric displacement as $D_i = \varepsilon_0 E_i + P_i$. For easy comprehension, Eq. (1.15) can be simplified by assuming isothermal conditions and expressing it in a one-dimensional form, considering polarization variation along just one crystallographic direction [56]:

$$\psi = \frac{1}{2}c\varepsilon^2 + \frac{1}{2}\kappa P^2 + \frac{1}{2}q\varepsilon P^2 + \frac{1}{4}\xi P^4 + \frac{1}{6}\gamma P^6 \ldots \tag{1.16}$$

Eq. (1.16) was used to develop the classical Landau – Devonshire's theory of barium titanate [57], [34], [35], that describes the free energy of a bulk ferroelectric crystal by

associating zero energy to the cubic non-polar state. The stresses and electric fields can be derived from Eq. (1.16) as,

$$\sigma = \frac{d\psi}{d\varepsilon} = c\varepsilon + \frac{q}{2}P^2 \tag{1.17}$$

$$E = \frac{d\psi}{dP} = \kappa P + q\varepsilon P + \xi P^3 + \gamma P^5 . \tag{1.18}$$

Eq. (1.17)-(1.18), describe the relation between field quantities, such as strain and polarization, which can be verified through experimental methods. For example, under zero stress condition, Eq. (1.17) can be written as $c\varepsilon + \frac{q}{2}P^2 = 0$. This indicates that the strain is proportional to polarization squared, $\varepsilon \propto P^2$. Likewise under zero strain condition, Eq. (1.18) reduces to $E = \kappa P + \xi P^3 + \gamma P^5$, from which an expression for spontaneous polarization can be derived. First note that κ is the measurable dielectric permittivity for small polarization values. Then, the free energy of the ferroelectric system is minimum at the spontaneous polarization, and therefore solving, $\frac{d\psi}{dP} = E = 0$, two solutions for *P* are obtained, namely $P = 0$ or $\kappa + \xi P^2 + \gamma P^4 = 0$. Neglecting the fourth order term which is often relatively small, we have $P^2 \sim -\frac{\kappa}{\xi}$ and this spontaneous polarization value in $BaTiO_3$ can be measured through experimental methods [58]. Hence κ and ξ are measurable. Another example of the use of phenomenology to relate experimental measurements is the derivation of susceptibility from Eq. (1.18). Susceptibility in ferroelectrics is defined as the rate of change of polarization with respect to an electric field, and this physical quantity can be measured experimentally. Differentiating Eq. (1.18) with respect to polarization under zero stress condition, and setting $P = 0$ an expression for susceptibility, $\chi = \frac{1}{\kappa}$ is derived. These

examples illustrate an advantage of phenomenological modelling, which helps to relate and understand experimental observations.

Next, strain-free isothermal conditions are assumed and the free energy expression in Eq. (1.16), is written in simple polynomial form as,

$$\psi = \frac{1}{2}\kappa P^2 + \frac{1}{4}\xi P^4 + \frac{1}{6}\gamma P^6 ... \tag{1.19}$$

Allow, the coefficient, κ to be temperature dependent around the Curie point ($T \sim T_c$), given by $\kappa = \kappa_c (T - T_c)$ [54]. The other coefficients in Eq. (1.19) are taken to be independent of temperature. The free energy, ψ in Eq. (1.19) can then be plotted as a function of polarization, *P* at three temperatures: $T > T_c$, $T = T_c$ and $T < T_c$ [59] as shown in Fig. 1.10.

Fig. 1.10 describes the energy well for $BaTiO_3$ in its cubic state ($T > T_c$), at the Curie temperature ($T = T_c$) and in its tetragonal state ($T < T_c$). For $T > T_c$, $BaTiO_3$ is in the paraelectric state and possesses minimum energy at zero polarization. The energy well has a single minimum at $P = 0$. At temperatures equal to the Curie point, $T = T_c$, the energy well is observed to widen. For temperatures below the Curie point $T < T_c$,

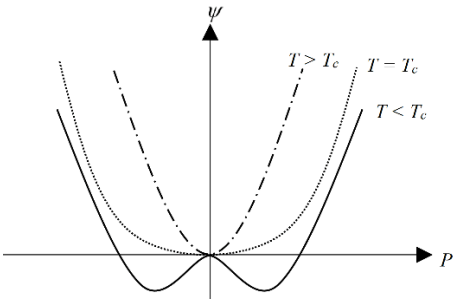

Figure 1.10: Schematic representation of the free energy curve, ψ as a function of polarization, *P* at three temperatures: $T > T_c$, $T = T_c$ and $T < T_c$, where T_c is the Curie temperature [56]. Reprinted from Ref. [56], with permission of Springer.

the energy-polarization curve adopts a ‘double-well’ structure indicating two minimum energy states in the ferroelectric phase. These minimum energy states correspond to the spontaneous polarization states of the ferroelectric crystal. Further details of the free energy equation are explained in the context of a phase-field model in chapter 2.

A variety of modelling approaches have been developed to predict ferroelectric behaviour at different length scales. These can be broadly categorised as macroscopic (few micrometres), microscopic (nanometres) and atomistic (Angstrom) models. Next, a brief overview on these modelling approaches is described and the associated challenges are discussed.

Macroscopic models

Models that predict bulk properties of ferroelectric crystals, for example strain hysteresis loops [60], can be categorized under macroscopic models [24], [25], [61], [62] These models are built on the data or material properties obtained at the microscopic scale, and typically assume homogeneous properties and averaged electromechanical fields to predict the net ferroelectric behaviour.

An example of a macroscopic model is the switching model of Hwang et al. [60]. The key concept here is that ferroelectric switching occurs if the applied electric field or stress exceeds a critical value, inducing a net change in remnant strain and polarization [60], [61]. The micro-electromechanical switching models have been employed to describe the electric response and strain hysteresis loops in ferroelectrics under proportional stress and electric field loading [63], [67], [68], see Fig. 1.11(a-b). An advantage of these models is that they provide insight into the source of observed hysteresis, for example, Fig. 1.11 indicates that the polarization versus electric field hysteresis arises from the combined effect of polarization switching and the linear

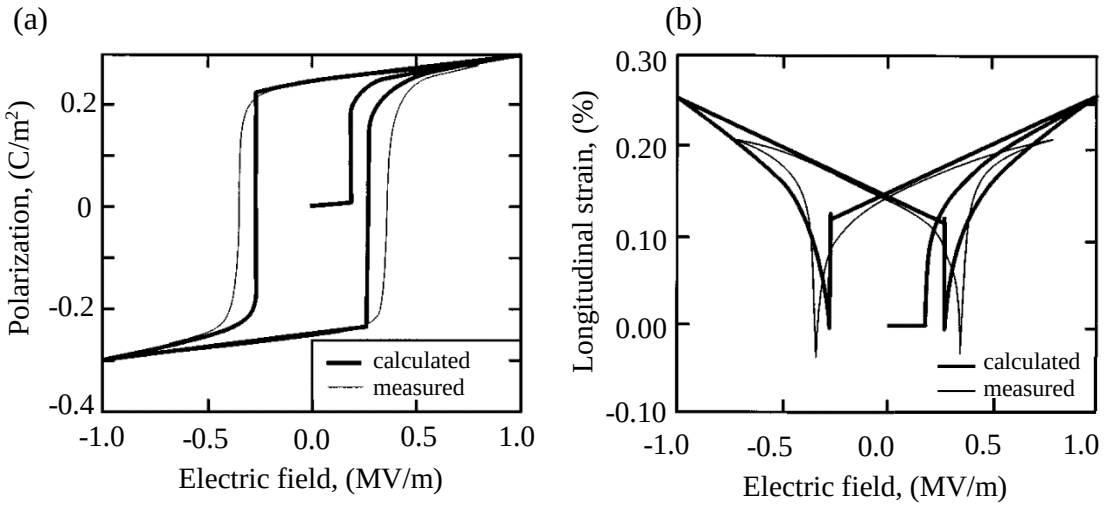

Figure 1.11: A comparison of the simulations from a macroscopic polarization switching model and the measured 8/65/35 PLZT values showing (a) polarization vs. electric field hysteresis loop (b) longitudinal strain vs. electric field butterfly loop, with no applied stress. The figures are modified from [63]. Reprinted from Ref. [63], with permission from Elsevier.

dielectric effect. These models also offer computational simplicity and speed.

A challenge faced by the macroscopic models is their inability to capture the effect of domain configurations in polarization patterns on macroscopic properties such as ferroelectric switching [65]. The macroscopic models approximate internal stress, electric fields to be homogenous at some scale, and specify averaged elastic, electric and piezoelectric properties that are derived from those of a single crystal [60]. However, at the nanoscale, the size of an individual domain can be comparable to the overall size of a ferroelectric device, and the averaged approximations would be invalid [66], [67]. Macroscopic models also commonly neglect the domain wall energy contribution while accounting for the overall energy of ferroelectric system, and so are

unsuitable for exploring nanoscale ferroelectric properties or to be employed as a tool to design conceptual devices at the nanoscale [68].

Microscopic models

With the current trend of miniaturization in electronics there has been a growing interest in the study of nanoscale properties. This has led to advances in modelling techniques at the nanoscale [21]–[23], [69]. At the nanoscale, features such as distortion of electric fields near cracks, stresses developed in thin films due to lattice mismatch at the substrate or misfit stresses at domain interfaces, can have significant or even dominant effects on ferroelectric properties [48], [49], [70]. Modelling of these effects is critical to the development of nanoscale devices such as actuators or energy harvesters [1], [3].

Microscopic models commonly account for the presence of local effects such as internal stresses and electric fields. For example, the phase-field models [29], [71], account for energy contributions from domain walls, elastic and electric potentials, to predict realistic material behaviour at equilibrium. These models have been employed to study domain energetics [68], to map intergranular stresses in thin films [22] and to explore domain wall movements under electro-mechanical fields [71], see Fig. 1.12. These advantages of phase-field models indicate their potential to be used as a design tool for nanoscale devices, and further details are described in section 2.2 of chapter 2.

The Monte Carlo simulation technique [72]–[74] is another numerical approach used to solve a phenomenological model. In this technique, domain behaviour is simulated by treating a ferroelectric as a group of electric dipoles. These simulations are able to produce relative orientations of dipoles across domain boundaries, and predict the collective behaviour of electric dipoles, simulating the overall domain behaviour at

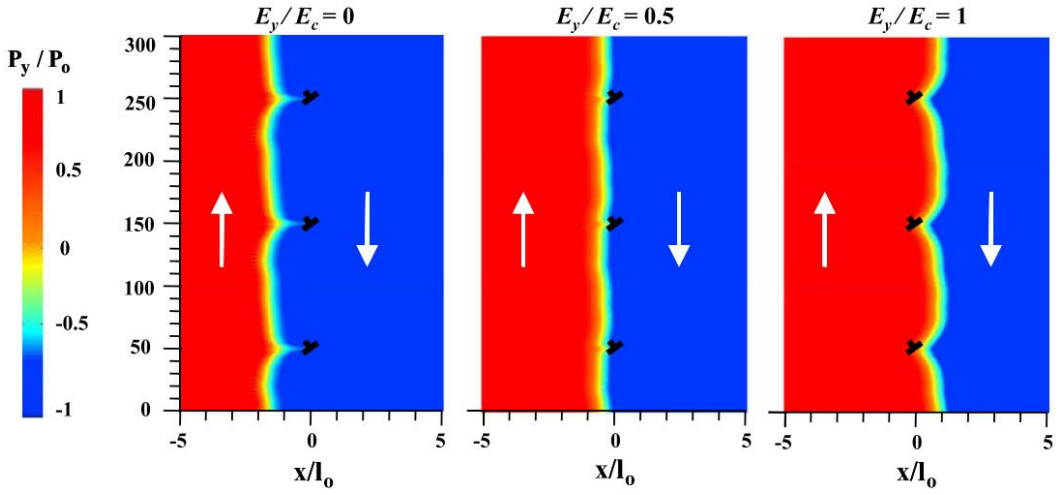

Figure 1.12: Phase-field simulations of a domain wall interacting with dislocations under an external electric field, E_y [75]. Reprinted from Ref. [75], with permission from Elsevier.

nanoscale [73]. These models have been employed to investigate the temporal evolution of domain patterns at different temperatures [73] and sizes in $BaTiO_3$ [74], see Fig. 1.13(a - c).

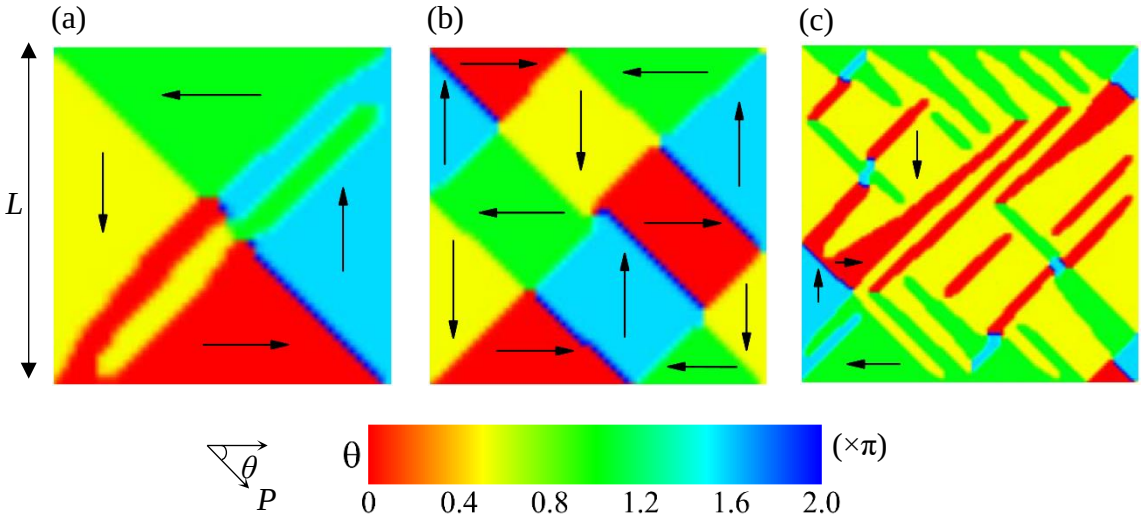

Figure 1.13: Monte Carlo simulations of domain patterns formed in $BaTiO_3$ of different sizes L labelled numerically (a) L = 41 (b) L = 55 (c) L = 126. The arrows show polarization orientation in domains [74]. Reprinted from Ref. [74], with the permission of AIP Publishing.

Both the phase-field method and Monte Carlo simulation, approach an equilibrium state through energy minimization. In the phase-field method, both the mechanical and electrical equilibrium equations are solved at each iteration, while Monte Carlo simulations often assume mechanical equilibrium to be attained much faster than electric dipole relaxation [74]. Although such an assumption makes the Monte Carlo simulations computationally less intensive in comparison to the phase-field methods, these models do not accurately solve elastic strain interactions at the nanoscale. These interactions can affect domain arrangements and evolution, and hence an approach based on the phase-field method is more reliable to design nanoscale devices.

Atomistic models

The advances in synthesis of ferroelectric crystals and ability to attain data at atomic level, have led to the study of structural and chemical complexity [75]–[77]. Progress in atomistic scale modelling which predicts the lattice structure and atomic interactions, has led to a growing interest in the origin of ferroelectricity. Examples of this category of models include the first-principles method [76], and molecular dynamics models [77]. These models assume a starting state at absolute zero temperature with a defined lattice structure. In the first-principles method, the atomic forces are modelled using quantum-mechanical methods and the atoms are allowed to adjust position to approach a minimum energy state. Meanwhile, the molecular dynamics model treats the atoms in a crystal structure to be connected as if through nonlinear ‘springs’, and the arrangement of atoms is based on minimizing the energy stored in these springs [78]. Both these methods have been applied to discover new

materials, as they typically require little or no empirical input, and they can investigate hypothetical crystal structures [79].

A shortcoming in the first principles approach is that the calculations are carried out at absolute zero temperature, and extrapolation to other temperatures is not completely reliable. Further, atomistic and molecular dynamics models can be practically applied to study ferroelectric properties only at the scale of a few unit cells up to a few thousand unit cells. Simulation of nanoscale domain patterns is computationally expensive in comparison to continuum models.

Overall, the macroscopic models predict bulk ferroelectric behaviour assuming averaged properties, while atomistic models predict ferroelectric crystal structure and help investigate atomic or molecular properties of the material. However both these methods are not ideal for the study of nanoscale ferroelectrics. Microscopic models such as phase-field methods which account for nanoscale features such as domain walls, and predict realistic material behaviour at equilibrium are currently powerful modelling tools at this scale. In this thesis, the phase-field modelling approach is used for its advantages in describing ferroelectric behaviour at the nanoscale. Further details on a phase-field model developed by Landis and co-workers are discussed in section 2.2 of chapter 2.

1.4 Layout of thesis

My doctoral study aims to apply a phase-field model to the development of nanoscale ferroelectric device concepts and to the exploration of ferroelectric properties at the nanoscale. A phase-field model originally developed by Landis and co-workers

[29], [68] is used to explore $BaTiO_3$ properties at the nanoscale. In my research, I have applied the phase-field model:

(1) to demonstrate nano-actuator concepts based on ferroelectric switching [80]–[82],

(2) to study the scaling and surface effects on nanoscale polarization patterns [83], and

(3) to study the stability of periodic polarization patterns in tetragonal ferroelectrics at the nanoscale [84]–[86].

I have coded the phase-field model in Fortran, based on original code by the Landis group, but extending it to solve for three dimensional topologies. The results from my study provide insight into ferroelectric behaviour at the nanoscale and explore the prospects of $BaTiO_3$ in nanoscale devices. Throughout, an attempt is made to relate the simulations to experimental evidence.

Chapter 2 describes the theory of the Landis phase-field model and the finite element framework used for computations. This chapter illustrates the simulation techniques, such as the control of polarization viscosity in achieving equilibrium domain patterns, and discusses the types of domain walls in tetragonal ferroelectrics. Chapter 2 also describes the extension of the phase-field model to solve for three dimensional structures and discusses the computational power requirements for these simulations. This chapter illustrates simple simulations to validate the Landis phase-field model and to provide confidence in its use for further study.

Chapter 3 demonstrates nano-actuator concepts based on ferroelectric switching using the phase-field model as a design tool. An actuation cycle is demonstrated in three designs of device namely a ‘clamped’, an ‘embedded’ and a ‘bending’ actuator. The mechanical strains which accompany ferroelectric switching are several times greater than the strains attained due to the piezoelectric effect alone. The domain evolution during an actuation cycle is tracked and the actuation force is calculated using

the phase-field model. The space of design parameters which can be controlled through manufacturing processes, such as aspect ratio and electrode coverage, is explored to increase the actuation strains produced by the actuators. The resulting device designs are predicted to be about an order of magnitude more effective than simple piezoelectric devices.

Chapter 4 explores several issues that arise in nanoscale devices: scaling effects, the effect of surface conditions and the effect of crystallographic orientation. These features affect the nature of polarization patterns, for example vortices, that form. Generic configurations of nanodot/nanowire cross-sections that are expected to form minimum energy flux closure states, monodomains, or non-ferroelectric states, depending on size and surface conditions are explored. The free energy of several commonly occurring polarization patterns is calculated and plotted as a function of nano-wire width. Surface energy and surface conductivity are shown to have significant effects on domain patterns at the nanoscale. A ‘phase-diagram’ is developed which indicates the minimum energy domain patterns at various combinations of scale and surface condition. The results from the study are discussed in the context of experimental observations of ferroelectricity in nanoparticles, and provide new insight into the experiments.

In chapter 5, the stability of nanoscale periodic polarization patterns in barium titanate is explored. In a previous work [87], certain periodic polarization patterns were identified to form as minimum energy states in tetragonal ferroelectrics. While some of these polarization patterns with stripe-like features are commonly observed, other patterns with vortex-like structures are rarely seen. In this chapter, the stability of eight previously identified periodic polarization patterns is tested using the phase-field model. A periodic structure of $BaTiO_3$ is modelled with zero average stress and electric

field boundary conditions, which allows the domain pattern to adopt any periodic values of strain and electric potential needed to stabilize at equilibrium. The response of periodic domain patterns to electro-mechanical fields is explored and possible paths of domain evolution which lead to the formation of complex domain patterns is indicated. A concept design for a thin film energy harvester containing a stripe laminate pattern is demonstrated.

Chapter 6 presents a discussion of the contents of the thesis and speculates on the future outlook. The spirit of the current doctoral study is to provide insight on nanoscale behaviour of ferroelectrics and to explore the prospects of using ferroelectrics in nanoscale devices such as actuators and energy harvesters. The results on nano-actuator device concepts and design parameter optimization might benefit the industrial application of ferroelectrics. The study on scaling effects and surface conditions helps explain recent experimental observations on nano-ferroelectricity and could serve as an initial step for nanoscale experimentation in the future. The phase-field model extended to solve for three dimensional topologies serves as a potential tool to further explore evolution of ferroelectric domains in a 3D architecture and is ‘realistic’ enough to engineer nanoscale devices. The research on periodic laminate patterns aims to provide further insight on the stability of polarization patterns observed in nature and explores the prospects of a new design of energy harvester.

2

Phase-field model of ferroelectrics

The phase-field method models a diffuse interface between two ‘phases’ by a continuous variation of an order parameter. This enables us to model the variation in composition at the interface or to track interface movement. In ferroelectrics, the ‘phases’ are not phases in the ordinary sense, but instead represent domains and are distinguished by their order parameter – polarization. The diffuse interfaces in ferroelectrics are the domain walls that produce gradients of polarization, strain and electric potential. In the current study, a Fortran code of the phase-field model in two dimensions, developed by Landis and co-workers [29] is employed. This code is extended to solve for three dimensional ferroelectric structures.

The aim of the present chapter is to describe the theory of the phase-field method and the implementation of Landis phase-field model in a finite element framework. In this chapter the time dependent Ginzburg-Landau equation is derived and its working is demonstrated through a simple model. Next, the constitutive relationship of the Helmholtz free energy used in the Landis model and the steps involved in the Fortran code are described. Finite element simulation techniques, such as the initialization of phase-field simulations and control of domain evolution, are discussed. The model is tested in simple configurations to validate its solutions. Next, the extension of the finite element code to solve for three dimensional ferroelectric

structures is demonstrated, and finally, practical constraints arising due to the computational power requirements of the phase-field simulations are discussed.

2.1 The Ginzburg-Landau theory – a simple example

The Landau-Devonshire theory described by Eq. (1.15) in section 1.3, models the properties of a uniformly polarized bulk ferroelectric system at phase transition. However, this theory ignores any spatial gradients in polarization. During the cubic-tetragonal phase transition, multiple domains separated through domain walls typically form in ferroelectrics. At the nanoscale, the energy contribution from these domain walls becomes significant, and the net free energy of a ferroelectric system would need to account for such contributions. By accounting for energy due to polarization gradient, and then minimizing the total energy, phase-field methods can simulate domain structure at the nanoscale.

The Landau-Ginzburg theory is a generalized theory of energy minimization, originally developed in the context of superconductivity, but applicable to a variety of physical phenomena. In the context of ferroelectrics, the theory describes the free energy of a ferroelectric system by accounting for the change in polarization values at the domain walls [56]. The phase-field model is based on this Landau-Ginzburg theory. This theory tracks an **order parameter** – a physical quantity that identifies the local domain state at each point in space, for example polarization in the case of ferroelectrics. Note that strain is not a suitable order parameter in $BaTiO_3$ as it fails to distinguish domains with opposite polarization oriented along the same crystallographic axes. On the other hand, polarization takes unique values for each type of domain and has a gradient across all domain walls. Adding an energy contribution due to

polarization gradient in Eq. (1.15), the Landau-Ginzburg theory describes the Helmholtz free energy density ψ as:

$$\psi = \alpha\left(\nabla P^2\right) + \frac{1}{2}\kappa P^2 + \frac{1}{4}\xi P^4 + \frac{1}{6}\gamma P^6 + \frac{1}{2}c\varepsilon^2 + \frac{1}{2}q\varepsilon P^2 \tag{2.1}$$

The coefficient values in Eq. (2.1) can be derived from experimental data or first principles calculations. Here, $\alpha(\nabla P^2)$ is the simplest possible term that can account for the polarization gradient at domain walls or near surfaces and helps to describe a realistic ferroelectric behaviour at the nanoscale. The energy must depend on ∇P and the dependence must be of order at least $(\nabla P)^2$ for symmetry. The series expansion of polarization terms, $(\frac{1}{2}\kappa P^2 + \frac{1}{4}\xi P^4 + \frac{1}{6}\gamma P^6)$ in Eq. (2.1) represents the bulk energy of polarized domains in a ferroelectric specimen. These terms define the shape of the free-energy well, where a spontaneously polarized domain is associated with minimum energy. Internal stress fields due to lattice misfit and the piezoelectric coupling effects are accounted by the elastic energy term, $\frac{1}{2}c\varepsilon^2$ and the piezoelectric term, $\frac{1}{2}q\varepsilon P^2$ respectively.

Phase-field models based on the Landau-Ginzburg theory can describe domain evolution and domain arrangement in ferroelectrics. By including gradients of the order parameter in the free energy, Ginzburg-Landau models provide a simulation method based on energy minimization. The derivation of this simulation method or the time dependent Ginzburg-Landau (TDGL) equation is next described. In order to simplify the TDGL derivation, the free energy, ψ is expressed only in terms of polarization, $\mathbf{P}$ as, $\psi = \psi\ (\mathbf{P}, \nabla\mathbf{P}, \nabla\mathbf{P} \otimes \nabla\mathbf{P}, \ldots)$, and the dependence on $\nabla\mathbf{P}$ can be expressed as a Taylor series sum as,

$$\psi = f(\mathbf{P}) + \frac{a_1}{1!}|\nabla\mathbf{P}| + \frac{a_2}{2!}|\nabla\mathbf{P}|^2 + \frac{a_3}{3!}|\nabla\mathbf{P}|^3 + \frac{a_4}{4!}|\nabla\mathbf{P}|^4 + \ldots \tag{2.2}$$

Here a_i for i = 1, 2, 3… are assumed constants. In Eq. (2.2) the $\nabla\mathbf{P}$ dependence should be even for symmetry, and it follows that, the free energy ψ is given by,

$$\psi = f(\mathbf{P}) + \frac{a_2}{2!}|\nabla\mathbf{P}|^2 + \frac{a_4}{4!}|\nabla\mathbf{P}|^4 + \ldots \tag{2.3}$$

The simplest case of the free energy expression, upon neglecting the contribution from the higher order terms is,

$$\psi = f(\mathbf{P}) + \frac{a_2}{2}|\nabla\mathbf{P}|^2 . \tag{2.4}$$

In Eq. (2.4), it can be noted that the energy of the ferroelectric system (where the domain patterns are typically associated with non-uniform polarization) is described as a sum of the local polarization, $f(\mathbf{P})$, and that of its immediate environment, $\frac{a_2}{2}|\nabla\mathbf{P}|^2$.

For simplicity, consider a 1-dimensional region of infinite extent $-\infty \le x \le +\infty$, with P being a scalar order parameter. Let the region have cross-sectional area A. Then the net energy, Ψ is obtained on integrating Eq. (2.4):

$$\Psi = A\int_{-\infty}^{\infty} \psi \, \mathrm{d}x = A\int_{-\infty}^{\infty} f(P) + \frac{a_2}{2}\left|\frac{\mathrm{d}P}{\mathrm{d}x}\right|^2 \mathrm{d}x. \tag{2.5}$$

Next, in order to minimize this net energy of the ferroelectric system, a variation of Ψ is considered,

$$\delta\Psi = A\int_{-\infty}^{\infty}\left(\frac{\mathrm{d}f}{\mathrm{d}P} - \alpha\frac{\mathrm{d}^2P}{\mathrm{d}x^2}\right)\delta P \mathrm{d}x . \tag{2.6}$$

The phase-field simulations achieve minimization of the free energy by a relaxation process that allows the ferroelectric system to approach equilibrium. For a simple example with linear kinetics, the rate of change of polarization, $\dot{P}$, is given by:

$$\dot{P} = -\frac{1}{\beta}\frac{\delta \Psi}{\delta P}. \tag{2.7}$$

Here β is often called a 'polarization viscosity' constant. Making use of Eq. (2.6) gives the classical time dependent Ginzburg-Landau (TDGL) equation:

$$\beta \dot{P} = \alpha \frac{\mathrm{d}^2 P}{\mathrm{d}x^2} - \frac{\mathrm{d}f}{\mathrm{d}P}. \tag{2.8}$$

Eq. (2.8) describes an energy minimization process with gradient terms, but does not specify the constitutive behaviour of the material for which a specific $f(\mathbf{P})$ is needed. In order to demonstrate the working of the TDGL equation, a simple model of $f(P)$ that describes a multi-well potential is considered. That is, $f(P)$ is a double quadratic function which has minima at the spontaneous polarization values, for example,

$$f(P) = \gamma (P+1)^2 (P-1)^2. \tag{2.9}$$

Eq. (2.9) generates the multi-well potential as shown in Fig. 2.1, with minimum at $P = -1$ and $P = 1$. To further simplify Eq. (2.9), $\gamma = 1$ is chosen. Eq. (2.9) generates a particular form of the time dependent Ginzburg-Landau equation, and can be used to demonstrate certain solutions of interest, for example the formation of a domain wall at equilibrium.

In order to demonstrate the working of the TDGL equation, a one dimensional (1D) region of extent $-3 \le x \le 3$, is considered, see Fig. 2.2. An initial polarization state for this 1D region is shown in Fig. 2.2 – two types of domains with $P = -1$ and $P = 1$ separated by a sharp interface is assumed in the initial state. The plot of polarization variation as a function of position, x in this initial state is shown in Fig. 2.3(a). Here, the aim is to employ the TDGL equation to simulate a continuous polarization variation across the domain wall at equilibrium.

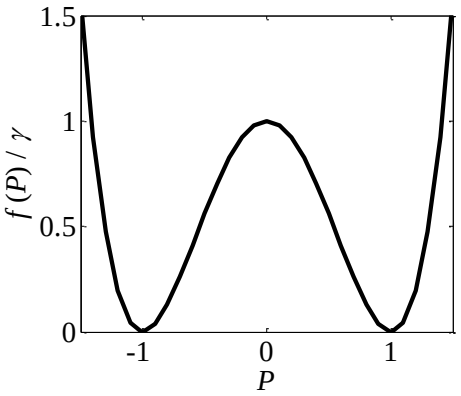

Figure 2.1: Schematic illustration of $f(P)$ describing a multi-well potential, with minima at $P=-1$ and $P=1$.

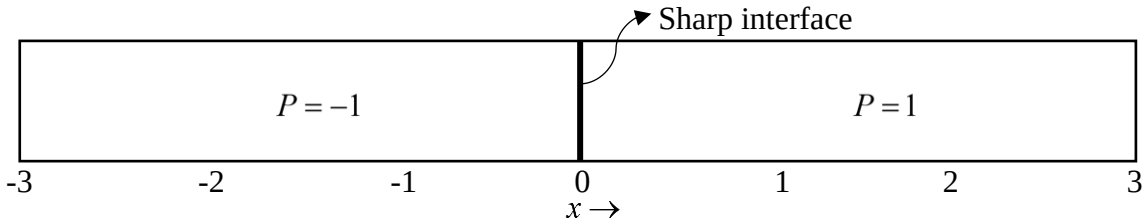

Figure 2.2: Schematic illustration of polarization variation across the region $-3 \le x \le 3$, with a sharp interface at $x=0$.

The TDGL equation to be solved is obtained as follows: at first, the derivative of $f(P)$ in Eq. (2.9) is substituted in Eq. (2.8), and $\alpha = 1$ is used for numerical simplification. This results in a second order differential equation in P,

$$\frac{\mathrm{d}^2 P}{\mathrm{d}x^2} - 4(P^3 - P) = \beta \frac{\mathrm{d}P}{\mathrm{d}t}. \tag{2.11}$$

Eq. (2.11) is a form of the TDGL equation and is solved iteratively to numerically simulate the polarization variation at equilibrium ($\beta = 0$). In the initial state the polarization values corresponding to Fig. 2.2 are substituted in Eq. (2.11) and the polarization viscosity is set at $\beta = 100$; the polarization increments, $\mathrm{d}P$ are

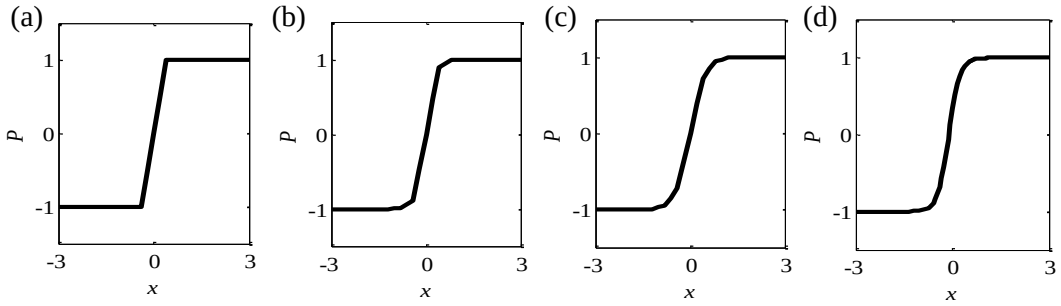

Figure 2.3: Variation of polarization across region x, as the polarization viscosity β is decreased from 100 to 0 during the phase-field simulation. (a) The initial state, at $\beta = 100$; and (b) at $\beta = 50$ and (c) $\beta = 1$; and finally (d) at equilibrium, $\beta = 0$. Note that subfigures (b) and (c) do not show equilibrium states.

evaluated by linearly reducing the value of β in steps of $\Delta\beta = 1$, while the time increment is held constant at $\mathrm{d}t = 1\mathrm{s}$; the evolution of polarization is then calculated by incrementing the values of P as, $P^{t+\mathrm{d}t} = P^t + \mathrm{d}P$. For the system described in Fig. 2.2, the evolution of polarization across region x is shown in Fig. 2.3(b-c). Here, the sharp change in polarization at the domain wall begins to smooth/diffuse as the value of β is reduced.

Finally, the polarization variation at equilibrium is solved by evaluating, $\frac{\mathrm{d}^2P}{\mathrm{d}x^2} - \frac{\mathrm{d}f}{\mathrm{d}P} = 0$ or $\frac{\mathrm{d}^2P}{\mathrm{d}x^2} - 4(P^3 - P) = 0$ in the range $-3 \le x \le 3$. This equation can be expressed in a linear differential equation form as,

$$\left(\frac{\mathrm{d}P}{\mathrm{d}x}\right)^2 = 4\left(\frac{P^4}{2} - P^2\right) + c \tag{2.12}$$

and solved with the boundary conditions $\frac{\mathrm{d}P}{\mathrm{d}x} \to 0$ as $P \to \pm 1$, giving $c = 2$. Setting $P = 0$ at $x = 0$, the polarization variation across region x at equilibrium, from Eq. (2.12) is shown in Fig. 2.3(d). Here, a diffuse domain wall is formed. The evolution

of the domain wall with a sharp polarization gradient, Fig. 2.3(a), to a diffuse form, see Fig. 2.3(b-d), is the result of energy minimization using the TDGL equation. This example demonstrates the behaviour of the TDGL equation using a simple model of $f(P)$.

The Landis phase-field model is based on the same concept of the time-dependent Ginzburg-Landau equation [29] but is a more complicated application. This results in a slightly different form of the governing equation,

$$\beta \dot{P}_i = \left(\frac{\partial \psi}{\partial P_{i,j}} \right)_{,j} - \frac{\partial \psi}{\partial P_i} . \tag{2.13}$$

Here, $P_{i,j}$ represents a gradient in polarization and ψ is the energy function. Eq. (2.13) is the TDGL equation used in the present phase-field model and is derived similarly to Eq. (2.8). However, the energy function, ψ used in Eq. (2.13) is a more complicated energy potential accounting for the constitutive behaviour of the ferroelectric, such as the electrical, mechanical and coupling properties. The constitutive form of the energy function used in the Landis model is discussed in the next section.

2.2 The Landis phase-field model

In ferroelectrics, phase-field models have been used for a variety of applications [22], [66], [67], [89]: for example, Dayal and Bhattacharya [42] explored domain patterns and domain evolution in complex geometries without any a priori assumptions on electrode arrangement and dielectric properties. L. Q. Chen and co-workers [22] applied phase-field modelling techniques to investigate thin film properties, such as the effect of substrate strain on Curie temperature. Morozovska et al. [30] employed a

phase-field approach to study size effects on polarization patterns, while Cao and Cross [90] described fine scale tetragonal twin structures in perovskite ferroelectrics. The phase-field model developed by Landis and co-workers [29], [68] was used to study nanoscale ferroelectric behaviour such as domain energetics [68], domain wall interactions with dislocations [29], and domains near crack tips in ferroelectric materials [91]. Abdollahi and Arias [92] propose a phase-field model that couples the microstructure evolution and propagation of cracks in ferroelectric materials. The differences between these various phase-field models [22], [29], [42], [92] that have been developed are subtle, and can be distinguished on the basis of the terms included in the free energy expression. For example, Völker et al. [93] employ multiscale modelling methods to derive Helmholtz free energy coefficients for the phase-field model from atomistic simulations.

In the Landis phase-field model, the Helmholtz free energy, ψ of the system is calculated as a function of strain, ε_{ij}, electric displacement, D_i, polarization, P_i, and polarization gradient, $P_{i,j}$. The free energy expression, $\psi(\varepsilon_{ij}, D_i, P_i, P_{i,j})$ chosen by Su and Landis [29] takes the form:

$$\begin{aligned}\psi = &\frac{1}{2}a_{ijkl}P_{i,j}P_{k,l} + \frac{1}{2}\bar{a}_{ij}P_iP_j + \frac{1}{4}\bar{\bar{a}}_{ijkl}P_iP_jP_kP_l \\ &+ \frac{1}{6}\bar{\bar{\bar{a}}}_{ijklmn}P_iP_jP_kP_lP_mP_n + \frac{1}{8}\bar{\bar{\bar{\bar{a}}}}_{ijklmnrs}P_iP_jP_kP_lP_mP_nP_rP_s \\ &+ b_{ijkl}\varepsilon_{ij}P_kP_l + \frac{1}{2}c_{ijkl}\varepsilon_{ij}\varepsilon_{kl} + \frac{1}{2}f_{ijklmn}\varepsilon_{ij}\varepsilon_{kl}P_mP_n \\ &+ \frac{1}{2}g_{ijklmn}\varepsilon_{ij}P_kP_lP_mP_n + \frac{1}{2\kappa_0}(D_i - P_i)(D_i - P_i).\end{aligned} \tag{2.14}$$

Here, the coefficients $\mathbf{a}\ldots\bar{\bar{\bar{\mathbf{a}}}}, \mathbf{b}, \mathbf{c}, \mathbf{f}$ and $\mathbf{g}$ are derived to fit the material properties of a monodomain single crystal barium titanate as measured by Li et al. [58] at room temperature $(\sim 22°\text{C})$ and are listed in the appendix of this thesis. κ_0 is the permittivity

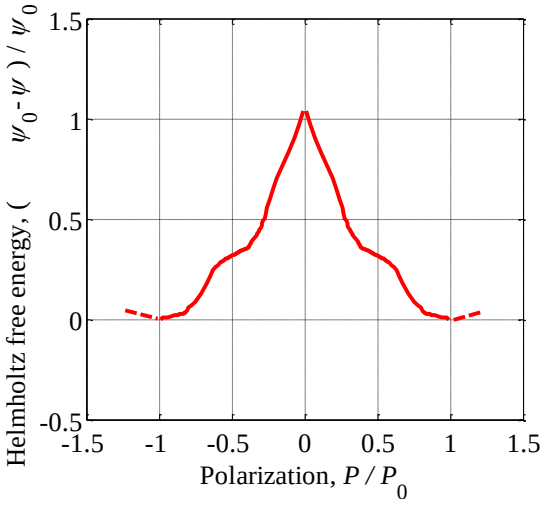

Figure 2.4: Free energy curve from Eq. (2.14). ψ_0 represents the energy per unit volume of a spontaneously polarized monodomain, and $P_0 = 0.26\text{C/m}^2$ for barium titanate.

of free space and is equal to 8.854×10^{-12} F/m. The free energy curve in Eq. (2.14) is plotted as a function of polarization in Fig. 2.4, and possesses minimum energy at the spontaneously polarized states, $P = \pm P_0$. In Fig. 2.4, the free energy is normalized as $\tilde{\psi} = (\psi_0 - \psi)/\psi_0$, where ψ_0 is the free energy per unit volume of a spontaneously polarized monodomain. The normalization of other physical quantities used in the present work are described in detail in section 2.3.

The energy contributions appearing in the free energy expression, Eq. (2.14) are,

(a) Gradient energy, $\left(\frac{1}{2} a_{ijkl} P_{i,j} P_{k,l}\right)$: This energy contribution also referred to as the exchange energy, accounts for variations in polarization at the domain walls or near surfaces. The coefficient a_{ijkl} is treated as a scale, $a_0 \sim 1\times10^{-10}\text{Vm}^3/\text{C}$ and is important in determining the domain wall thickness and the domain wall surface energy.

(b) Bulk energy, $\left(\frac{1}{2}\bar{a}_{ij}P_iP_j+\frac{1}{4}\bar{\bar{a}}_{ijkl}P_iP_jP_kP_l+\ldots+\frac{1}{8}\bar{\bar{\bar{a}}}_{ijklmnrs}P_iP_jP_kP_lP_mP_nP_rP_s\right)$: These terms in Eq. (2.14) are used to describe the non-convex energy landscape of the free energy curve, whose minima are located at the spontaneous polarization states, see Fig. 2.4. Higher order terms in the bulk energy expression, such as the eighth rank polarization term in the equation allow for adjustments of the energy barriers in $90°$ switching [94], while the sixth rank polarization term introduced by Landis and co-workers [29] fits the elastic, piezoelectric and dielectric properties of the tetragonal phase in its spontaneous state. Prior to the introduction of the higher order polarization terms, the elastic energy contribution primarily arose from the elastic energy coefficient tensor $\mathbf{c}$. This implied that the elastic properties at the tetragonal phase were the same as at the cubic phase. However the highly anisotropic nature of barium titanate in its tetragonal state causes variation in elastic properties that are different from the cubic state [95]. Thus the bulk energy contribution described in the Landis phase-field model is more accurate in fitting the free energy curve.

(c) Elastic-piezoelectric energy, $\left(b_{ijkl}\varepsilon_{ij}P_kP_l+\frac{1}{2}c_{ijkl}\varepsilon_{ij}\varepsilon_{kl}+\frac{1}{2}f_{ijklmn}\varepsilon_{ij}\varepsilon_{kl}P_mP_n\right.$

$\left.+\frac{1}{2}g_{ijklmn}\varepsilon_{ij}P_kP_lP_mP_n\right)$: These terms are used to fit the elastic and piezoelectric properties of the material near its spontaneous state. Landis and co-workers [29] have introduced the additional terms with tensors $\mathbf{f}$ and $\mathbf{g}$ in their model, in order to allow for a more accurate characterization of the material properties. For example, these tensors help to fit the piezoelectric coefficients near the spontaneous

state, which was previously not possible in phase-field models that accounted for energy contribution from the term with the **b** tensor alone.

(d) Free space energy, $\left(\frac{1}{2\kappa_0}(D_i - P_i)(D_i - P_i) \right)$: This accounts for the energy stored in free space occupied by the material.

Further details and the values of the tensorial coefficients used in Eq. (2.14) are listed in the appendix and given in detail in the work of Landis and co-workers [29], [68].

The phase-field model is solved in a finite element framework. Here, the nodal degrees of freedom are given by mechanical displacement, u_i, electric potential, ϕ, and polarization, P_i. An overview of the finite element formulation employed by Su and Landis [29] for a two-dimensional (2D) system is illustrated in Fig. 2.5(a-e) as a flowchart.

In Fig. 2.5(a), a mesh with 8-noded quadratic elements each with four Gauss points or integration stations is generated. Subsequently, an array of the nodal degrees of freedom **d** is defined. The displacement and force boundary conditions (as defined by the problem to be solved) are next applied to the finite element mesh. The numerical modelling of domain wall kinetics is controlled by gradually reducing polarization viscosity, β. It is worth noting that the kinetics of domain wall motion in $BaTiO_3$ are not universally agreed upon [96], [97]. As a result, the phase-field model only reliably solves for equilibrium states, in which $\beta \to 0$. In order to approach equilibrium, the model assumes linear kinetics but then reduces the β value incrementally. That is, the simulation is typically started by assigning a large value to polarization viscosity, such as $\beta = 1000$ and its value is gradually reduced to zero. A detailed description of controlling β values during a typical phase-field simulation is given in section 2.5.

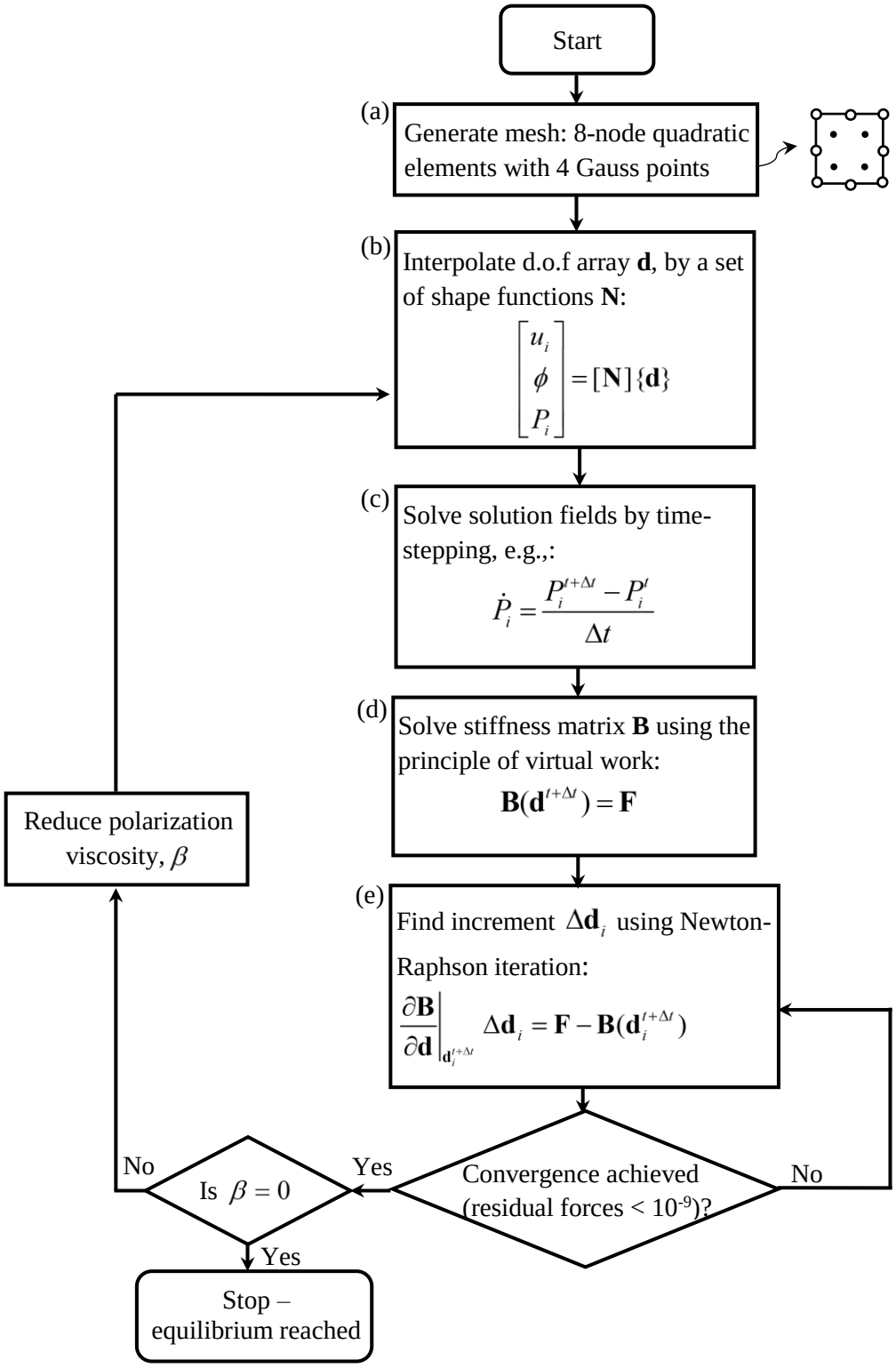

Figure 2.5: A flowchart of the finite element code for the Landis phase-field model.

In Fig. 2.5(b), the field quantities, such as strain ε_{ij}, electric field E_i, are interpolated from the nodal quantities to the integration stations within each element, using quadratic shape functions **N**. Next, the phase-field model predicts domain evolution by integrating the governing equations in time. That is, the nodal quantities (displacement, electric potential, polarization) and the polarization rates are stepped forward in time, see Fig. 2.5(c). Further details on the integration scheme employed by Su and Landis in the Fortran code are given in Ref. [29] and are listed in the appendix of this thesis. The integrated values of nodal displacement at time $t+\Delta t$ and the nodal force vector **F** can be related using a stiffness matrix **B**, see Fig. 2.5(d). The equation in Fig. 2.5(d) is then solved using Newton-Raphson iteration, see Fig. 2.5(e). Each iteration is carried out for up to 20 steps, with the increments in displacement values, $\Delta\mathbf{d}$ calculated at each step. For example in Fig. 2.5(e), *i* is the current step counter in a given Newton-Raphson iteration, and the increment $\Delta\mathbf{d}_i$ is computed for $\mathbf{d}_i^{t+\Delta t}$ as $\mathbf{d}_i^{t+\Delta t} = \mathbf{d}_{i-1}^{t+\Delta t} + \Delta\mathbf{d}_i$. This computation is continued until the solution converges – i.e., the calculated values of residual displacements are small $(<10^{-9})$. This way, the solution for nodal degrees of freedom at time step $t+\Delta t$ is obtained. The next iteration is carried out by reducing the value of polarization viscosity, β, and the solution marches forward through time. Equilibrium is reached when $\beta = 0$ and the phase-field simulation is complete. The nodal displacements are calculated at equilibrium and are used to compute the field quantities, such as the strain, ε_{ij}, electric field, E_i, and polarization gradient, $P_{i,j}$, at the integration points within each element. The gradients are required to calculate the free energy ψ of the ferroelectric system. The values of

stress, σ_{ij}, and electric displacement, D_i, are calculated as derivatives of the free energy as discussed in section 1.3, of chapter 1.

In this thesis, the Landis phase-field model is used because of its several advantages: first, this phase-field model solves for both mechanical and electrical equilibrium equations in order to find the minimum energy domain configuration. By solving both the equilibrium equations, the accuracy in finding a minimum energy state is high in comparison to other models [74] where often electrical equilibrium equations only are solved to identify minimum energy states. Second, it describes the energy contribution from the higher order polarization terms that allows for adjustments in elastic, piezoelectric and dielectric properties near the spontaneously polarized state and correctly fitting the energy barriers for $90°$ switching. For example, previous works commonly assumed coefficients for the elastic energy term in Eq. (2.1), based on the cubic state of $BaTiO_3$, and did not accurately describe the elastic properties at the spontaneously polarized state [94], [96]. This is significant because of the highly anisotropic nature of tetragonal $BaTiO_3$, where the elastic and dielectric moduli vary by a factor of 10 or more with direction. To counter this problem, Landis and co-workers derived the free energy terms that model elastic properties with tetragonal crystal symmetry. They introduced additional elastic and piezoelectric energy terms, which allow the model to fit the low symmetry phase in the spontaneous ferroelectric state. Finally, the Landis model accounts for the non-linear change in piezoelectric coefficient that can be observed from the changing slope of the butterfly loop in the strain-electric field curve shown in Fig. 1.5(b) and Fig. 1.6(b) at different positions on the curves.

The Landis phase-field model faces challenges with respect to the domain wall dynamics. For example, there is a need for detailed thermodynamic and kinetic input, with respect to domain wall movement and domain evolution, in the model. The lack of

these kinetics input limits the model's ability to simulate the dynamic dielectric response of ferroelectrics [56] which otherwise would provide interesting insights on nanoscale phenomena such as domain nucleation [97]. In the current study, this drawback is overcome by considering only equilibrium domain patterns and exploring their equilibrium response to electro-mechanical fields. It is also noted that the works of Landis and co-workers solve for two-dimensional (2D) topologies only [56]. This prevents the simulation from modelling out-of-plane polarized domains. In the current doctoral research, the 2D phase-field model has been extended to solve for three dimensional (3D) topologies and this has enabled the study of 3D periodic polarization patterns in chapter 5. Although the Landis phase-field model has certain limitations, it is currently one of the most powerful tools available to study nanoscale ferroelectric behaviour and to develop conceptual device designs [66]. In sections 2.4-2.8 of this chapter, the Landis phase-field model is employed to study certain simple examples such as simulating a monodomain or domain pattern with a 180° wall. The physical quantities such as stress, electric field or free energy that appear in these simulations are normalized and the corresponding constants are described in the next section.

2.3 Normalization

Normalization can be described as representing physical quantities, such as stress or electric field, in a dimensionless form. The physical quantities that are computed during the phase-field simulations in the present work have been normalized, and are listed in Table 2.1. Note the tensorial physical quantities in Table 2.1 are represented along one-dimension.

Table 2.1 represents the normalizations of commonly occurring physical quantities in the present work. The polarization and strains are normalized by $P_0 = 0.26\text{C/m}^2$ and $\varepsilon_0 = 0.0082$ respectively, which arises from the spontaneous state of barium titanate. Note that $BaTiO_3$ has tetragonal symmetry, and possesses a transverse spontaneous strain $\varepsilon_0^t = -0.0027$. $E_0 = 21.82\text{MV/m}$ is the normalization constant for electric field, and corresponds to the critical field required to cause homogeneous $180°$ switching of a spontaneously polarized monodomain in barium titanate. By equating mechanical and electrical energies, the normalization for stress is derived as $\sigma_0 = E_0 P_0 / \varepsilon_0 = 692\text{MPa}$. The characteristic length scale in this model is $l_0 = \sqrt{a_0 P_0 / E_0} = 1\text{nm}$, where $a_0 = 1\times10^{-10}\,\text{Vm}^3/\text{C}$ is a coefficient used in specifying the gradient energy term in Eq. (2.14) [29]. The electric potential normalization is derived from the electric field and length scale normalizations as $\phi_0 = E_0 l_0 = 0.022\text{V}$. Finally,

Physical quantities	Normalizing constant	Units	Normalized quantity
Polarization, P	$P_0 = 0.26\text{C/m}^2$	C/m^2	P / P_0
Strain, ε	$\varepsilon_0 = 0.0082$	–	$\varepsilon / \varepsilon_0$
Electric field, E	$E_0 = 21.8247\text{MV/m}$	MV/m	E / E_0
Stress, σ	$\sigma_0 = E_0 P_0 / \varepsilon_0 = 692\text{MPa}$	MPa	σ / σ_0
Electric potential, ϕ	$\phi_0 = E_0 l_0 = 0.022\text{V}$	V	ϕ / ϕ_0
Length, l	$l_0 = 1\text{nm}$	nm	l / l_0
Free energy, ψ	$\psi_0 = -3.03\text{MJ/m}^3$	MJ/m^3	$(\psi_0 - \psi) / \psi_0$

Table 2.1: Normalization constants of physical quantities used in the present work.

the Helmholtz free energy per unit volume is normalized as, $\tilde{\psi} = (\psi_0 - \psi)/\psi_0$, where $\psi_0 = -3.03\text{MJ/m}^3$ corresponds to the energy per unit volume of a spontaneously polarized monodomain. Here $\psi_0 < 0$, while $\psi = 0$ corresponds to the cubic state with $P_i = 0$. Note that the quantities $\psi, P_i, P_{i,j}$ and $\dot{P}_i$ in the TDGL equation, Eq. (2.13) are all normalized, and hence polarization viscosity, β in the present work is represented as a dimensionless number.

The phase-field model is next tested in simple configurations, such as modelling a monodomain pattern in a 2-dimensional region of barium titanate. The properties of the monodomain are explored at the spontaneous state, and the finite element techniques, such as initialisation of phase-field simulations are discussed.

2.4 Formation of domains

In this section the Landis phase-field model is first employed to simulate a monodomain in a 2-dimensional (2D) region of barium titanate. The properties of the monodomain at its spontaneous state are explored using phase-field simulations.

At first, a two-dimensional (2D) square region of side, L = 20nm is modelled with plane strain and plane electric field conditions. In Fig. 2.6 the corner node ‘A’ at $(x_1, x_2) = (0,0)$ is modelled with fixed supports, that is $u_1 = u_2 = 0$; while node ‘B’ at $(x_1, x_2) = (L,0)$ is modelled with a roller support, $u_2 = 0$. This boundary condition prevents translation and rotation of the 2D region, and is referred to as “simple support” boundary condition for future discussions. In Fig. 2.6, the electric potential of the nodes along the boundaries of the 2D region, namely $x_1 = 0$, $x_2 = 0$, $x_1 = L$ and $x_2 = L$ are set to zero, $\phi = 0$. This boundary condition allows for a non-zero net polarization in the

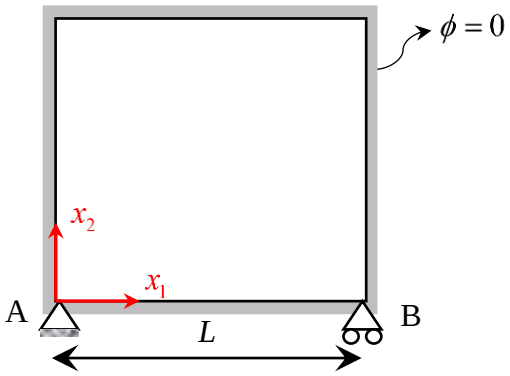

Figure 2.6: Simple support boundary conditions on a square region of $BaTiO_3$, L = 20nm.

domain pattern, and can support a monodomain.

Next, a finite element mesh is generated for the 2D region. The mesh contains 400 square elements, each of size 1nm, see Fig. 2.7(a). Note that the element size is comparable to the unit cell size of $BaTiO_3$ (~ 4Å). It is reasonable to question the validity of the continuum hypothesis. The purpose of assuming the material to be a continuum in the current work is to meaningfully represent features such as domain walls and polarization patterns. The phase-field simulation is initialized by assigning random polarization values on each node of the finite element mesh. The polarization on a node in 2D simulations given by $\mathbf{P} = P_1 x_1 + P_2 x_2$ is assigned as follows: the magnitudes of the polarization components P_i for $i = 1, 2$ are each assigned a random value in the range $-\frac{P_0}{2} \le P_i \le \frac{P_0}{2}$, where $P_0 = 0.26\text{C/m}^2$ is the spontaneous polarization of barium titanate. Then the maximum magnitude of net polarization, $|\mathbf{P}|$ on each node is, $|\mathbf{P}| \le \sqrt{(\pm P_0/2)^2 + (\pm P_0/2)^2} \approx 0.71 P_0$. For future reference in initialising 3D simulations with random polarization values, the P_3 component of polarization is also

taken into account. The direction of the polarization vector on each node is dependent on the values of P_i that are randomly assigned. For example in a 2D simulation, the angular direction of a polarization vector on any node measured from the x_1-axis is given by $\tan^{-1}(P_2 / P_1)$. The other nodal degrees of freedom, namely the displacements, u_i, and electric potential, ϕ, are initialised at zero. For future reference, this initial state is referred to as the "random polarization field" state. From this initial state, the phase-field model solves for equilibrium domain patterns. A typical domain evolution process is shown in Fig. 2.7(a-d).

A monodomain with net polarization, $P_2 = -P_0$ is observed at equilibrium, see Fig. 2.7(d). The monodomain pattern possesses net strains, $\varepsilon_{11} = -0.0027$ and $\varepsilon_{22} = 0.0082$, that correspond to the spontaneous strains of barium titanate. The phase-field model evaluates the free energy per unit volume of the monodomain to be equal to $\psi_0 = -3.03\text{MJ/m}^3$ at equilibrium. This value corresponds to the minimum possible free

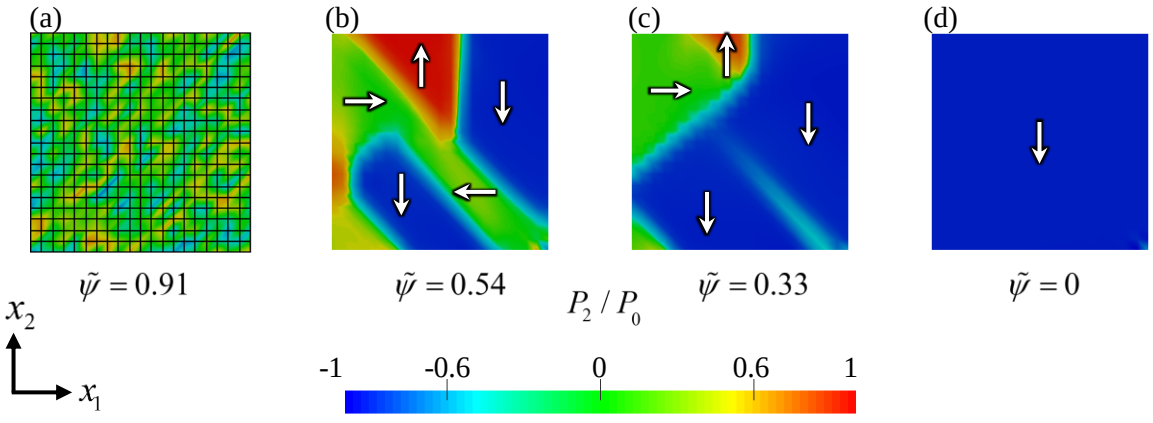

Figure 2.7: Polarization patterns along x_2-axis during the phase-field simulation. (a) showing random polarization field and mesh in the initial state; (b)-(c) showing intermediate states during the phase-field simulation; (d) polarization pattern at equilibrium. $\tilde{\psi}$ is normalized free energy of the domain pattern.

energy and is used as a normalisation constant for free energy in the present work. Therefore, $\tilde{\psi} = \frac{\psi_0 - \psi}{\psi_0}$ is zero for a monodomain in its spontaneous state, see Fig. 2.7(d).

It is interesting to note, if the phase-field simulation was started with a different initial state i.e., the initial polarization values on each node were assigned a random number different from that in Fig. 2.7(a), a new domain pattern can be found at equilibrium. For example in Fig. 2.8(a-d), the phase-field simulation was initialised with a different set of random numbers, and resulted in the formation of a monodomain polarised along the $+x_2$ axis. This example illustrates that the phase-field model can find multiple equilibrium patterns, based on the initial state. However, note that a 180° rotation of the monodomain in Fig. 2.8(d) results in the monodomain formed in Fig. 2.7(d). $\tilde{\psi}$ for both the monodomain patterns formed at equilibrium is zero. That is, in both these cases, the phase-field model has solved for a global minimum energy domain pattern.

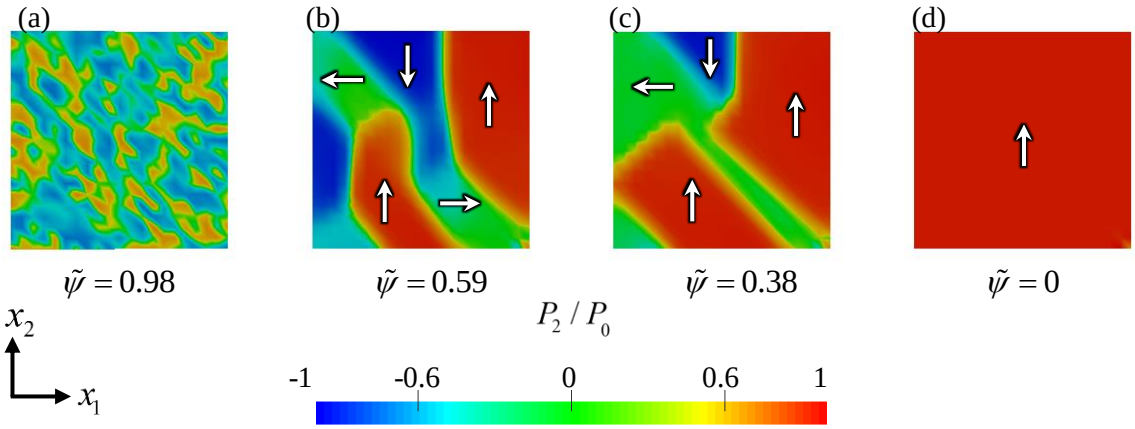

Figure 2.8: Polarization patterns along $x_2 -$axis during the phase-field simulation initialised with a random polarization field. (a) initial state; (b)-(c) showing intermediate states during the phase-field simulation; (d) polarization pattern at equilibrium. $\tilde{\psi}$ is normalized free energy of the domain pattern.

Next, a second method of initialization of the phase-field simulation is discussed. Here, a 2D square region of side L = 20nm, is modelled with the boundary conditions described in Fig. 2.6. For initialization of the phase-field simulation, a chosen polarization pattern is imposed on the 2D square region. That is, the nodes of the finite element mesh are specified with spontaneous polarization values that correspond to the domains in the chosen polarization pattern. The polarization variation in the domain walls is neglected and thus the domain wall is a sharp interface in the initial state. The nodal displacement and electric potential values are set to zero in the starting state, see Fig. 2.9(a). This initial state is referred to as an "imposed polarization pattern" state. It is expected that this method of initialization allows the phase-field model to solve for an equilibrium state with a polarization pattern similar to the imposed pattern. For example, in Fig. 2.9(a), a domain pattern with a 180° wall is imposed in the initial state. This imposed domain pattern is relaxed to find an equilibrium state, see Fig. 2.9(b-d).

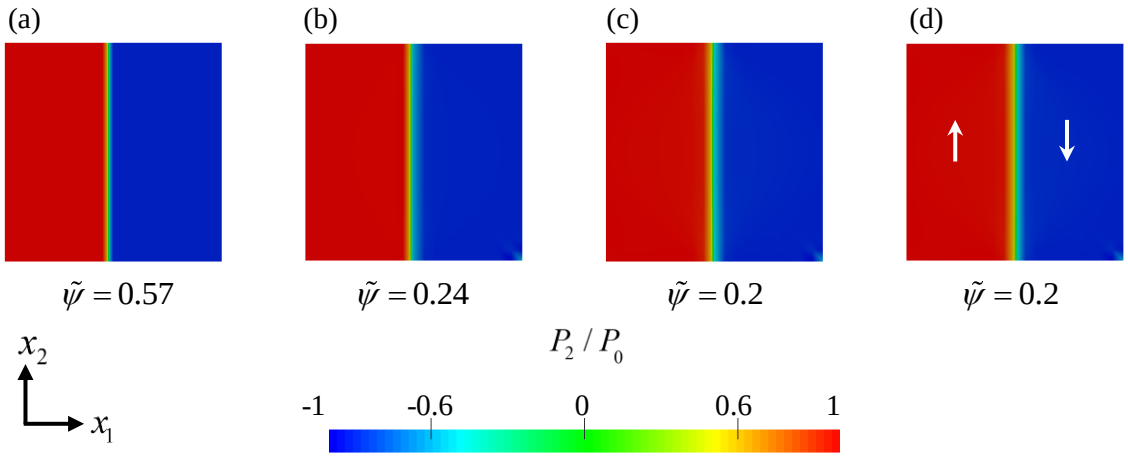

Figure 2.9: Polarization patterns along x_2-axis during the phase-field simulation initialised with an imposed pattern (a) initial state; (b)-(c) showing intermediate states during the phase-field simulation; (d) polarization pattern at equilibrium. $\tilde{\psi}$ is normalized free energy of the domain pattern.

At equilibrium, Fig. 2.9(d), the appearance of a broad 180° domain wall is observed. Here, it is interesting to note that the boundary conditions on the 2D square region in Fig. 2.7 and Fig. 2.9 are exactly the same. However, the phase-field model finds different domain patterns at equilibrium based on the initial states of the simulations. Note, the same equilibrium pattern was obtained when elements of 0.5nm size are used indicating the phase-field simulations to be mesh independent. The domain pattern formed at equilibrium, $\beta = 0$ in Fig. 2.9(d) is of a higher energy state than a monodomain. That is, Fig. 2.9(d), contains a 180° domain wall that contributes to additional gradient energy of the system.

The lack of uniqueness in the equilibrium domain patterns arises because the phase-field model solves for a local equilibrium pattern that does not necessarily correspond to a global energy minimum. For example, Fig. 2.9(d) is stable at equilibrium with a local energy minimum at $\tilde{\psi} = 0.2$, and does not correspond to the global energy minimum achieved by a monodomain with $\tilde{\psi} = 0$. In the present work, this issue is explored, by testing the stability of the domain patterns formed at equilibrium. That is, external electric fields or stresses are applied to disturb the domain pattern from its equilibrium state, and the phase-field model is employed to minimize the net energy of this domain pattern. For example, the equilibrium domain pattern formed in Fig. 2.9(d) is disturbed by applying an external electric field. Here, electrodes are modelled at $x_2 = 0$ and $x_2 = L$ on the equilibrium domain pattern formed in Fig. 2.9(d). While the nodes along $x_2 = 0$ are electrically grounded, a finite electric potential $\phi = -0.92\phi_0$ is applied to the nodes along $x_2 = L$. This sets up an electric field, $E_2 = 1\text{MV/m}$ across the 2D square region. The presence of an external field disturbs the equilibrium state, Fig. 2.10(a), and the applied field is switched off, i.e. ϕ

on the top electrode is reduced to zero. The electric potential ϕ on the nodes along $x_1 = 0$ and $x_1 = L$ are also set to zero, thereby restoring the 2D square region in Fig. 2.10 to the boundary conditions described by Fig. 2.6. The disturbed domain pattern is allowed to relax towards equilibrium, see Fig. 2.10(b-d). For example, in Fig. 2.10, the $+P_2$ domain grows in size, while the $-P_2$ domain reduces in size. The domain pattern evolves towards a monodomain in the equilibrium state, with $\tilde{\psi} = 0$ corresponding to a global energy minimum. This is an example of a phase-field simulation where a domain pattern in local equilibrium was disturbed to find a global energy minimum solution.

Next, an electric field, E_2 is applied across a monodomain pattern taking it around a hysteresis loop. Recall the typical hysteresis for ferroelectrics that was shown in Fig. 1.8. Here, a 2D square region of barium titanate with side $L = 20\text{nm}$ is modelled with simple supports. Electrodes are modelled on the upper (at $x_2 = L$) and lower (at

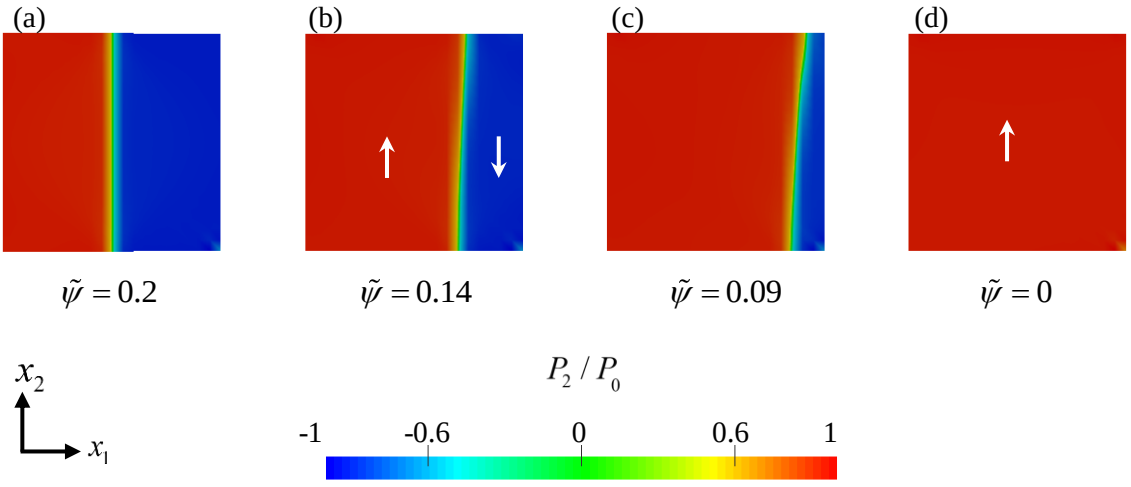

Figure 2.10: Polarization patterns along $x_2 - \text{axis}$ during the phase-field simulation, on disturbing the initial state in equilibrium by applying an electric field impulse. (a) initial state; (b)-(c) showing intermediate states during the phase-field simulation; (d) polarization pattern at equilibrium. $\tilde{\psi}$ is normalized free energy of the domain pattern.

$x_2 = 0$) surfaces, while the nodes along $x_1 = 0$ and $x_1 = L$ are insulated. The net polarization along the x_2- axis, $\bar{P}_2$ of the domain pattern formed on the 2D square, is calculated as an average of the P_2 values in the finite element mesh; that is $\bar{P}_2 = \int P_2 \mathrm{dV/V} = \sum_{i=1}^{n} P_2\big|_i \Big/ n$, where n is the total number of nodes in the finite element mesh of the 2D square region.

In the initial state with $E_2 = 0$, a random polarization field is applied and a monodomain pattern with spontaneous polarization $\bar{P}_2 = -P_0$ is stabilized at equilibrium, indicated by 'A' in Fig. 2.11. Next, an electric field, E_2 is applied along the $+x_2-$axis, with its magnitude incremented in steps of $1\mathrm{MV/m}$. The net polarization of the monodomain changes, from $\bar{P}_2 = -P_0$ to $\bar{P}_2 \approx -0.80P_0$, along AB. At the coercive electric field, $E_c = E_2 = 26\mathrm{MV/m}$ the net polarization in the monodomain reorients with the applied electric field, see BC in Fig. 2.11. Next, on reducing

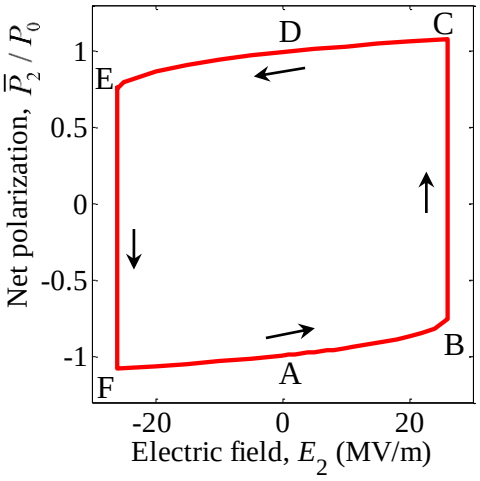

Figure 2.11: Hysteresis loop illustrating a plot of the net polarization along x_2-axis versus the applied electric field.

E_2 from 26MV/m to 0, the monodomain reaches a spontaneously polarized state with, $\bar{P}_2 = P_0$, along CD. Similarly, on cycling the electric field along the $-x_2-$axis, indicated by D-E-F-A, the net polarization in the monodomain switches with the applied electric field and finally returns to the initial state at 'A'.

In Fig. 2.11, it is interesting to note that the value of the coercive electric field, $E_c = 26\text{MV/m}$ is many times greater than the coercive fields experimentally observed in bulk barium titanate [58], [98]. The large value of E_c can be attributed to several reasons, however, the dominant effects are because the current phase-field simulations in Fig. 2.11 are carried out on a 2D square region and with insulated sides $(x_1 = 0 \text{ and } x_1 = L)$. The current simulation models a nanoscale 2D model with plane strain and plane electric field conditions. This boundary condition does not allow the polarization to switch out-of-plane, and thereby contributes to an increase in coercive electric field of barium titanate. This is similar to the increase in coercive electric field values observed for a thin film in comparison to a free standing bulk ferroelectric crystal – because polarization switching in thin films is restricted by substrate strain [99], [100]. The insulated sides restrict the formation of a 90° domain wall and only allow for uniform 180° switching of the domain pattern, and thereby also increase the coercive field value. Other reasons such as a uniformly polarised monodomain or the absence of domain walls in the initial state contribute to large electric fields for polarization switching. This is generally not experienced in experiments at the bulk scale, because there are multiple domains and domain walls. Upon applying an electric field across the bulk samples, the domain walls move resulting in polarization switching at much lower electric field values.

In the next section domain walls in tetragonal ferroelectrics are simulated using the phase-field model. In barium titanate, two types of domain walls are commonly observed, namely the 180° and 90° walls; these are explored using the Landis phase-field model.

2.5 Domain walls in the phase-field model

Here, the 180° and 90° domain walls in barium titanate are simulated on a 2D square region using phase-field methods. A 2D square region of side L = 20nm is modelled with simple support boundary conditions, as described in Fig. 2.6. In the initial state, domain patterns containing sharp 180° and 90° domain interfaces are imposed on the square region, see Fig. 2.12(a-b). These initial states are relaxed towards equilibrium using the phase-field model.

In Fig. 2.12(a-b), the sharp interfaces of the 180° and 90° domain walls become smooth and appear broader at equilibrium. These domain walls are typically 2-3nm wide and therefore possess a steep polarization gradient. In the 180° domain wall where $P_2 / P_0 \to 0$, see Fig. 2.12(a), the barium titanate crystal possesses a near cubic structure and produces misfit with the neighbouring tetragonal lattice. This misfit can be observed in the equilibrium state of the domain pattern in Fig. 2.12(a): the region at/around the 180° domain wall is under tension due to the cubic structure of crystal lattice, while the region far away from the 180° wall is relaxed and in the tetragonal state. Similarly, in the 90° domain walls the tetragonal shape of barium titanate crystal lattice, with sides $c > a$ causes misfit in the lattice structure. This lattice misfit causes adjacent domains across the 90° domain wall to rotate through an angle $\sim 0.63°$ in barium titanate as shown in Fig. 2.12(b). The displacements on the equilibrium states of

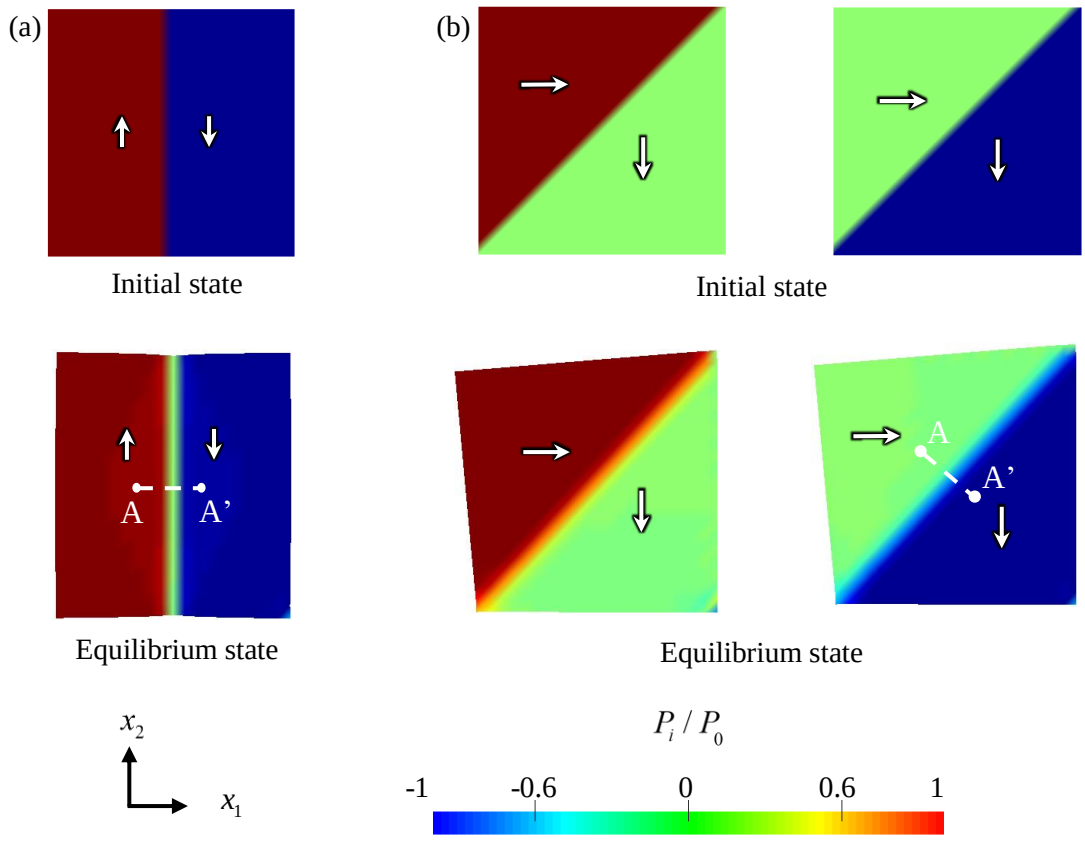

Figure 2.12: Phase-field simulations of (a) 180° (b) 90° domain walls. Subfigures illustrate the initial and equilibrium states of the domain patterns. Note that in the equilibrium states, the displacements are exaggerated to illustrate deformation.

the domain patterns in Fig. 2.12(a-b) are exaggerated to show deformation.

The variation in polarization across the two types of domain walls along the line AA' = 4nm is shown in Fig. 2.13. Here, $P_{\|}$ is defined as the net polarization value that is parallel to the domain wall. That is, for a 180° domain wall $P_{\|}$ is equal to the P_2 value and varies between a minimum of $-P_0$ to a maximum of $+P_0$. While, for a 90° domain wall, $P_{\|}$ is calculated as $(P_1 - P_2)/\sqrt{2}$. The value of $P_{\|}$ for a 90° domain wall is in the range $-P_0/\sqrt{2}$ to $+P_0/\sqrt{2}$. For both the 180° and 90° domain wall case, the

polarization $P_{\|}$ reaches its spontaneous value away from the domain walls. This can be observed by the flat lines in the polarization curves of Fig. 2.13. At the domain walls, the polarization value changes as indicated by the gradient.

The widths of the 180° and 90° domain walls can be calculated from Fig. 2.13 using a tangent method. This method is illustrated using the polarization variation across the 180° domain wall as an example, see Fig. 2.14. Here, a best fit straight line is first drawn tangential to the polarization curve at its point of peak gradient, for example line BB in Fig. 2.14. The flat lines corresponding to the spontaneous polarization values in domains are next extended to meet BB at points 'R' and 'S'. The domain wall width is then given by the perpendicular distance between R and S. For example, the width of a 180° domain wall in Fig. 2.14 is measured to be $w \sim 1.6$nm. A drawback of this tangent method in measuring the domain wall width is that the perpendicular distance RS, neglects the polarization variation observed to the left of

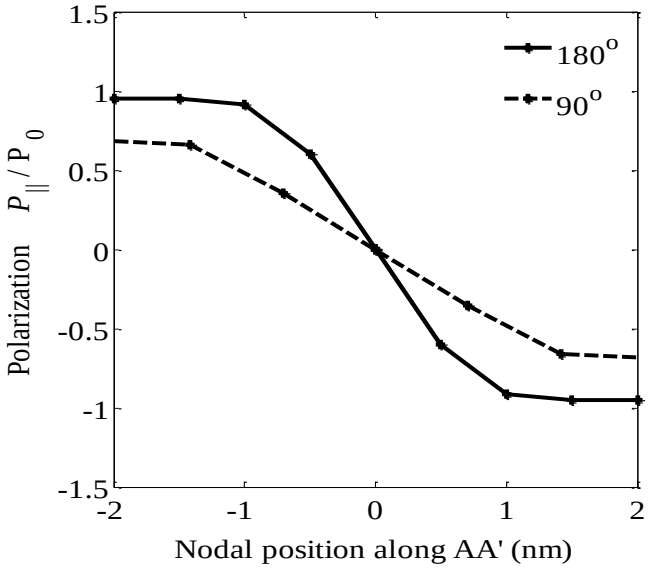

Figure 2.13: Polarization variation along AA' across the 180° and 90° domain walls, as illustrated in Fig. 2.12(a-b). AA' = 4nm and $P_{\|}$ is the polarization parallel to the domain walls.

point R and to the right of point S in Fig. 2.14. Hence, in the tangent method, the entire polarization variation across the domain wall is not captured, and the values of domain wall width are generally smaller than expected from the graph. Alternatively, the domain wall widths can be measured as a perpendicular separation between points on the polarization curve at $P_{\parallel} = \pm 0.9 P_0$. That is points indicated by red markers in Fig. 2.14 correspond to $P_{\parallel} = \pm 0.9 P_0$, and the perpendicular distance between these markers, *w'* is measured as the domain wall width. Using this $\pm 0.9 P_0$ method, the width of a 180° domain wall is measured to be 1.95nm and the width of the 90° domain wall is 2.93nm. These values of the domain wall width are in agreement to within $\pm 2.3 - 2.5\%$ with the results from Su and Landis [29], and the atomistic simulations by Padilla et al. [101].

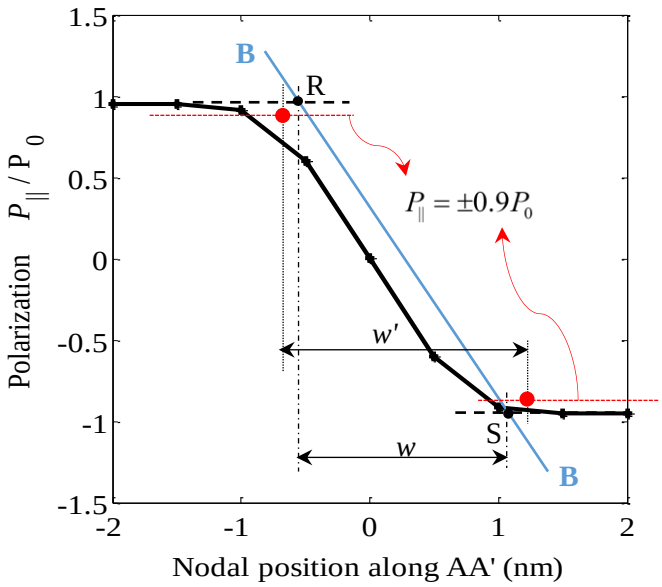

Figure 2.14: Schematic illustration of measuring a 180° domain wall width using the tangent method and the $\pm 0.9 P_0$ method.

Next, the variation in stresses and electric fields across the 180° and 90° domain walls along AA' in Fig. 2.12(a-b) are explored. In Fig. 2.15 the stresses that are parallel and perpendicular to the 180° domain wall are plotted along AA'. Note, $\sigma_0 = 692\text{MPa}$ is the normalization constant for stress, as discussed in section 2.3. In Fig. 2.15, in the direction parallel to the 180° domain wall, tensile stresses with a peak magnitude of $\sim 0.8\sigma_0$ are present in the walls. This can be explained by the presence of near cubic crystal lattice at the 180° domain wall where $P_2 / P_0 \to 0$. The cubic crystal lattice experiences tensile stresses caused by the neighbouring tetragonal lattice in the polarized domains. On the other hand, the polarized domains neighbouring the 180° domain wall, experience a compression of $\sim -0.1\sigma_0$ in the direction parallel to the wall. The stresses perpendicular to the 180° domain wall are nearly zero.

Next, the stresses parallel and perpendicular to the 90° domain wall are plotted in Fig. 2.16(a). The net stresses parallel and perpendicular to the 90° domain wall are calculated as $(\sigma_{11} + \sigma_{22})/2$ in the transformed co-ordinate axes. In Fig. 2.16(a), it can

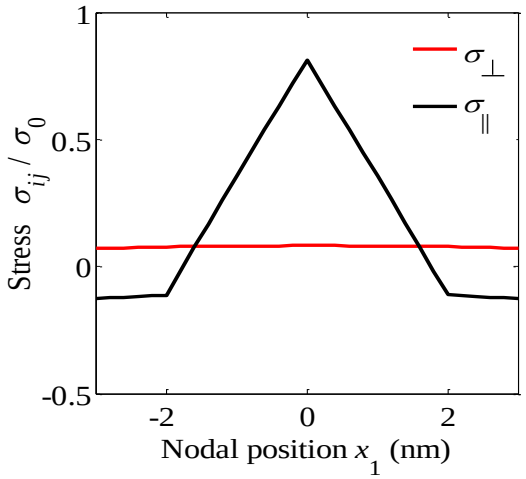

Figure 2.15: Variation in stress along AA' in Fig. 2.12(a) across the 180° domain wall.

be noted that the $90°$ domain wall experiences tensile stresses in the direction parallel and perpendicular to the wall, with a peak magnitude of $\sim 0.11\sigma_0$. It is interesting to note that the tensile stresses in the $180°$ domain wall are greater in magnitude compared to the stresses in the $90°$ domain wall. A possible reason for the relatively small stresses in the $90°$ domain wall is attributed to the rotation of domains adjacent to the $90°$ domain wall as shown in Fig. 2.12(b). These rotations relieve the lattice misfit stresses at the $90°$ walls, and such rotations are not observed at the $180°$ domain wall junction.

The electric field is everywhere zero in the square region in Fig. 2.12(a) containing the $180°$ domain wall. However, in Fig. 2.12(b) non-zero values of electric potential are present in the square region containing the $90°$ domain wall. The variation of electric potential along AA' across a $90°$ domain wall is plotted in Fig. 2.16(b). A sharp electric potential gradient is observed at the $90°$ domain wall resulting in a net

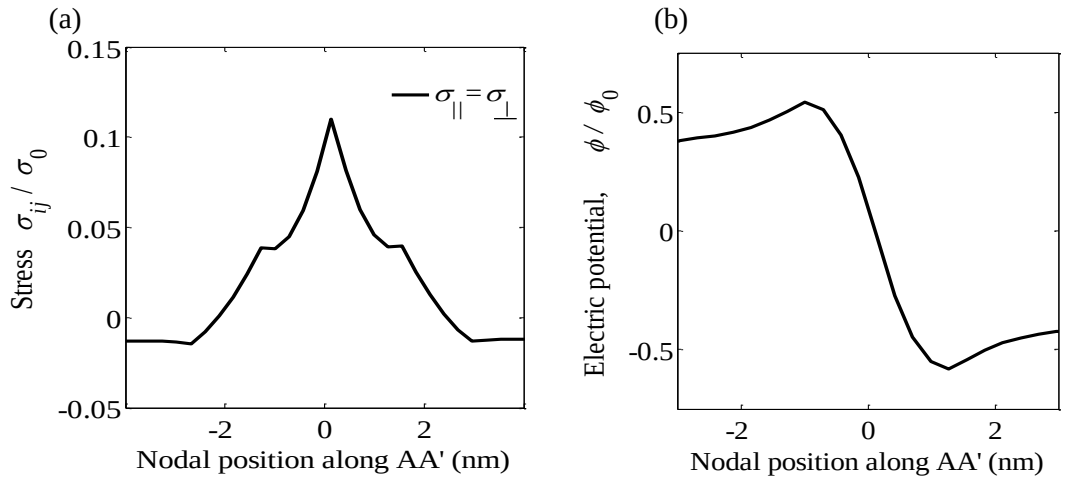

Figure 2.16: Variation in (a) stress and (b) electric potential values along AA' in Fig. 2.9(b) across the $90°$ domain wall.

electric field. Note that the domain pattern in Fig. 2.12(b) has a non-zero average polarization. The electric field produced in the $90°$ domain wall opposes this non-zero average polarization. It is also interesting to note that the electric potential in the polarized domains is not a constant and produces a weak electric field that opposes the electric field produced at the $90°$ domain walls. Further details on the $180°$ and $90°$ domain walls, such as minimum separation between two domain walls at equilibrium, are explored in the context of periodic polarization patterns in chapter 5.

The presence of external loads such as stresses or electric fields can cause domain wall movement. The domain wall kinetics in barium titanate is not universally agreed upon [96], [97], and hence the phase-field model is here used only to solve for equilibrium states. However, in order to reach the equilibrium state the phase-field model used in the present work assumes linear kinetics. This numerical modelling of domain wall kinetics is next discussed.

The Landis phase-field model uses polarization viscosity, β (a parameter that is inversely related to domain wall speed) to control domain wall movement. That is, in a typical phase-field simulation, the equilibrium state is reached by gradually reducing the β value from a large positive number to zero. The β value is reduced to zero over 800 Newton-Raphson iterations. This allows for a smooth domain evolution process by controlling β. An example of a β value control pattern during a typical phase-field simulation is shown in Table 2.2.

In Table 2.2, the first 50 iterations are carried out at large values of polarization viscosity, $\beta = 1000$. This is because the starting states of phase-field simulations are initialised with either a random polarization field or by imposing a chosen polarization pattern with sharp interfaces; the nodal displacements and electric potential values are

No. of Newton-Raphson iterations	Polarization viscosity β	
50	1000	→ Initial state
100	100	
100	50	
100	10	
150	5	
200	1	
80	0.5	
10	0.05	
10	0.005	
1	0	→ Equilibrium reached

Table 2.2: Control of the polarization viscosity, β in a typical phase-field simulation.

set to zero in these initial states. These starting states are typically far from equilibrium, and require high polarization viscosity, β to converge. Once the initial iterations have converged, that is the residual forces and residual displacements calculated at the end of an iteration are small $<10^{-9}$, the β value is reduced and the process is repeated. This method can be considered as identical to stepping the phase-field simulation forward in time, with time increments inversely proportional to β. Equilibrium is reached when the Newton-Raphson iteration converges for $\beta = 0$.

When the residual forces and displacements assume large values ($>10^{9}$), the Newton-Raphson iterations do not converge and the phase-field simulation is divergent. In these cases there is no equilibrium state whose nodal values of the degrees of

freedom are sufficiently close to the current state to be found by the Newton-Raphson scheme. Then the phase-field model has encountered a state too far from equilibrium. Instabilities can be observed when two domain walls approach each other to form needle-like domains or a small domain area is enclosed near to a boundary. The numerical methods involved in resolving such domain pattern instabilities are next explored.

Consider the phase-field simulation shown in Fig. 2.10. Here an external electric field was applied to disturb a domain pattern containing a 180° wall. This phase-field simulation encountered instability when the 180° domain wall approached the boundary of the 2D square. This instability is illustrated in Fig. 2.17(a-d). Here, as the domain wall approached the boundary of the 2D square, the Newton-Raphson iteration with $\beta = 1$ diverges, see Fig. 2.17(d). The nodal values u_i, P_i and ϕ calculated in the Newton-Raphson iteration just before the divergent step in Fig. 2.17(d) are stored in a separate file.

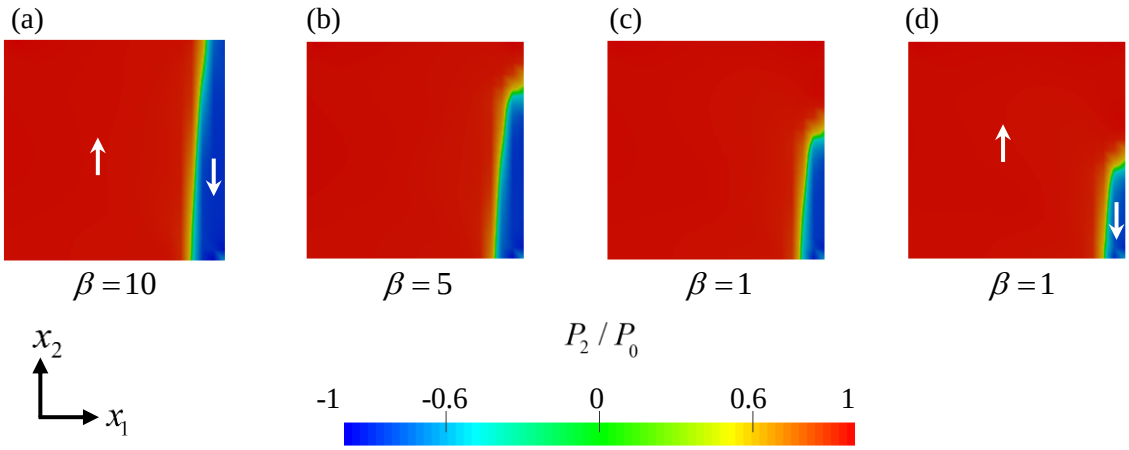

Figure 2.17: Subfigures (a-d) illustrate phase-field simulations with an instability during domain evolution process. The polarization viscosity β is decreased from 100 to 0 during the phase-field simulation, and the subfigure (d) indicates the polarization pattern at which the Newton-Raphson iteration did not converge.

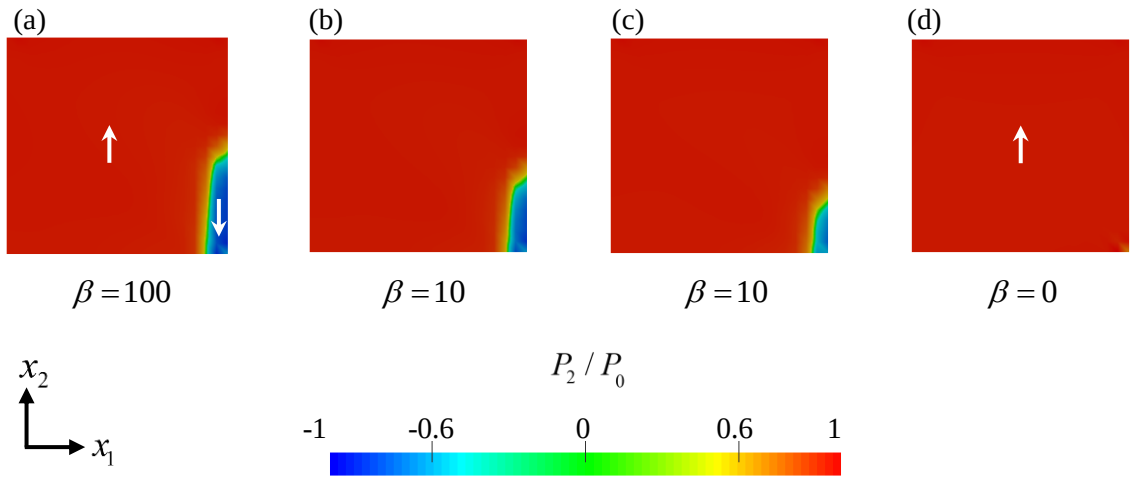

Figure 2.18(a-d): Phase-field simulations resolving the instability in Fig. 2.17 by increasing the β values leading to the formation of a monodomain at equilibrium.

The numerical methods employed to resolve this instability in the subsequent phase-field simulation are as follows: at first, the 2D square region in Fig. 2.18(a) is modelled with identical boundary conditions imposed on Fig. 2.17(d). The phase-field simulation is then initialised by imposing the nodal values of u_i, P_i and ϕ obtained from the stored files before the simulation diverged. Next, the value of polarization viscosity, β is assigned a high value, e.g., $\beta = 100$ – to enforce slow domain wall movement and to solve for increments of u_i, P_i and ϕ over small time steps. Once the initial iterations converge, the polarization viscosity is lowered to $\beta = 10$, and the process continues until the system transits through the instabilities and approaches a stable domain pattern, see Fig. 2.18(b-c). The β values are further reduced until at $\beta = 0$, the iterations converge and a monodomain pattern at equilibrium is formed, see Fig. 2.18(d). Using this technique several instabilities encountered in the present work are passed through.

So far, single domain walls in tetragonal barium titanate have been explored through phase-field simulations. A typical ferroelectric specimen contains multiple domains and domain walls that are arranged to form a compatible pattern at equilibrium. These polarization patterns can range from a few nanometres in size up to several micrometres, and are important to the design and working of nanoscale ferroelectric devices such as memory elements. In the next section, the phase-field simulations are employed to explore a compatible polarization pattern in $BaTiO_3$. The internal fields, for example local stresses and electric fields, developed in the polarization patterns are also explored.

2.6 Polarization patterns

As discussed in chapter 1, the domains in a ferroelectric are commonly arranged in a compatible fashion, e.g., the head-to-tail polarization arrangement, to form a polarization pattern. These polarization patterns can cause internal stresses, which are dependent on domain configuration. In this section, a vortex polarization pattern is studied and its associated internal stress fields are explored. The vortex polarization pattern could be used to enhance memory storage density, however it is intriguing to note that these polarization patterns are elusive in experiments, even when the experimenters set out to make a vortex structure [102]. This contrasts strongly with magnetic materials, where vortex arrangements of magnetization are well known [103], [104].

A vortex polarization pattern is simulated using phase-field methods, see Fig. 2.19(a). A square region of barium titanate of side $L = 20$nm is modelled with simple supports and traction free surfaces. The boundaries of the square region are

electrically insulated, i.e., the surfaces are free of electric charges. On initializing the phase-field simulation with a random polarization field, the model solves for a vortex domain pattern at equilibrium, see Fig. 2.19(a). This vortex pattern contains quadrant domains arranged to form a polarization flux closure, and is referred to as the 'classic polarization vortex'. Now, in order to understand the internal stress fields developed in the vortex polarization pattern, let us first consider a simple case of a $90°$ domain wall in barium titanate. A $90°$ domain wall is associated with misfit strains due to difference

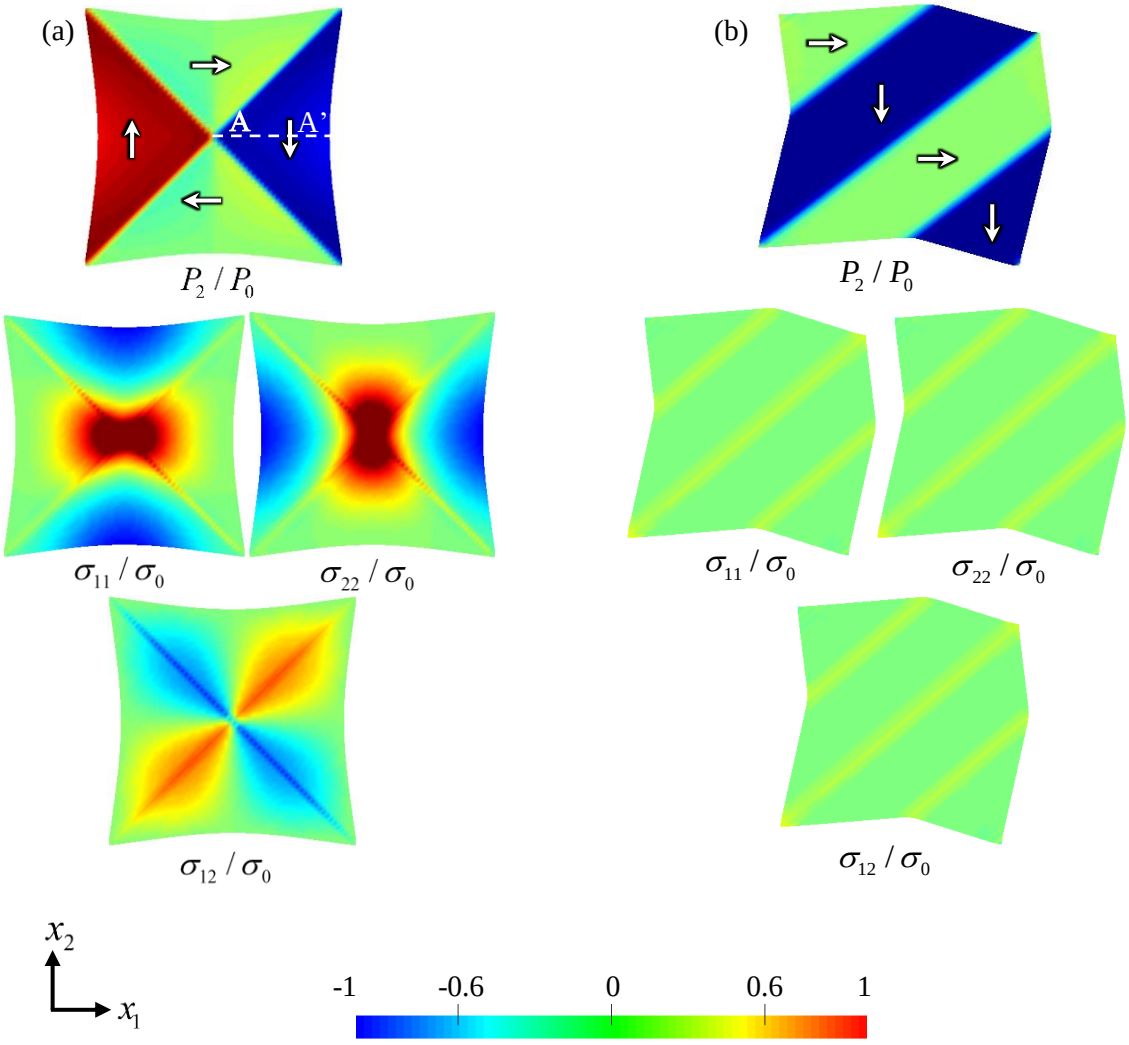

Figure 2.19: Phase-field simulations of (a) a vortex polarization pattern and (b) a periodic polarization pattern with stripe-like features.

arising from the tetragonal $c:a$ ratio. These strains can be relieved by allowing the crystal lattice to rotate through an angle of $\sim 0.63°$ in barium titanate. Hence, if these $90°$ domains are arranged to form a stripe-like pattern, see Fig. 2.19(b) where the domains are allowed to rotate, the polarization pattern is stress-free except at the domain walls. However, if these $90°$ domains are arranged to form a polarization flux closure or a vortex pattern as shown in Fig. 2.19(a), the domains are internally stressed. Subfigures in Fig. 2.19(a-b) illustrate the stress fields developed in the vortex and the stripe-like polarization pattern.

From Fig. 2.19(a) it can be noted that upon circulating a junction of domains no net rotation of the crystal lattice is permissible. By circulating the vortex polarization pattern, four consecutive lattice rotations of $0.63°$ are encountered. As a consequence the domains in Fig. 2.19(a) are stressed, since the set of domain walls at the junction would have otherwise produced a net rotation. The pattern of internal stresses developed is similar to that of a disclination resulting in stress fields that decay with distance from the vortex core.

The axial stresses, σ_{11} and σ_{22} in the vortex pattern are plotted along AA' with increasing distance from the vortex core, see Fig. 2.20(a). The shear stress on AA' is nearly zero. In Fig. 2.20(a), the dependence of axial stress, σ_{ii} on the radial distance from the vortex core, x is shown. Fig. 2.20(b) suggests that these stresses do not follow a simple power law dependence on x. The stresses in the vortex domain pattern can be approximately described by the stresses due to a disclination. In an elastic (non-ferroelectric) solid, the disclination fields are given by an Airy's stress function of the form $\phi = r^2 \ln r$ in polar (r,θ) coordinates. However, in this case the material is assumed isotropic and non-polar. This gives rise to a logarithmic variation in stress with

radial position. The best fit stress curves based on the Airy's stress potential are shown in Fig. 2.21.

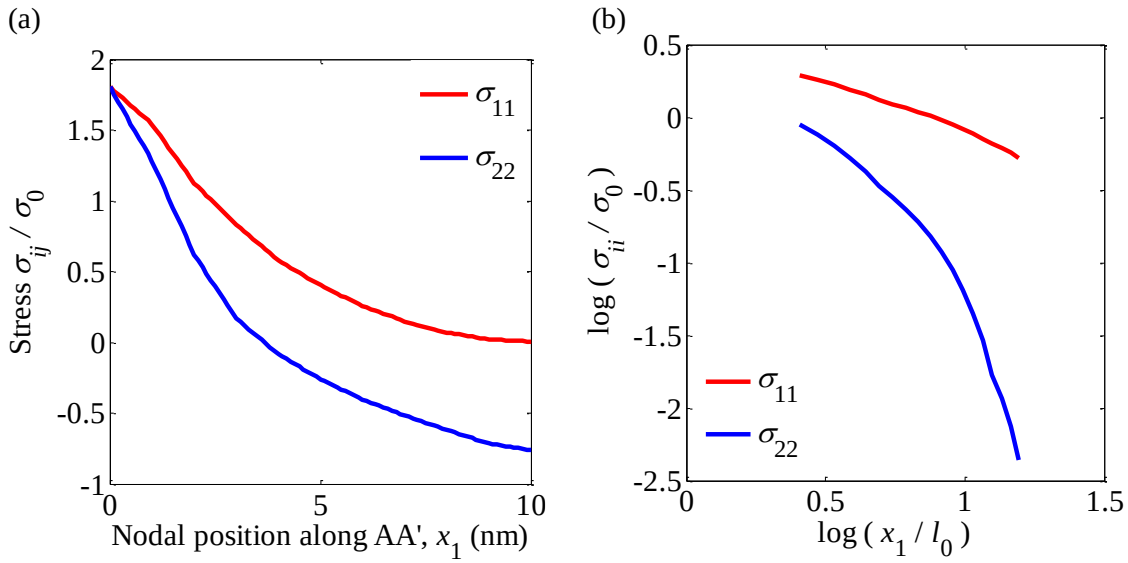

Figure 2.20: (a) Variation in axial stresses in the vortex polarization pattern with increasing distance from the core. (b) A log-log plot of the stress curves from Fig. 2.20(a)

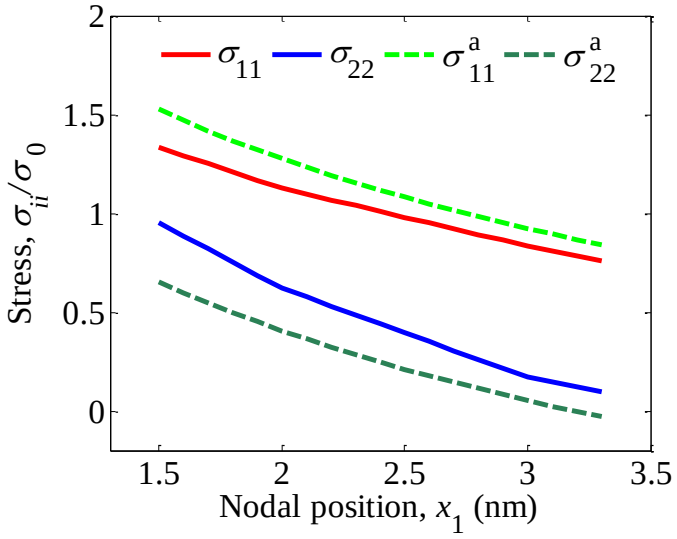

Figure 2.21: Stress fields of a disclination in an isotropic sheet σ^a_{11} and σ^a_{22}, and the stress variation, σ_{11} and σ_{22} in the vortex polarization pattern.

The key point from Fig. 2.20(a-b) and Fig. 2.21, is that the stress fields in a vortex domain pattern decrease with increasing distance from the core; these fields can be approximately explained by the presence of a disclination. The vortex pattern possesses a highly stressed core that significantly contributes towards the net energy of the domain pattern. This increases the energy per unit volume of the vortex domain pattern and may explain why it is elusive in nature. However, the stresses in the vortex pattern decay with increasing distance from the core, indicating a potential of stabilising these patterns at greater length scales, such as of the order of a few micrometres. Further details on the effect of scale and surface conditions on the formation of vortex polarization patterns are studied in chapter 4.

2.7 Three dimensional modelling

Until now only two-dimensional (2D) phase-field simulations were considered. These 2D phase-field simulations help to visualise the polarization pattern evolution with in-plane domains and provide insights on domain arrangements. However, the 2D phase-field model poses certain limitations: first, the predicted polarization pattern contains domain arrangements within a single plane, and domains with out-of-plane polarization are not allowed. This limits the study of three dimensional (3D) arrangements of domains. Second, the 2D phase-field simulations for example in the $x_1 - x_2$ plane, model domain walls to extend indefinitely in the $x_3 -$ direction. In these simulations, the polarization in the domain walls can curve in the $x_1 - x_2$ plane, but are not allowed to curve in the $x_1 - x_3$ or $x_2 - x_3$ planes. Experimental observations in ferroelectrics indicate the formation of curved domain walls in some polarization patterns [53], [105]. Also, note that engineered devices are always 3D, so the 2D

models may predict incorrect domain patterns. In certain cases – specifically plane strain, plane electric field conditions, the 2D model should be realistic. These limitations serve as a motivation to extend the existing finite element code of the 2D phase-field model to solve for three dimensional topologies.

Extending the phase-field model to solve for three dimensional topologies involves the following tasks:

(a) updating the finite element solver to generate a 3D mesh with brick elements;

(b) identifying new gauss points or integration stations for the brick elements and modelling the associated shape functions;

(c) computing the gradients, e.g., strain, electric field, by including the nodal displacements along the x_3 – axis;

(d) extending the stiffness matrix to solve for additional degrees of freedom, e.g., u_3, P_3.

The finite element solver employs three dimensional brick elements for 3D phase-field simulation, see Fig. 2.22(a). These are typically modelled as cubes of side

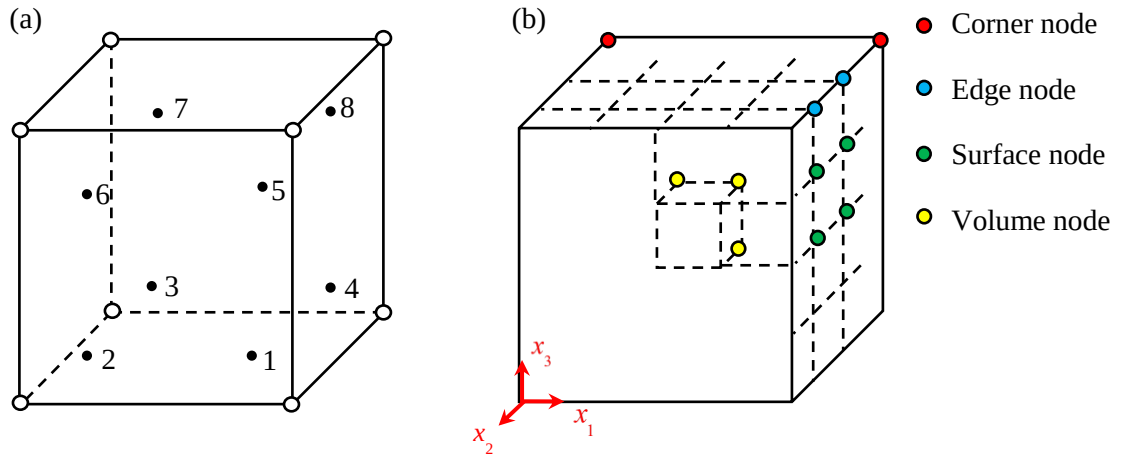

Figure 2.22: Schematic illustration of (a) 8 node brick element with 1, 2…8 indicating the position of Gauss points and (b) finite element mesh generated for a 3D phase-field simulation indicating the types of nodes based on their position.

1nm. Each node of the brick element possesses seven degrees of freedom, namely displacement u_1, u_2, u_3, electric potential ϕ, and polarization P_1, P_2, P_3. The element illustrated in Fig. 2.22(a) possesses 8 integration stations or Gauss points. The field values are interpolated to the Gauss points using the shape function of a 8-noded brick element [106], as discussed in section 2.2.

In a 3D mesh, different types of nodes are identified based on their positions, see Fig. 2.22(b):

(a) Corner nodes: The nodes present at the corners of the 3D structure, for example cuboidal structures possess 8 corner nodes.

(b) Edge nodes: Nodes present along edges of the 3D structure, for example along the lines $x_1 = 0, x_2 = 0, x_3 = 0 \ldots$

(c) Surface nodes: Nodes that are present on the surfaces of the 3D structure, for example on planes $(x_1, x_2) = 0, (x_1, x_3) = 0 \ldots$

(d) Volume nodes: Nodes present in the volume of the 3D structure.

Next, the computation of gradients in each element, for example the strain, electric field and polarization gradients are updated/extended to accommodate the additional degrees of freedom along the x_3 – axis. That is, in 3D phase-field simulations the nodal degrees of freedom such as u_3 and P_3 are evaluated, and the computation of gradients such as the strains, ε_{ij}, or electric fields, E_i, are updated to include these values. Likewise, the calculation of stresses, internal forces and the free energy of the system are updated to include the additional contributions from the three dimensional system. Finally, the stiffness matrix is extended to allow for the computation of additional nodal degrees of freedom.

Upon extending the phase-field model to solve for 3D topologies, it was first tested by simulating a monodomain pattern, and comparing its properties at the spontaneous state with the 2D simulation results. A 3D structure $10\text{nm}\times10\text{nm}\times3\text{nm}$, is modelled with simple supports as shown in Fig. 2.23. Here, a single corner node is clamped, while three other corners have roller supports. These boundary conditions prevent translation or rotation of the 3D structure. A finite element mesh with brick elements of side 1nm is generated. The electric potential, ϕ of the surface nodes on the 3D structure is set to zero, allowing the model to attract non-zero surface charges. A random polarization field is set up in the initial state and the finite element solver is allowed to approach equilibrium, see Fig. 2.24(a-d).

In Fig. 2.24(a-d), the phase-field model solved for a monodomain pattern at equilibrium, $\beta = 0$. Here, the monodomain pattern has a spontaneous polarization value of $P_0 = 0.26\text{C/m}^2$, spontaneous strains $\varepsilon_{11} = -0.0027$, $\varepsilon_{22} = 0.0082$, and $\varepsilon_{33} = -0.0027$. The free energy per unit volume of the 3D monodomain at equilibrium is $\tilde{\psi} = 0$, and

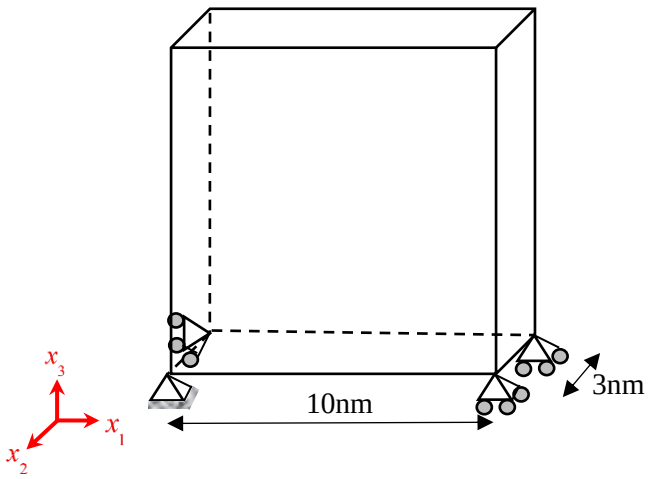

Figure 2.23: Boundary conditions on a 3D structure with simple supports.

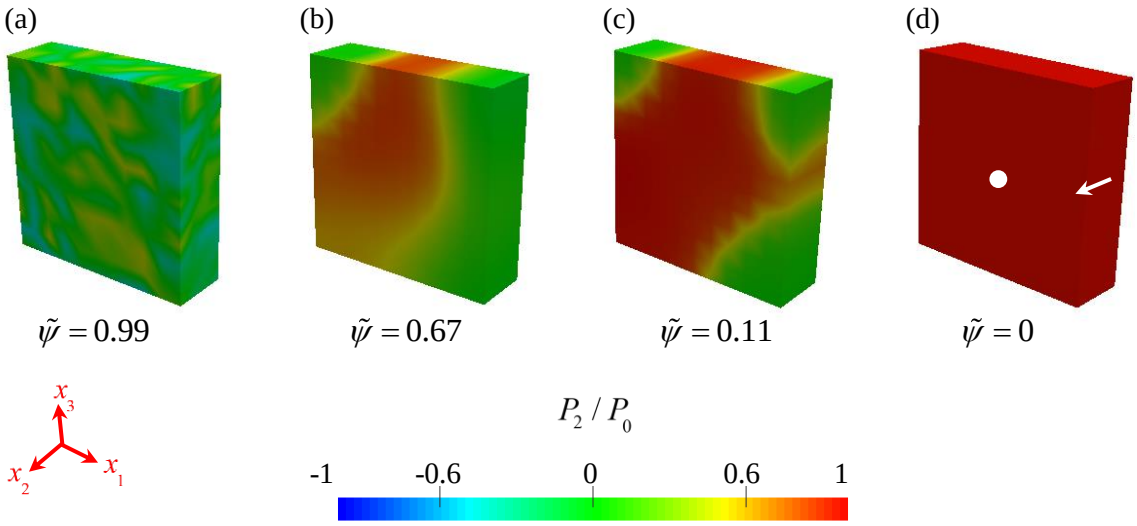

Figure 2.24: 3D phase-field simulation leading to the formation of a monodomain with $P_2 = P_0$. Subfigures (a-d) illustrate the polarization pattern along $x_2 -$axis during the phase-field simulation. (a) initial state with random polarization field; (b)-(c) showing intermediate states during the phase-field simulation; (d) polarization pattern at equilibrium. $\tilde{\psi}$ is normalized free energy of the domain pattern

matches the spontaneous state of barium titanate. These results agree with the 2D phase-field simulations, and help to validate the 3D simulation.

Note that Fig. 2.24 illustrated the formation of a monodomain polarized along $+x_2 -$ axis when initialised with a random polarization field. Monodomains polarized along each of the other five crystallographic axes were attained when the simulations were started with different sets of random polarization values, see Fig. 2.25.

Next, the 3D phase-field model is tested to simulate domain walls. To test the formation of 180° walls a 3D structure of size $16\text{nm} \times 3\text{nm} \times 2\text{nm}$ is modelled with simple supports with traction free surfaces as shown in Fig. 2.23. The electric potential on the surface nodes is set to zero, allowing the 3D structure to attract surface charges.

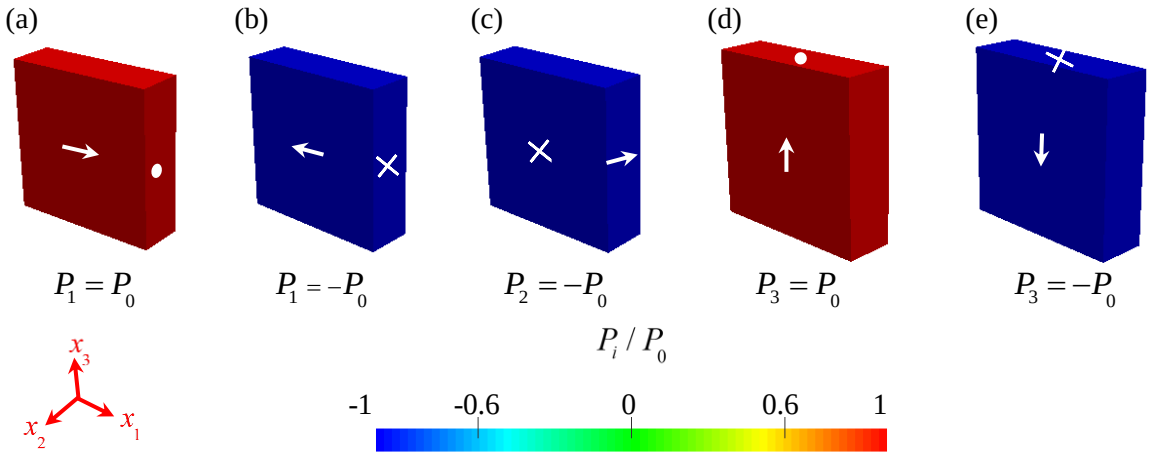

Figure 2.25 (a-e): Phase-field simulations illustrating the formation of a monodomain polarized along the five different crystallographic axes.

In the initial state, a band domain pattern containing two 180° domain walls is imposed and this is then relaxed towards equilibrium, see Fig. 2.26. The 180° domain walls broaden at equilibrium, and the out-of-plane polarized domains are stabilised

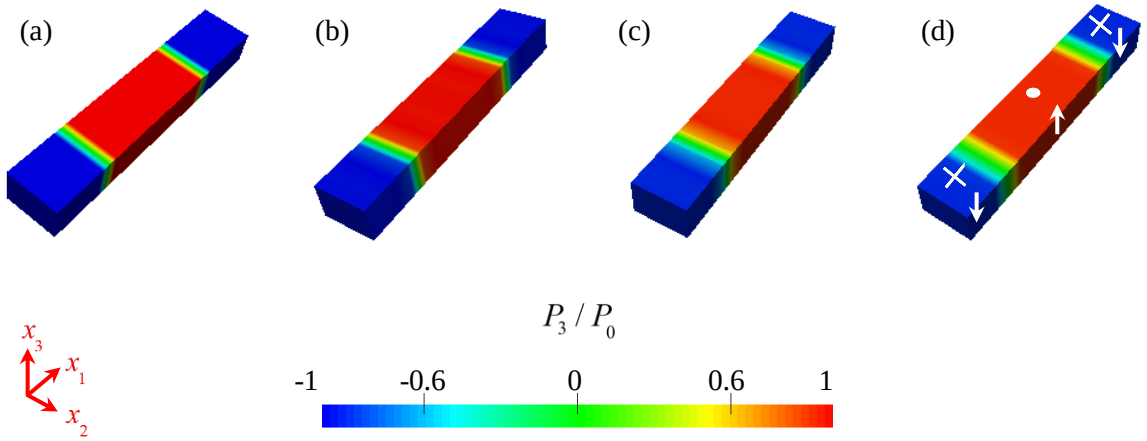

Figure 2.26: Phase-field simulations leading to the formation of a band domain pattern. (a) initial state (b)-(c) showing intermediate states during the phase-field simulation; (d) polarization pattern at equilibrium.

illustrating an advantage of the 3D phase-field model. The width of the 180° domain wall is calculated to be 2nm and agrees with the solutions from the 2D phase-field model. These band patterns are also found as equilibrium solutions along both the out-of-plane crystallographic directions, i.e., along x_3 and x_2 axis in Fig. 2.27(a-b).

Finally, to check for formation of 90° domain walls, a finite element mesh of a plate-like 3D structure of size 12nm×12nm×5nm is generated with brick elements of side 1nm, see Fig. 2.28. The 3D structure is modelled with simple supports and traction free surfaces as described by Fig. 2.23, while the surface nodes are insulated. In the initial state, a random polarization field is generated, see Fig. 2.28(a), and the system is allowed to approach equilibrium, see Fig. 2.28(b-d). A vortex polarization pattern with in-plane domains is an expected solution, and was found at equilibrium. These elementary tests help to validate the 3D phase-field model, and provide confidence to use this model in chapter 5 for studying the stability of more complex periodic polarization patterns. Next, the computational power required by phase-field simulations is discussed.

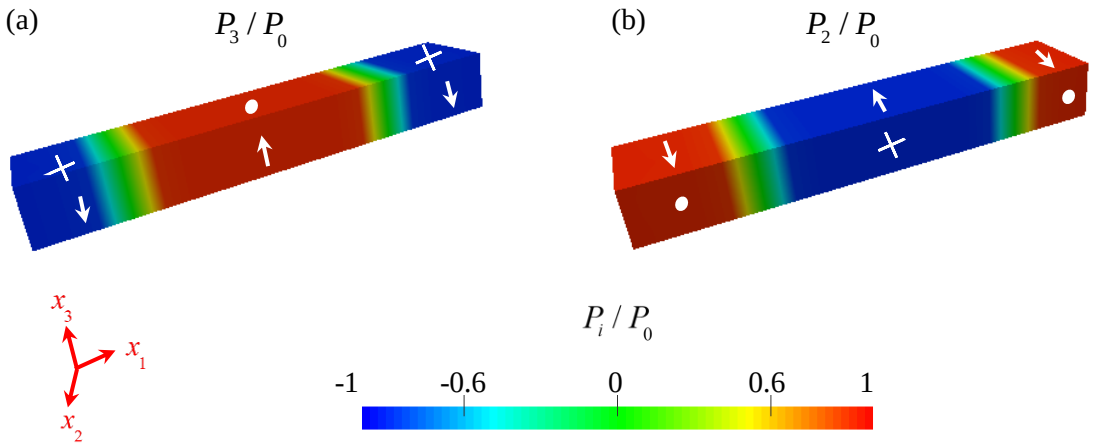

Figure 2.27: Phase-field simulations illustrating the formation of band patterns along two crystallographic axes.

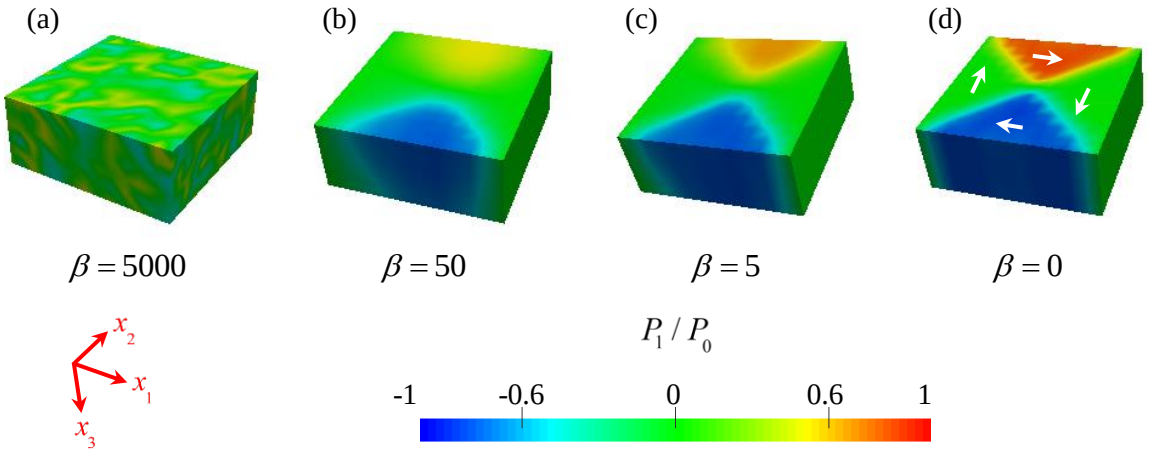

Figure 2.28: A vortex polarization pattern simulated using the 3D phase-field model.

2.8 Computational power

The phase-field model is one of the most powerful tools currently available to develop nanoscale ferroelectric devices. However, this model demands large computational power in terms of random access memory (RAM) requirements and simulation time. The computational power required is mainly determined by the size of the stiffness matrix that is to be solved by the finite element code. That is, in the finite element code, a master stiffness equation of the form $\mathbf{Bd} = \mathbf{F}$ is solved. Here $\mathbf{B}$ is the master stiffness matrix, $\mathbf{d}$ is the nodal degrees of freedom vector, and $\mathbf{F}$ is the nodal force vector. Each element of the stiffness matrix is assigned a double precision type integer that is associated with 8 bytes of memory space. This character type ensures accuracy of the finite element simulations and minimizes the truncation errors that could potentially affect the simulations during instabilities. The RAM required is typically determined by the total number of degrees of freedom, N and the memory space allocated to each variable in the stiffness matrix. Note that the 3D phase-field simulations require relatively greater memory space, due to the increase in degrees of

freedom per node and decrease in the factorization capabilities of the stiffness matrix. The presence of multipoint constraints, for example in periodic boundary conditions, further contributes to increasing the memory and computational time required by the finite element solver.

The computational memory, M required for simulating a square region of side, L is measured by executing the Fortran code. This code optimizes the stiffness matrix and estimates the RAM required for simulation. For 2D phase-field simulations (assuming no multipoint constraints) the computational memory, M scales with increasing size of the square simulation region, L as shown in Fig. 2.29. From Fig. 2.29, the approximate power law relationship between the computational memory, M and the square size, L is $M = kL^3$ where k is a constant. This indicates that the computational memory required for 2D simulations scales almost cubically with increasing size of the square. Similarly, the computational time required per Newton-Raphson iteration increases with increase in size of the finite element mesh. The phase-field model used in the current work is a serial code, i.e., each part of the code is solved sequentially and the computational time scales with increasing memory size. For example, using a desktop computer (Intel® Core™ i5-3570 CPU @3.40GHz processor) the total simulation time for a 60nm 2D square is of order of a few days. Parallelization of the finite element code could minimize the computational time and is beyond the scope of the current work. Based on the computational power practical constraints, the 2D phase-field simulations in the current work are confined to a maximum size equivalent to a square of side 60nm.

A similar increase in computational memory required to solve a 3D finite element problem is observed. Additionally, modelling of multi-point constraints (for periodic boundary conditions in chapter 5) leads to increased computational power requirements for the simulations. The limited RAM availability and increasing

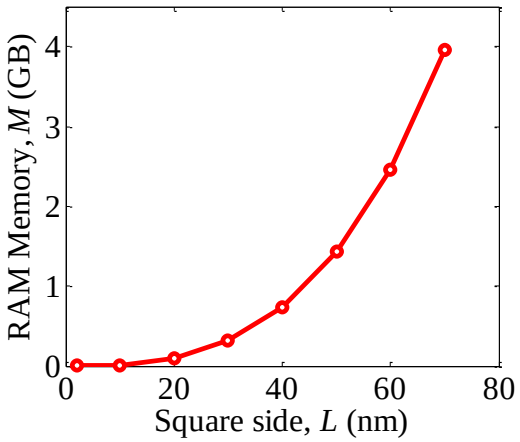

Figure 2.29: The computational memory for a 2D phase-field simulation with finite boundary conditions, such as those illustrated in section 2.3. The data represented here is for an Intel® Core™ i5-3570 CPU @3.40 GHz processor; 3.40GHz is the clock speed of the CPU core.

computational power, places a practical constraint on the maximum size ($L \sim 25\text{nm}$) of the cube that can be simulated. At $L \sim 25\text{nm}$ the polarization patterns that can form are limited, given the minimum number of domains and domain walls that can be accommodated in the cube. For example, in a single plane in a cube of side $L = 25\text{nm}$ a maximum of 2-3 domain walls can be fitted. This limits the formation of complex polarization patterns with multiple domain walls that can be predicted from the 3D phase-field simulation.

The limited RAM availability issue can be solved by using many processing units of a supercomputer [107] for greater computational power, but this would generally require parallelization of the code and is proposed for future work. Alternatively, a smaller plate-like structure of sides $L \times L \times s$, where $L >> s$ can be employed for 3D simulations. The larger surface area provided by the plate-like 3D

structure encourages the formation of polarization patterns with multiple domain walls and this geometry is used in chapter 5.

Overall, the phase-field simulations are computationally intensive, with 3D simulations requiring additional memory space and solution time. The maximum size of the finite element model that can be generated is limited by the computer RAM size and computational time. These requirements have encouraged the current study to focus primarily on 2D phase-field simulations, with 3D simulations carried out only where necessary in order to understand domain pattern stability, such as in chapter 5.

2.9 Conclusion

The Landis phase-field model employed in this thesis is a powerful tool currently available to simulate nanoscale ferroelectric devices. First, this model describes the Helmholtz free energy of barium titanate near its spontaneous state more accurately than several prior methods. It does this by accounting for additional terms that describe the elastic, piezoelectric and dielectric properties of the material. Second, the model ensures to attain both mechanical and electrical equilibrium in the system prior to marching forward in time. Some previous models did not explicitly solve for equilibrium. Third, unlike macroscopic models, the phase-field model can illustrate the domain evolution path and track domain wall movements. These features make the Landis phase-field model suitable for development of nanoscale devices and to study the effect of electro-mechanical boundary conditions on their working. In the current work, the Landis phase-field model has been extended to solve for three dimensional topologies. However, due to the practical constraints on computational memory and time, most of the work in this thesis has been limited to two dimensional simulations with plane strain and electric field conditions.

3

Nano-actuator concepts based on ferroelectric switching

Piezoelectric actuators are known to achieve high power density and positioning accuracy, however their widespread application is limited because of low values of piezoelectric coefficient [108]. In a typical piezoelectric, where the hysteresis effect is ignored, a linear relation exists between the strain and applied electric field. Piezoelectric strain constant, d is typically of the order of 10^{-9}m/V resulting in a practical limit of around 0.1% for actuation strain. The achievable displacements in these devices can be amplified through designs that use the piezoelectric strain to cause curvature of a beam, for example bimorphs [109].

Consequently it is an attractive idea to exploit the much greater mechanical strains that accompany ferroelectric switching for actuation. The aim of this chapter is to employ the phase-field model as a design tool to demonstrate nano-actuator concepts based on ferroelectric switching. In this chapter, the actuation cycle is demonstrated in three designs, namely the 'clamped', the 'embedded' and the 'bending' actuators. The space of design parameters, such as aspect ratio, electrode coverage and substrate strain, is explored for the embedded and the bending actuators to enhance the achievable displacements. Finally, the potential applications of ferroelectric nano-actuators based on design and performance are discussed. The actuation strains achieved through

ferroelectric switching are several times greater than the strains produced by typical piezoelectric actuators in market.

3.1 Mechanical bias concept

A problem which prevents the ferroelectric switching approach from widespread use is that, applying a cyclic electric field across a ferroelectric specimen produces $180°$ switching as shown in Fig. 3.1(a). In this type of switching minimal actuation strains are produced due to no strain change in the crystal lattice structure. However, enhanced strains arise from $90°$ ferroelectric switching. The $90°$ switching is not achieved by using just cyclic electric fields, because there is no external bias to orient the polarization at $90°$ to the applied electric field. This problem is resolved in the present work using a mechanical bias concept, see Fig. 3.1(b), where the ferroelectric material mechanically interacts with an underlying substrate. Here, a pre-stressed substrate produces in-plane domains that then switch out of plane only in the presence of an external electric field, Fig. 3.1(b). This $90°$ polarization switching is accompanied by a change in the crystal lattice structure resulting in actuation strains of $\sim(c-a)/a$. On removal of the electric field, in-plane domains are again formed due to the presence of substrate strain, ε_{sub}. This mechanical bias concept forms the basis of the nano-actuator designs developed in this chapter.

The conceptual actuator designs proposed are dependent on thin film technologies capable of fabricating films of the order of 10nm thickness with comparable feature sizes [110]. At this scale, the ferroelectric element may contain a few domains, which under charge-free conditions are predicted to form closed polarization loops or flux closures. Investigation on these nanoscale domain patterns

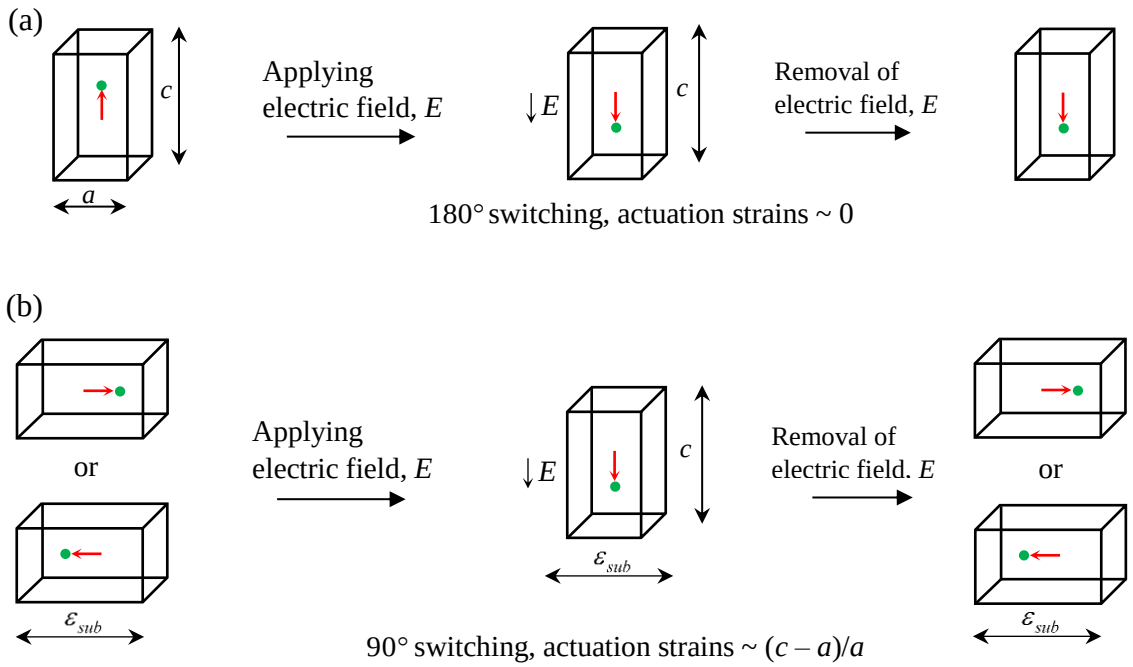

Figure 3.1: Schematic representation of mechanical bias concept demonstrating polarization switching by application of electric field, E (a) in the absence of substrate strain (b) in the presence of substrate strain, ε_{sub} .

has intensified in recent times to explore their prospects in nanoscale applications such as memory elements, sensors or energy harvesters. The role of factors such as strain and electric field on domain evolution has been studied [111], [112], indicating that in principle the nanoscale domains could be controlled in ferroelectric devices.

In this work, the working principle of ferroelectric nano-actuators is demonstrated using a phase-field model. The general concept of nano-actuators presented here consists of a nano-scale region of barium titanate, which forms a flux closure or vortex domain pattern in the initial state. These domain patterns contain polarizations in only one plane with domain walls perpendicular to this plane, allowing the actuators to be modelled in two dimensions with plane strain and electric field conditions. The actuation cycle is demonstrated in three designs of nano-actuators, and

their design parameters are further explored to enhance achievable actuation strains. In the first design named as the 'clamped' actuator, the region of ferroelectric material is envisaged to be clamped into a pre-strained state by mechanical boundary conditions that simulate the device substrate, see Fig. 3.2(a). The actuator is covered on two surfaces by continuous electrodes that are assumed to be sufficiently thin and compliant that they do not mechanically constrain the device. In the second design, named the 'embedded' actuator, a monocrystalline $BaTiO_3$ thin film is envisaged, which has been deposited within a channel in a pre-stressed substrate, see Fig. 3.2(b). Upon relaxing the substrate a known in-plane strain is imposed upon the ferroelectric film. In both the clamped and embedded actuators, the pre-strain selected is such that the ground state of the ferroelectric forms a polarization flux closure with mainly in-plane domains. This is defined to be the initial state of the actuation cycle. Actuation is then driven by applying

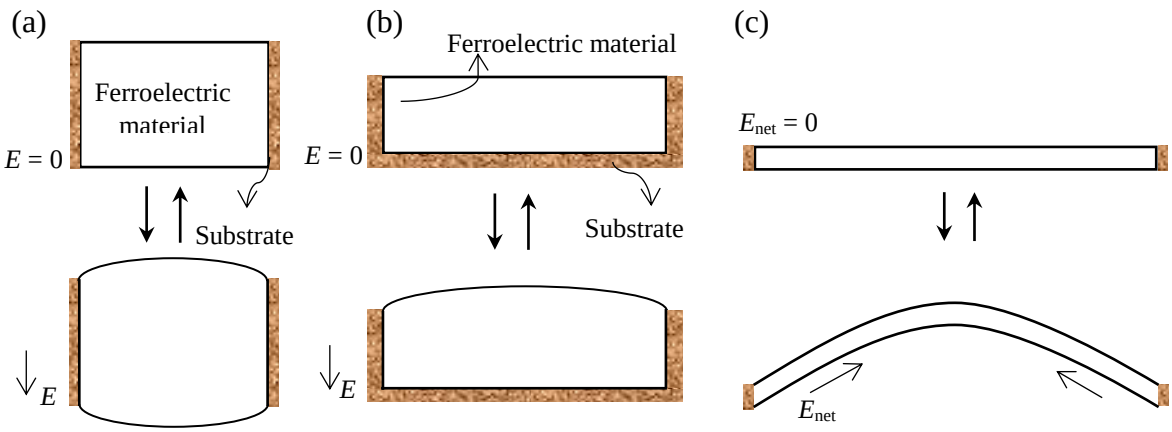

Figure 3.2: Schematic illustration of the structural design of (a) clamped (b) embedded and (c) bending actuators. Each subfigure illustrates the initial and actuated states of the nano-actuators, with E representing the external electric field (E_{net} is the net electric field in the bending actuator). Note that the polarization patterns formed in the actuators have complex arrangements and are discussed in section 3.2-3.5.

an electric field using surface electrodes. The ground state is recovered when electric field is removed. A third design, named the 'bending' actuator, uses a slender beam-like element of monocrystalline $BaTiO_3$ with multiple electrodes to produce a domain pattern that deforms the actuator into an arched shape, see Fig. 3.2(c). A detailed description of the bending actuator design is given in section 3.4. This achieves greater displacements than both the clamped and embedded actuators, at the cost of reduced actuation force. The design parameters, such as the aspect ratio of the embedded actuator or the electrode coverage in the bending actuator, are explored to enhance the achievable actuation strains.

In the next section, the design of the clamped nano-actuator is described and the working principle is demonstrated using phase-field simulations. The polarization pattern evolution under an external electric field is mapped for this nano-actuator. The strains achieved at the end of the actuation cycle are measured and the actuator response to external pressure is explored.

3.2 Clamped actuator

The clamped actuator comprises a patch of barium titanate of length L and height *H*, and is modelled in two dimensions – see Fig. 3.3. Here, nominal dimensions $L = H = 20\text{nm}$ are used. The device is modelled in a state of generalized plane strain in the $x_1 - x_2$ plane such that the strain in the $x_3 -$ direction is equal to the lattice $a -$ strain for barium titanate. This corresponds to assuming a depth in the $x_3 -$ direction much greater than the cross-sectional dimensions, and is consistent with mechanical clamping of the ferroelectric element by the substrate. Note that this condition makes polarization in the $x_3 -$ direction unfavourable and so enforces polarization in the $x_1 - x_2$ plane. The

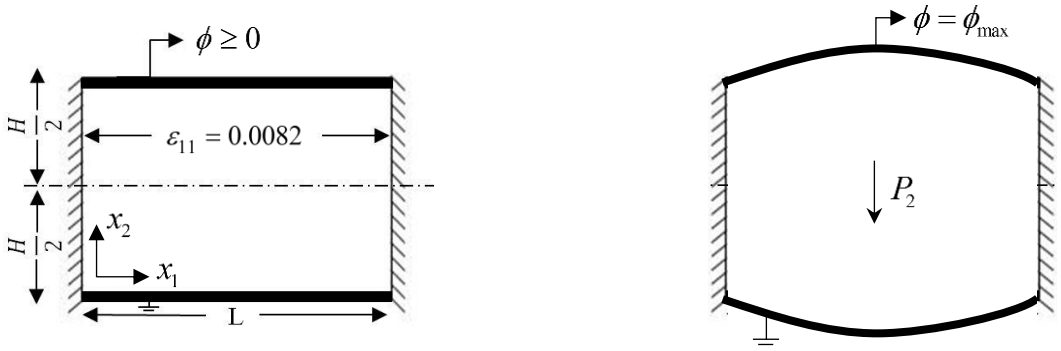

Figure 3.3: Schematic representation of boundary conditions on the clamped actuator in its initial and actuated states.

clamped actuator is sandwiched between upper and lower electrodes and is rigidly bound to the substrate at $x_1 = 0$ and $x_1 = L$, as shown in Fig. 3.3. The substrate imposes a pre-strain with respect to the cubic state of $BaTiO_3$ by $\varepsilon_{11} = 0.82\%$. Surface electrodes at $x_2 = 0$ and $x_2 = H$ are used to apply electric field parallel to the $x_2 -$ axis, with the lower electrode held at zero voltage and voltage ϕ applied at the upper electrode. The cycle proceeds by increasing voltage ϕ on the upper electrode until actuation is achieved and then reducing ϕ to zero. The actuation strain ε_A in the clamped actuator during the cycle is defined by an average displacement of the upper surface of the device with respect to the reference axis at $x_2 = H/2$, as shown in Fig. 3.3.

The initial polarization state in the nano-actuator is simulated by allowing the clamped actuator to find an equilibrium polarization pattern by forming a flux-closure with $\phi = 0$. This is attained by setting up a 'randomized' polarization field in the initial state, where nodal polarization values, P_i is randomly chosen from the range $-P_0/2 \leq P_i \leq P_0/2$, with $P_0 = 0.26 \text{C/m}^2$. The nodal values of displacement and electric potential in the initial state are set to zero, and the system is solved for equilibrium.

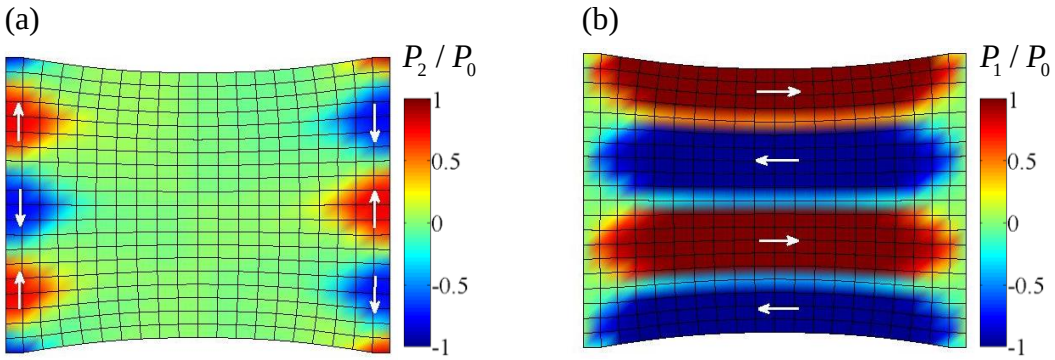

Figure 3.4: Initial polarization pattern adopted by the clamped actuator at $E_2 = 0$ with (a) P_2 / P_0 values (b) P_1 / P_0 values. The deformed configuration is shown with displacements exaggerated.

Fig. 3.4(a-b) shows the initial flux-closure polarization pattern formed in the clamped actuator with $\phi = 0$. Note that the upper and lower surfaces of the actuator have adopted a curved shape with displacements exaggerated. This curvature at the actuator surfaces is due to the imposed initial boundary conditions: the in-plane tensile strain ε_{11} has induced polarisation in $\pm x_1 -$ direction throughout most of the device. Since the stress-free states with polarization in the $\pm x_1 -$ direction have negative ε_{22}, the region close to the centre of actuator has contracted in the $x_2 -$ direction. This explains the concavity on the upper and lower surfaces.

Equilibrium states in the actuator are solved using the Ginzburg-Landau equation:

$$\left(\frac{\partial \psi}{\partial P_{i,j}} \right)_{,j} - \frac{\partial \psi}{\partial P_i} = \beta \dot{P}_i. \tag{3.1}$$

The evolution of the domain pattern is tracked through equilibrium configurations with polarization viscosity $\beta = 0$. These equilibrium domain configurations are attained by

allowing the model to step through a range of β values varied in decreasing order, $\beta = 5000 \text{ to } 0$. Non-zero β values are used only in intermediate steps towards equilibrium, or where an equilibrium configuration cannot be found due to instability. The governing differential equations are solved using finite element methods with 8-noded quadratic elements of 1nm size. The details of controlling the phase field simulations are discussed in section 2.2 of chapter 2.

To actuate the device, the electric potential ϕ on the upper electrode is increased in steps of 0.1V up to a maximum voltage of 2.2V. At each voltage step, an equilibrium state is found. Fig. 3.5 shows the evolution of the polarization pattern along the x_2-direction in the clamped actuator during the actuation cycle. As the strength of electric field is increased, domains with polarization $P_2 \approx -P_0$, aligned in the direction of applied field, increase their size at the expense of domains with polarization $P_2 \approx +P_0$, oriented opposite to the field, see Fig. 3.5(a-b). The latter domains shrink in size but do not disappear at this stage. Meanwhile, the shape and size of the central domains with net polarization along the $\pm x_1-$direction changes and deformation of the upper and lower surfaces is observed. Note the decrease in concavity of these surfaces as domains with non-zero P_2 spread to the centre, Fig. 3.5(c-d). The formation of needle-like domains can be observed in Fig. 3.5(e); at this stage, the finite element solution did not converge on an equilibrium state, and so the polarization viscosity β is controlled to allow the solution to evolve towards equilibrium. At $E_2 = 55\text{MV/m}$, complete reorientation in polarization to align with the applied field can be observed. Thereafter no further change in the polarization pattern occurs up to the peak applied field of $E_2 = 110\text{MV/m}$, though non-linear piezoelectric straining continues to occur.

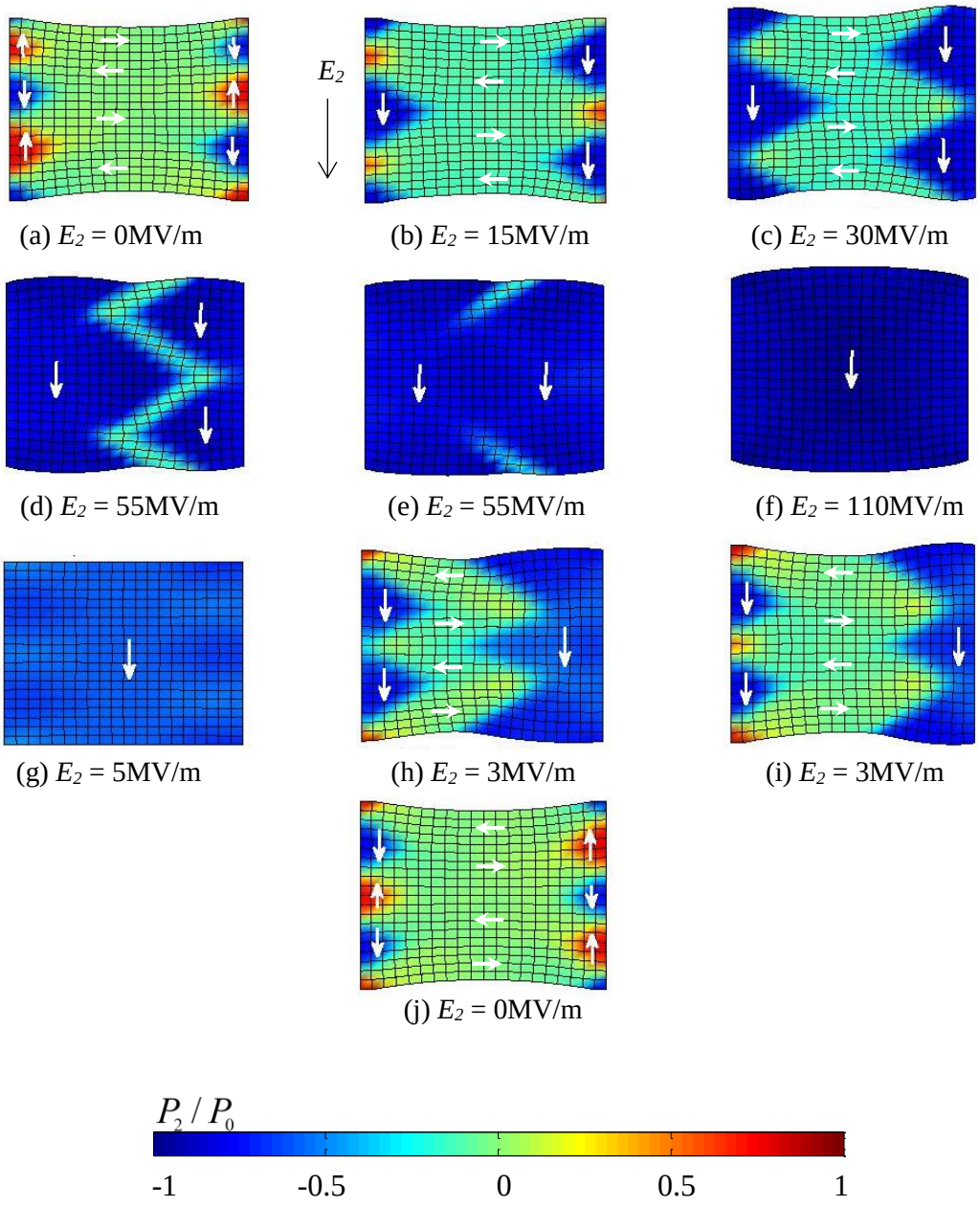

Figure 3.5: Actuation cycle in the clamped actuator, with the subfigures (a-j) demonstrating polarization evolution from the initial state 'a' to the final state 'j'. The deformed configuration is shown with exaggerated displacements.

The fully actuated state is shown in Fig. 3.5(f). The actuation strain ε_{A}, which is defined as the ratio of the mean displacement of the upper surface in the x_2-direction

to the device height, H is calculated to be $\approx 0.35\%$ for the clamped actuator. This compares favourably with the 0.1% that can typically be achieved by piezoelectrics.

Upon decreasing ϕ on the upper electrode, the clamped actuator retains a net polarization in the $-x_2-$direction, though its magnitude decreases slightly. This is accompanied by a change in shape of the actuator, Fig. 3.5(f – g) through the non-linear piezoelectric effect. When $E_2 = 3\text{MV/m}$ the mechanical constraints start to force the actuator back towards the initial state. Domains with non-zero P_1 evolve in the central region of the actuator, while the domains with net $-P_2$ recede, Fig. 3.5(h – i). On reducing the electric potential, ϕ, to zero, the actuator settles back into a state equivalent to the initial state in terms of the actuated displacement. However, it is interesting to note that the sense of the polarization vortices has reversed relative to the initial state shown in Fig. 3.5(a).

The Fig. 3.5 depicts the evolution of polarization patterns in the clamped actuator under a cycle of positive-going electric field. As observed, the domain evolution affects the shape of the device due to the strains that accompany ferroelectric switching through the cycle. The actuation strain ε_{A} of the clamped actuator is related to the applied voltage as shown in Fig. 3.6, where labels a-j indicate the points on the voltage-strain curve corresponding to the polarization patterns shown in Fig. 3.5. It can be observed in Fig. 3.6 that the actuation cycle for the clamped actuator starts with a non- linear displacement of the upper surface through stage a – c. This corresponds to initial growth of domains aligned in the direction of applied electric field. On increasing the electric potential further, there is a steep rise in the actuation strain during stage c-d; the majority of polarization switching occurs in this stage. On attempting to solve the system of governing equations at point ‘d’, instability is encountered and the evolution

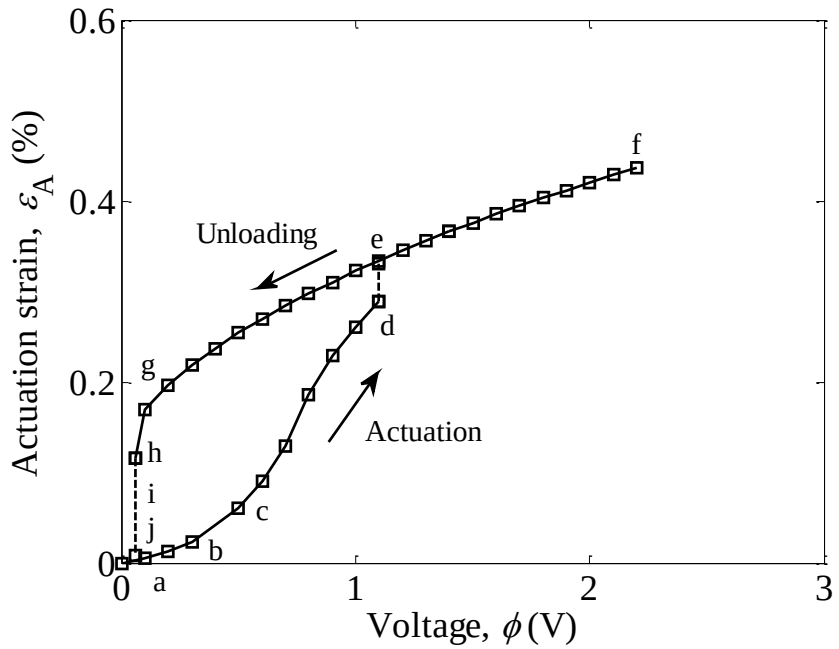

Figure 3.6: Voltage-strain curve for the clamped actuator. The labels on the graph correspond to the polarization patterns shown in Fig. 3.5.

of domains during stage d-e is computed out of equilibrium, using a finite value of polarization viscosity. During stage d-e, shown by a dashed line in Fig. 3.6, the herringbone-like pattern evolves into a needle-like domain pattern, which eventually recedes leaving a single domain with polarization aligned to the electric field. Thereafter the changes in displacement of the top electrode are due to non-linear piezoelectric behaviour as indicated by labels e-f in Fig. 3.6. On unloading the applied electric field by decreasing the electric potential on the upper electrode, the deformation of the clamped actuator follows a non-linear path f-h; during this stage the actuator supports a non-zero net polarization in the negative x_2 – direction though its magnitude decreases with the decreasing electric field. This decrease in polarization is accompanied with mechanical deformation of the upper surface of the device, gradually

decreasing the actuation strain as shown in Fig. 3.6. At point ‘h’, the mechanical bias due to imposed in-plane stress in the material along x_1- axis takes over forcing the actuator to return towards its initial ground state. This transition is again out of equilibrium (stage h-j) and the polarization viscosity β was controlled to allow the solution to evolve towards equilibrium. Stepping down the electric potential to zero results in the clamped actuator returning to its ground state. In Fig. 3.6 the actuation strains produced by the clamped actuator on settling into the final equilibrium state, is nearly zero indicating the negligible effects caused due to the formation of an equivalent domain pattern (flux-closure with opposite sense) in the final state.

The behaviour of the clamped actuator when resisted by a constant blocking force is next considered. The force is applied in the form of pressure uniformly distributed over the nodes on the upper surface of the device. The evolution of domains in the clamped actuator working against pressure, $p = 500\text{MPa}$ and the corresponding voltage-strain curve of the actuator are shown in Fig. 3.7 and Fig. 3.8 respectively. As may be expected, when working against an external pressure, the clamped actuator requires greater electric field strength to become fully actuated, see Fig. 3.8. Similarly, the application of pressure reduces the maximum strain achieved by the actuator.

At a uniform pressure, $p = 500\text{MPa}$ on the upper surface of the clamped actuator, the domain patterns during the actuation cycle change, resulting in small kinks in the voltage-strain curve at this pressure (Fig. 3.8). These kinks correspond to instabilities associated with the appearance or disappearance of certain features in the domain pattern. For example, the first such kink occurs at $\phi \sim 0.78\text{V}$, corresponding to $E_2 \sim 39\text{MV/m}$. At this point, a domain polarized in the $-x_2-$direction at the top left corner of the actuator shrinks in size and disappears – see Fig. 3.7(c - d). A similar

transition occurs at $\phi \sim 1.14\text{V}$ or $E_2 \sim 57\text{MV/m}$; in this case a domain polarized in the $+x_1-$direction disappears from the top surface of the device, see Fig. 3.7(d-e). Finally, at $\phi \sim 1.32\text{V}$, $E_2 \sim 66\text{MV/m}$ an asymmetric herringbone domain pattern is observed to form - see Fig. 3.7(e). Further increase in electric field leads to an intermediate state –

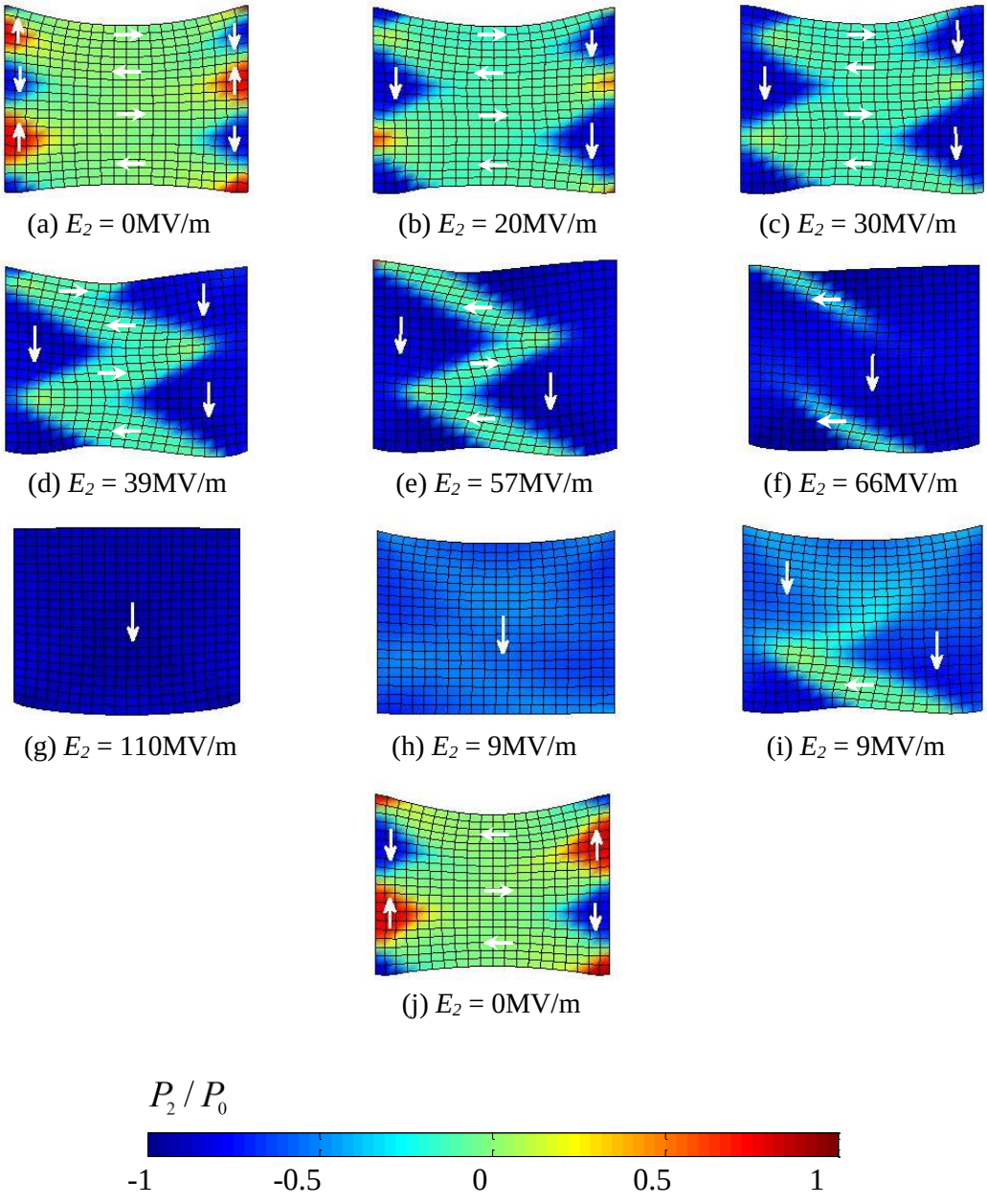

Figure 3.7: Actuation cycle in clamped actuator under a load of uniform pressure, $p = 500\text{MPa}$.

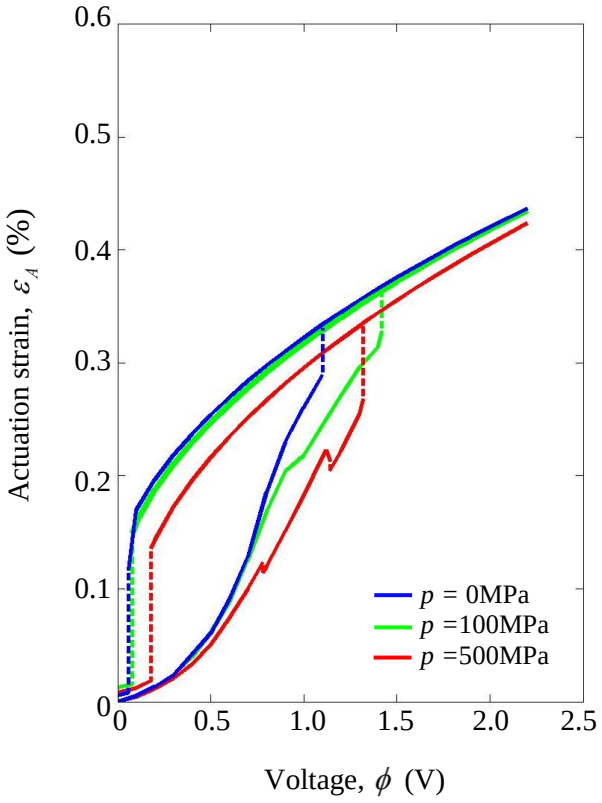

Figure 3.8: Voltage-strain curves for clamped actuator under uniform pressure, p .

Fig. 3.7(f). Needle-like domain formation is observed on increasing the voltage until the complete reorientation of polarization to the applied electric field is attained. The polarization patterns which evolve in the clamped actuator under load differ from those observed in Fig. 3.5, where no external loads were applied. These differences account for the change in shape of the voltage-strain curve as seen in Fig. 3.8. This figure also indicates that the clamped actuator returns to its ground state at greater values of applied electric potential when under an external load.

The clamped actuator can produce actuation strains of about $\varepsilon_{\mathrm{A}} = 0.35\%$ and can work effectively against external pressures of $p = 500\mathrm{MPa}$, without significant reduction in actuation displacements. However, the design of the clamped actuator can be improved to reduce the difficulties encountered in manufacturing the device. For

example, the lower surface of the clamped actuator is not mechanically bound and is free to deform. This 'free' lower surface of the clamped actuator is likely to present manufacturing difficulties, while the fabrication technology is fairly advanced in deposition of thin films at the nanoscale [113]. This design can thus be improved by binding the lower surface to a substrate, similar to a thin film configuration. Another issue that arises in the clamped actuator is the small separation between the binding side constraints provided by the substrate, which result in a strong mechanical constraint against displacement in the x_2-direction, so limiting the maximum actuation strains achieved. This effect can be minimised by increasing the separation between the mechanically 'clamped' boundaries, while also ensuring the repeatability of the actuation cycle through ferroelectric switching. This serves as a motivation to next explore an improvised design called the "embedded" actuator, which is envisaged to be a region of thin film embedded on three sides by a constraining substrate. The actuation cycle in the embedded actuator is next demonstrated using the phase-field model.

3.3 Embedded actuator

The embedded actuator concept is shown in cross-section in Fig. 3.9. The device consists of a layer of barium titanate of length L and height H, sandwiched between upper and lower electrodes and rigidly constrained by surrounding material on three sides. The electrodes are modelled as thin compliant conductors that do not constrain the actuator. The embedded actuator is representative of $BaTiO_3$ deposited on a lower electrode in a channel etched into the substrate, and capped with an upper electrode. The pre-strain could then be achieved by compressive pre-stress in the substrate during the deposition stage, and subsequent relaxation of the substrate to

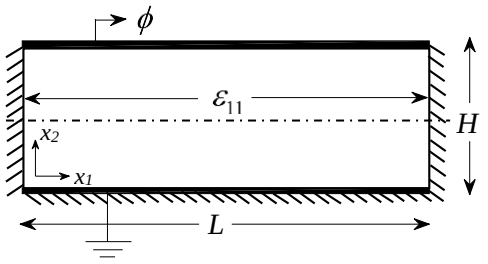

Figure 3.9: Schematic representation of the boundary conditions on the embedded actuator.

stretch the device. The resulting in-plane pre-strain ε_{11} is used to bias the device in favour of in-plane domains when no electric field is applied. A similar device could be produced from a continuous thin film on a conductive substrate, with an upper electrode covering a portion of length L. In this case, there would be some fringing of electric field at the device edges and compliance of the surrounding material, which are neglected in the current model. The device is modelled with plane strain and electric field conditions. An actuation cycle starts from an equilibrium ground state with zero voltage on the upper and lower electrodes. The lower electrode is maintained at zero volts throughout the cycle, while the voltage, ϕ on the upper electrode is increased until actuation is achieved. Subsequently the voltage, ϕ is reduced to zero during unloading. The actuation strain in the embedded actuator during the cycle is defined by the average displacement of the upper surface of the device. The typical element size used for modelling the embedded actuator is 0.5nm.

To demonstrate the actuation cycle, an embedded actuator of size $L = 45\text{nm}$ and $H = 15\text{nm}$, with in-plane pre-strain $\varepsilon_{11} = 0.82\%$ relative to the initial cubic state of the $BaTiO_3$ crystal is modelled. Note that the $180°$ domain wall thickness that arises from the model is approximately 2nm. A length about three times the device thickness is

chosen to reduce the end effects of the surrounding substrate on the device performance. Electric field $E_2 = \phi / H$ is applied along the negative x_2- axis. When $E_2 = 0$, an equilibrium configuration is found with domains oriented to form a flux closure polarization pattern, see Fig. 3.10. This is taken to be the ground state of the actuation cycle. It can be observed that the upper surface has adopted a curved shape. This is attributed to the domains with polarization parallel to the x_1- axis, which form because of the locked-in tensile strain ε_{11}. Under stress-free conditions, polarization along the x_1-axis is accompanied by negative or compressive strain along the x_2- axis. Mechanical clamping on the edges of the embedded actuator prevent contraction of the edges at $x_1 = 0$ and $x_1 = L$, resulting in a concave upper surface as observed in Fig. 3.10.

As the magnitude of E_2 is increased, the polarization begins to reorient so as to align with the applied field. This switching process is accompanied by ferroelectric

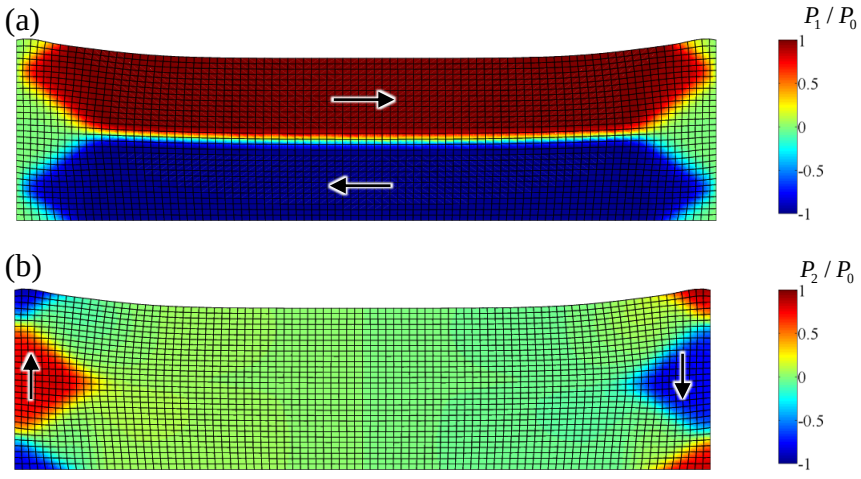

Figure 3.10: Initial polarization pattern adopted by the embedded actuator at $E_2 = 0$ with (a) P_1 / P_0 values (b) P_2 / P_0 values. The deformed configuration is shown with displacements exaggerated.

strains which displace the top electrode of the embedded actuator. Fig. 3.11 shows the domain evolution in the embedded actuator and the actuation cycle starts with a vortex-like structure, Fig. 3.11(a). Increasing the strength of applied field E_2 across the actuator, domains with polarization aligned with the field grow at the expense of oppositely polarized domains which eventually disappear, see Fig. 3.11(a-c). The domain evolution is coupled with mechanical deformation of the upper surface. At $E_2 = 50\text{MV/m}$ a herringbone-like domain pattern is formed, Fig. 3.11(d), and on increasing the electric field to $E_2 = 55\text{MV/m}$ a banded domain evolves, Fig. 3.11(e-f). The transition from the herringbone-like domain pattern to a banded domain pattern passes through an unstable transition as shown in Fig. 3.11(e-f) at $E_2 = 55\text{MV/m}$. At a critical value of electric field, $E_2 = 85\text{MV/m}$, the actuator makes a transition through an unstable needle-like pattern of domains, Fig. 3.11(g-h), and settles to a uniformly polarized single domain, Fig. 3.11(i) – the actuated state of the device. Note that the field strength required for full switching is much less than the breakdown strength of thin-film barium titanate [114]. During the stages shown in Fig. 3.11(g-i), the finite element solver did not find an equilibrium solution and the domain evolution is simulated by controlling the polarization viscosity β to allow the solver to approach equilibrium.

An actuation strain ε_{A} can be defined, relative to the ground state, as the ratio of average displacement of the top electrode to the device height. Equivalently, the actuation strain ε_{A} is the volume average of the strain change $\Delta\varepsilon_{22}$ from the ground state. In the actuated state of the embedded actuator, a strain of $\varepsilon_{\text{A}} \sim 0.45\%$ is attained. Further strengthening of the electric field causes a rise in actuation strain through the

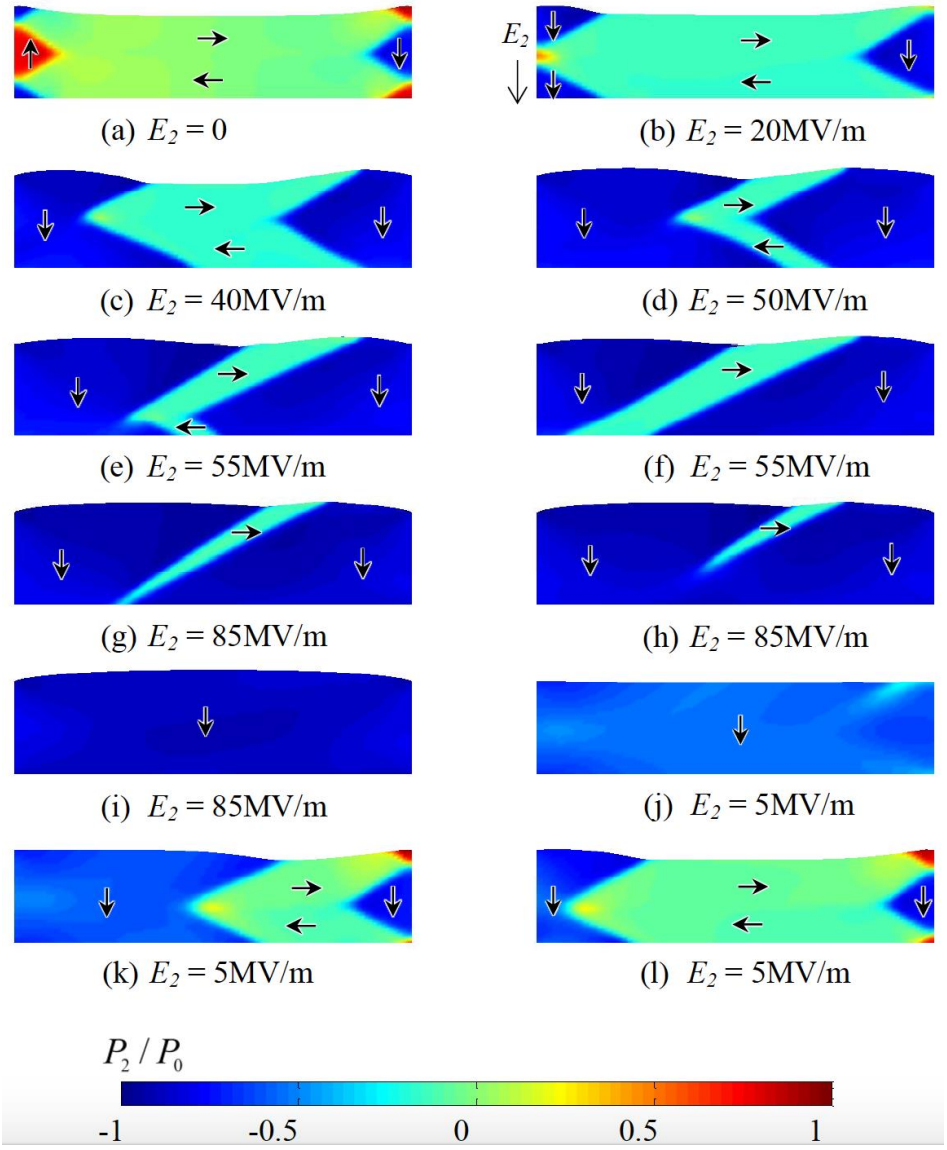

Fig. 3.11: Actuation cycle in the embedded actuator, showing P_2 / P_0 values of polarization. The deformed configuration is shown with displacements exaggerated.

piezoelectric effect. It is of interest to note the stress levels in the actuator. In the fully actuated state a tensile stress of about 2GPa develops in the x_1- direction, comparable to the stresses observed in a $BaTiO_3$ nanogenerator [115]. These stresses are also comparable to residual stresses in ferroelectric films that are typically of order a few hundreds of MPa. In nanoscale $BaTiO_3$ films, defects like cracks are constrained only to be a few nanometers in size, and hence the fracture stresses can be expected to be over

2GPa. The tensile stresses in embedded actuator are due to the substrate constraining the device and preventing contraction in the $x_1 - x_3$ or the out-of-plane direction. The tensile stresses will act to return the device to the ground state after unloading.

On unloading the electric field from its peak value, the embedded actuator retains the single domain state until $E_2 = 5\text{MV/m}$. The actuation strain and polarization along the $x_2 -$ axis gradually decrease, see Fig. 3.11(i-j). At $E_2 = 5\text{MV/m}$, the system goes out of equilibrium and needle-like domains with in-plane polarization nucleate, Fig. 3.11(k). This evolves into a herringbone-like domain pattern and finally returns the actuator to its initial vortex-like flux closure state, completing the actuation cycle, Fig. 3.11(k-l). Note that the transitions through unstable states during the actuation cycle occur at $E_2 = 55\text{MV/m}$, $E_2 = 85\text{MV/m}$ during loading and at $E_2 = 5\text{MV/m}$ during unloading. In each case the finite element solver did not find equilibrium solutions and the transition is modelled by using non-zero β values to relax the system towards equilibrium. However, it was observed the exact route taken during such unstable transitions is highly sensitive to the choice of β values, and this could affect the overall pattern of domains. Effectively the β values used control the rate at which the system passes through an instability. Furthermore the system could also settle into an anticlockwise vortex state symmetrically opposite to the clockwise vortex of Fig. 3.11(a). This sensitivity in the exact route followed by the pattern of domains did not significantly affect the actuation strain or the ability of the device to operate cyclically.

The voltage-strain curve for the embedded actuator is shown in Fig. 3.12(a), where the unstable transitions are indicated by dashed lines. The labels a-l in

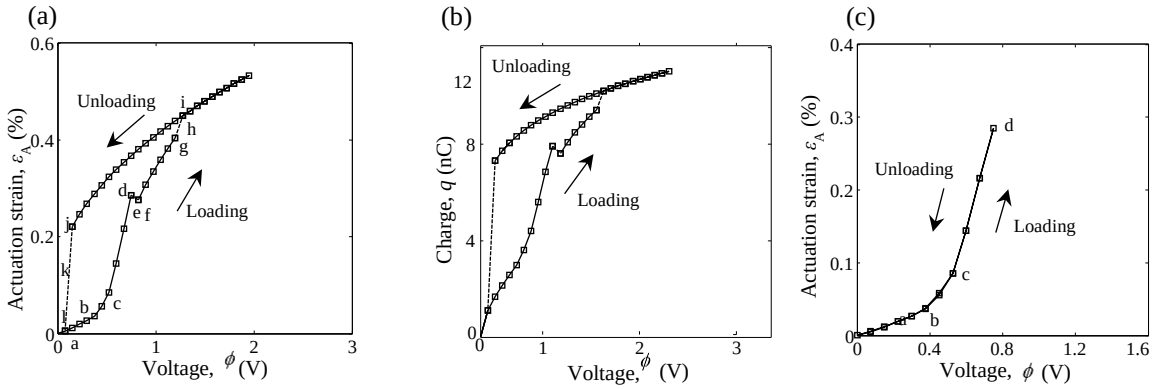

Figure 3.12: Embedded actuator (a) Voltage-strain curve with complete domain switching (b) Corresponding voltage-charge curve (c) Voltage-strain curve with partial switching. Labels correspond to the states shown in Fig. 3.10 (a-l).

Fig. 3.12(a) indicate the corresponding polarization patterns in Fig. 3.11(a-l). The gradual increase in actuation strain during stage a-c corresponds to the initial growth of domains with polarization aligned along the applied electric field. The following rapid strain increase (c-h) occurs as these domains spread towards the device center. The simulation between e-f and h-i, is out of equilibrium and small time steps with a finite polarization viscosity are used to allow the simulation to reach a single domain state.

During the unloading cycle, the actuation strain of the embedded actuator decreases as indicated by labels i-j. Finally from j-l the domain pattern reverts towards its initial state, once again out of equilibrium. The total charge collected on the upper electrode during the actuation cycle is shown in Fig. 3.12(b). It should be noted that the hysteresis in the voltage-strain and voltage-charge curves arises entirely from the unstable transitions: at all other points, the model is incrementally moving between equilibrium states that are "nearby" in the sense that the changes in domain pattern are also incremental. Consequently, by choosing a peak value of applied electric field less than 55MV/m, that is $\phi < 0.82\text{V}$, the device can be operated without hysteresis. This is illustrated in Fig. 3.12(c), where the applied electric field is limited to $E_2 = 50\text{MV/m}$

($\phi < 0.75\text{V}$) thereby avoiding unstable transitions. The loading curve in Fig. 3.12(c) is identical to the corresponding part of Fig. 3.12(a), while the unloading curve follows the loading curve. The voltage-strain curve then shows no hysteresis to within the model precision, and results in a peak actuation strain of 0.28%.

The embedded actuator can be improved by exploring the space of design parameters to enhance its achievable actuation strains. In this regard, variation of the aspect ratio $A_r = L/H$ and the imposed in-plane strain ε_{11} are considered. Both these parameters could be controlled through the manufacturing processes. Other parameters, for example the size or scale of the devices should be considered for a full optimization and is intended as future work. However, it is found that increasing the device size by a factor of 3 or more typically resulted in the formation of complex domain patterns that are not necessarily repeatable upon cycling: The device is truly a nano-actuator in that it relies upon its small scale to work.

First, the variation of the aspect ratio A_r of the embedded actuator is considered, with height held constant at $H = 15\text{nm}$. Fig. 3.13(a) indicates the variation in actuation strains ε_A, attained on ferroelectric switching as a function of the device aspect ratio. Aspect ratios in the range 0.4 to 1 result in low values of actuation strain, typically $\varepsilon_A < 0.1\%$. These device designs are effectively clamped against actuation by the surrounding substrate material. On increasing the aspect ratio to $A_r = 3$, a steep rise in actuation strain to $\varepsilon_A = 0.45\%$ is observed: in this regime the device functions as illustrated in Fig. 3.11, and increasing A_r steadily reduces the influence of end constraint. Beyond $A_r \sim 3.5$, further increase in A_r does not contribute a significant increase of actuation strain, which saturates at about $\varepsilon_A = 0.5\%$. In this regime, the

actuator did not reliably return to the ground state upon unloading. The small step increase in actuation strain when A_r = 3.5, results from an increase in the applied

(a)

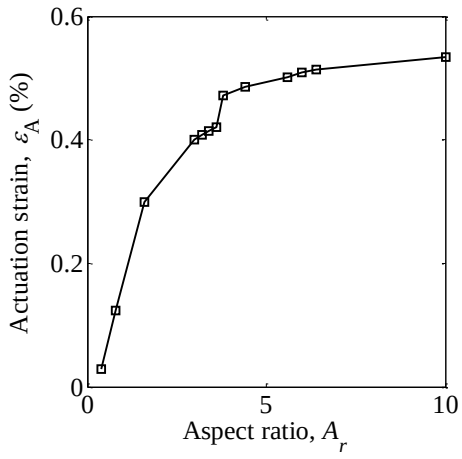

(b)

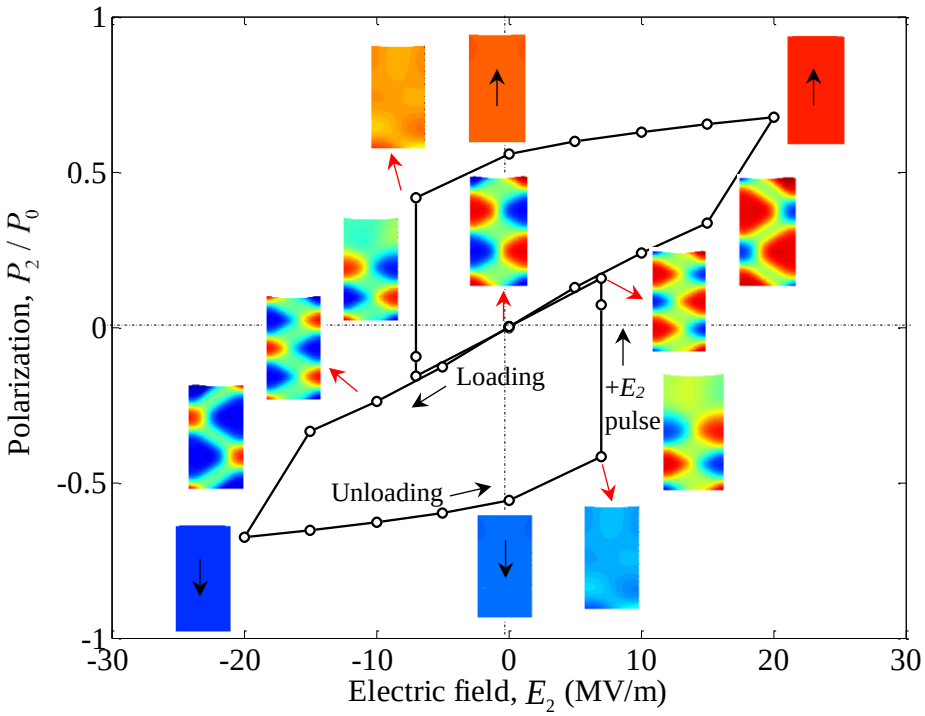

Figure 3.13: (a) Parametric study for the embedded actuator (height, H = 15nm) showing the effect of varying the aspect ratio, A_r (b) Hysteresis loop at aspect ratio A_r = 0.4, indicating a potential application as a memory element. Inset schematics illustrate P_2 / P_0 in the domain patterns.

electric field required to reach the fully actuated state. This was caused by a change in the domain patterns that form during the transition to the single domain state. To summarise, it is found that $A_r \sim 3$ provides a satisfactory compromise, giving a high value of actuation strain, while maintaining a stable actuation cycle.

It is interesting to note that at aspect ratio $A_r \sim 0.4$ ($L = 6\text{nm}, H = 15\text{nm}$) the simulated device did not return to the ground state when the upper electrode voltage ϕ is reduced to zero. Instead, a single domain state polarized in the $-x_2-$direction, is found to be retained after unloading, see the hysteresis loop in Fig. 3.13(b). A negative voltage pulse or a positive electric field, $E_2 = 7\text{MV/m}$ is required to initiate the formation of a flux-closure pattern. Consequently the voltage applied on the upper electrode is reduced to below zero, to allow the device to return to its initial state. However a stronger electric field, $E_2 > 7\text{MV/m}$ could flip the polarization into a stable single domain state with $+P_2$ polarization. Here again, the initial flux-closure state is not attained on reducing the applied electric field, E_2 to zero. A negative electric field $E_2 = -7\text{MV/m}$, is then required to return the device to the flux-closure domain pattern. Therefore this device can possess three stable states of polarization pattern at $E_2 = 0$, as shown in Fig. 3.13(b). This indicates a potential of the device with $A_r \sim 0.4$ to be used as a tri-state memory element, though it should be noted that the device length here is only a few domain wall widths, which could present practical difficulty for manufacture. On the other hand, its small size, and simplicity of operation, could be advantageous for a high density non-volatile memory.

Next the effect of in-plane residual strain ε_{11} on the achievable actuation strain is studied. Here, ε_{11} is varied, while the aspect ratio is kept constant at $A_r = 3$. The

strain ε_0 = 0.0082 corresponding to the spontaneous strain of $BaTiO_3$ in the tetragonal phase is set as a maximum residual in-plane strain value and $\varepsilon_{11}/\varepsilon_0$ is varied in the range zero to unity. When $0.84 < \varepsilon_{11}/\varepsilon_0 < 1$, the embedded actuator behaves as indicated in Fig. 3.11. There is a maximum actuation strain of 0.46% occurring when $\varepsilon_{11}/\varepsilon_0$ = 0.84, however there is relatively little gain from varying ε_{11} within this range, see Fig. 3.14(a). On reducing the in-plane residual strain below $0.84\varepsilon_0$, the actuator remains in a uniformly polarized single domain state during cycling and so the strain enhancement due to $90°$ ferroelectric switching is lost. This indicates the importance of the mechanical biasing by substrate strain in stabilising in-plane domains in the ground state.

Finally, the response of the embedded actuator to a uniform distribution of pressure, *p* on its upper surface is studied. An aspect ratio $A_r = 3$ and in-plane substrate strain $\varepsilon_{11}/\varepsilon_0 = 1$ is chosen for this study. Fig. 3.14(b) shows the actuation strains achieved for a range of pressure $p = 0 - 4000\text{MPa}$. In the phase-field simulations of the embedded actuator under external pressure, a greater voltage is required to actuate the device under an external load and in practice applied pressures greater than 500MPa may be difficult to achieve. However, the simulations allow us to find a theoretical blocking pressure, $p \sim 1500\text{MPa}$, at which the actuation strain ε_A drops to a small value $\approx 0.3\%$.. For pressures $p > 2000\text{MPa}$, the actuation strain either drops to values close to zero or to negative values, see dashed line in Fig. 3.14(b). This indicates that the embedded actuator fails to work against loads greater than 1500MPa. Since the actuation strain is not greatly affected by applied pressure in the range 0 - 500MPa, the embedded actuator can be effective in areas where the target is to achieve a maximum

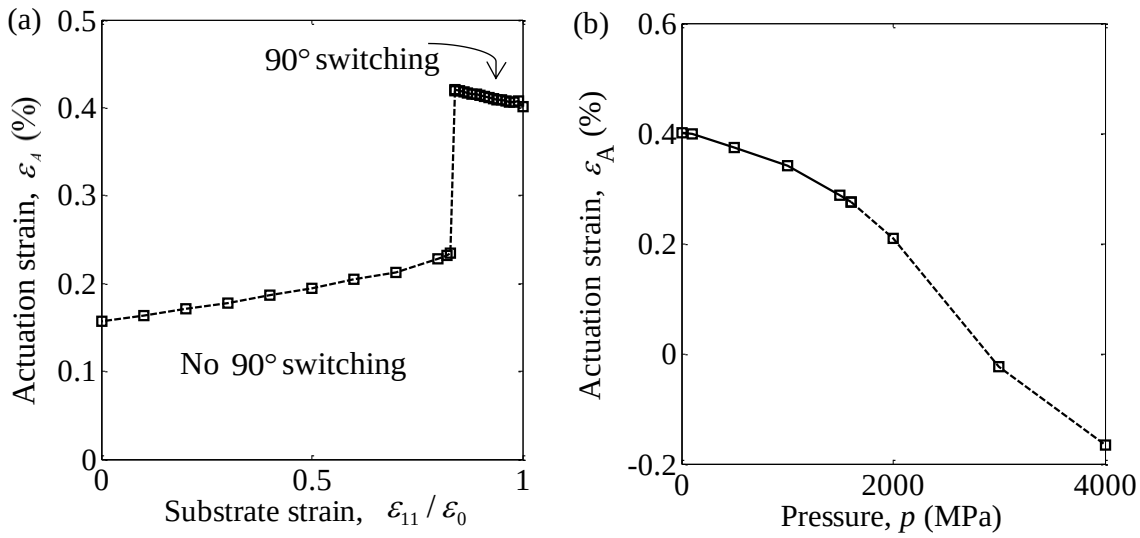

Figure 3.14: The actuation strains achieved by the embedded actuator on varying the (a) substrate strain, ε_{11} and under the effect of (b) uniform pressure loading, p.

force, with displacement and efficiency as secondary criteria. Potential applications for embedded actuators can be envisaged in actuation of a nanoscale gripper or tweezers which require a specified force, and minimal displacement [116].

The actuation strains produced by the embedded actuator are relatively large in comparison to those of the clamped actuator. However, the work done per unit depth by the embedded actuator against p = 500MPa is estimated to be ~ 1.4nJ/m, while the electrical energy dissipated is approximately ~ 11nJ/m. These values indicate low efficiency of this device, at about 13%: further improvement would be desirable for cyclic applications such as pumps or oscillators. Next an actuator design that generates greater displacements, using a mechanism in the form of bending a slender beam is explored. Here, the idea is to design an actuator that can translate small displacements along the x_1-axis into amplified lateral or sideways displacements, using the concept of bending a slender beam.

3.4 Bending actuator

The concept of the bending actuator is to enhance displacements by exploiting the large sideways displacement attained on bending a slender beam fixed at its ends. This sideways displacement can be achieved by inducing a longitudinal strain along the beam length. Based on this concept, a design for a bending actuator of nominal dimensions 365nm length × 15nm height is shown in Fig. 3.15(a). The ends of the actuator are rotated by an angle $\theta = 3°$ and clamped in this state, inducing an initial curvature that stabilises bending towards the $+x_2-$direction. These mechanically clamped edges are maintained at 5V throughout the actuation cycle. Electrodes of width, e = 17nm are modelled in pairs along the top and bottom surfaces of the actuator with a nominal spacing of s = 35nm measured between the centres of adjacent electrodes. The electrode pairs are numbered, $k = 0\ldots5$ as shown in Fig. 3.15(a). Note that a reference line is defined at x_2 = 15nm, and that the position of the k = 0 electrode in the initial state is below this reference line, indicated by marker 'A' in Fig. 3.15(b). The actuation strain, ε_A for the bending actuator is then defined as ratio of the *average displacement* of the k = 0 electrode to the device height of 15nm, see Fig. 3.15(b). That

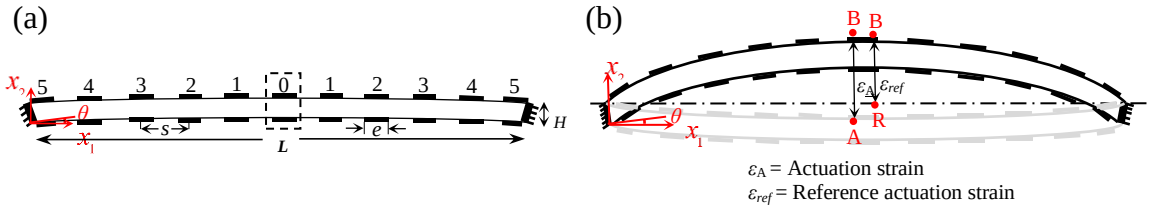

Figure 3.15: (a) Schematic diagram of bending actuator. The dashed boundary indicates electrode pairs which are numbered $k = 0\ldots5$. (b) Representation of strains defined for the bending actuator.

is, the average displacement is measured as the total separation between the initial position of $k = 0$ electrode at 'A' and the actuated position of $k = 0$ electrode at 'B', see Fig. 3.15(b). For future discussion a reference actuation strain ε_{ref} is introduced, which is defined as the ratio of *net displacement* of the $k = 0$ electrode from the reference line located at $y = 15$nm (i.e., distance between markers 'R' and 'B' in Fig. 3.15(b)) to the device height.

The operating principle of the bending actuator is to cycle the slender ferroelectric beam between a curved "on" state and a flat "off" state. In order to achieve this operation a pattern of electrodes shown in Fig. 3.15(a) is chosen. The electrodes on the top ($y = 15\text{nm}$) and bottom ($y = 0$) surface of the bending actuator are referred to as the upper and lower electrodes respectively. The key idea of using this pattern of electrodes is to produce an average electric field that is along the beam length in the "on" state (bending the device); and perpendicular to the beam length in the "off" state (flattening the device). This average electric field is achieved by distributing the voltage on the electrodes as follows,

(a) the electric potential applied to the upper electrodes, ϕ_U is of the form, $\phi_U = \phi_0 + k\phi_1$. Here ϕ_0 and ϕ_1 are constants with values of 2.5V and 0.5V respectively, and k is the electrode pair number shown in Fig. 3.15(a). For example, the electric potential on a $k = 0$ electrode is $\phi_U = \phi_0 = 2.5\text{V}$. An example of the voltage distribution on the upper surface of the bending actuator is illustrated schematically in Fig. 3.16(a);

(b) the electric potential applied to the lower electrodes, ϕ_L is of the form, $\phi_L = \alpha(\phi_U) = \alpha(\phi_0 + k\phi_1)$, see Fig. 3.16(a). Here, α is the loading parameter that is varied from 0 to 1, taking the actuator between the "off" and "on" states

respectively. By controlling α, a nominal electric field $E_{\text{nom}} = \alpha\phi_1 / s$ is set up along the length of the actuator. For example, when $\alpha = 0$, the lower electrodes are at zero voltage and $E_{\text{nom}} = 0$, see Fig. 3.16(b). Note, non-zero electric field perpendicular to the beam length is present in each electrode pair (e.g., between the upper and lower electrodes in electrode pair $k = 0$). This results in an average electric field along the $-x_2-$ axis that flattens the beam in the initial state of the device. On increasing the value of α in steps of 0.1, the average electric field along the $-x_2-$axis decreases, and the value of E_{nom} along the beam length

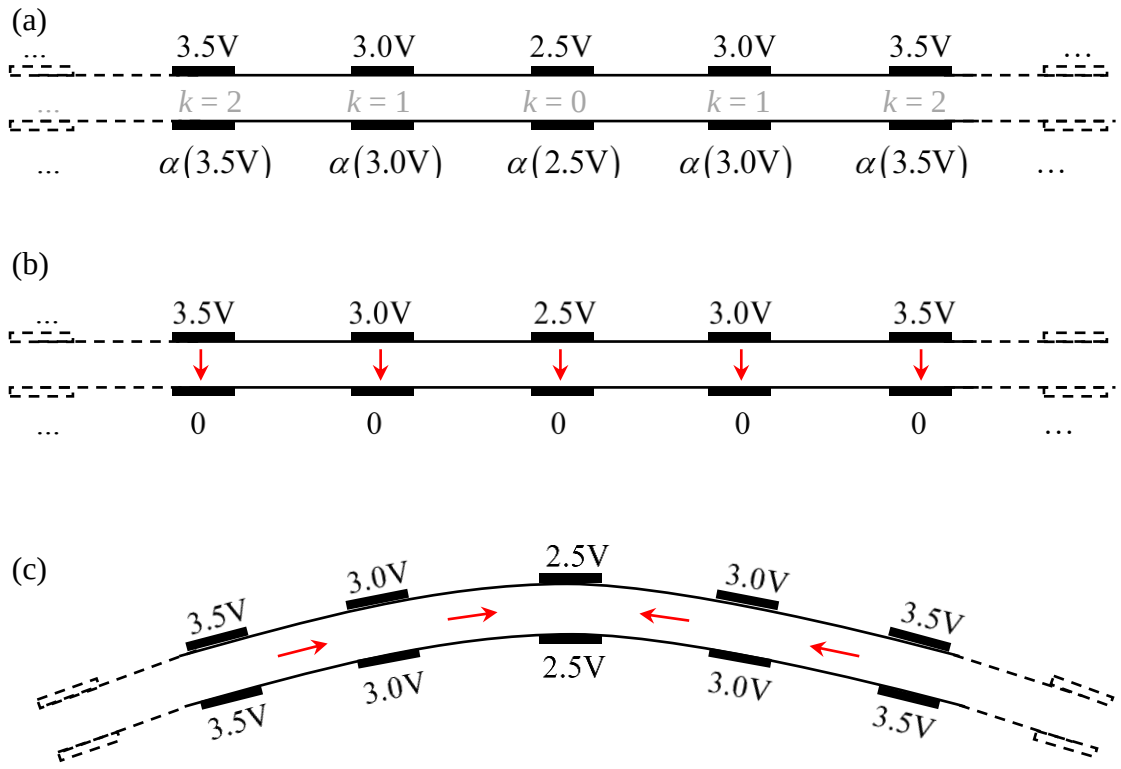

Figure 3.16: Schematic illustration of the operating principle of bending actuator. (a) Generic pattern of voltage distribution across the representative k = 0,1,2 electrodes; (b) initial state of the actuator with $\alpha = 0$; (c) actuated state of the actuator with $\alpha = 1$.

increases. At $\alpha = 1$ the voltage distribution on the lower electrodes is shown in Fig. 3.16(c). Here E_{nom} is maximum and along the length of the beam and corresponds to the actuated state of the device.

For later use, the voltage $\phi_{\text{nom}} = \alpha\phi_1$ is introduced, representing the net potential difference between adjacent electrodes on the lower surface. The effect of this distribution of electrode voltages is to produce an average electric field in the x_2- direction in the "off" state, and an electric field in the $\pm x_1-$ direction in the "on" state; this activates 90° ferroelectric switching in the bending actuator.

Fig. 3.17(a-j) depicts domain evolution in the actuation cycle of the bending actuator. An enlarged view of the polarization patterns in Fig. 3.17(a-j) over a section of the bending actuator is shown in Fig. 3.18(a-j), wherein the polarization directions along both axes are indicated using arrows.

When $E_{\text{nom}} = 0$, the bending actuator settles into a ground state with polarization pattern as shown in Fig. 3.17(a). On increasing E_{nom}, domains aligned with the $\pm x_1-$ direction nucleate and grow, see Fig. 3.17(b-d). Ferroelectric switching extends the actuator along its length, but the presence of end constraints force this extension to be accommodated by bending. At a critical value of electric field E_{nom} = 14.3MV/m the simulation makes an unstable transition to the fully actuated state, Fig. 3.17(e-f), resulting in actuation strain $\varepsilon_{\text{A}} \sim 15\%$. On reducing the value of applied electric field to E_{nom} = 11MV/m there is a rapid decrease in the actuation strain, Fig. 3.17(g-h). New domains nucleate from the clamped edges and spread towards the device centre, Fig. 3.17(g-i). The appearance of $90°$ domains at the ends of the beam in Fig. 3.17(g) begins to flatten the device returning it to its ground state, completing the actuation

cycle. Note that the domain pattern in the bending actuator can settle into a ground state with opposite polarization orientation, Fig. 3.17(j), in comparison to the initial state of the actuator, Fig. 3.17(a). Thus the actuation cycle need not be repeatable in terms of the domain pattern formed, however this does not significantly affect the actuation strain. A closer observation of domain evolution during the actuation cycle can be made from Fig. 3.18.

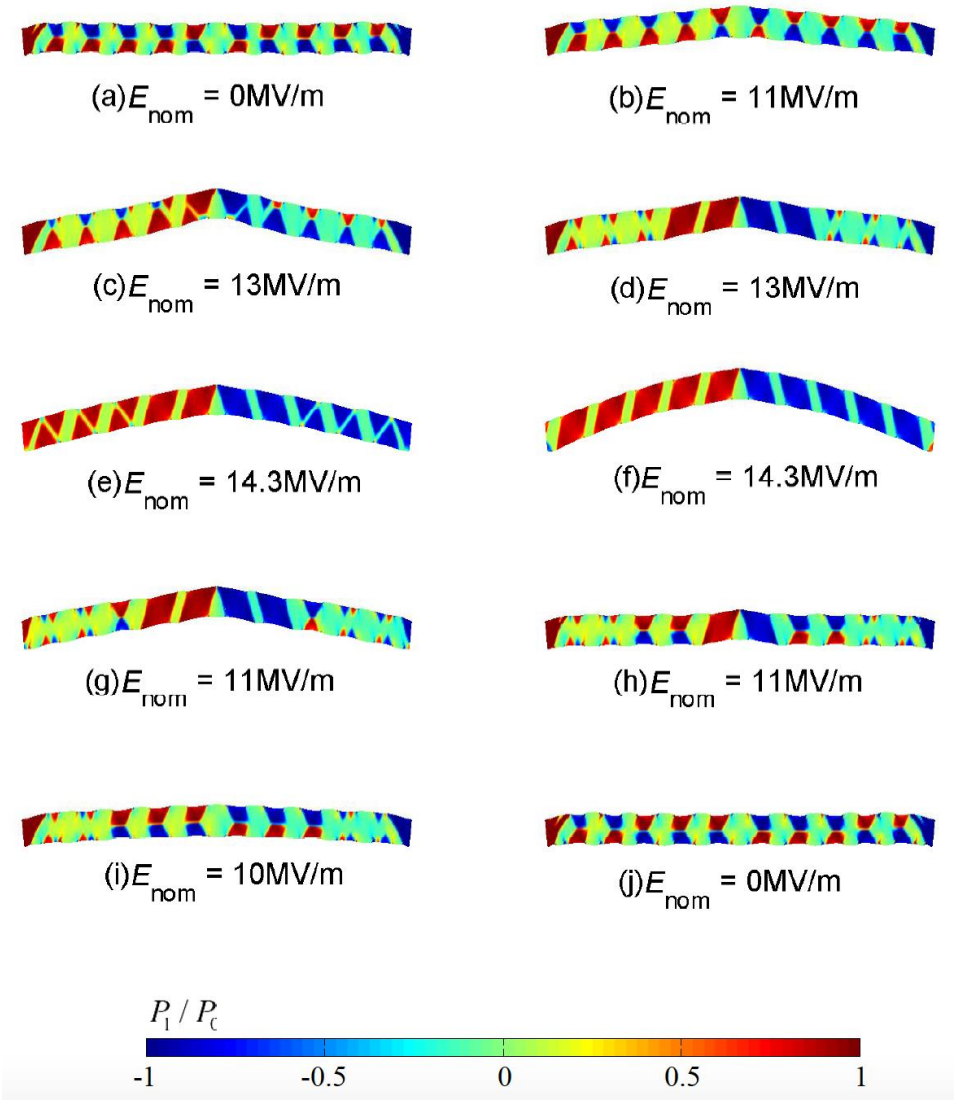

Figure 3.17: Actuation cycle in the bending actuator, showing polarization in the x_1- direction. Note: displacements on the deformed mesh are exaggerated to help visualisation of the actuation process.

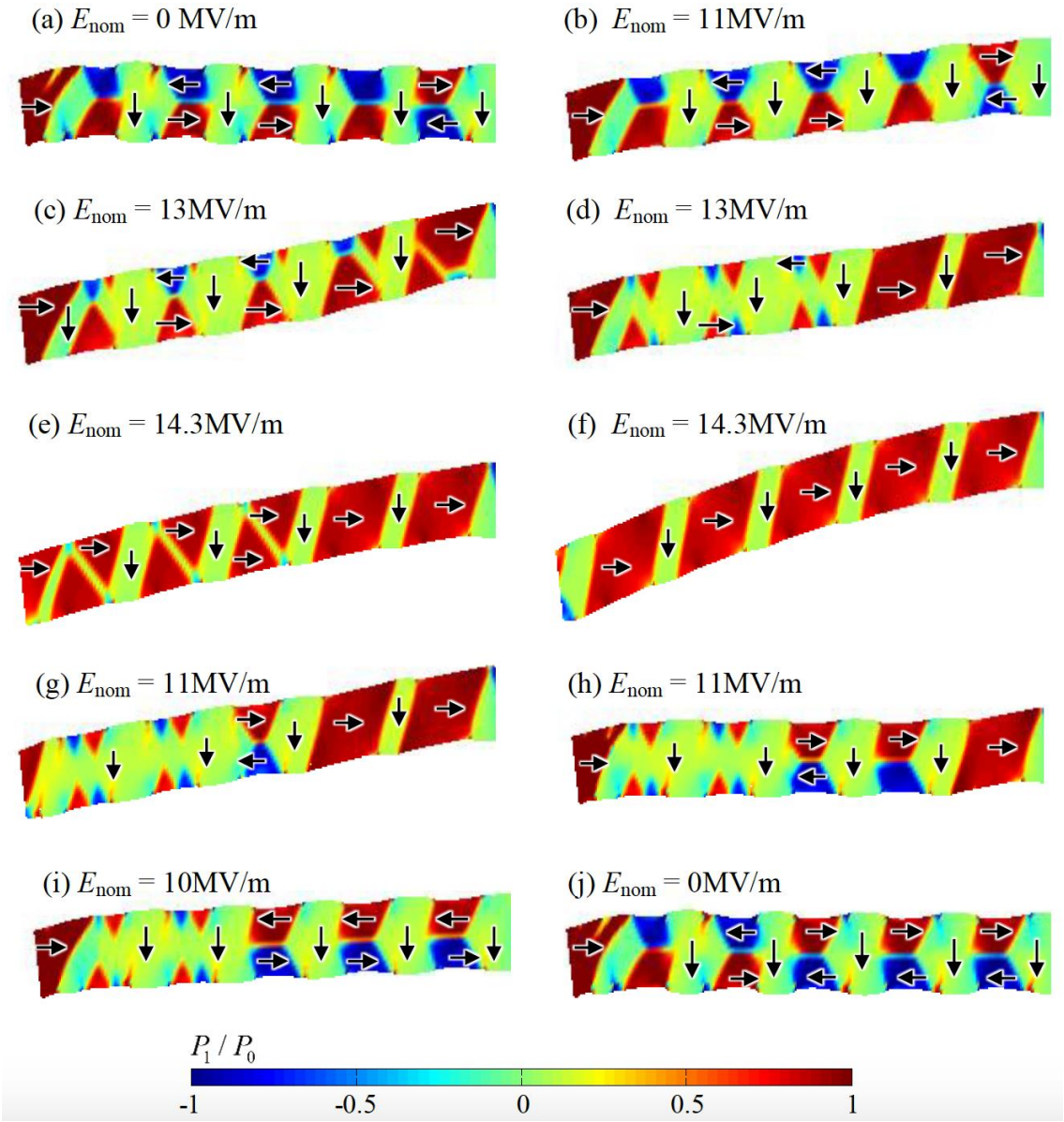

Figure 3.18(a-j): Enlarged view of the polarization patterns in a section of bending actuator during the actuation cycle. (a-f) illustrate the disappearance of domains polarized opposite to E_{nom} and depict the nucleation of domains aligned in the direction of the applied electric field. Subfigures (g-j) illustrate the domain evolution during the unloading cycle. The inset arrows indicate polarization directions in the domain pattern.

A voltage-strain curve for the bending actuator is shown in Fig. 3.19(a). The actuation occurs during stages a-f, with a-e representing a gradual actuation as domains grow in equilibrium, and e-f representing an out-of-equilibrium stage. The unloading stages f-i follow a series of transitions corresponding to the nucleation and growth of domains that restore the original state of the actuator. The peak actuation strain of 15% is attained in the bending actuator. This actuation strain represents a displacement about 10 times greater than that of the embedded actuator and many times greater than the strains in a conventional piezoelectric device. Note that the local strain at any material element does not exceed 0.8%. The voltage-strain curve for the bending actuator shows hysteresis due to the transition of domain patterns through non-equilibrium states. In order to show the voltage-charge behaviour of this actuator, a work-equivalent charge q_{nom} is defined such that $\phi_{\text{nom}}\delta q_{\text{nom}} = \int_s \phi \delta q ds$. Here ϕ is the surface voltage, and δq is an increment of surface charge density, with the integral conducted over the area of the

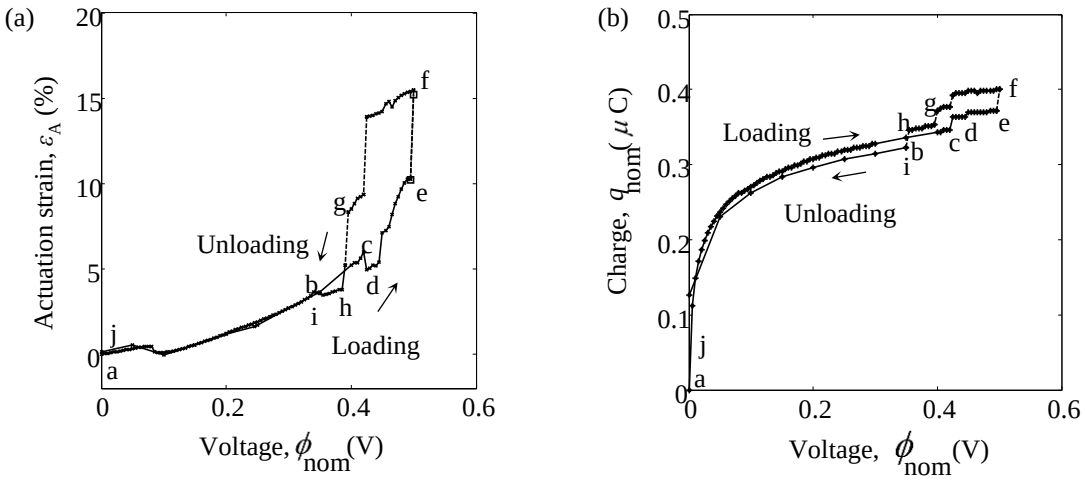

Figure 3.19: Bending actuator (a) Voltage-strain curve (b) Voltage-charge curve. Labels correspond to the states shown in Fig. 3.17.

surface electrodes. Fig. 3.19(b) shows the work-equivalent charge during the actuation cycle. This shows a steep increase in charge early in the loading cycle ($\phi_{\text{nom}} < 0.1$V), indicating that the initial polarization state is highly mobile. This is consistent with the presence of non-zero electrode voltages and hence the presence of electric fields even in the "off" state. Small changes in voltage result in domain wall movement. Fig. 3.19(b) also shows hysteresis in the voltage-charge cycle indicating energy dissipation during the unstable transitions.

Next, a parametric study of the bending actuator is carried out, by exploring design parameters such as the electrode coverage, $e_c = e/s$, and angle of end rotation, θ, at the beam ends, see Fig. 3.20(a-b). The schematic diagram in Fig. 3.20(a) illustrates the variation of the electrode coverage on a representative unit cell of the bending actuator. The subfigures illustrate the variation of electrode width, e and the spacing size, s for $e_c << 1, e_c = 0.5$ and $e_c \sim 1$. In the present work, the effect of electrode coverage, e_c is varied in the range 0.2 - 0.8. Values beyond this range would require features, such as electrodes or gaps between adjacent electrodes to be smaller than 5nm, which is taken as a practical limit for manufacture. The effect of varying $0.2 \le e_c \le 0.8$ on the actuation strain is next explored. Here, the "on" and "off" states of the bending actuator are separately modelled for different values of e_c through a virtual process of slow electrode growth on the actuator surface. For example, the "on" state of the bending actuator with $e_c = 0.2$ is first simulated. Starting from this state and maintaining the pattern of voltages ϕ_U and ϕ_L on electrodes constant (that is at $\alpha = 1$), the electrode coverage is incremented in steps of 0.1 upto $e_c = 0.8$. This is done by increasing the electrode width *e*, while the spacing *s* is held constant. The vertical

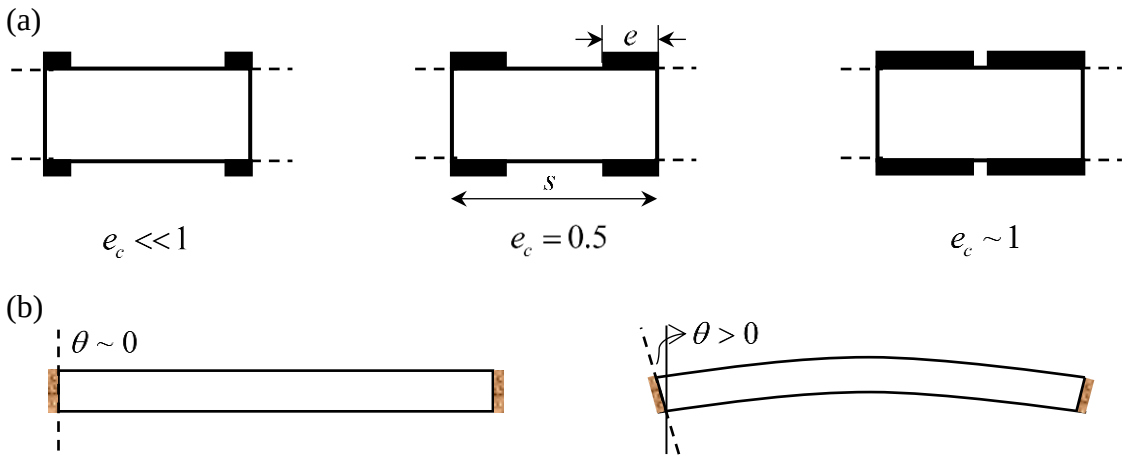

Figure 3.20: Schematic illustration of varying (a) electrode coverage, e_c over a unit cell of the bending actuator and (b) angle of rotation, θ of the device.

displacement of the bending actuator in the "on" state is measured at each value of e_c. Likewise, the "off" states of the bending actuator at different values of e_c are simulated, starting from $e_c = 0.2$. The position of the $k = 0$ electrode for each value of e_c is measured in the off state. Based on these measurements of the $k = 0$ electrode in the on and off states, the actuation strain of the device is calculated and plotted as a function of electrode coverage, see Fig. 3.21(a).

This method of virtual electrode growth allows the actuation strain for each design to be estimated without simulating the entire actuation cycle. These estimates are open to significant error because the complex domain patterns present in the actuated state are not necessarily reproduced if actuation is achieved by a different route. For a check on the reliability of the estimates, the full actuation cycle from ground state to actuated state is simulated at selected e_c values. While small differences in domain pattern of the actuated state are observed, the estimated actuation strains are generally within $\pm 3\%$ of the full-cycle value.

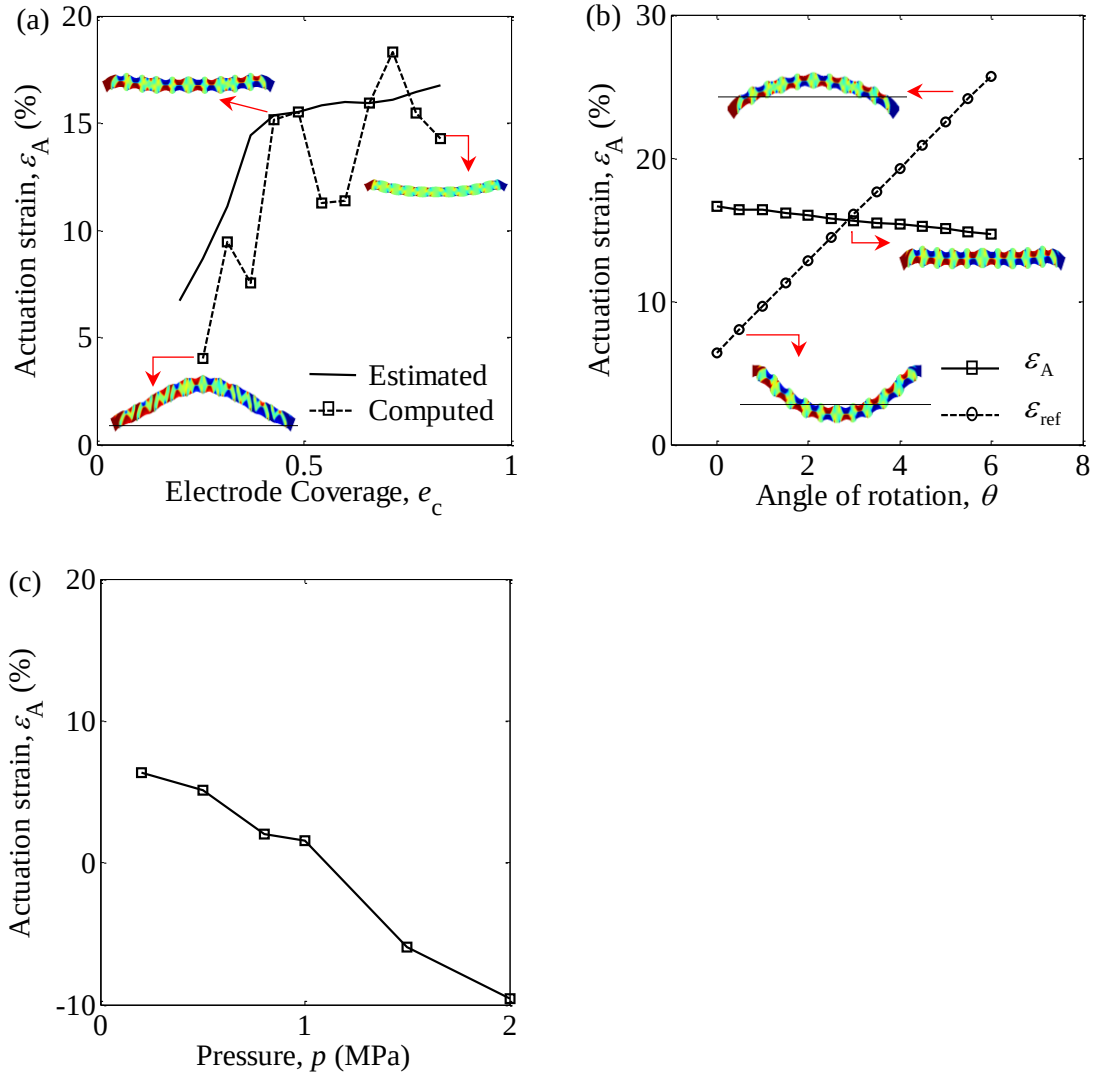

Figure 3.21: Selection of design parameters for the bending actuator: (a) variation of electrode coverage, e_c; (b) variation of angle of end rotation, θ (that is, nodal positions at the ends of the bending actuator are incrementally changed, see Fig, 3.20(b), to simulate rotation of the end supports); (c) actuation strain when working against pressure p. Inset schematics show the ground state of the bending actuator.

To understand the variation in behaviour, note that in the "off" state, domains polarized parallel to the x_2-axis form between the upper and lower electrode of each

electrode pair. These domains tend to shorten the beam length giving a flat initial state. But when the electrode coverage is low (e_c = 0.2 to 0.35), a combination of triangular and banded domains appear in the ground state. This domain pattern provides an initial upward curvature to the "off" state of the device and the actuation strain, which measures the change between "off" and "on" is small. Increasing the electrode coverage increases the actuation strain, up to about e_c = 0.5, at which point the actuator cycles between a nearly flat "off" state and a curved "on" state. Further increase in e_c does not significantly affect the actuation strain.

Next, the variation of the angle of end rotation θ is explored, holding e_c constant at 0.45. A schematic illustration of varying the angle of end rotation is shown in Fig. 3.20(b). Once again, the "on" and "off" states are traced by holding ϕ_U and ϕ_L constant, this time making incremental changes to the positions of nodes at the beam ends to simulate rotation of the end supports. This is done by changing θ in the range $0° - 6°$, see Fig. 3.21(b). Here the upper limit corresponds to the beam adopting an arc shape, with the upper surface strained by ε_0 relative to the lower surface. Varying θ did not have a significant effect on the actuation strain of the device. However, the reference actuation strain, ε_{ref} which accounts for net displacement of the bending actuator from a reference line at y = 15nm linearly increases with θ. For $\theta < 3°$ the actuator adopts a downward curvature in the ground state, while at $\theta = 3°$ the beam is nearly flat; it is curved upward for $\theta > 3°$, see inset schematics in Fig. 3.21(b). Hence the values of ε_{ref} and ε_{A} are approximately the same when θ = 3° and this configuration is chosen for further study.

Finally, the response of the actuator working against a uniform pressure *p*, applied over the upper surface, is tested. The slender design of the bending actuator limits its capability to work against loads: at *p* = 1MPa, the achievable actuation strain is reduced to $\varepsilon_A \sim 1\%$ and further increase in the load blocks the actuator, see Fig. 3.21(c). This indicates that the potential applications of an actuator are closely linked to its design. The potential applications for the nano-actuators explored in this work are discussed in the next section.

3.5 Applications

The design and efficient performance of the nano-actuators discussed in this chapter are largely determined by the nature of application. That is, an actuator is commonly selected for a task, if the forces and displacements produced by the actuator are in agreement with the requirements of the task. Following Huber et al. [117], a 'performance chart' mapping potential actuator applications based on the magnitude of blocking pressure and actuation strain is shown in Fig. 3.22.

In Fig. 3.22, the actuators can be broadly categorized into force-type, displacement-type and work-type actuators. In the force-type actuator, the primary aim is to generate larger forces or work against large blocking pressures, while the achievable displacements are treated to be secondary. For example, Fig. 3.22 shows that the bulk piezoelectrics and bulk magnetostrictors produce significant blocking pressures in the range 10-1000MPa, but offer small actuation strains ~0.1%. The clamped and embedded actuators explored in this chapter work effectively against loads of up to 500MPa and can be classified as force-type actuators. The force-type actuators find applications in automobile fuel injectors [118], where the pressurised fuel is to be

injected at precise time intervals for efficient combustion. Force-type actuators are also used in nano-tweezers or grippers [119], where the actuators are required to generate large forces to 'grasp' an object, while producing small displacements. Table 3.1, illustrates some examples of actuator applications, such as in the fields of automotive industry [118], [120], biomedical applications [119], [121] and instrumentation [122], [123].

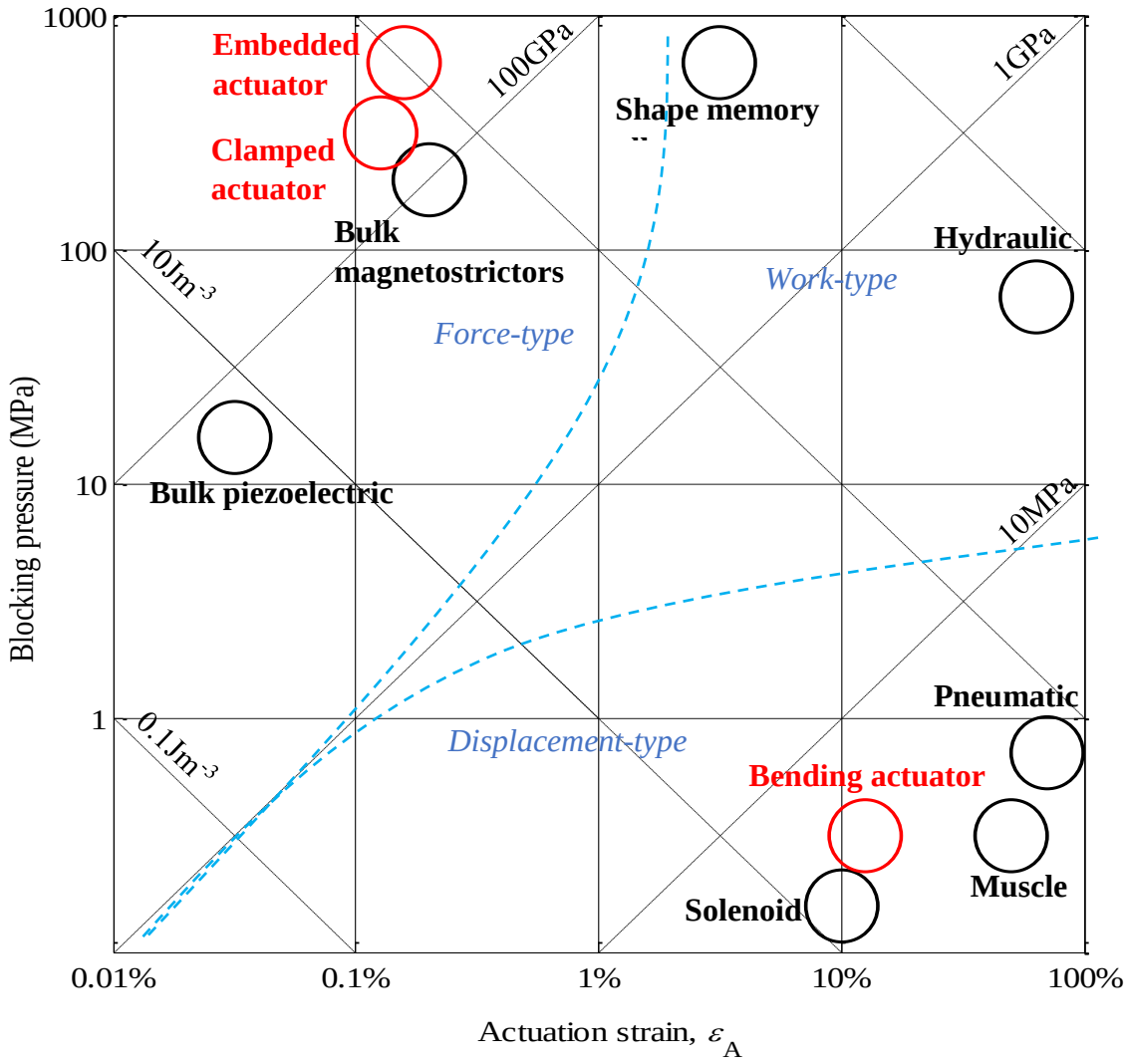

Figure 3.22: Performance chart for different actuator applications, modified from Huber et al. [117]. The markers in black indicate the approximate high end performance of various actuators/materials. The red markers indicate the performance of the nano-actuator concepts explored in this work.

By contrast, the displacement-type actuators can be defined to generate enhanced displacements with their ability to work against forces being a secondary objective, see Fig. 3.22. Pneumatic actuators [124] and solenoids typically offer large strains $10-100\%$, however work against small loads of magnitude <1MPa. For example, the chevron-beam actuators which are used to position micro-reflectors [125] are not subjected to work against heavy loads, but are required to generate large actuation displacements. A piezoelectric actuator with a five-bar mechanism [122] generates large displacements that enhance positioning control and manipulation of objects at the nanoscale. These actuators find applications as scanning probes in microscopes that offer precise positioning and control. Mosadegh et al. [124] demonstrate an application of the displacement-type pneumatic actuator in a 'braille' display. Here the actuators work against small loads arising from tactual reading but generate large displacements $\sim 700\mu$m, see Table 3.1. Displacement-type actuators also find applications in 'haptic' pressure devices [126]. These examples suggest that the bending actuator developed in this study is best suited for applications that require enhanced displacement at negligible loads, see Fig. 3.22. The bending actuator which generates actuation strain ε_{A} = 15% and has a blocking force of about 1MPa is thus classified as a displacement-type actuator.

Next, some applications are more readily specified by the work achieved in the actuator stroke and the efficiency of energy conversion. These types of actuators are classified as work-type actuators, see Fig. 3.22. The actuation of the braking system in automobiles [123] and the micro-pump device in drug delivery system [121] are classified under this category, see Table 3.1.

Force-type	Displacement-type	Work-type
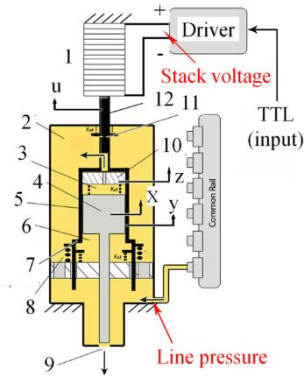	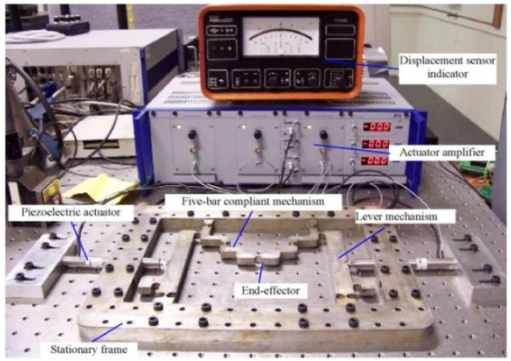	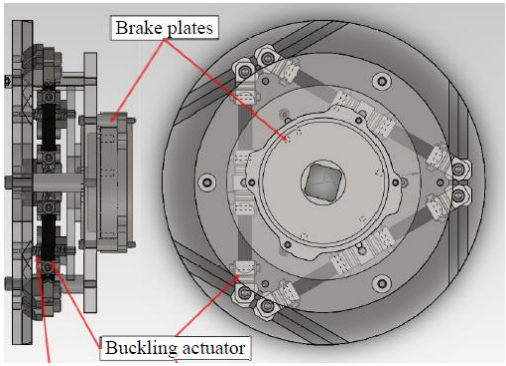
Piezoelectric stack actuators in fuel injectors [118]. Reprinted from Ref. [118], with permission from Elsevier.	Five-bar mechanism for enhanced control of nano-positioning and manipulation [122]. Reprinted with permission from Elsevier.	Piezoelectric buckling actuators for the efficient braking system in automobiles [123]
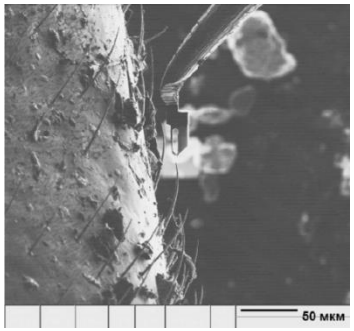	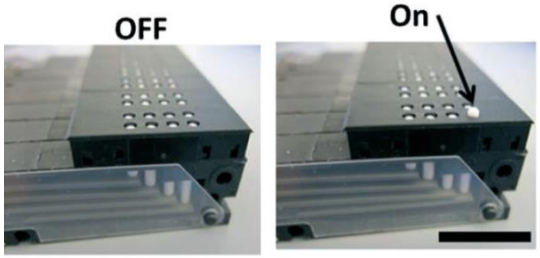	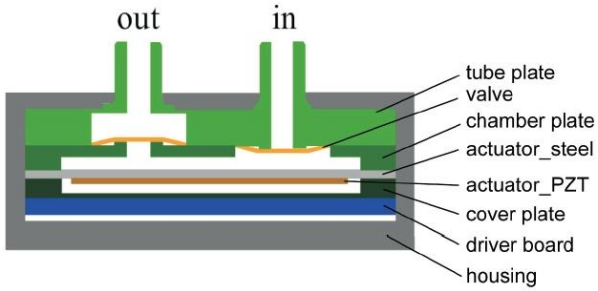
A shape memory alloy nano-tweezer selecting a fiber on a body of Culex pipiens [119].	Haptic application of pneumatic actuators for an electronic braille display [124]. Reproduced with permission of the Royal Society of Chemistry.	Micropump application in precision delivery of drugs or other fluids [121]

Table 3.1: Example applications of force-type, displacement-type and work-type actuator

Finally, some potential applications of the embedded and bending actuators, based on design, blocking pressure and actuation strains are considered. For example, the force-type embedded actuator, can be designed as a nano-tweezer or a nano-gripper as illustrated schematically in Fig. 3.23(a). This actuator can work against pressures of up to 500MPa and can be effectively used to grip nanoparticles. The displacement-type bending actuator, can be used in optical control, see Fig. 3.23(b). For example, the bending actuator can control the position of a small micro reflector, in an optics device.

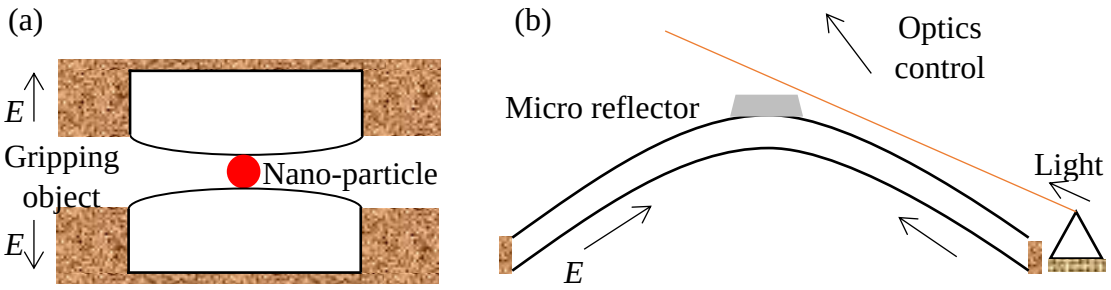

Figure 3.23: Schematic illustration of the a potential application of (a) embedded actuator in a nano-tweezer, and (b) the bending actuator in a optics control system.

3.6 Conclusion

Overall, the actuation strains produced by ferroelectric switching are several times greater in comparison to the piezoelectric actuators in market, and this could be exploited in nanoscale devices. The clamped and embedded actuators are bound by a substrate and driven by an electric field. These actuators produce strains of the order of 0.4%, while the bending actuator, controlled by a set of electrodes distributed along the beam length, exploits its slender nature to produce enhanced strains. The design parameters such as aspect ratio A_r and in-plane strain ε_{11} have been explored to enhance the achievable displacements for the embedded actuator. Aspect ratio $A_r \sim 3$ and substrate strain $\varepsilon_{11} = \varepsilon_0$ was found to be a good compromise, because of reduced end effects from mechanical clamping and reliability of a repeatable actuation cycle. The effect of electrode coverage e_c, and angle of end rotation θ, were explored for the bending actuator. An electrode coverage $e_c = 0.5$ and angle of end rotation $\theta = 3°$ was found satisfactory for the bending actuator. At these design parameter values, the bending actuator cycled between a flat ground state and a curved actuated state. This study of exploring the design parameter space for the actuators, also illustrated a potential application for the embedded actuator (at $A_r \sim 0.4$) as a tri-state memory element.

4

Scaling and surface effects on polarization patterns

Kittel's theory [127] predicts the formation of a closed loop structure of magnetic domains in ferromagnetic nanoparticles. These structures are commonly referred to as flux-closures or vortices, and have been widely observed in ferromagnets. It is intriguing to note that although ferroelectrics are analogous to ferromagnets in that they form domains, vortices formed from ferroelectric domains are rarely seen. Several theories of ferroelectrics also predict the formation of vortex domain patterns. For example, in chapter 3 the phase-field simulations of the embedded nano-actuator illustrated the formation of a closed loop structure of polarized domains in the initial state. These polarization vortices are important to the design of nanoscale actuators, and possess tremendous potential in increasing the storage density of memory devices [20].

In this chapter, the elusive nature of the vortex polarization pattern is explored using phase-field methods. Generic configurations of barium titanate nanowire cross-sections are modelled and the energies of the vortex polarization patterns are calculated. The effects of scaling, surface energy, surface conductivity and orientation of the nanowire cross-section on the formation of vortex polarization patterns are explored.

4.1 Vortex domain pattern

Recently, a significant amount of research has been directed towards finding polarization vortices and studying their nanoscale properties in detail [19], [71], [102], [128]–[135]. Polarization flux closures in the form of bundles of 90° stripe domains oriented to form a vortex have been imaged by McGilly and Gregg in $PbZr_{(0.42)}Ti_{(0.58)}O_3$ nanodots [136]. Similar stable flux closures have been observed by McQuaid et al. [135] in $BaTiO_3$. However, these flux-closures consist of 90° stripe domains and so differ from the classic polarization vortex illustrated in Fig. 4.1(a), which is a well-known structure in ferromagnetic materials [103], [104]. Polarization patterns consisting of dipole flux closures or quadrupole chains, see Fig. 4.1(b), have been observed [130], but these have 180° domain walls at their core and so they too differ from the classic polarization vortex. Although, the direct observation of polarization rotation Fig. 4.1(c) which facilitates the formation of a vortex has been established

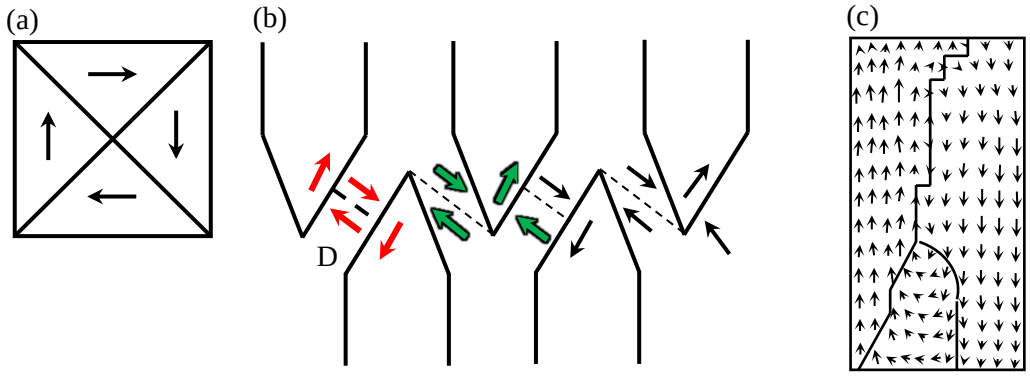

Figure 4.1: Schematic representation of polarization patterns (a) Classic polarization vortex as predicted by Kittel [127] (b) Needle domains showing dipole flux closure “D” after McGilly et al. [130] (c) Flux-closure along 180° domain wall, after Jia et al. [138].

[138], the classic vortex polarization pattern continues to be elusive. This leads to the question – Why are polarization vortices not seen in experiments?

In the present work, commonly occurring polarization patterns consisting of vortex and stripe domains formed on the cross-section of a barium titanate nanowire are modelled using phase-field methods. The effect of scaling these domain patterns on their free energy is explored, and the internal stress, strain and electric field developed at equilibrium are discussed. Next the effects of surface energy and conductive boundaries on the formation of polarization patterns in nanowire section are studied. A 'phase diagram' which identifies the minimum energy equilibrium domain pattern for each combination of surface energy and nanowire width is mapped for both insulating and conductive boundary conditions. Finally, the effect of orientation of the nanowire section at an angle to the crystallographic axis of barium titanate is explored. The results indicate that a classic polarization vortex in $BaTiO_3$ is favorable only in a narrow range of conditions. Furthermore, surface energy, conductive boundary conditions and orientation of the cross-section can significantly affect the formation of polarization vortices – leading to complex domain patterns or loss of ferroelectricity. The length scale at which a polarization vortex is energetically favorable is found to be smaller than the typical size of nanoparticles in recent experimental studies in tetragonal ferroelectrics.

4.2 Methods

A $BaTiO_3$ nanowire in the tetragonal phase, with square cross-section is modelled in isothermal conditions. The wire is assumed to extend indefinitely out of the model plane, such that plane strain and electric field conditions apply. Minimum

cross-sectional widths of the nanowire, L = 20nm are considered, noting that ferroelectricity has been observed in $BaTiO_3$ structures from a few nanometers in size upwards [139], [140]. The wire is assumed to be simply supported, with traction free and charge free surfaces as shown in Fig. 4.2.

The Helmholtz free energy ψ, of the domain pattern formed on the nanowire section is described by the phase-field model as a sum of the gradient energy ψ_g, and the domain energy ψ_d:

$$\psi = \psi_g + \psi_d \tag{4.1}$$

The gradient energy ψ_g, includes energy due to polarization variation at domain walls or near surfaces and is given by:

$$\psi_g = \frac{1}{2} a_{ijkl} P_{i,j} P_{k,l} \tag{4.2}$$

The domain energy ψ_d, accounts for the contributions from bulk, elastic, piezoelectric and dielectric energy, due to distortion away from the spontaneously polarized state and is described by:

$$\begin{aligned}\psi_d = {} & \frac{1}{2}\bar{a}_{ij}P_iP_j + \frac{1}{4}\bar{\bar{a}}_{ijkl}P_iP_jP_kP_l \\ & + \frac{1}{6}\bar{\bar{\bar{a}}}_{ijklmn}P_iP_jP_kP_lP_mP_n + \frac{1}{8}\bar{\bar{\bar{\bar{a}}}}_{ijklmnrs}P_iP_jP_kP_lP_mP_nP_rP_s \\ & + b_{ijkl}\varepsilon_{ij}P_kP_l + \frac{1}{2}c_{ijkl}\varepsilon_{ij}\varepsilon_{kl} + \frac{1}{2}f_{ijklmn}\varepsilon_{ij}\varepsilon_{kl}P_mP_n \\ & + \frac{1}{2}g_{ijklmn}\varepsilon_{ij}P_kP_lP_mP_n + \frac{1}{2\kappa_0}(D_i - P_i)(D_i - P_i)\end{aligned} \tag{4.3}$$

The nodal values of displacement u_i and polarization P_i are computed using the phase-field model, and enable the computation of strain ε_{ij} and polarization gradient $P_{i,j}$

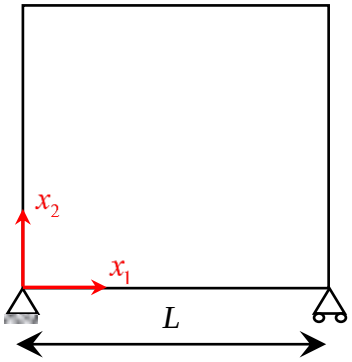

Figure 4.2: Schematic representation of boundary conditions on the nanowire cross-section.

respectively. These values are then employed to calculate the energy density of the domain patterns, as discussed in section 2.2 of chapter 2. The element size chosen for these simulations is such that a 180° domain wall spans four elements, i.e., the typical element size is 0.5nm.

The simulations are initialised with a randomized polarization field, where the magnitude of polarization component on each node (P_i for $i = 1,2$) is assigned a value in the range, $\frac{-P_0}{2} \le |P_i| \le \frac{P_0}{2}$. Here, $P_0 = 0.26\text{C/m}^2$ and the domain patterns are relaxed to approach equilibrium. A detailed description of initialising the phase-field simulation with a randomised polarization field is discussed in section 2.4 of chapter 2. Different sets of randomized polarization fields are generated in the initial state at a given nanowire size, to identify the commonly occurring domain arrangements at equilibrium. Next, the domain patterns formed on nanowire sections of increasing width $20\text{nm} \le L \le 45\text{nm}$ are explored.

The equilibrium domain patterns formed at the nanowire width L = 20nm are shown in Fig. 4.3. Here, the phase-field model finds multiple domain configurations at equilibrium, when initialised with different polarization states. The presence of the

insulated boundary condition enforces the formation of flux closures; however these patterns differ based on the number and type of domains contained in them. This difference accounts for the range of normalized free energy values $\tilde{\psi} = 0.53 - 0.61$ for the domain patterns in Fig. 4.3. $\tilde{\psi} = (\psi_0 - \psi)/\psi_0$, where ψ_0 is the free energy per unit volume of a spontaneously polarized monodomain and further details of the normalization constants are given in section 2.3 of chapter 2. Note that the equilibrium domain patterns are not necessarily global minimum energy states for the given set of boundary conditions. Several local energy minima can be found by varying the order parameter (polarization field). However, the formation of the classic polarization vortex is seen here, at the 20nm length scale. Similar simulations are next carried out at

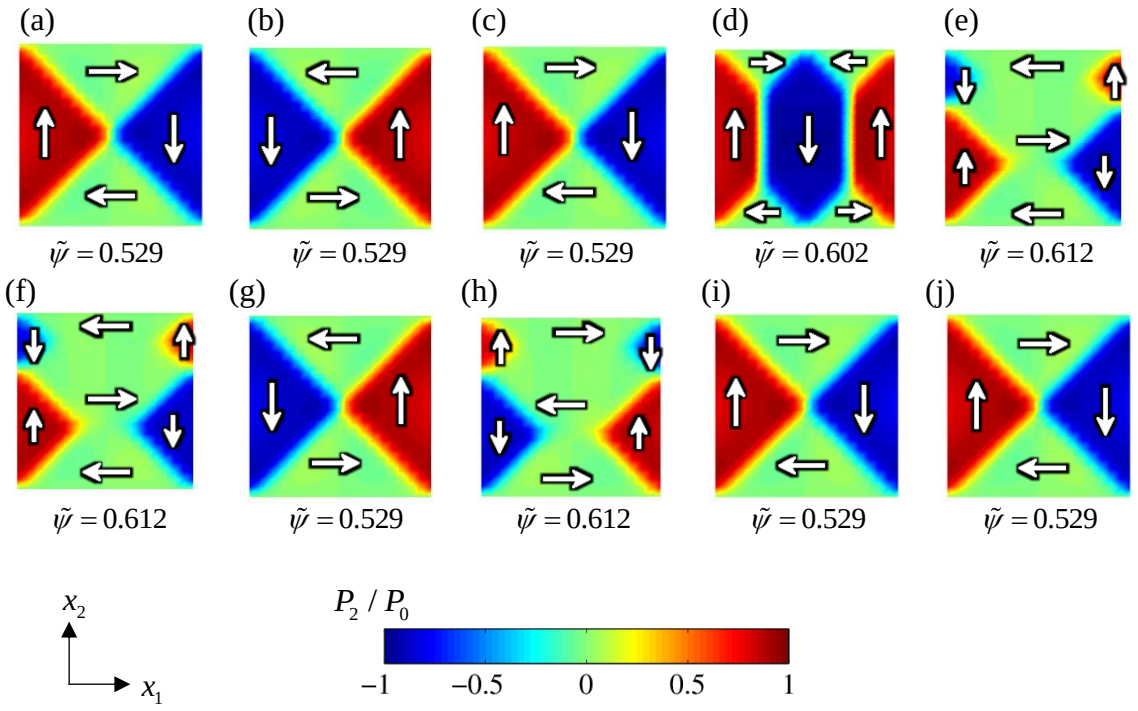

Figure 4.3: Equilibrium domain patterns in nanowire cross-section at L = 20nm. The subfigures (a-j) illustrate polarization patterns formed at equilibrium, when the phase-field simulations were initialized with different sets of randomized polarization fields. $\tilde{\psi}$ is the normalized free energy for each domain pattern at equilibrium.

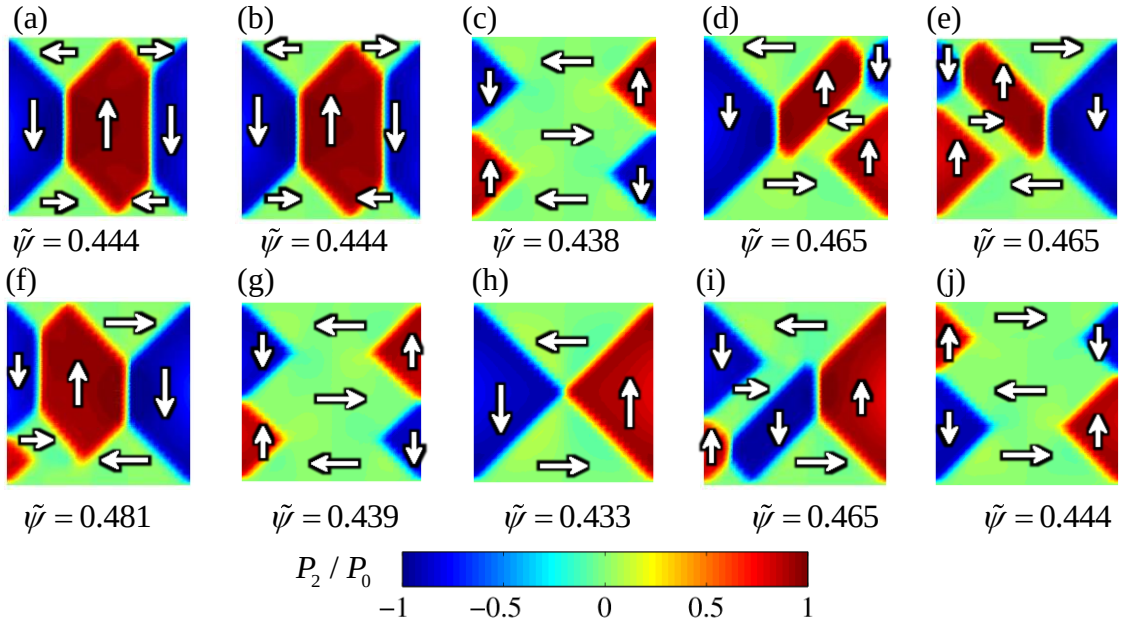

Figure 4.4: The subfigures (a-j) illustrate equilibrium domain patterns in nanowire section at L = 30nm, when phase-field simulations were initialized with different sets of randomized polarization fields. $\tilde{\psi}$ is the normalized free energy of the domain pattern.

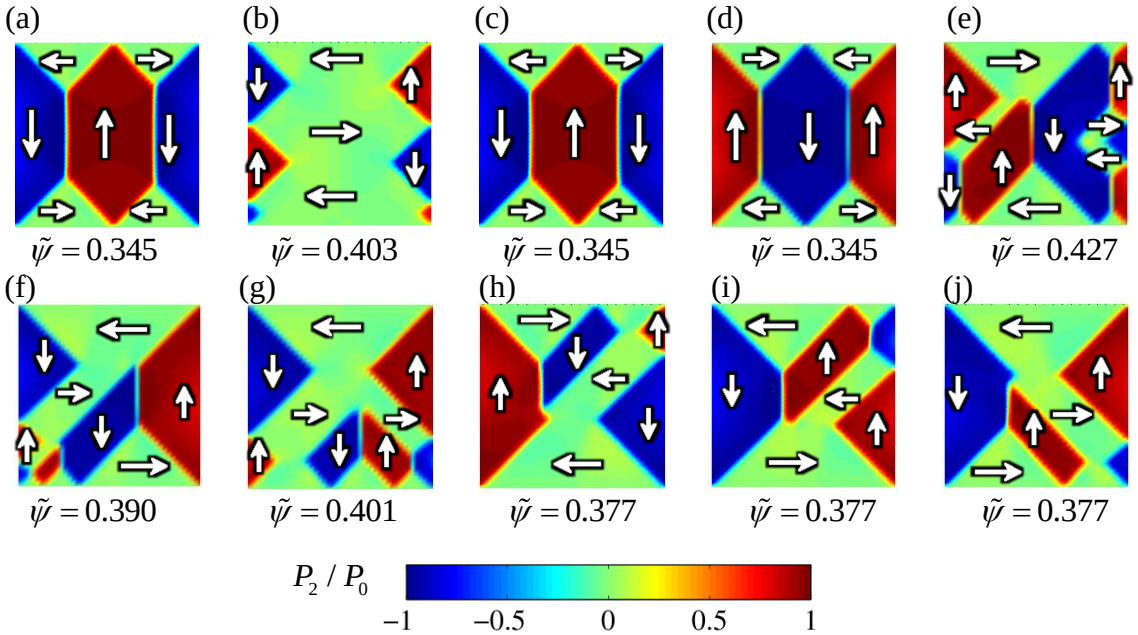

Figure 4.5: The subfigures (a-j) illustrate equilibrium domain patterns in nanowire section at L = 45nm, when phase-field simulations were initialized with different sets of randomized polarization fields. $\tilde{\psi}$ is the normalized free energy of the domain pattern.

increased nanowire widths, $L = 30\text{nm}$ and $L = 45\text{nm}$ as shown in Fig. 4.4(a-j) and Fig. 4.5(a-j) respectively.

At L = 30nm, a domain pattern with double flux closures each containing a $180°$ domain wall is common, for example see Fig. 4.4(a), with normalized free energy for the domain patterns varying in the range $\tilde{\psi} = 0.433 - 0.481$. The classic vortex is occasionally seen (Fig. 4.4(h)). At L = 45nm flux-closures with multiple stripe-like features are typical, see Fig. 4.5(f), and possess $\tilde{\psi}$ in the range 0.345 – 0.427. On increasing the nanowire width size, the probability of the formation of a classic $90°$ vortex domain pattern (Fig. 4.1(a)) reduces and the normalized free energy range decreases.

Next, domain patterns formed on nanowire sections with varying length scale are explored. Here, the nanowire sections with width $20\text{nm} \le L \le 45\text{nm}$ are simulated with elements of size 0.5nm, starting with a randomized polarization field in the initial state. Note that the simulations illustrated in Fig. 4.6 were carried out with element size of 0.25nm, and similar results were obtained. As such there is not very significant mesh dependency. The free energy of the domain patterns formed at each value of L is computed and shown in Fig. 4.6.

A gradual decrease in the normalized free energy of the domain patterns with increasing nanowire width is observed; the normalized free energy curve approximately follows $\tilde{\psi} = KL^{-0.4}$ where K is a constant. From randomized starting initial state and for the range of cross-sectional widths explored, the simulation converged on equilibrium states which frequently resulted in one of the three types of domain arrangement shown in Fig. 4.7(a–c); Similar domain patterns were also seen by Xue et al. [74] where these structures were found using Monte Carlo methods.

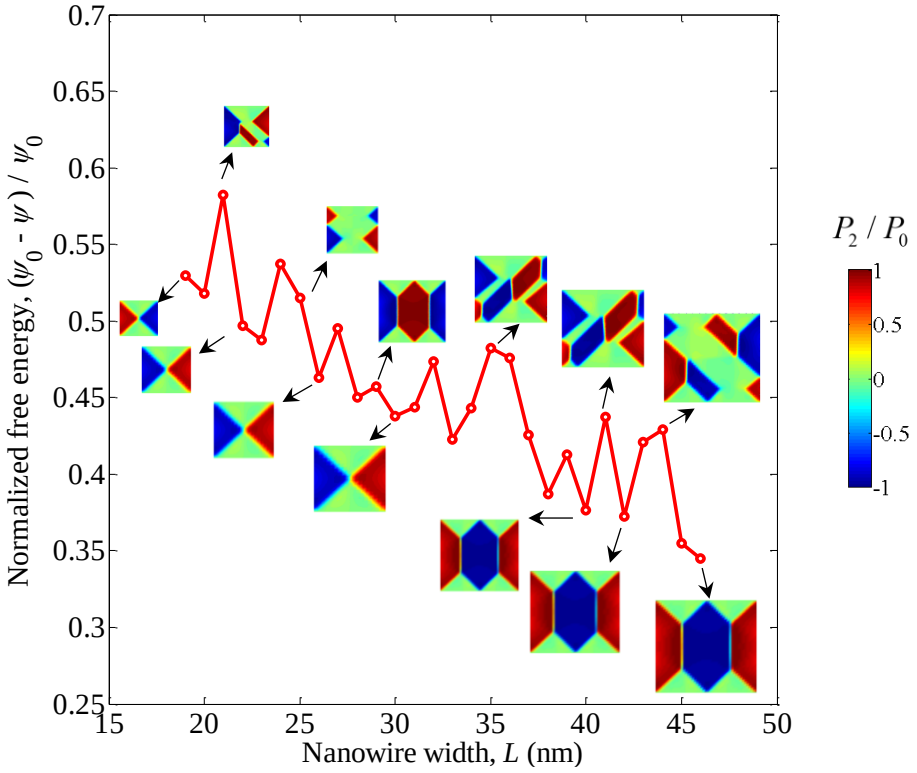

Figure 4.6: Free energy curve for domain patterns formed on nanowire sections of width, L. Inset diagrams indicate the polarization P_2 for the domain patterns at equilibrium.

The first polarization pattern seen in Fig. 4.7(a) consists of four quadrant domains fitting together to form a classic vortex and is referred to as a type I domain pattern. The type II domain pattern is identified with two vortices and stripe domains as shown in Fig. 4.7(b). In the type II domain pattern the $90°$ vortex core is separated into domain junctions by the introduction of a $180°$ domain wall. This structure is closely related to the double-closure pattern with domain wall vertices as observed by McQuaid et al. [131] and has been discussed by Srolovitz and Scott [141] as an energetically favoured pattern in comparison to type I. The type III domain pattern shown in Fig. 4.7(c) is a more complicated domain pattern containing a combination of flux closures and stripe-like domain patterns. Having established three types of polarization

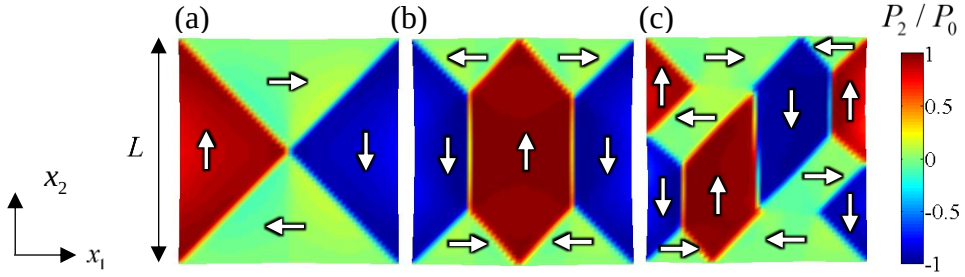

Figure 4.7: Polarization, P_2, of the three commonly occurring polarization patterns in nanowire sections, $L = 40$nm, (a) type I (b) type II (c) type III.

patterns with vortex and stripe domains that can typically form on the nanowire section, the effect of scaling on these domain patterns is next studied.

4.3 Scaling effects

Nanowire cross-sections of size 20–80nm are simulated with initial conditions that forced each of the three patterns of Fig. 4.7 to form. This is achieved by initializing the simulation with the polarization at each node set to match one of the domain patterns in Fig. 4.7, while the nodal displacements and electric potential are initialized at zero. If the simulations reached equilibrium without pattern change, this indicated the stability of the pattern and the associated energy is thus found as a function of size. The internal stresses and electric fields developed in each of the domain patterns are also studied. As the size is increased, the type I pattern remained stable, but other patterns became energetically favorable.

The resulting free energy for each of the three types of polarization patterns obtained from the phase-field simulations is shown in Fig. 4.8(a) as a function of nanowire width, L. The energy curves in Fig. 4.8(a) for the three types of polarization patterns decrease with increasing size of the cross-sectional widths. This is explained by

the reduction in percentage of the domain wall volume fraction with increasing size, which reduces the gradient energy contribution per unit volume of the domain pattern. At smaller nanowire widths, $L < 30$nm, the type I domain pattern is of lower energy in comparison to types II and III, due to lower volume fraction of domain walls. The energy curves of type I and type II cross at $L \sim 34$nm indicating a dependence of minimum energy state upon nanowire width. The type III pattern is not stable for $L < 35$nm: even if the simulation is started with polarization matching the type III pattern, other flux closures with lower energy form. The lower size limit for stability of the type III pattern is indicated by "A" in Fig. 4.8(a). Also shown in Fig. 4.8(a) are the results obtained from starting the simulations with randomly polarized states, taken

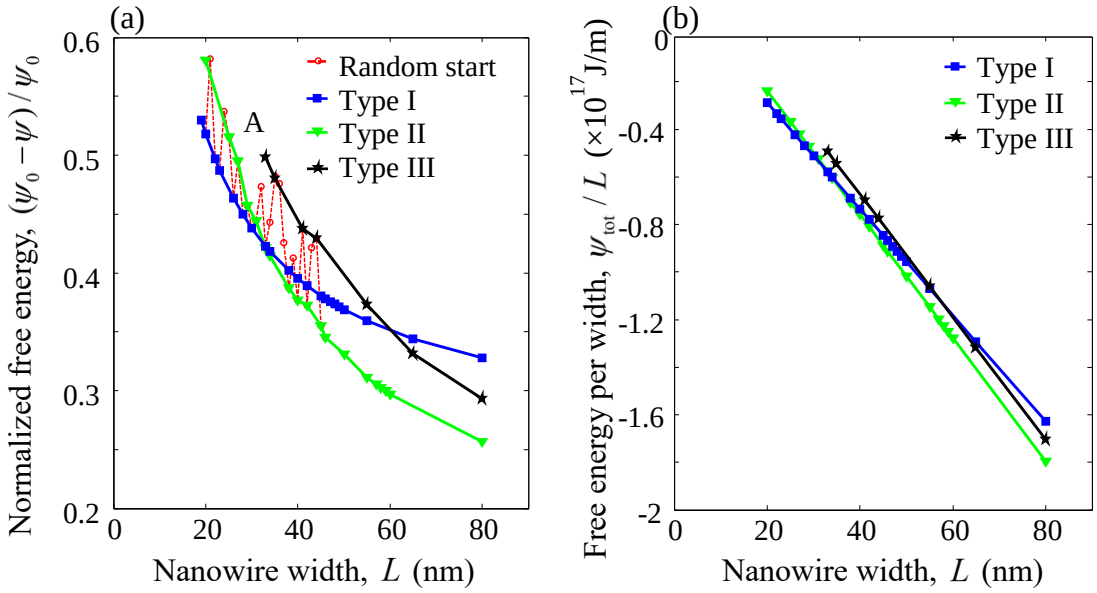

Figure 4.8: (a) Normalized free energy values as a function of nanowire width for three types of polarization patterns obtained from phase-field simulations. (b) Total free energy per unit width, ψ_{tot}/L versus L, showing best fit straight lines.

from Fig. 4.6. These data jump back and forth between the main three types of polarization pattern indicating that the stable state found is highly dependent on the initial conditions.

Since the model size is much larger than the intrinsic length scale due to domain wall width, the total energy in volume V due to polarization gradient, $\int \psi_g \mathrm{d}V$, scales approximately with domain wall area. Defining the volume to have an out-of-plane depth D, the gradient energy of a given domain pattern is proportional to the area LD. The domain energy in volume V is $\int \psi_d \mathrm{d}V$, and it scales with the volume of polarized domains as a function of L^2D. The total free energy ψ_{tot} for a domain pattern is then defined as $\int \psi \mathrm{d}V$. From Eq. (4.1) the total free energy in volume V is then given approximately by:

$$\psi_{\mathrm{tot}} = aLD + bL^2D \tag{4.4}$$

where the coefficients a and b for each type of polarization pattern can be estimated using linear regression of the data in Fig. 4.8(b), see results in Table 4.1.

For a given nanowire width, L, the gradient energy, ψ_g of the three types of polarization patterns is related by type III > type II > type I, as the domain patterns represented by type II and III possess more domain wall per unit volume in comparison to type I. However, the domain energy ψ_d for these domain patterns follows the reverse order type I > type II > type III (Table 4.1). This is due to the relatively large elastic energy arising from disclinations at the $90°$ vortex core in type I domain pattern, which is reduced by the introduction of $180°$ domain walls in the other patterns. Thus the multidomain patterns, such as type II and III, reduce their domain energy at the cost of

Pattern	a ($\times 10^{16}$ J/m^2)	b ($\times 10^{24}$ J/m^3)
Type I	1.57	-2.23
Type II	2.80	-2.59
Type III	3.59	-2.60

Table 4.1. Coefficients a and b governing energy contributions to the total energy for the three types of polarization pattern.

increased domain wall energy. This can also be seen qualitatively from the mechanical and electrical fields present in the various patterns at equilibrium. The in-plane components of stress σ_{ij} and strain ε_{ij} for the three types of polarization patterns at $L = 40\text{nm}$ are shown in Fig. 4.9(a–c), while the electric fields E_i developed are shown in Fig. 4.10(a-c). Tensile stresses of the order of σ_0 are observed at the domain junctions which arise from misfit stresses, while compressive stresses are observed in the uniformly polarized domains. The key observation from Fig. 4.9 is that the type I pattern contains a highly stressed central region (see σ_{11}, σ_{22} plots in Fig. 4.9(a)), while the type II and type III patterns as shown in Fig. 4.9(b, c), have reduced average stress magnitude because of the formation of bands of $180°$ domains. Thus the elastic energy contribution arising from these stress fields is smaller in the type II and III domain patterns. This is consistent with the appearance in the type II and III patterns of regions whose strain values are close to those of the monodomain in a spontaneously polarized state. As expected, these spontaneously polarized domains possess near zero stresses, while similar spontaneously polarized domains are not found in the type I

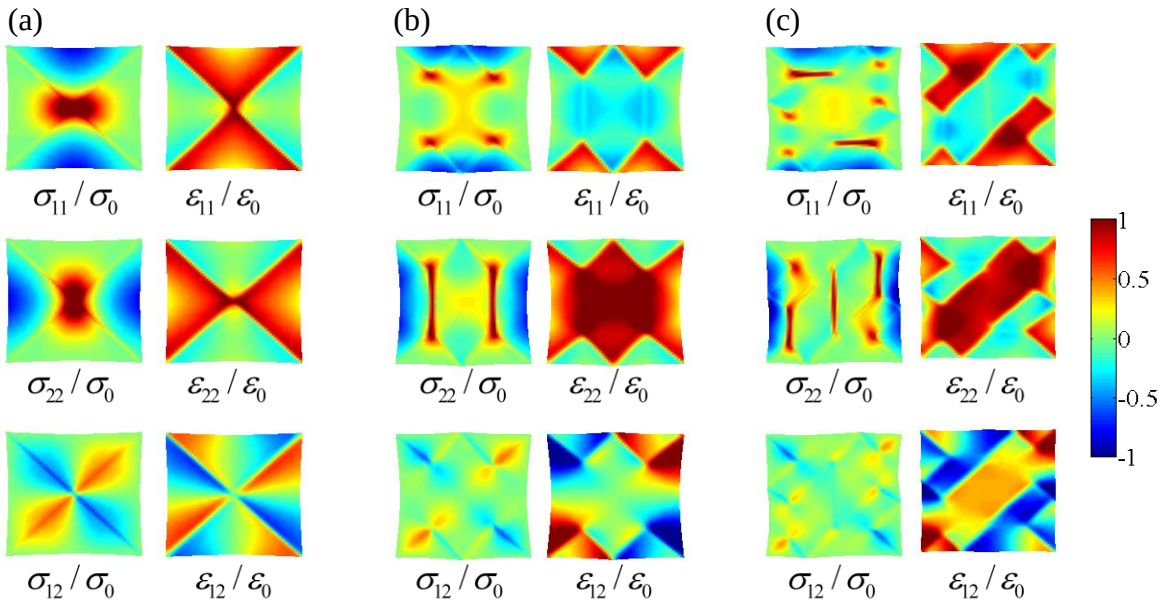

Figure 4.9: Normalized stress σ_{ij} and strain ε_{ij} fields in the three types of polarization pattern (a) type I (b) type II (c) type III, where $\sigma_0 = 692\text{MPa}$, $\varepsilon_0 = 0.0082$.

pattern. This indicates a significant contribution from elastic energy to the net energy of the type I pattern.

Local electric fields develop at 90° domain walls in the three types of polarization patterns, while near zero or negligible electric fields are observed at the 180° domain walls and in the rest of the domain pattern, see Fig. 4.10(a-c). The direction of electric fields developed at the 90° domain walls produces a depolarizing effect on the neighboring domains. At these domain walls, the ferroelectric crystals are not in their spontaneous states due to misfit stresses. In type II and type III domain patterns, the depolarization field also exists at the domain junctions as seen in Fig. 4.10(b, c).

When $L < 34\text{nm}$, the percentage contribution of the gradient energy ψ_g to ψ is significant at about 30%, thereby causing polarization patterns with greater domain wall area to possess greater energy, Fig. 4.8(a). This makes the classic polarization vortex

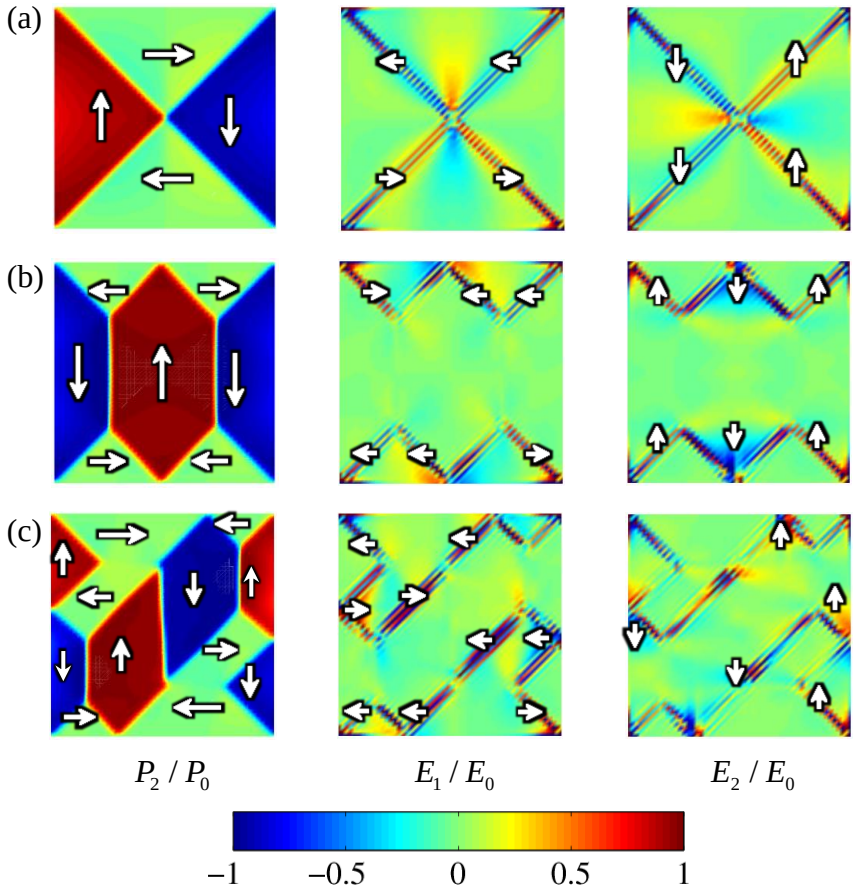

Figure 4.10: Electric fields E_i developed in the equilibrium domain patterns (a) type I (b) type II (c) type III. $E_0 = 21.82\text{MV/m}$.

(type I) energetically favorable when $L < 34\text{nm}$. However, for $L > 50\text{nm}$ the domain energy ψ_d is a primary contributor to the net energy of the polarization pattern. Thus for $L > 50\text{nm}$, polarization patterns with stripe domains become favorable. The balance of the energy contributions: ψ_g, ψ_d and nanowire width, L determines the minimum energy polarization pattern, Fig. 4.8(a, b). From Eq. (4.4) the energy is well fitted by $\frac{\psi_{\text{tot}}}{L^2 D} = \frac{a}{L} + b$, and in the limit as L becomes large, total energy per unit volume, $\frac{\psi_{\text{tot}}}{L^2 D} \to b$. Hence the curves in Fig. 4.8(a) asymptotically approach a constant energy per unit volume. This suggests that the type III domain pattern will become favorable

at larger scales. However in the present study calculations did not go beyond $L = 80\text{nm}$ due to computational power requirements discussed in section 2.8 of chapter 2; it is likely that other low energy patterns will become favorable before the cross-over from type II to type III is reached.

4.4 Surface energy effects

Up to this point, the effects of surface energy on polarization patterns were neglected. However, at the nanoscale, surface energy γ is known to affect the formation of ferroelectric domains [142]–[144]. For $BaTiO_3$ nanowires, experiments and theoretical considerations suggest γ values of about 0.68N/m [140], [145], however the presence of depolarization field and surface layer effects have led to much greater estimates of γ, around 10N/m [145]. Other authors found values within this range depending on shape and surface conditions including chemical environment [143], [144]. Hence, in the following phase-field simulations, surface energy values in the range $0\text{N/m} \le \gamma \le 10\text{N/m}$ are considered.

Morozovska et al. [30] model the effect of a surface tension proportional to local curvature of cylindrical nanoparticles and nano-rods, via the free energy function. In the present work involving a square cross-section nanowire, a surface tension proportional to local curvature results from non-zero γ. That is, in the nanowire section containing flux-closure patterns, the polarization is parallel to the nanowire section boundaries. In these cases, the surface tension can be approximated as a force parallel to the nanowire boundaries [146], except at the corners where the forces add up resulting in a non-zero value. This effect of surface tension can be approximated by applying surface force boundary conditions at corners only, neglecting second order effects on surface

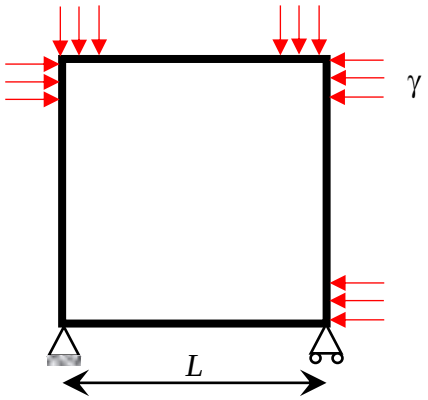

Figure 4.11: Schematic representation of modelling surface energy γ on a square nanowire cross-section with insulated surfaces.

curvature due to deformation, as shown in Fig. 4.11. Note that nanowire cross-sectional corners with constrained displacements are not subjected to these surface forces in the simulation. The surface effect on the Helmholtz free energy ψ in a narrow region near the nanowire surface is also neglected. Local polarization orientation relative to the surface could also affect the value of γ, resulting in an anisotropic, or orientation dependant surface tension. However, since this study focuses on flux closures, it is expected for the polarization to be parallel to the surface and so this effect can be neglected. A charge free or an insulated surface is considered by applying the zero normal component of electric displacement $D_i n_i = 0$ along the surface nodes of the nanowire.

Here, a nanowire section is initialized with a domain pattern identified to possess minimum energy at a given size (see Fig. 4.8(a)). For example, at a cross-section size, $L = 20\text{nm}$ the type I domain pattern is calculated to possess lowest energy. The simulation is therefore initialised with the nodal values of displacement, electric potential and polarization of the type I domain pattern. Surface energy γ is

subsequently modelled by applying corner forces on this domain pattern and incremented in steps of 1N/m. Equilibrium domain patterns are found at the end of each step. The effect of surface energy on nanowire sections with varying width is thus explored. To vary the width L, the simulation is started with a new size and the corresponding minimum energy pattern, with $\gamma = 0$.

A "phase-diagram" mapping the minimum energy equilibrium state for each combination of γ and L, with the insulating boundary conditions, is shown in Fig. 4.12. Boundaries on the diagram indicate approximately the location of points where the polarization patterns associated with the adjacent regions have equal energy; markers show specific points calculated on each boundary.

In an insulated nanowire section, Fig. 4.12, type I polarization pattern is the minimum energy arrangement in a region with $10\text{nm} < L < 30\text{nm}$ approximately, and surface energy, $\gamma < 4\text{N/m}$. At larger nanowire widths a similar range of surface energy favors the type II domain pattern as the lowest energy state. Insulated $BaTiO_3$ nanowires are non-ferroelectric for combinations of high values of surface energy, $\gamma > 4\text{N/m}$ and low values of width, $L < 10\text{nm}$. This is manifested in the model by the disappearance of tetragonality $\varepsilon_{11} = \varepsilon_{22} = 0$ and polarization $P_1 = P_2 = 0$. However, at greater values of nanowire widths (L > 40nm) ferroelectric properties are retained; the domain patterns formed are significantly affected by surface energy. Here, complex patterns with multiple domains are favored. Note that the markers which divide type I and type II domain patterns in Fig. 4.12, change towards smaller values of L with increasing surface energy. This indicates that the length scale at which the vortex domain pattern can be a low energy solution decreases with increasing values of surface energy.

The equilibrium domain patterns formed at L = 20nm along section AA' in Fig. 4.12 are shown in Fig. 4.13(a-d). The type I domain pattern is retained with negligible changes up to surface energy of $\gamma \sim 3\text{N/m}$, see Fig. 4.13(a). At $\gamma = 4\text{N/m}$, the type I or the vortex domain pattern is no longer found at equilibrium and a domain pattern with a $180°$ wall at its centre appears, see Fig. 4.13(b). Meanwhile, unit cells at the corners of nanowire section approach the cubic state, as these regions are in

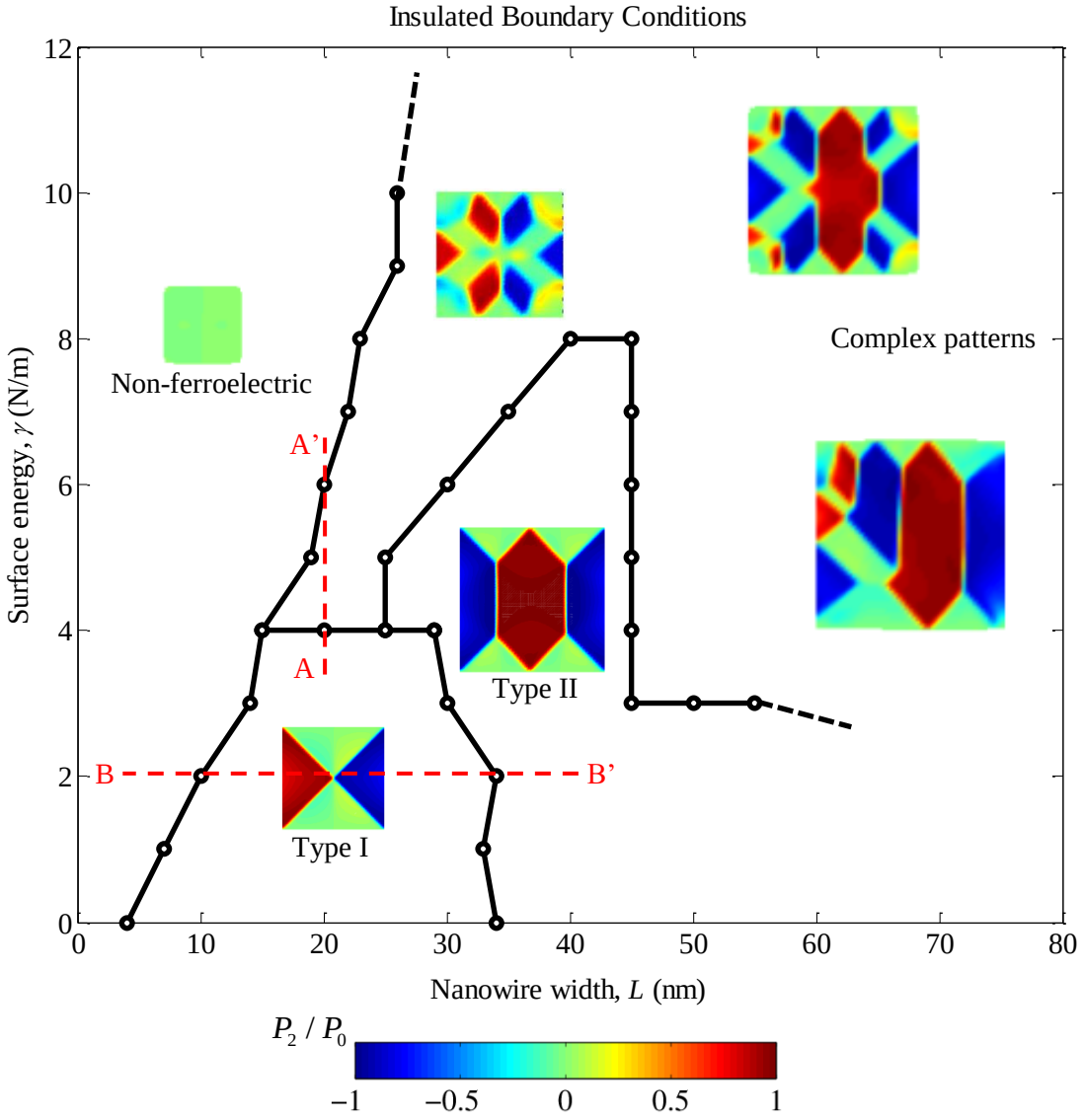

Figure 4.12: Phase diagram showing minimum energy domain patterns with insulating boundary conditions. Inset diagrams show typical patterns of polarization P_2 / P_0.

proximity to the applied surface forces. On increasing the surface energy to $\gamma = 5\text{N/m}$, stripe-like domains appear leading to the formation of complex domain patterns, see Fig. 4.13(c). At $\gamma = 6\text{N/m}$, the nanowire section loses ferroelectricity as shown in Fig. 4.13(d).

The average c/a ratio or tetragonality for $BaTiO_3$ in the nanowire section L = 20nm varies with surface energy, and is calculated as

$$\left\langle \frac{c}{a} \right\rangle = 1 + \int \left| \frac{1+\varepsilon_{22}}{1+\varepsilon_{11}} - 1 \right| \frac{\text{dV}}{\text{V}}$$

where ε_{ij} is the strain evaluated at the Gauss points or integration points in each element and V is the volume of the domain pattern assuming unit depth. Fig. 4.14 shows the variation of the c/a ratio with increasing surface energy γ. At $\gamma = 0$, the tetragonality is estimated to be ~1.004, which is less than the 1.01 value that corresponds to the spontaneous strain state of $BaTiO_3$. This deviation in the tetragonality is attributed to the presence of non-spontaneously polarized unit cells at the domain walls and near the nanowire surfaces. The average c/a ratio decreases

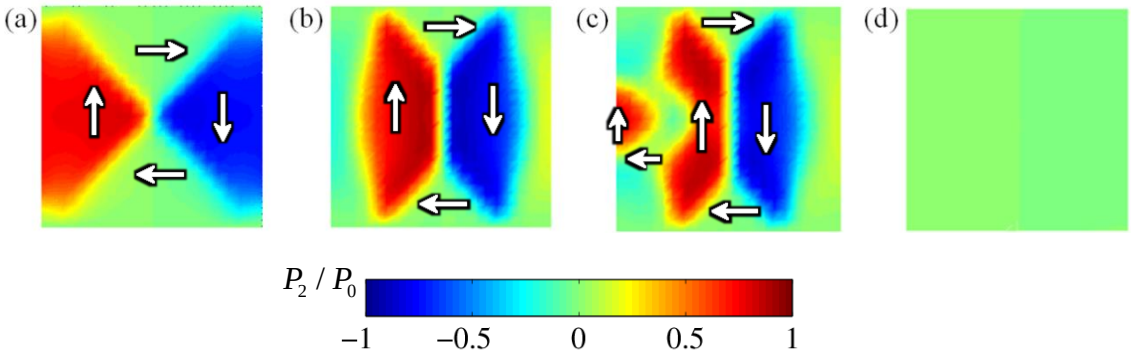

Figure 4.13: Equilibrium domain patterns formed along AA' in nanowire section of L = 20nm for surface energy (a) $\gamma = 3\text{N/m}$ (b) $\gamma = 4\text{N/m}$ (c) $\gamma = 5\text{N/m}$ (d) $\gamma = 6\text{N/m}$.

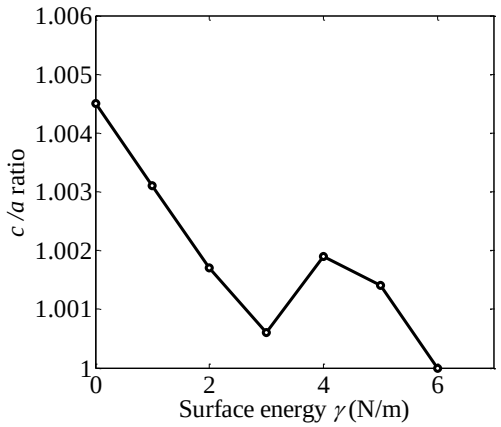

Figure 4.14: The c/a ratio for a vortex (type I) domain pattern of size $L = 20\text{nm}$ with increasing surface energy.

with increase in surface energy, except at γ = 4N/m where the average tetragonality of the domain pattern increases. This increase is due to the appearance of polarized domains at the edges of the nanowire section which was previously non-ferroelectric. A complex polarization pattern with stripe-like domains is commonly found in this range of surface energy value. On increasing the surface energy to γ = 6N/m, $c/a \to 1$ as the nanowire section becomes non-ferroelectric and attains a cubic state.

The equilibrium domain patterns formed along BB' in the phase-diagram, with surface energy γ = 2N/m are shown in Fig. 4.15. For L < 10nm, the nanowire section is non-ferroelectric. A type I domain pattern is found to be stable and is a minimum energy state for nanowire widths in the range 10nm < L < 33nm. At L = 34nm, both type I domain pattern and type II domain patterns can form in equilibrium, however a type II domain pattern is of lower energy as indicated on the phase-diagram. Similar simulations are carried out at different γ values to identify the minimum energy domain patterns on the phase-diagram.

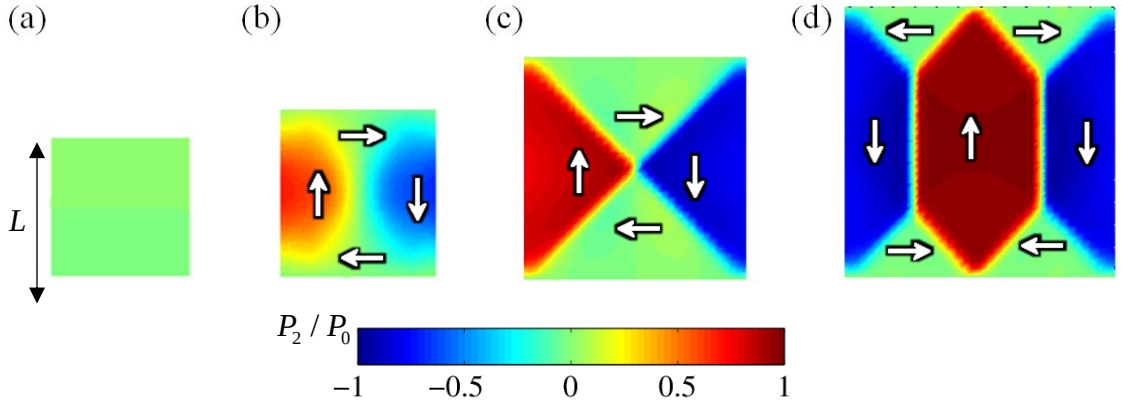

Figure 4.15: Equilibrium domain patterns formed along BB' at surface energy γ = 2N/m for nanowire widths, (a) L = 9nm (b) L = 10nm (c) L = 32nm (d) L = 34nm.

4.5 Surface conductivity effects

The effects of scaling and surface energy on the domain pattern formation are significant and have been demonstrated using phase-field simulations. However, these effects were studied on a section with insulated surfaces, and the effect of surface conductivity has not yet been explored. The presence of conductive surfaces can be expected to assist in the development of surface charges, which might affect the formation of vortex domain patterns. These surfaces can be envisaged to arise in conductive environments with charged particles, such as hydrogen H^+ and hydroxyl OH^- ions that accumulate on a ferroelectric surface, and support a non-zero average polarization. For example, nano-particles in humid air commonly attract a layer of water molecules that can dissociate into ions to enable a redistribution of charge.

In this section the conductive surfaces are modelled by applying zero voltage, $\phi = 0$ on the boundary nodes as shown in Fig. 4.16. The surface forces and simple supports are modelled as before. A monodomain pattern is then found to be stable with

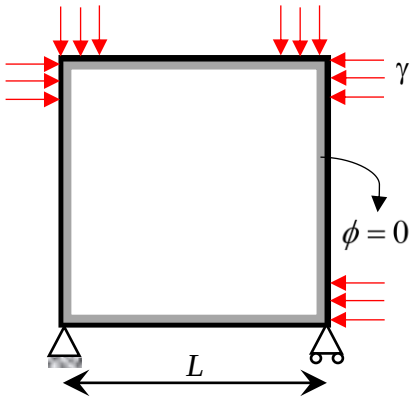

Figure 4.16: Schematic representation of surface energy γ, modelled using surface forces and surface conductivity ϕ boundary condition on a square nanowire cross-section.

conductive surfaces and zero surface energy across a very wide range of widths L. This is consistent with the fact that the nanowire section is free to attract charges to stabilize a net polarization in the spontaneous state. Starting from this initial state, surface energy γ is incremented in steps of 1N/m, and the equilibrium domain configurations are found.

A phase-diagram corresponding to each combination of γ and L of a nanowire with conductive surfaces is shown in Fig. 4.17. Scaling of the nanowire width with surface energy up to 2N/m has negligible effect on the monodomain pattern found to be stable throughout this range. However, with the surface energy $\gamma > 4\text{N/m}$ and nanowire widths $10\text{nm} < L < 20\text{nm}$, complex domain patterns with multiple band-like domains are observed. In these domain patterns, the unit cells close to the edges of the nanowire section are in the cubic state. For surface energy $\gamma > 4\text{N/m}$ and nanowire widths $L < 10\text{nm}$, a non-ferroelectric region is observed where all unit cells in the nanowire section are in the cubic state.

Next, it is interesting to compare the phase-diagrams of nanowire sections modelled with insulated, see Fig. 4.12, and conductive boundary conditions, see Fig. 4.17. The non-ferroelectric region in the phase-diagram with conductive surfaces is narrower than the corresponding region for a nanowire with insulated surfaces. This is because the conductive boundaries attract surface charges that support a net polarization

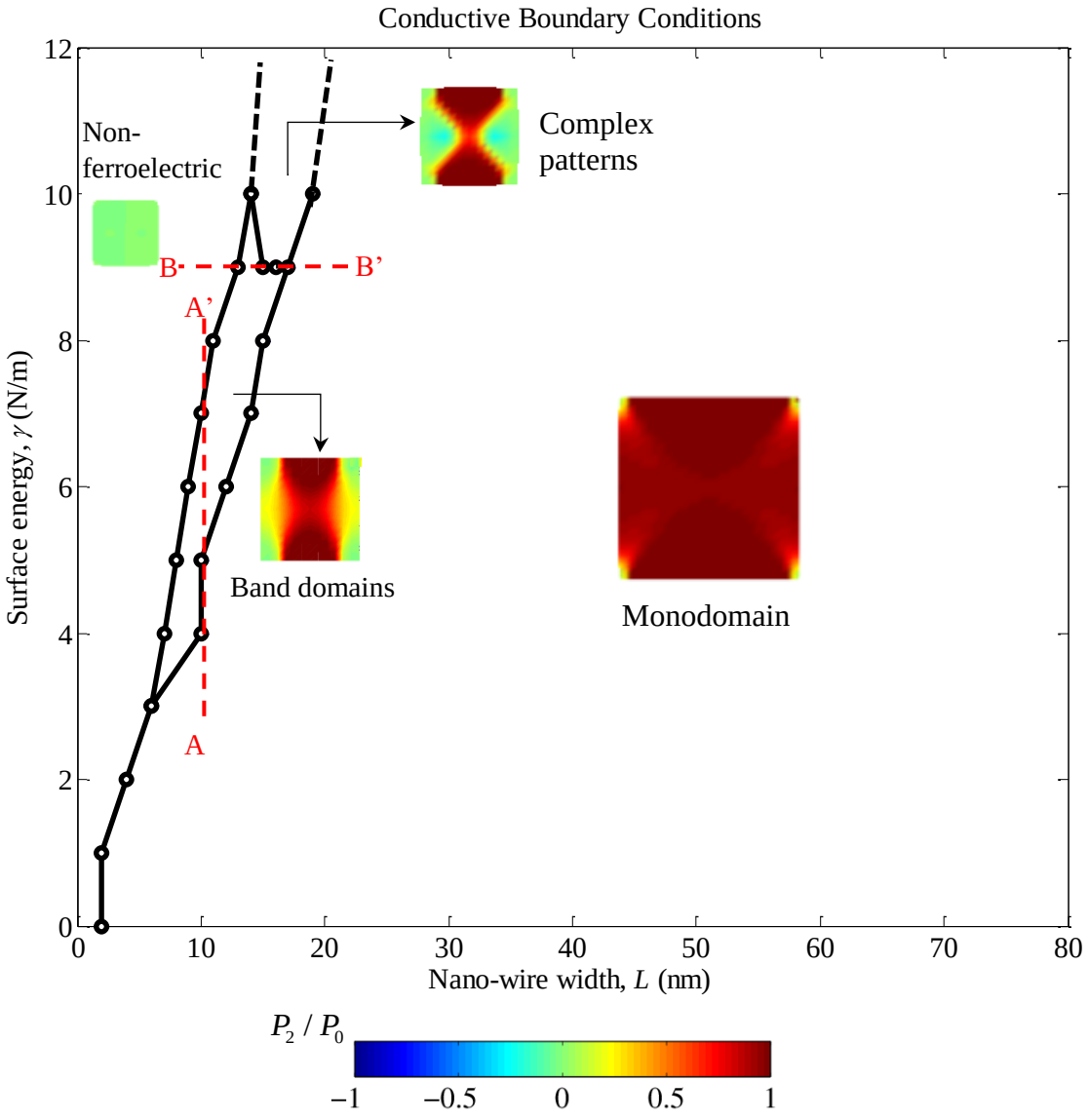

Figure 4.17: Phase diagram showing minimum energy domain patterns formed on nanowire sections with conductive surfaces. Inset diagrams show typical patterns of polarization P_2 / P_0.

in the nanowire section for sizes $10\text{nm} < L < 20\text{nm}$, despite large values of surface energy, $\gamma > 4\text{N/m}$. By contrast, the nanowire with insulated boundaries does not allow for the formation of surface charges, and is non-ferroelectric for $L < 20\text{nm}$ and $\gamma > 4\text{N/m}$. For nanowire sizes, $L > 20\text{nm}$ and surface energy, $\gamma < 10\text{N/m}$ a simple monodomain pattern is a low energy solution with conductive boundaries. However in this range of L and γ, nanowires with insulated boundaries tend to form complex domain patterns with multiple domains and domain walls as a low energy pattern. Complex domain patterns are also found in nanowires with conductive boundaries, however these patterns only occupy a small region $10\text{nm} < L < 20\text{nm}$ and $\gamma > 4\text{N/m}$. Finally, Fig. 4.17 indicates that the vortex domain pattern does not occur as a low energy solution in a nanowire with conductive surfaces.

A closer look at the equilibrium domain patterns formed at $L = 10\text{nm}$ in Fig. 4.17 with increasing surface energy along the section AA' is given in Fig. 4.18. Here, the increase in surface energy narrows the polarized region in the nanowire section forming a band-like pattern, that finally collapses to a cubic state at $\gamma \sim 8\text{N/m}$.

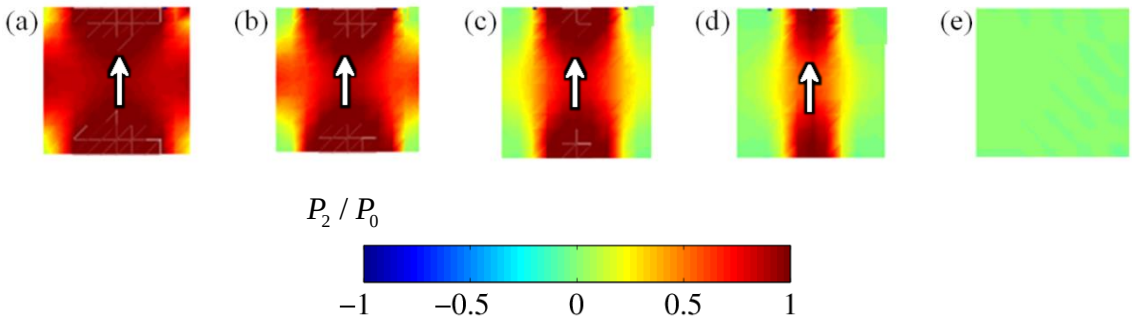

Figure 4.18: Equilibrium domain patterns formed along AA' at surface energy values (a) 3N/m (b) 5N/m (c) 6N/m (d) 7N/m (e) 8N/m.

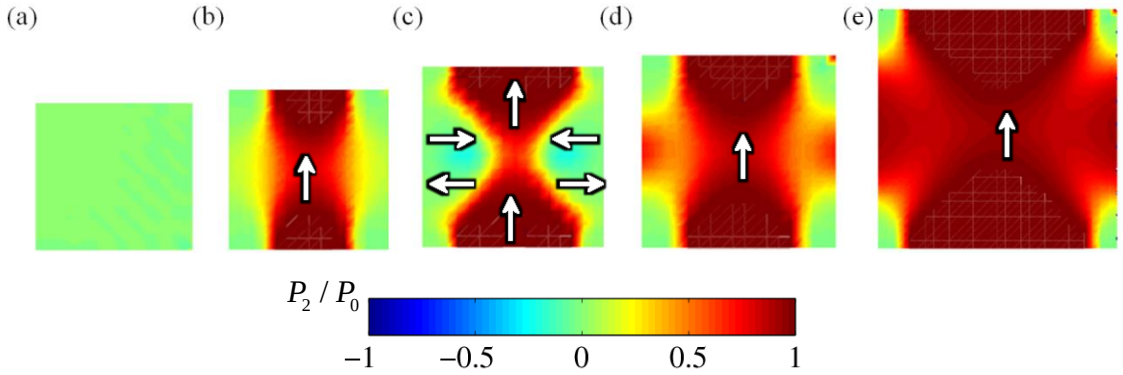

Figure 4.19: Equilibrium domain patterns formed along BB' at surface energy γ = 9N/m at nanowire width, L (a) 12nm (b) 13nm (c) 16nm (d) 17nm (e) 30nm.

The domain pattern transition from the non-ferroelectric through to the monodomain state at γ = 9N/m, along the line BB', is shown in Fig. 4.19. At this surface energy, nanowire widths L < 12nm are non-ferroelectric, while band-like domain patterns sandwiched in a non-ferroelectric region appear at L = 13nm. Increasing L to ~16nm P_1 domains appear, resulting in the formation of 90° domain walls. As the width increases, the effect of surface energy on the domain patterns decreases, and a uniformly polarized monodomain is supported for L > 30nm.

The average c/a ratio or tetragonality of barium titanate with conductive surfaces is plotted as a function of surface energy as shown Fig. 4.20(a). At L = 20nm and $\gamma = 0$, the ratio is about 1.01 and is consistent with the value predicted for $BaTiO_3$ by Hoshina et al. [139]. The tetragonality reduces with increasing surface energy, however this decrease is more gradual than that of Fig. 4.14 (with insulated surfaces) and higher values of surface energy are required to force the $BaTiO_3$ nanowire into the cubic state with conductive surfaces. At γ = 12N/m, the c/a ratio rises as a complex domain pattern is formed and this differs from the monodomain formed at lower values of surface energy. At γ ~21N/m the c/a ratio is ~1 indicating the cubic structure of

$BaTiO_3$ in its non-ferroelectric state. Next, the variation of the c/a ratio at surface energy $\gamma = 5\text{N/m}$ is explored across a range of nanowire width, see Fig. 4.20(b). The nanowire section is non-ferroelectric up to L~7nm, beyond which the effect of surface energy is minimal and a monodomain is found at equilibrium at increasing widths of the nanowire section. This drop in tetragonality with decreasing size of the nanowire section is similar to the experimental observations made on $BaTiO_3$ nanoparticles by Hoshina et al. [139], see Fig. 4.21. In this study, the size dependence of tetragonality is reported and a gradual increase in the c/a ratio is noted, with increasing size of the sample. Tetragonality is lost, that is $c/a \to 1$ for a nanoparticle of size ~30nm, indicating phase transformation from the tetragonal state to a cubic state at this size, see Fig. 4.21. On the other hand, the phase-field simulations indicate such a transformation to occur at L ~ 7nm. This difference in sizes between the experimental observation and the present phase-field study can be attributed to the following reasons: at first, the $BaTiO_3$ nanoparticle is three dimensional, where the polarization is allowed to switch out of plane. By contrast, the phase-field simulations are two-dimensional (2D) with

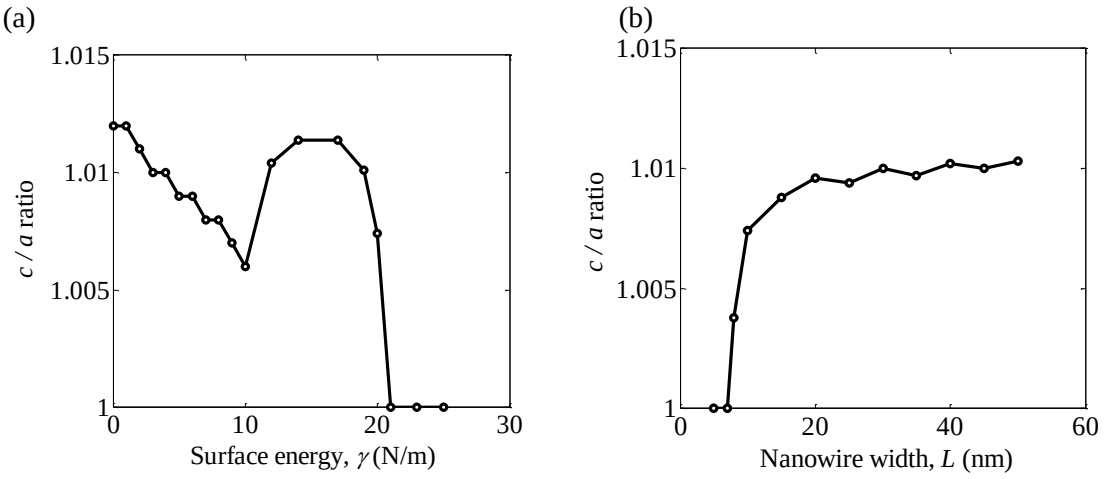

Figure 4.20: The c/a ratio for domain patterns formed with conductive surfaces as a function of (a) surface energy at L = 20nm (b) nanowire size with $\gamma = 5\text{N/m}$.

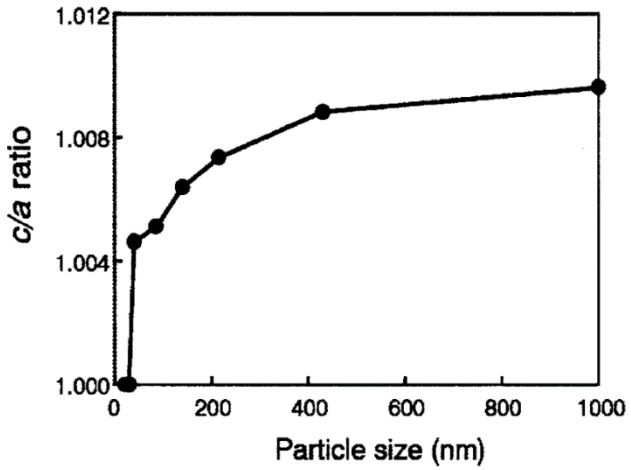

Figure 4.21: Experimental observation of particle size dependence of tetragonality (c/a) for $BaTiO_3$ fine particles with sizes 20nm to 1000nm, obtained from Hoshina et al. [139].

in-plane strain and electric field conditions. This prevents out-of-plane polarization switching and could possibly assist in retaining the in plane tetragonal state at smaller sizes of the nanowire section. Secondly, the $BaTiO_3$ nanoparticles in Hoshina et al. [139] are prepared from a thermal decomposition process. This differs from the phase-field simulations, where a monodomain in various nanowire sizes is modelled and subjected to surface forces. The presence of a uniformly polarized monodomain in the initial state (i.e., absence of domain walls) of the nanowire section, can be expected to require large surface forces or small nanowire sizes to undergo uniform phase transformation. Further, the presence of defects in $BaTiO_3$ nanoparticles, the temperature at which the experiment was conducted ($\sim 24°C$) could also affect the nanoparticle size at which the tetragonality approaches 1.

4.6 Orientation of nanowire section

So far, nanowire sections with boundaries parallel to the $BaTiO_3$ crystallographic axes were considered. In these cases polarized domains formed parallel to the boundaries and under insulating conditions a classic vortex domain pattern containing 90° quadrant domains was found. However, this may not happen in nanowire sections whose boundaries are at an angle to the crystallographic axes. This is because insulating conditions place an energy penalty on any polarization component normal to a surface, while the multi well free energy function favours polarization along the crystallographic axes. To explore this orientation effect on the formation of domain patterns, an 'angled' nanowire section modelled with simple supports, traction-free and charge-free boundary conditions as shown in Fig. 4.22 is employed. Note that these

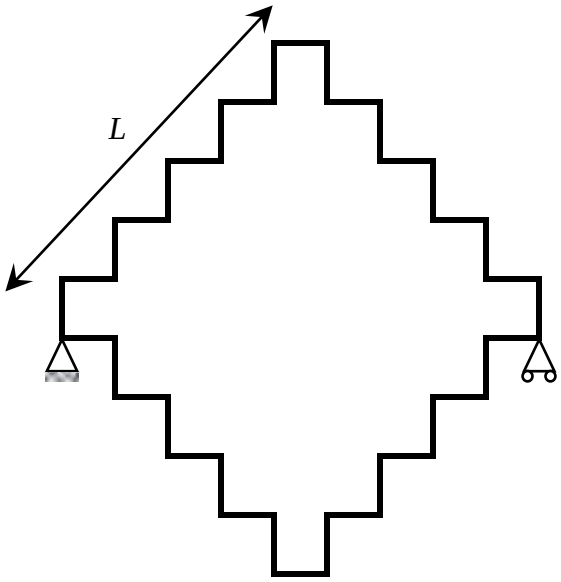

Figure 4.22: Schematic representation of the boundary conditions on the angled nanowire section.

boundaries possess step-like features of ~1nm in size, comparable to atomic steps in the $BaTiO_3$ surface. The lattice parameter is ~4Å.

The simulations are initialized with a randomized polarization field, and the domain patterns formed in nanowire sections of size in the range 22nm to 53nm are explored. Examples of typical domain patterns formed on these sections are shown in Fig. 4.23.

The presence of charge-free or insulated boundary conditions leads to the formation of flux closures in Fig. 4.23. These domain patterns contain numerous small stripe-like domains, which possess pointed or sharp corners at the boundaries of the nanowire cross-section. Since the nanowire section is modelled at an angle to the crystallographic axis, the polarized domains do not form parallel to the boundaries of the nanowire section. These boundaries frustrate the flux-closure domain arrangement, leading to the formation of multiple stripe-like domains. The nanowire region close to

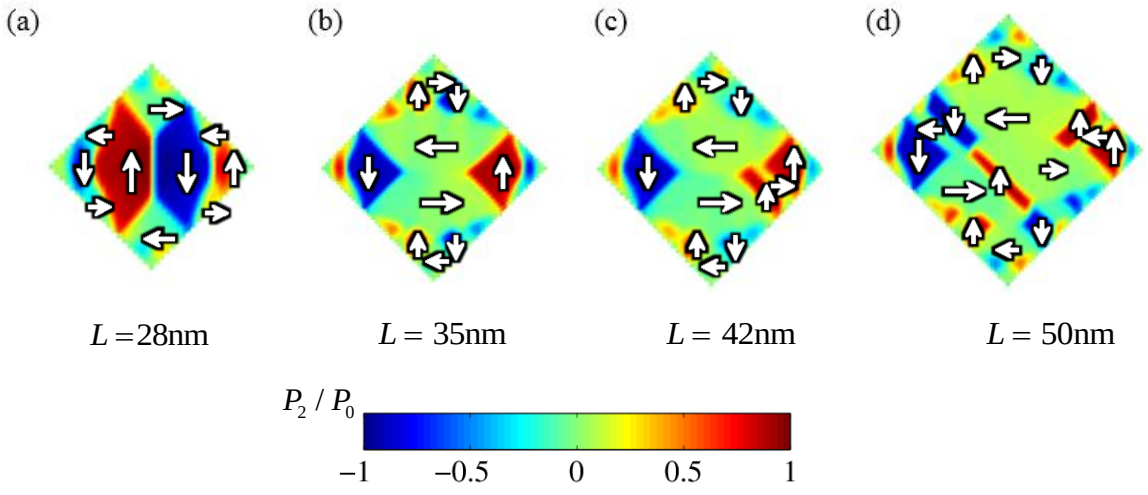

Figure 4.23: Typical domain patterns formed on the angled nanowire section of $BaTiO_3$ with insulated boundary conditions.

the boundary is non-ferroelectric $\left(\frac{c}{a}=1\right)$. Similar vortex-like domain patterns have been observed in larger $BaTiO_3$ nanodots by Schilling et al. [147], see Fig. 4.24. These domain patterns were found to contain several bundles of stripe-like domains, when the nanodots were cut out at an angle to the crystallographic axis. Unfortunately, as the

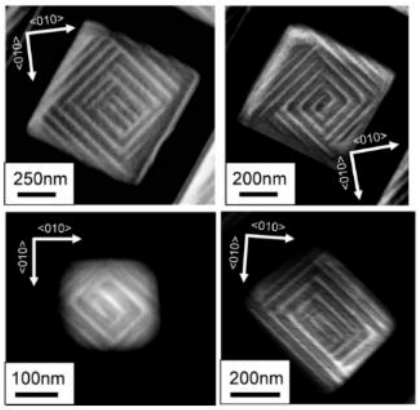

Figure 4.24: Scanning transmission electron microscopy images showing packets of $90°$ stripe domains formed in $BaTiO_3$ dots [147]. Reprinted with permission from Ref. [147]. Copyright 2009 American Chemical Society.

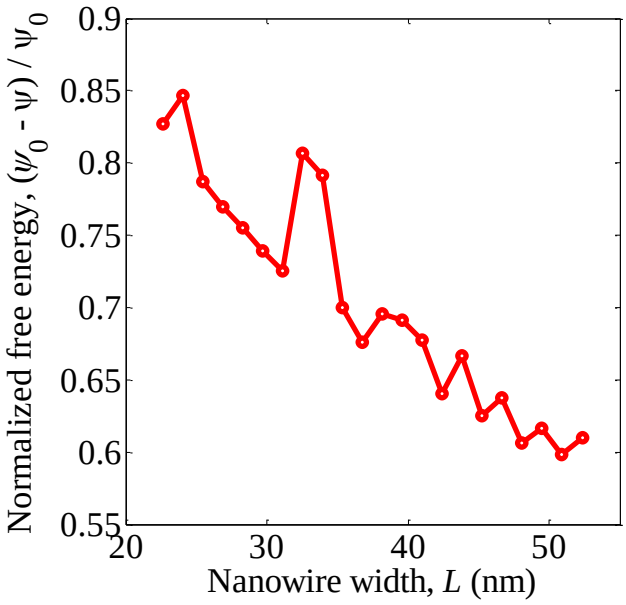

Figure 4.25: Free energy curve for the angled nanowire cross-section.

computational costs scale steeply with nanowire width as discussed in section 2.8 of Chapter 2, the current simulations are limited to about 53nm size nanowire sections.

The normalized free energy, $\tilde{\psi} = (\psi_0 - \psi)/\psi_0$, of the various domain patterns formed in the angled nanowire cross-section as a function of its width is shown in Fig. 4.25. This again follows the relation $\tilde{\psi} = KL^{-0.4}$ with K constant, as found in the square nanowire section aligned to the crystallographic axes, see Fig. 4.6. From Fig. 4.6 and Fig. 4.25, it is interesting to note that although $\tilde{\psi} = KL^{-0.4}$ is valid for both the nanowire sections, the value of $\tilde{\psi}$ is larger for an angled section in comparison to a square section for a given size L. This is because the domain patterns formed on the angled sections typically contain several domain walls which contribute to the increased energy of the domain patterns. Further, the unit cells along the edges of the angled section are non-ferroelectric and are in the cubic state. This is because the insulated boundaries do not allow polarization normal to the surface, and the crystallographic direction of polarization in the unit cells is not favoured. This non-ferroelectric state contributes to increased energy of domain patterns formed in the angled section.

4.7 Discussion and comparison with experiments

The phase-field study on the effects of scaling, surface energy, surface conductivity and orientation of the nanowire section are consistent with several aspects of experimental observations. In this section, the available literature on polarization patterns observed in experiments are discussed and compared with the results from the phase-field simulations.

The classic (type I) polarization vortex with $90°$ quadrant domains has not yet been clearly observed in ferroelectrics, even when the experimenters are setting out to

make these vortex patterns [102], [129], [130], [133]–[136], [148]. For example, McQuaid et al. [135] pole a single crystal $BaTiO_3$ and subsequently remove the electric field to relax the domains towards a flux-closure domain pattern. In this experiment, platinum electrodes are used due to its low conductivity which could facilitate the formation of a vortex pattern. However, the results indicate the formation of a mesoscale flux-closure polarization pattern in $BaTiO_3$ that contains several stripe domains, see Fig. 4.26(a). This pattern differs from the classic (type I) polarization vortex that contains uniformly polarized quadrant domains. In another experiment by L. -W. Chang et al. [132] a thin lamellae of lead ziroconate niobate – lead titanate is cooled through its Curie temperature to facilitate the formation of a vortex polarization pattern. The thin lamella is expected to favour in-plane polarized domains and cooling the material allows for the domain states to evolve under natural conditions. Once again, flux closures with multiple $90°$ stripe patterns are observed to form at equilibrium, see Fig. 4.26(b). Although the work identifies the presence of a flux-closure pattern with uniformly polarized domains at the junction of the stripes, these patterns do not contain the $90°$ vortex core as expected for a classic polarization vortex. Other experiments [131], [133], [136] identify the formation of vortex-like or flux-closure domain patterns, however the observations differ from that of a classic polarization vortex, see Fig. 4.26(c-e).

This lack of experimental observations of the classic (type I) polarization vortex, despite the favourable experimental conditions, such as low conductivity electrodes, can be explained by two factors. First, the scale and surface energy effects discussed in section 4.3 and 4.4 respectively are important. Typical experiments [102], [129], [130], [133]–[136], [148] which map in-plane polarization patterns use sample sizes of order 100nm upwards see Fig. 4.26. The phase-field simulations conducted in the present

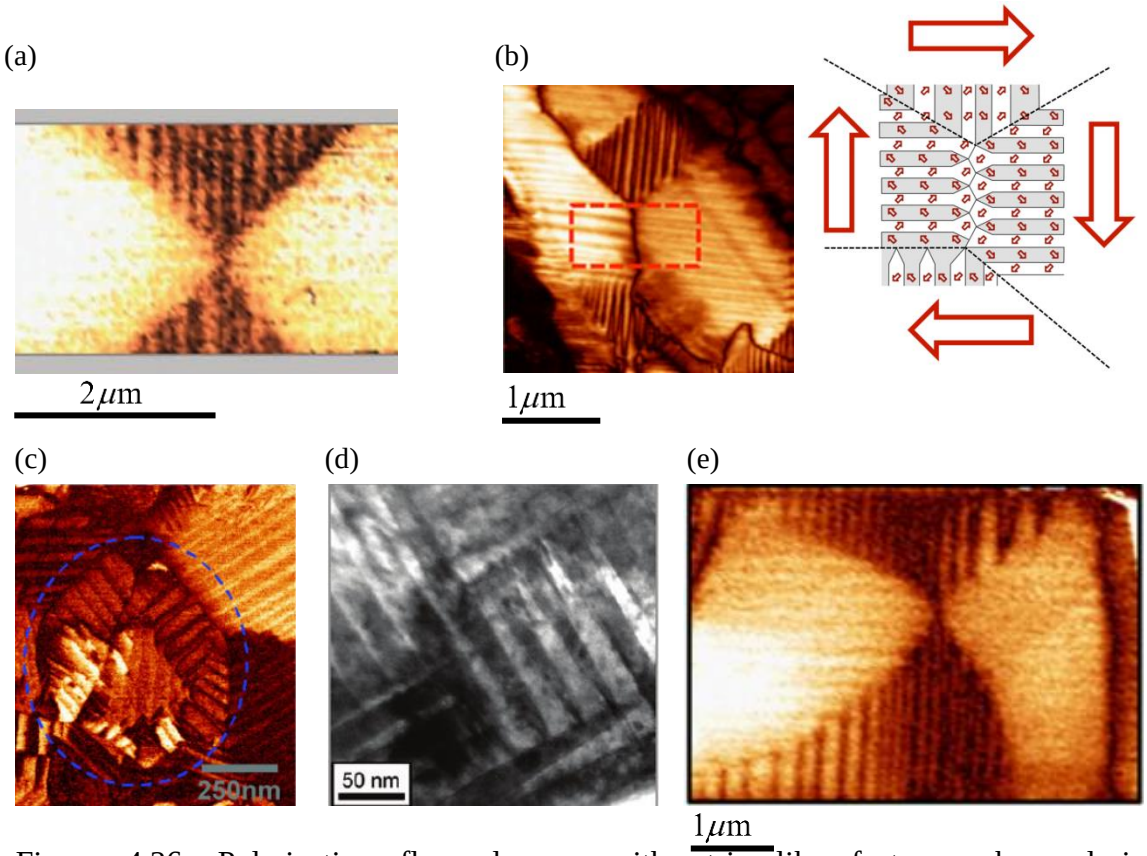

Figure 4.26: Polarization flux closures with stripe-like features observed in (a) mesoscale single crystal $BaTiO_3$ [135] (b) single crystal PZNPT lamella [132] (c) polycrystalline PZT [133] (Copyright 2010 by the American Physical Society) (d) lead zirconate titanate nanodots [136] (e) $BaTiO_3$ platelets [131]. Copyright 2011/2013/2014 American Chemical Society.

work suggest that the type I vortex is a high energy state at this length. The classic vortex domain pattern is identified to possess low energy for length scales up to ~35nm. At large length scales, >35nm, polarization patterns with 180° domain walls at the vortex core (type II) are predicted to form. Domain patterns similar to the type II polarization pattern have been observed in experiments that identify flux closure domain patterns at the junction of domain bundles [130], [148], see Fig. 4.27(a-b). At length scales 80nm upwards, complex domain patterns with several stripe-like features

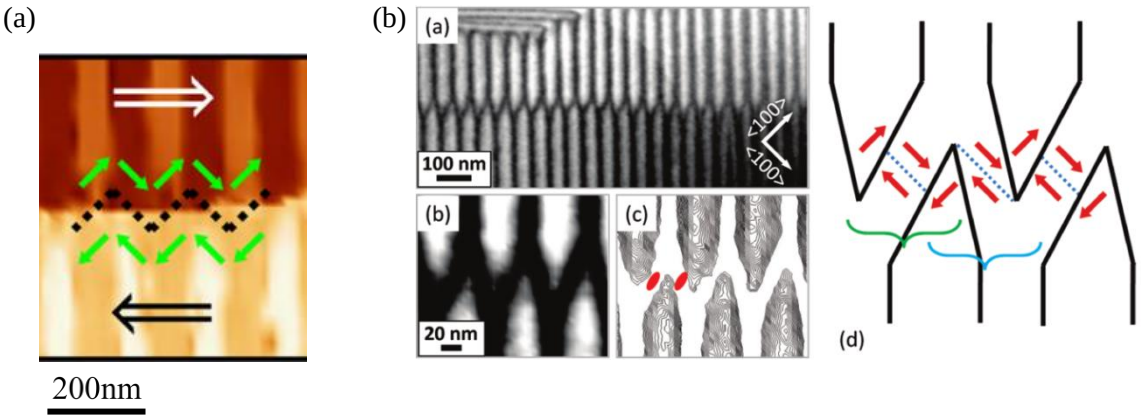

Figure 4.27: Band-like domains with 180° domain wall at the vortex core observed in $BaTiO_3$ lamella. Images modified from (a) McGilly and Gregg [148] (b) McGilly et al. [130]. Reprinted from Ref. [148] and [130], with permission of AIP Publishing and American Chemical Society, respectively.

are calculated to be of lower energy. This is consistent with the experimental observations, where complex domain patterns including several or many domains are typical [102], [130], [136].

A second reason for the possible lack of vortex polarization patterns can be attributed to the surface conditions discussed in section 4.5. Surface environments in experiments often include polar or ionic species that may act as charge carriers, providing some conductivity [140], [147], [149], [150]. In these conductive conditions the phase-field simulations suggest that the type I vortex is unlikely to form. This can be observed in experiments where complex domain patterns with polarization normal to the surfaces form as a result of surface charges. For example, in the work by Schilling et al. [147], the 90° domains form and arrange into quadrant packets with outward polarization, to minimize the energy due to uncompensated surface charges, see Fig. 4.28(a). In another work by the same research group, [150] a quadrupole domain configuration, see Fig. 4.28(b) was formed in response to the electrostatic boundary

conditions. These features indicate that the presence of surface charges do not favour the formation of a vortex pattern, and are consistent with the phase-field simulations in section 4.5.

In Fig. 4.28(b), the shape of the nanodot, i.e., the crystallographic orientation of the ferroelectric specimen, also affected the polarization pattern formed at equilibrium. That is, the boundaries of the nanodot were oriented at an angle to the crystallographic axis. This angled orientation caused increased frustration in the polarization patterns, encouraging the formation of multiple stripe-like domains [147]. This effect was also seen in the phase-field simulations (section 4.6) that explore the effect of orientation of the nanowire section on the formation of polarization patterns.

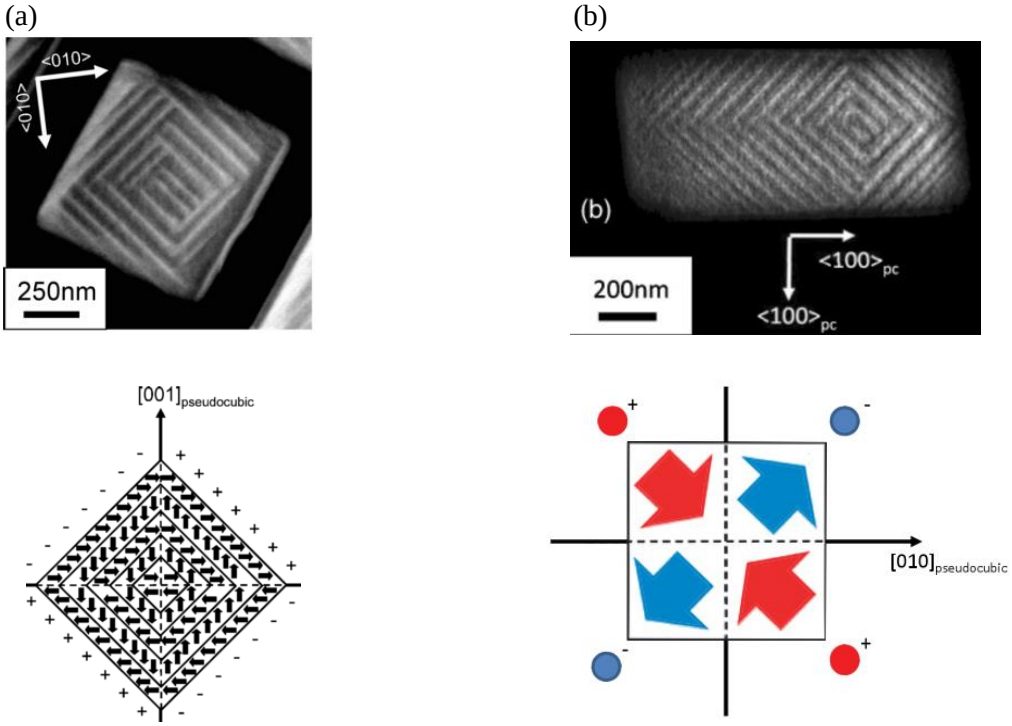

Figure 4.28: Complex domain patterns formed with charge compensated boundary conditions in (a) $BaTiO_3$ nanodots [147] (b) $BaTiO_3$ platelets [150]. Subfigures illustrate the stripe domain pattern with a schematic illustration of the polarization orientation in these patterns. Reprinted with permission from American Chemical Society and American Physical Society, respectively.

Other features of the phase-field simulation results that agree with experimental observations include the loss of tetragonality at small scales; this has been observed in barium titanate nanowires at scales of 10nm or less [151]–[153]. In the work by Spanier et al. [140], ferroelectric phase transition (from tetragonal to cubic phase) in $BaTiO_3$ nanowires placed in an environment of hydroxyl (OH) and carboxylate (R-COO) adsorbates is depressed at smaller length scales. That is, for large surface energy and temperatures below Curie point, nanowires are typically expected to be non-ferroelectric. However, when the nanowires are placed in a conductive environment, ferroelectricity is supported. This is because the polarization in the nanowires is stabilized by surface charges. This observation of ferroelectricity at smaller nanowire sizes is consistent with the phase-diagram for nanowires with conductive boundaries in Fig. 4.17.

So far, the experimental observations in ferroelectrics indicate that a classic polarization vortex (type I) is elusive in nature. Finally, it is of interest to consider why vortices *do* form in magnetic materials. Although ferromagnets possess analogous properties to ferroelectrics, it is important to note a key difference in properties between the two materials. That is, it is impossible to separate magnetic south and north poles (that is, they always exist in pairs), while uniformly polarized monodomains are observed in ferroelectrics [154]. Spontaneously polarized monodomains (electric monopoles) exist in ferroelectrics even in the absence of an external electric field and represent the low energy state of these materials. By contrast, magnetic monopoles are a high energy state in the absence of a magnetizing field. Thereby under natural conditions (free of external magnetic field) magnetic domains arrange to a pattern that minimizes the total energy – an important part of which is the magnetic stray field energy [155]. A common example of a magnetic domain pattern that reduces the stray

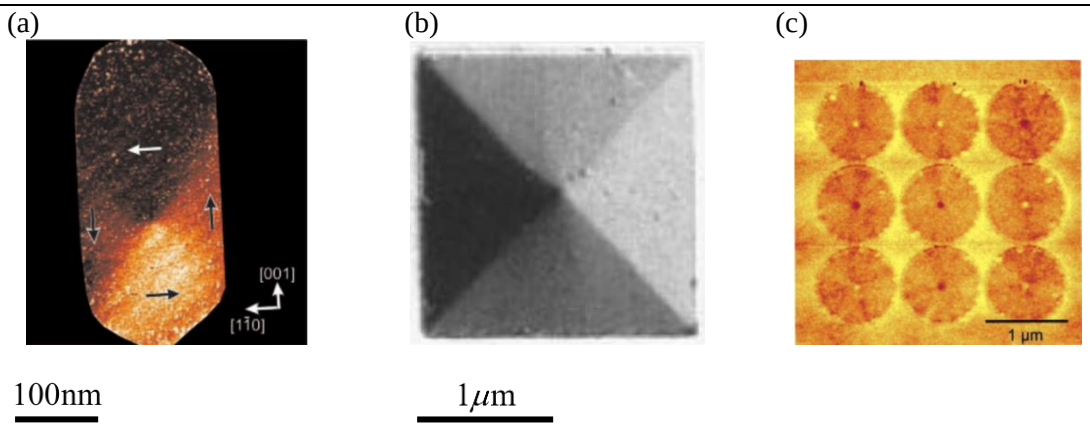

Figure 4.29: Modified images of classic vortex patterns formed with magnetic domains in (a) Fe island [156]. (b) Permalloy [158]. Reprinted with the permission of AIP Publishing. (c) Permalloy nanodisks [103]. Reprinted with permission from AAAS.

field energy is a vortex pattern, and was predicted by Kittel [127] to form in ferromagnetic nanoparticles. These classic vortex patterns with magnetic domains are experimentally verified [103], [104], [156]–[158] and are found in Fe islands [156] and permalloys [103], [158], see Fig. 4.29(a-c). While similar patterns are high energy states in the case of a ferroelectric material, making their formation less favourable.

4.8 Conclusion

A phase-field simulation was employed to study the effects of scale and surface conditions on the polarization patterns that can form in $BaTiO_3$ nanowires. There exists a narrow range of scale and surface conditions for which the classic single polarization vortex is likely to form. The study thus provides an insight into the absence of experimental observation of polarization vortices: typical experiments do not operate in the regime where such vortices are energetically favorable. At scales on the order of a hundred nanometers, the classic single vortex is unlikely to appear because stress relief favours patterns of multiple domains. At smaller scales, ferroelectricity is plagued by surface effects that affect the formation of a single vortex, making it elusive.

5

Periodic domain patterns at the nanoscale

So far, domain patterns formed on a two-dimensional plane of finite size were considered. A typical ferroelectric specimen of few micrometers in size contains many polarized domains that could be arranged to form a periodic pattern. For example in Fig. 5.1, 90° domains are arranged to form a periodic lamellar pattern with stripe-like features [47].

Ferroelectrics form domain patterns that minimize their energy subject to imposed boundary conditions. The arrangement or pattern of these domains is of great importance in determining the properties of a ferroelectric at the nanoscale [159], [160]. For example, the effective piezoelectric coefficients depend upon the fractions of different domain types present [161], and enhanced actuation can be achieved by using specific domain patterns [18]. Engineered configurations of domains have been used to

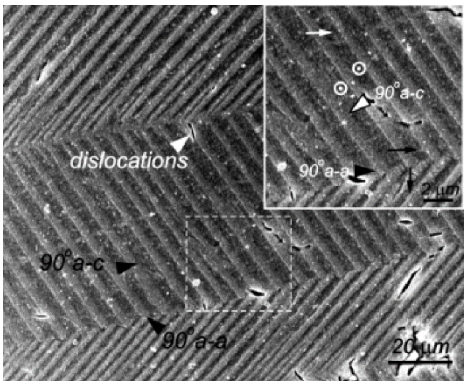

Figure 5.1: Representative microstructures of a periodic domain pattern in $BaTiO_3$ [47].

make improved actuators, sensors and energy harvesting devices [65]. Periodic domain patterns are significant to the working of devices that employ ferroelectrics as thin films or beams [3], [4], [162].

In a linear, constrained theory, that neglects domain wall energy, certain periodic domain patterns have been identified as minimum energy states. However, at the nanoscale, domain wall energy becomes significant, and the stability of these domain patterns at this scale is not known. In this chapter, the phase-field model, which accounts for gradient energy and strain energy contributions, is employed to explore the stability of periodic domain patterns at the nanoscale. The stress, electric field, and domain wall energies are computed, and the effect of scaling is discussed. An application of a periodic domain pattern in a conceptual design of an energy harvester is demonstrated.

5.1 What determines the pattern of domains?

Where any two domains meet, a domain wall forms, as discussed in section 2.5 of chapter 2. The domain walls are associated with surface energy that is proportional to the wall area. But there is also potential energy, proportional to domain volume, associated with externally applied stresses and electric fields. Minimization of energy then produces a competition between the individual energy contributions, leading to the formation of specific patterns. In the absence of external loads, a single domain state minimizes energy; likewise, for boundary conditions consistent with a uniform stress or electric field, the single domain state is an energy minimizer. However, boundary conditions that impose an average strain or electric displacement can lead to a mixture of domains. Once a mixture of domains becomes favourable, energy minimization

produces arrangements of domains that relieve internal stresses and electric fields. Thus “head-to-tail” polarization arrangements [47], [52], [130] form across domain walls and the spontaneous strains in adjacent domains commonly satisfy compatibility conditions. The compatibility conditions in terms of strain are well known from the crystallographic theory of martensite [163], [164], where certain domain arrangements, for example Fig. 5.2(a) are identified as energy minimizers. Where these conditions cannot be met, the resulting misfit strains cause internal stresses, see Fig. 5.2(b) and incompatible polarization causes electric fields; both produce a contribution to the net energy. The compatibility rules give a “constrained theory” that has been widely used to study pattern formation in ferroelectrics and other materials [88],[166]. Here, this approach is used to provide a starting point for the simulations.

The fact that the domain wall energy scales with area, while the potential energy scales with volume, introduces an intrinsic, material specific length scale. Thus energy minimization can determine both the pattern of domains, and the scale at which this pattern forms. At a sufficiently coarse scale, the domain wall energy becomes negligible, and a constrained theory, based on compatibility alone, is sufficient.

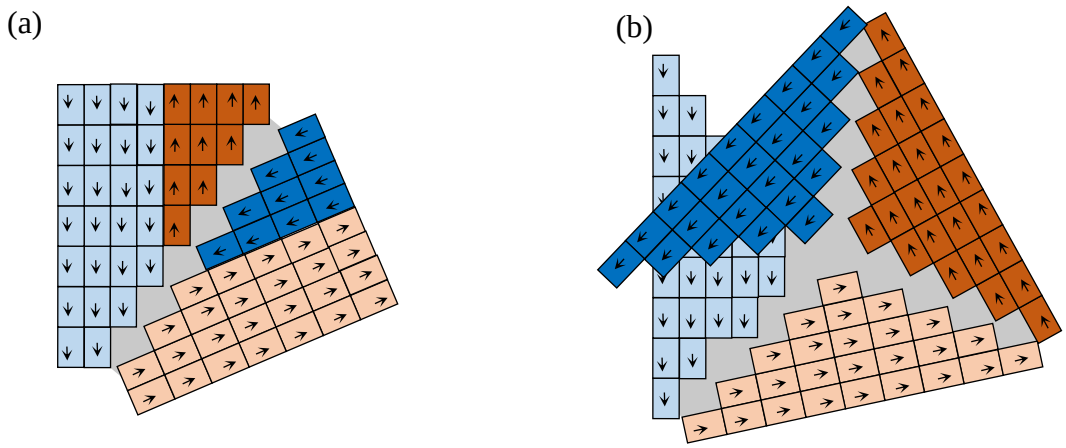

Figure 5.2: Schematic illustration of (a) a stress-free domain pattern, (b) a domain pattern with misfit. Images modified from the thesis of Tsou [165].

However, for the prediction of fine domain patterns, the contribution of domain wall energy becomes significant. The key length scale for typical ferroelectrics is of order nanometers, comparable with the finest spacing of observed domains [167]–[169].

Of course, the materials may not behave as perfect minimizers of energy. Kinetics has a central role in determining the ways that domains can evolve. However, at present the knowledge of kinetic laws for the evolution of ferroelectric domains is limited. Furthermore, the multi-well nature of the energy dictates that even if the system is driven towards minimum energy, it may only reach a local energy minimum. Defects, such as trapped charge [170], dislocations [171], dopant atoms [46] and so forth, also play a role, affecting both the energetics and kinetics. Nevertheless, substantial progress in understanding domain patterns has been made by considering energy minimization in perfect crystals.

Domain patterns in ferroelectrics commonly take the form of nearly periodic laminations [52], [150], [172]. A rank-1 laminate can be defined, as a pattern comprising alternating layers of two domain types, each of which is a single crystal variant. Examples include alternating bands of $180°$ or $90°$ domains. Similarly, simple laminations can themselves be layered together to produce a higher rank laminate. Further details on labelling the laminates are discussed in section 5.2. Based on the linear constrained theory of laminates, Tsou et al. [88] identified several rank-2 periodic domain patterns in tetragonal ferroelectrics, see Fig. 5.3(a-h). Of the domain patterns in Fig. 5.3, a layered stripe domain pattern, see Fig. 5.3(a) and the herringbone domain pattern, see Fig. 5.3(b), are both well-known and commonly observed [47], [52], [53], see Fig. 5.4. Meanwhile, certain other patterns are rarely seen in experiments [84], [102], though elements of these patterns sometimes appear [130].

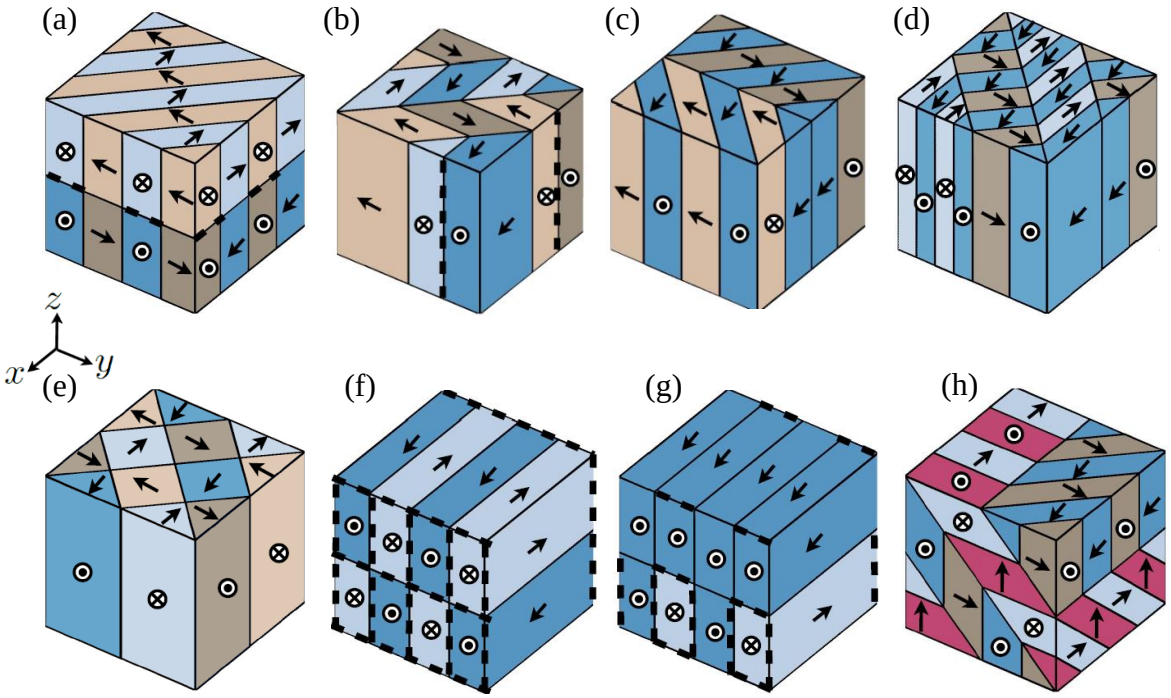

Figure 5.3: Periodic cells of the eight compatible rank-2 domain patterns identified by Tsou et al. [88] using a linear constrained theory of laminates. Images are modified from Tsou et al. [88]. Copyright 2011 by the American Physical Society.

The theory employed by Tsou et al. [88] neglected gradient energy due to domain walls and the elastic/dielectric energy due to misfit strains at the junctions of domains. However, these factors could be expected to be of importance, especially at the nanoscale. This opens up the following questions: Among the periodic laminates identified by the constrained theory, which are stable when gradient and elastic energy are considered? Which patterns constitute global energy minima, and does this depend on scale? How do imposed states of average strain or polarization affect the stability and behavior of these domain patterns?

In the present work the Landis phase-field model [29] is used to study rank-1 and rank-2 periodic domain patterns in tetragonal ferroelectrics, at the nanoscale. The stability of these domain patterns in the absence of external loading is first tested. The

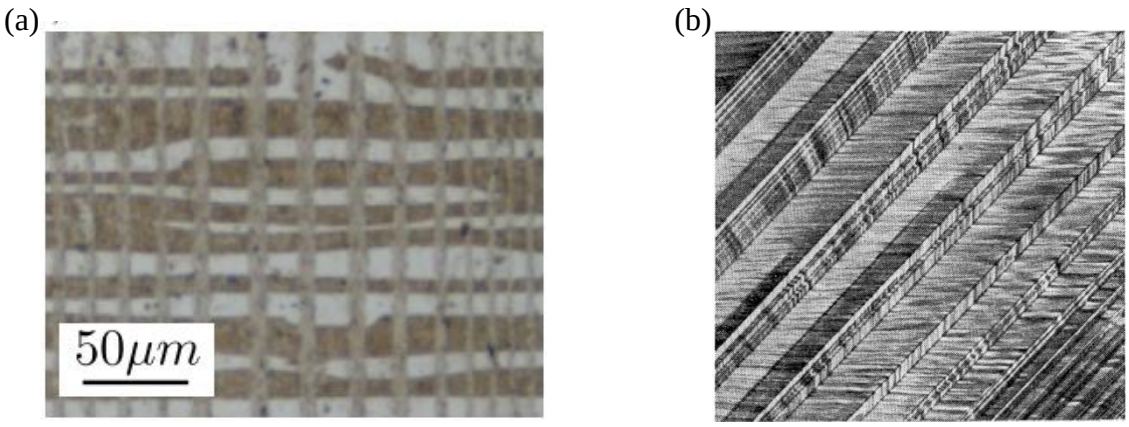

Figure 5.4: Experimental observation of domain patterns in barium titanate illustrating (a) the intersection of straight 90° domain walls in the layered stripe pattern [88], and (b) a herringbone pattern [53]. Copyright 1955 by the American Physical Society.

internal fields in the domain patterns are then examined, and the effect of scaling on internal energy is considered. The simple rank-1 laminates (stripe domain patterns) are found to be lower energy states than the more complex, rank-2 laminates. Several of the rank-2 patterns, when modelled at the nanoscale, collapse into simpler states. However, they can be stabilized by external loads such as electric field, average strain and polarization, and examples of this are given. Further, it is also shown that, with suitable loading, simple rank-1 domain patterns can be made to evolve into more complex, rank-2 patterns, suggesting a mechanism for the formation of complex domain patterns. The study provides insight into the domain patterns that may form in nanoscale tetragonal ferroelectrics, and on the effect of external loads on these patterns. The study also explores the potential application of a rank-1 stripe domain pattern in a conceptual design of energy harvester.

5.2 Laminates and periodic boundary conditions

The objective of the current study is to test the stability of periodic laminate patterns formed in tetragonal ferroelectrics at the nanoscale. To do this, a set of rank-1 and rank-2 periodic laminates identified by Tsou et al. [88] are modelled using phase-field methods. Following Tsou [88], [173] the multi-rank laminates are labelled on the basis of the crystal variants present in the domain pattern. There are six crystal variants in the polar tetragonal system, with distinct spontaneous polarization states as shown in Fig. 5.5(a). The structure of a multi-rank laminate consists of layers which are themselves subdivided into finer layers, the finest laminations comprising material of a single crystal variant. The arrangement of layers is readily described using a hierarchical tree structure [174], see Fig. 5.5(b). At the lowest level are single crystal variants, numbered according to their polarization orientation. Ascending the tree diagram, higher rank laminates are labelled so as to show the crystal variants present, reading from left to right across the lowest level of the tree. Thus, in Fig. 5.5(b), the

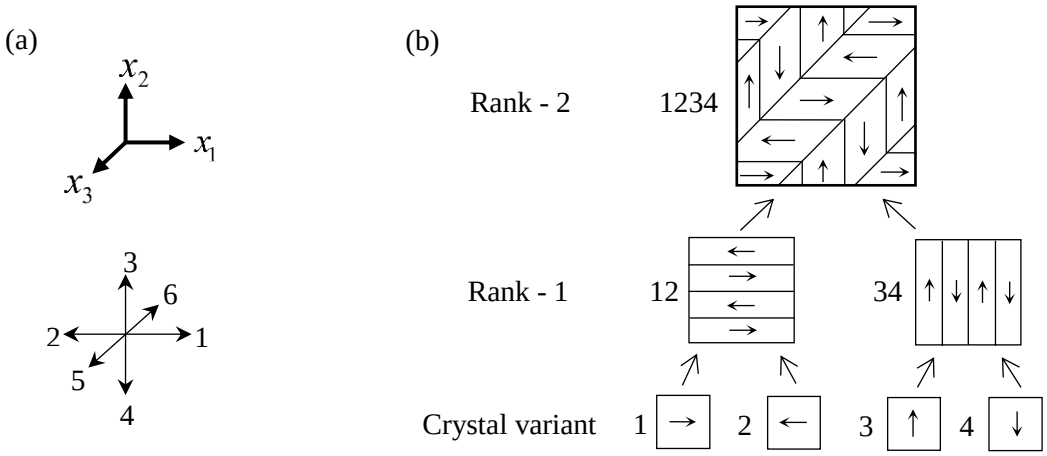

Figure 5.5: (a) Coordinate axes and polarization directions of the six crystal variants in the tetragonal system. (b) A rank-2 tree diagram illustrating the domain pattern “1234”.

rank-1 domain patterns are labelled as “12” and “34”. These rank-1 domain patterns can be laminated together to form a rank-2 herringbone domain pattern, labelled “1234”.

There are many laminate patterns that can be formed in this way. However, most are reflections, rotations or inversions of other patterns. Taking out these symmetrical copies, Tsou et al. [88] found just two distinct laminates of rank-1 and eight of rank-2. Here, nanoscale periodic cells of these periodic patterns are modelled and their equilibrium states are simulated using the Landis phase-field model.

The phase-field model is extended to solve three dimensional (3D) configurations, but several of the domain patterns considered have polarization in a single plane with all domain walls perpendicular to that plane, see Fig. 5.3(b-e). In these cases the prismatic nature of the patterns is exploited allowing them to be modelled in two dimensions (2D), with plane strain and plane electric field conditions. This is practically expedient because the simulations are computationally intensive as discussed in section 2.8 of chapter 2. However, modelling in 2D does limit the simulation by preventing out-of-plane polarization. Based on previous experience with a wider range of simulations, this restriction does not greatly affect the model outcomes. Domain patterns with out-of-plane polarizations are modelled in 3D.

To model a regular repeating laminate structure, periodic boundary conditions are imposed, see Fig. 5.6. A periodic square of side L = 40nm, Fig. 5.6(a), and a periodic cuboid with depth $D < L$, Fig. 5.6(b), are modelled in the 2D and 3D simulations respectively. A finite element mesh with square elements of size 1nm is generated for the 2D simulation, while 3D simulations involve brick elements of size 1nm. The chosen size of the elements, allows the domain walls to typically span over about three elements. A mid-element of the 2D/3D finite element model shown in

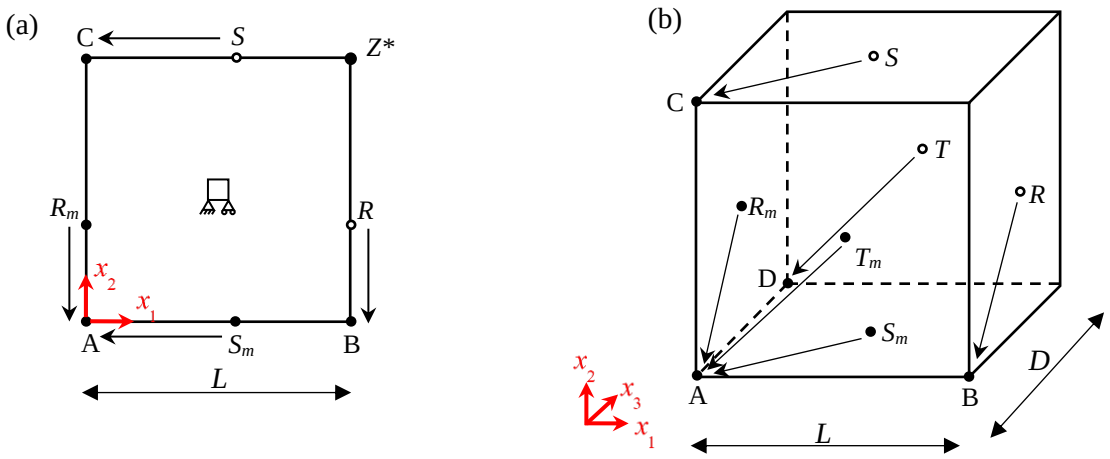

Figure 5.6: Schematic representation of the periodic cell and boundary conditions on (a) a square of side L (b) a cuboid of depth D. Arrows indicate the nodal relations in periodic boundary conditions.

Fig. 5.6(a-b) is identified and simple support boundary conditions are applied to it. These boundary conditions impose traction free surfaces, and prevent the translation or rotation of the periodic cell. In order to ensure periodicity, periodic boundary conditions are enforced on the boundary nodes. Here, the boundary nodes on the opposite edges of the periodic cell are identified in pairs, for example *R*-R_m, *S*-S_m in Fig. 5.6(a). These nodes control the displacement u_i, electric potential ϕ, and polarization P_i nodal degrees of freedom. For a typical node *R* along $x_1 = L$, these conditions are:

$$u_i(L, x_2, x_3)\big|_R - u_i(L, 0, 0)\big|_{\mathrm{B}} = u_i(0, x_2, x_3)\big|_{R_m} - u_i(0, 0, 0)\big|_{\mathrm{A}}$$

$$\phi(L, x_2, x_3)\big|_R = \phi(0, x_2, x_3)\big|_{R_m}$$

$$P_i(L, x_2, x_3)\big|_R = P_i(0, x_2, x_3)\big|_{R_m} \qquad i = 1, n\,. \tag{5.1a}$$

Here *n* is the number of dimensions, and for 2D simulations $x_3 = 0$. The notation ' $\big|_X$ ' is used to indicate a value at a node ' X ' as labelled in Fig. 5.6. Similar conditions

apply to a typical node *S* along $x_2 = L$,

$$u_i(x_1, L, x_3)\big|_S - u_i(0, L, 0)\big|_C = u_i(x_1, 0, x_3)\big|_{S_m} - u_i(0,0,0)\big|_{\mathrm{A}}$$

$$\phi(x_1, L, x_3)\big|_S = \phi(x_1, 0, x_3)\big|_{S_m}$$

$$P_i(x_1, L, x_3)\big|_S = P_i(x_1, 0, x_3)\big|_{S_m} \qquad i = 1, n \tag{5.1b}$$

and in the 3D case to nodes represented by *T* on plane $x_3 = D$,

$$u_i(x_1, x_2, D)\big|_T - u_i(0,0,D)\big|_D = u_i(x_1, x_2, 0)\big|_{T_m} - u_i(0,0,0)\big|_{\mathrm{A}}$$

$$\phi(x_1, x_2, D)\big|_T = \phi(x_1, x_2, 0)\big|_{T_m}$$

$$P_i(x_1, x_2, D)\big|_T = P_i(x_1, x_2, 0)\big|_{T_m} \qquad i = 1, n\,. \tag{5.1c}$$

At corners in 2D and at edges in 3D models, care is needed to avoid duplication of boundary conditions. In these cases, the corner/edge nodes are grouped together with one set of neighbouring nodes and are modelled with only one set of periodic boundary conditions given by Eq. (5.1). For example in Fig. 5.6(a), the corner node *Z**, is grouped together with the neighbouring nodes represented by *R* and is modelled with the periodic boundary conditions given by Eq. (5.1a) only. The periodic boundary conditions allow the domain pattern to adopt periodic strain fields $\varepsilon_{ij}(x_1, x_2, x_3)$ with zero average stress. That is, the strain fields ε_{ij} are dependent on the relative displacement between the corner nodes, for example node 'A' and node 'B', which are not bound. These corner nodes are free to adopt any displacement values u_i such that the periodic cell possesses zero average stress. Meanwhile, periodic values of electric potential ϕ with zero average electric field, and polarization P_i are imposed on the boundary nodes. The boundary conditions represented by Eq. (5.1) are later referred to as the "zero external load" conditions.

The phase-field simulation is initialized by imposing a polarization field consistent with the repeating unit of a laminate pattern on the periodic cell. The nodal polarization values are set equal to the spontaneous polarization of the domain, producing sharp discontinuities at domain walls in the initial state. The displacement and electric potential values are initialized at zero. Note that this initial state may not satisfy electro-mechanical compatibility conditions, however it provides a state of the order parameter P_i that approximates an equilibrium pattern.

During the early stages of each simulation, high values of polarization viscosity, β, are used to facilitate the resolution of domain walls into a continuous polarization field and displacement field. The sharp discontinuity at the domain walls rapidly relaxes, but the overall pattern of polarization is otherwise almost unchanged at this stage. Once this initial settling has occurred – a condition that will be referred to as the 'settled state' – the free energy of the pattern, though not necessarily yet in equilibrium, is calculated. Subsequently, larger relaxation steps are used, allowing the simulation to evolve towards equilibrium, with the possibility of changing the polarization pattern in the process.

Now, having described the boundary conditions on the periodic cell and the initialization of phase-field simulations, the model is next employed to simulate the simplest laminate patterns – rank-1 domain patterns.

5.3 Rank-1 domain patterns

At first, the stability of the rank-1 domain patterns under zero external load conditions as represented by Eq. (5.1) is tested. The two rank-1 domain patterns identified in tetragonal ferroelectrics are the "12" laminate pattern with alternating 180°

domain bands and the "14" laminate pattern with alternating 90° domain stripes, see Fig. 5.7. The bands/stripes in these periodic domain patterns can be modelled with different domain spacings, *s*. That is, the amount of perpendicular spacing, *s* between domains of a single crystal variant can be changed. Here, the "12" domain pattern is modelled with two different domain spacings $s = 20\text{nm}$ and 10nm defined along cross-section AA, see Fig. 5.7(a-b). Similarly the "14" domain pattern is modelled at two spacings, with $s = 14.1\text{nm}$ and 7.1nm defined along cross-section BB, as shown in Fig. 5.7(c-d).

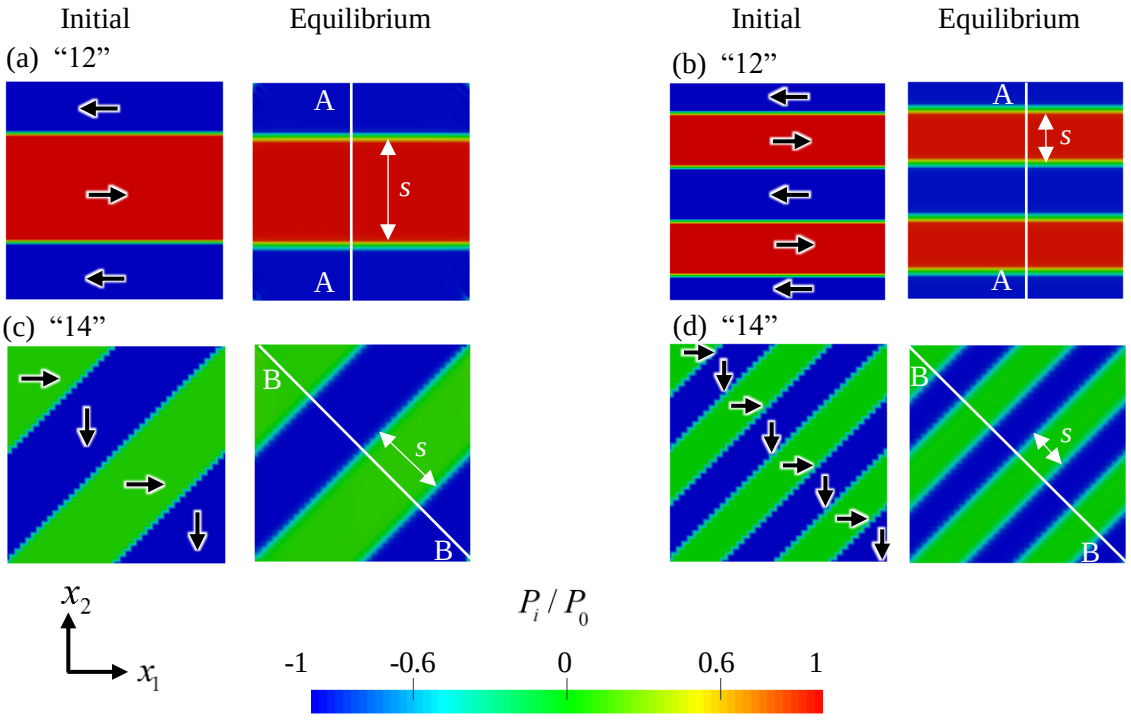

Figure 5.7: Testing the stability of rank-1 domain patterns under zero external load conditions. P_1 / P_0 values in (a) laminate "12" with $s = 20\text{nm}$, and (b) laminate "12" with $s = 10\text{nm}$. P_2 / P_0 values in (c) laminate "14" with $s = 14.1\text{nm}$, and (d) laminate "14" with $s = 7.1\text{nm}$. AA and BB indicate cross-sections perpendicular to the domain walls.

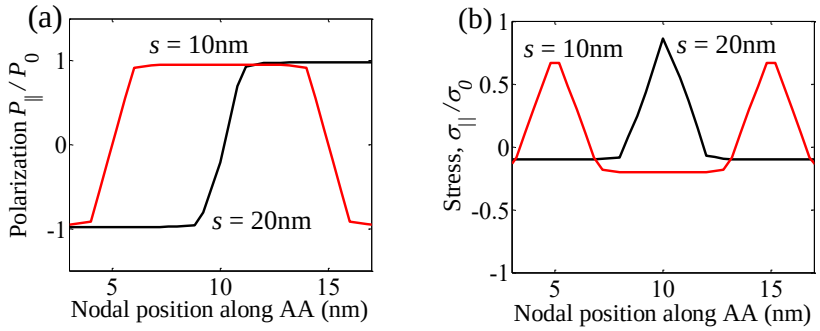

Figure 5.8: Nodal values of (a) polarization $P_{\|}$, parallel to the domain wall and (b) stress component $\sigma_{\|}$, parallel to the domain wall on cross-section AA in $180°$ band domain pattern.

At equilibrium, the sharp domain walls in the initial states become smooth, but the patterns are otherwise unchanged, see Fig. 5.7(a-d). In section 2.5 of chapter 2, the variation of polarization and stress across a single 180° and 90° domain walls modelled on a 2D plane with finite size were explored. Now, it is of interest to study the variation of polarization and stress across domain walls, when modelled with periodic boundary conditions. At first the variations across section AA in the 180° domain pattern "12" are shown in Fig. 5.8(a-b).

From Fig. 5.8(a), the domain wall width is close to 2nm and is consistent with the measurements of a 180° domain wall width in section 2.5 of chapter 2. It is interesting to note that the domain wall width is unaffected by changing the domain spacing from 10nm to 20nm in Fig. 5.7(a-b). These values are also consistent with the results from the quasi-one-dimensional analysis of tetragonal twins by Cao and Cross [91] and match separate calculations on domain wall width by Hlinka and Márton [41]. On moving away from the domain walls, the polarization magnitude is close to the

spontaneous value (within 1%) and there is no polarization perpendicular to the walls. The electric field is everywhere negligible.

At equilibrium, stresses develop parallel to the $180°$ walls as shown in Fig. 5.8(b), while stresses perpendicular to the walls are zero. Here, these stresses correspond to the values of σ_{11} and σ_{22} respectively. With spacing $s = 20\text{nm}$ the tensile stress peaks at about $0.85\sigma_0$ in the domain walls, balanced by compressive stresses of about $-0.1\sigma_0$ in the domains. On decreasing the spacing to $s = 10\text{nm}$, the peak stress reduces to about $0.65\sigma_0$, while the compressive stresses in the domains double in magnitude, becoming $-0.2\sigma_0$. The energy per unit area associated with the presence of domain walls was calculated using

$$\gamma_{\text{w}} = \frac{\int_V (\psi - \psi_0)\,\text{d}V}{A_{\text{w}}} \tag{5.2}$$

where A_{w} is the wall area within the periodic cell of volume V. It was found $\gamma_{\text{w}} \sim 13.1\text{mJ/m}^2$ when $s = 20\text{nm}$ and $\gamma_{\text{w}} \sim 12.6\text{mJ/m}^2$ for $s = 10\text{nm}$. This compares with the value of 14.8mJ/m^2 for the case $s \to \infty$ [29]. It is interesting to note that the domain wall energy in the periodic laminate is less than the energy of an isolated domain wall, and dependent upon the domain spacing. The decrease in stresses at the domain walls accounts for the difference. Similar magnitudes of domain wall energy have been found in previous investigations [101].

Next, the polarization variation on section BB in the $90°$ stripe domain pattern "14", with spacing of 14.1nm and 7.1nm, is shown in Fig. 5.9(a). Away from the domain walls, the polarization magnitude approaches P_0 with components of magnitude $P_0/\sqrt{2}$ parallel and perpendicular to the domain walls. From Fig. 5.9(a) the $90°$

domain wall width is ~3nm, in agreement with ref. [29] and calculations in section 2.5 of chapter 2.

At equilibrium, tensile stresses parallel and perpendicular to the $90°$ domain walls develop, balanced by compressive stresses in the domains, see Fig. 5.9(b). The stresses at the domain walls peak at about $0.14\sigma_0$ for $s = 14.1\text{nm}$ and reduce to $0.13\sigma_0$ when $s = 7.1\text{nm}$. This differs from the value of $\sim 0.33\sigma_0$ calculated for the case $s \to \infty$ [29]; the difference can be attributed to the fine spacing of the domains, which places the domains into significant compression and hence affects the stress distribution in the domain walls. The domain wall energies are calculated to be ~6.0mJ/m^2 for $s = 14.1\text{nm}$ and ~5.8mJ/m^2 for $s = 7.1\text{nm}$. These values are consistent with the energy calculations in [29]. The stresses developed in the $90°$ stripe domain pattern are rather low in comparison to the $180°$ band domain pattern, and this accounts for the difference in the $90°$ and $180°$ domain wall energies.

Non-zero local electric fields are developed at the $90°$ domain walls, as shown by the change in electric potential values in Fig. 5.9(c). Note that the "14" pattern has a

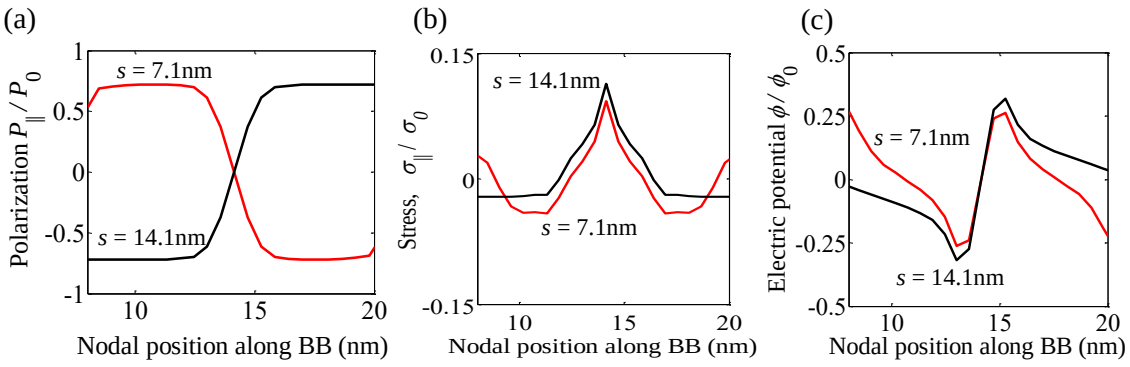

Figure 5.9: Nodal values of (a) polarization $P_{\|}$, parallel to the domain wall and (b) stress component $\sigma_{\|}$ and (c) electric potential ϕ on cross-section BB in the $90°$ stripe domain pattern.

non-zero average polarization. The electric fields are in the direction opposite to this net polarization, and cause deviation from the spontaneously polarized state at the walls. A consequence is that there are electric fields in the domains that are aligned with the average polarization. With $s = 14.1\text{nm}$ the change in electric potential across a domain wall is about $\Delta\phi \sim 0.6\phi_0$, corresponding to an electric field of magnitude $\sim 0.2E_0$. On decreasing the spacing to $s = 7.1\text{nm}$, $\Delta\phi$ drops to $\sim 0.5\phi_0$ with the corresponding electric field magnitude reduced to $\sim 0.17E_0$. However, the electric field in the polarized domains increases with decrease in spacing.

Domain spacing in the rank-1 laminates affects both the wall energy and the distribution of internal stresses or electric fields. Next the effect of domain wall position within a given rank-1 laminate is explored by changing the separation distance l_w of adjacent domain walls, while keeping the size of the periodic cell constant. Does varying the separation distance l_w affect the energy of the laminate?

Here, the $180°$ band domain pattern "12" with $s = 20\text{nm}$ and the $90°$ stripe domain pattern "14" with $s = 14.1\text{nm}$ is modelled and initialized with varying separation distance l_w. The patterns are tested under zero external load conditions, Eq. (5.1), and relaxed towards equilibrium. The volume average free energy is plotted as a function of separation distance in Fig. 5.10(a-b). For $1\text{nm} < l_w < 39\text{nm}$ in Fig. 5.10(a) and $4\text{nm} < l_w < 25\text{nm}$ in Fig. 5.10(b), the relaxation process produces no change in the domain pattern, apart from smoothing the domain walls. The free energy is almost independent of the domain wall separation for both laminates, indicating that the patterns are in neutral equilibrium. For $l_w \sim 1\text{nm}$ in the $180°$ band domain pattern and $l_w \sim 4\text{nm}$ in the $90°$ stripe domain pattern, the laminates are unstable: the pattern

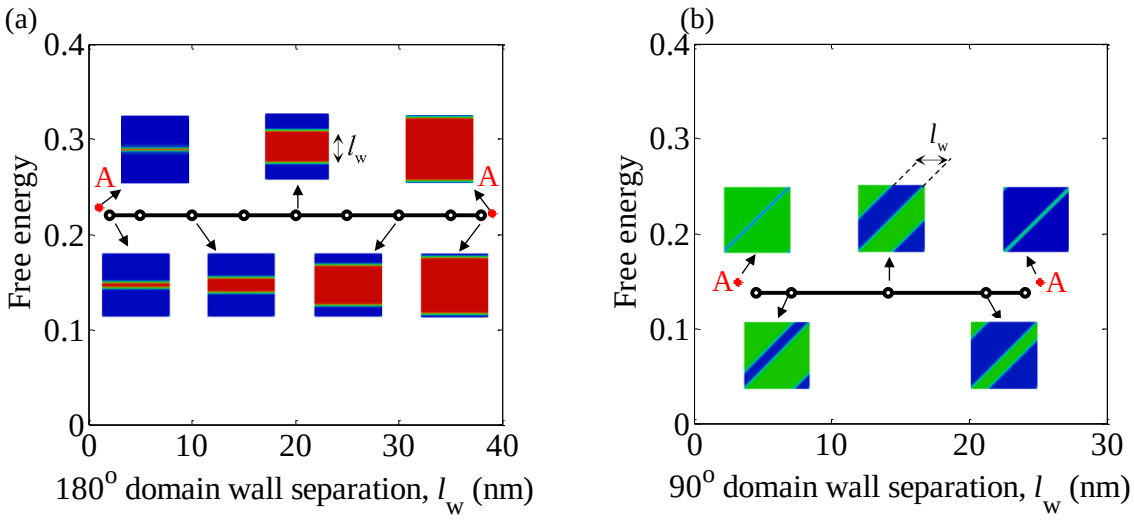

Figure 5.10: The volume average free energy of rank-1 domain patterns as a function of domain wall separation, l_w in (a) the laminate "12" (b) the laminate "14". Inset schematics denote polarization patterns. The solid line connects the free energy of domain patterns at equilibrium, while the markers 'A' at the far end of the plots indicate the free energy of unstable domain patterns in their settled states.

collapses to a monodomain. In these cases, the energy was calculated at the settled state, see markers 'A' at far ends in Fig. 5.10. Note that the domain patterns indicated by markers 'A' are not stable; however their free energy has been calculated upon the initial settling where the domain walls are resolved at large values of β steps. On allowing these patterns to approach equilibrium, by lowering β values, the pattern energy remains nearly constant before the pattern collapses into a monodomain.

The rank-1 polarization patterns with stripe-like features, such as the "14" laminate, see Fig. 5.7(c), have been ubiquitously observed in ferroelectric thin films or lamellae [47], [130], [175]. Thin film processing technology has advanced in recent times, enabling its fabrication at the industrial level [176]. This motivates to explore a

potential application of ferroelectric thin films containing the widely observed "14" laminate patterns. Next, a conceptual design of an energy harvester is demonstrated.

5.4 Energy harvester concept

An energy harvester is a device that converts the input mechanical energy, in the form of stresses/substrates strains, into electrical energy. Here, the energy harvester concept comprises a barium titanate thin film on a conductive substrate with a top electrode, see Fig. 5.11(a). The top electrode is maintained at a voltage ϕ, while the substrate is electrically grounded. In the initial state, the commonly observed periodic "14" laminate is modelled with zero net charge on the top electrode. On bending the substrate, a mechanical strain is induced in the ferroelectric film, causing the polarized domains to switch with the applied strain. For example in Fig. 5.11(b-c) – tensile strain along the length of the ferroelectric film causes the polarized domains aligned along x_1 – axis to grow in size, see Fig. 5.11(b); likewise, compressing the substrate, i.e., bending in the reverse direction, see Fig. 5.11(c), causes the domains polarized along the x_2 – axis to grow in size. This change in domain sizes generates a net electric charge

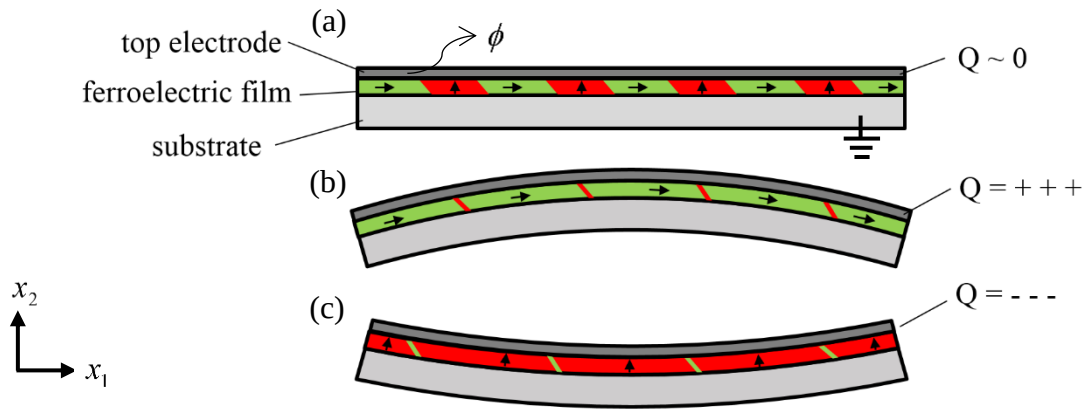

Figure 5.11(a-c): Schematic illustration of the working concept of the energy harvester.

on the top electrode that can be harvested. For example, with voltage ~0.1V on the top electrode, the energy harvester produces a charge of up to ~ 0.1C/m^2. On operating the harvester cycle at high frequencies (10Hz – 1kHz) such as from vibrations in the environment, an area power density of about 0.1 to 10W/m^2 can be produced. This power density is comparable to the power density of photovoltaic cells ($30\text{-}50\text{W/m}^2$) used in solar panels.

To explore this idea of a conceptual energy harvester, a square periodic cell of $BaTiO_3$ is modelled with plane strain and electric field conditions, see Fig. 5.12. A cell with side L = 40nm is chosen, because at this size the domain spacing in the "14" laminate is about 14.1nm and the pattern does not collapse to form a monodomain. An axial in-plane strain, ε_{11}, is induced by the conductive substrate modelled at $x_2 = 0$. At the top surface, $x_2 = L$ an electrode of area A, with voltage ϕ is modelled. Nodes along $x_1 = 0$ and $x_1 = L$ are modelled with periodic boundary conditions given by Eq. (5.1). The simulation is initialized by imposing a "14" laminate on the periodic cell with sharp interfaces. The voltage on the top electrode is zero, $\phi = 0$ and the substrate strain $\varepsilon_{11} = 0.3\varepsilon_0$ is applied at $x_2 = 0$. $\varepsilon_{11} = 0.3\varepsilon_0$ is chosen because the "14" laminate under

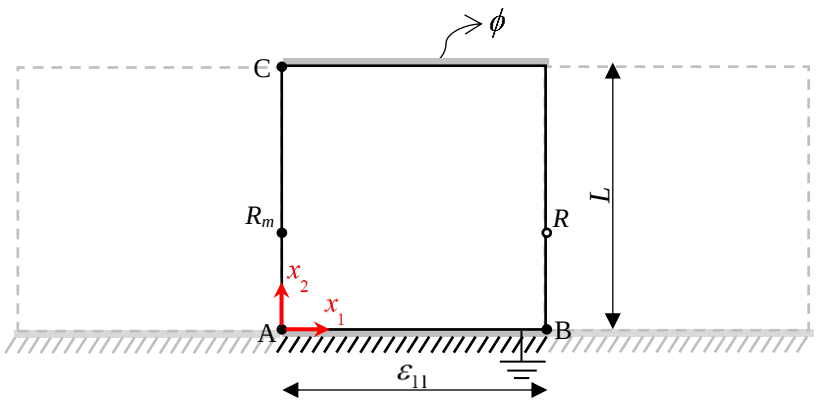

Figure 5.12: Schematic illustration of the boundary conditions on a periodic cell of the energy harvester.

zero external conditions adopts an average strain ε_{11}~$0.3\varepsilon_0$, see Fig. 5.7(c). The periodic cell of the energy harvester is solved using the phase-field model and at equilibrium a stripe-like pattern is formed, see Fig. 5.13(a). At $\varepsilon_{11}=0.3\varepsilon_0$ the domains in the periodic cell, that are polarized along the x_1-axis (P_1 domains) and the x_2-axis (P_2 domains) are of equal sizes and a net charge of ~0.13C/m^2 is generated on the top electrode. Starting from this state, the mechanical loading is applied to the energy harvester by incrementing substrate strain in steps of $0.05\varepsilon_0$. That is, the equilibrium

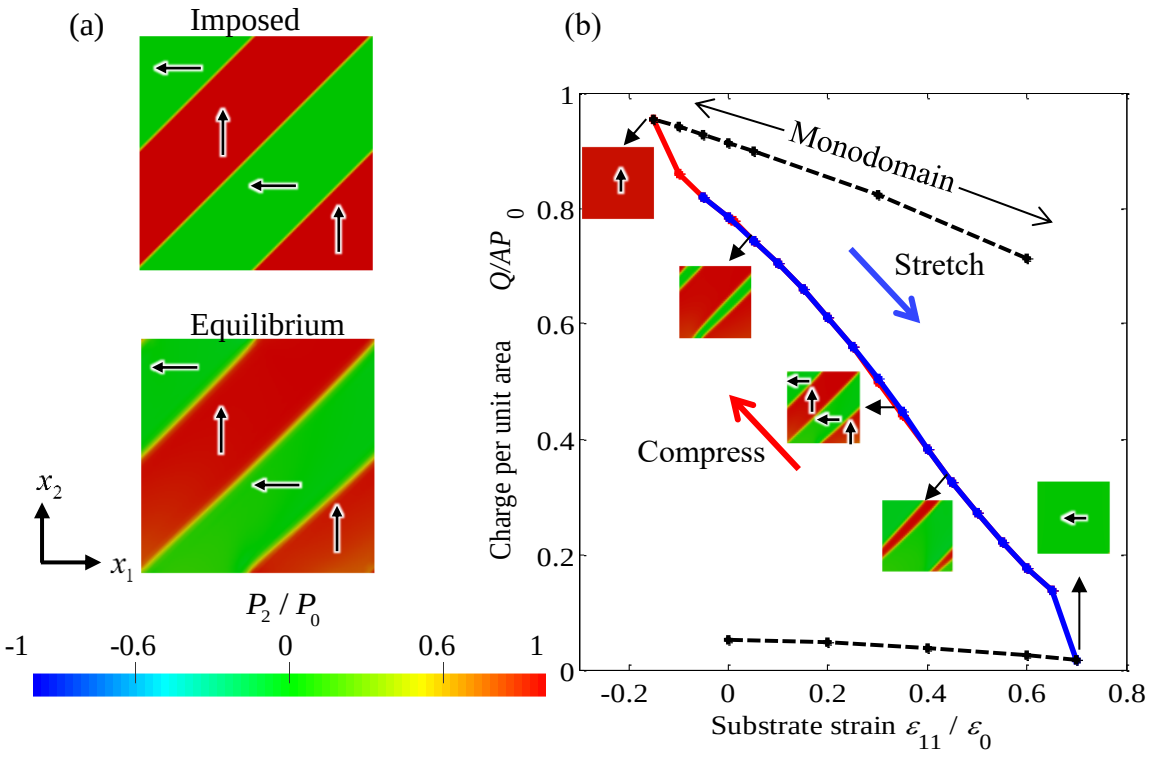

Figure 5.13: (a) Polarization pattern in the initial state of the energy harvester at $\varepsilon_{11}=0.3\varepsilon_0$ (b) Charge per unit area collected on the top electrode as a function of the substrate strain in the energy harvester. A is the area of the top electrode and $P_0=0.26\text{C/m}^2$. The cycle is performed at $\phi=0$ and inset figures illustrate the domain patterns polarized along the x_2- axis.

domain pattern formed at $\varepsilon_{11} = 0.3\varepsilon_0$ is taken as the initial state and the substrate strain is increased to $0.35\varepsilon_0$. The net charge per unit area collected on the top electrode is measured at each value of ε_{11} (with $\phi = 0$) and is shown in Fig. 5.13(b).

In Fig. 5.13(b), it can be noted that increasing the strain, reduces the net charge on the top electrode. This is because the sizes of P_2 domains decrease with increasing ε_{11}, see inset figures in Fig. 5.13(b). On compressing the substrate, the net charge on the top electrode increases. The key information in Fig. 5.13(b), is that for axial strains, $\varepsilon_{11} > 0.65\varepsilon_0$, or compressive strains $\varepsilon_{11} < -0.1\varepsilon_0$, the stripe-like features in the periodic cell disappear leading to the formation of uniformly polarized monodomain. Upon stretching/compressing the monodomain, the stripe-like features are not recovered, and the energy harvester cycle is not repeatable. As a result, the energy harvester is limited to operate within the range of substrate strain $0 \le \varepsilon_{11} \le 0.4\varepsilon_0$.

Next, the challenge is to extract electrical energy from a cycle of mechanical straining of the energy harvester. In order to achieve this, the voltage on the top electrode is varied during the energy harvester cycle. This allows electrical work to be extracted from the charge flow in/out of the top electrode. An example of this energy harvester cycle is illustrated through steps A-B-C-D using phase-field simulations in Fig. 5.14(a-j). The net charge per unit area collected on the top electrode of the energy harvester is shown in Fig. 5.15(a).

The domain evolution through step AB, is illustrated by Fig. 5.14(a-d). Here, the voltage on the top electrode is held constant at $\phi = 0$, while the substrate strain is decreased from $\varepsilon_{11} = 0.4\varepsilon_0$ in steps of $0.05\varepsilon_0$. This causes the P_2 domains to grow in size. At point B, where $\phi = 0$ and $\varepsilon_{11} = 0$, the net charge per unit area on the top

electrode is $\sim -0.8P_0$. Here, the substrate strain is held constant at zero strain and the voltage on the top electrode is lowered to -0.25V in step BC. During this step, a net

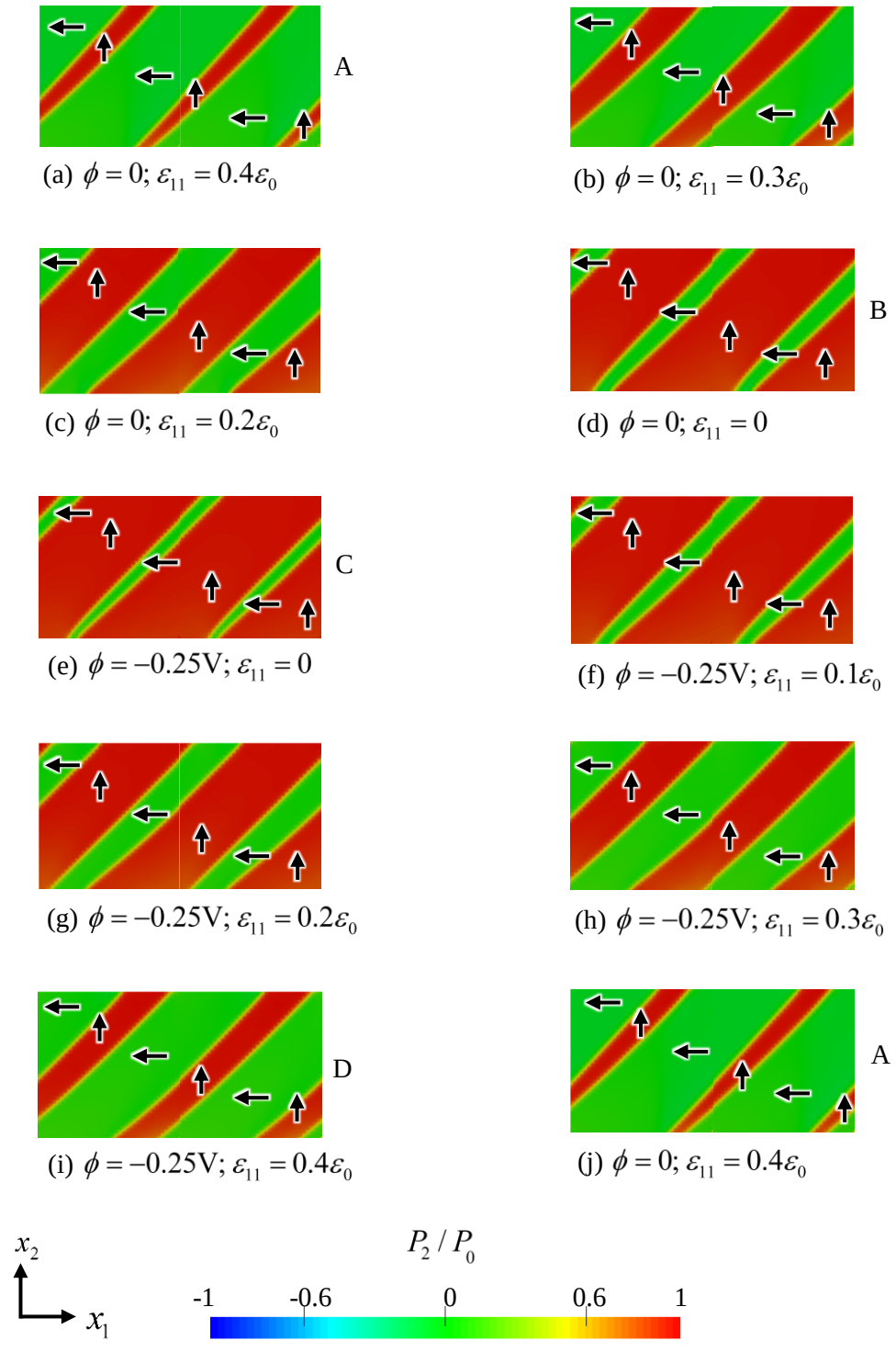

Figure 5.14: Domain patterns illustrating the working cycle of a conceptual energy harvester.

charge per unit area $\sim -0.1P_0$ flows on to the top electrode, and the domains polarized along x_2- axis further increase in size, see Fig. 5.14(d-e). In the subsequent step CD, the voltage on the top electrode is held constant at -0.25V and the substrate is stretched. Here the domains polarized along the direction of applied axial strain increase in size, see Fig. 5.14(f-i) reducing the net charge per unit area on the top electrode to $\sim -0.35P_0$. At point D where $\varepsilon_{11} = 0.4\varepsilon_0$, the substrate strain is held constant and the voltage on the upper electrode is increased to 0V. This causes the net charge per unit area to return to its initial state $\sim -0.2P_0$ and the corresponding change in the domain pattern is shown in Fig. 5.14(i-j). At $\phi = 0; \varepsilon_{11} = 0.4\varepsilon_0$ the energy harvester has returned to its initial state, and the cycle can be repeated. The electrical work done per unit area in this energy harvester cycle is ~ 0.04J/m^2. Table 5.1 describes the sequential steps A-B-C-D in this energy harvester cycle.

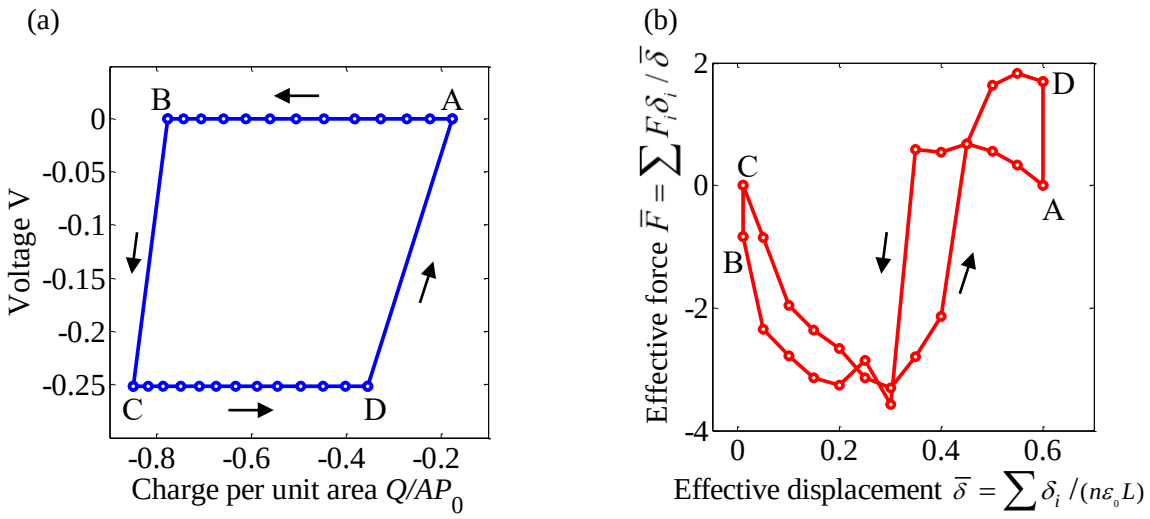

Figure 5.15: Plot of (a) voltage-charge (b) effective force-displacement in the energy harvester cycle shown in Fig. 5.14.

Step	Voltage	Substrate strain	Charge per unit area
AB	Constant at $\phi = 0$	Decreased $\varepsilon_{11} = 0.4\varepsilon_0 \rightarrow 0$	$Q/A = -0.2P_0 \rightarrow -0.8P_0$
BC	Decreased to $\phi = -0.25$V	Constant at $\varepsilon_{11} = 0$	$Q/A = -0.8P_0 \rightarrow -0.9P_0$
CD	Constant at $\phi = -0.25$V	Increased $\varepsilon_{11} = 0 \rightarrow 0.4\varepsilon_0$	$Q/A = -0.9P_0 \rightarrow -0.35P_0$
DA	Increased to $\phi = 0$	Constant at $\varepsilon_{11} = 0.4\varepsilon_0$	$Q/A = -0.35P_0 \rightarrow -0.2P_0$

Table 5.1: Sequential steps in the energy harvester cycle. The steps A-B-C-D correspond to the plots in Fig. 5.15(a-b). Q/A is the net charge per unit area on the top electrode.

An effective force-displacement curve for the energy harvester is plotted in Fig. 5.15(b). Here the effective displacement increment of the substrate nodes, $\bar{\delta}$ is calculated as $\bar{\delta} = \sum \delta_i / (n\varepsilon_0 L)$, where δ_i is the displacement of the *i*th node and *n* is the total number of nodes on the substrate. The effective force at the end of each step in the phase-field simulation is calculated as $\bar{F} = \sum F_i \delta_i / \bar{\delta}$, where F_i is the nodal force value. Hence the mechanical work done in each step is $\bar{F}\Delta\bar{\delta}$; equally, the mechanical work input to the system is the area under the $\bar{F}, \bar{\delta}$ curve. The total mechanical work calculated from the effective force-displacement plot is equal to the electrical work in the voltage-charge curve, and this value is ~0.04J/m^2. On operating the harvester at frequency 1kHz, a power density of ~40W/m^2 could be potentially generated, assuming ideal conditions. Note that the external harvesting circuit in this design is required to carry out voltage switching at a frequency matching the driving oscillations. It is anticipated that the device would be designed with a macroscopic resonance frequency

matching the available mechanical energy source. Such harvesting circuits have been designed for similar applications [177], [178].

A conceptual design of an energy harvester based on a rank-1 domain pattern was demonstrated using phase-field methods. Next the stability of higher rank laminates, namely the rank-2 domain patterns is explored.

5.5 Rank-2 domain patterns

Here, the stability of rank-2 periodic domain patterns is tested under the zero external load conditions. Among the rank-2 laminates identified by Tsou et al. [88], four domain patterns which contain polarization only in a single plane with domain walls perpendicular to that plane are first tested, see Fig. 5.16(a-d). All of the rank-2 domain patterns shown in Fig. 5.16(a-d) are modelled with zero average stress and electric field conditions, described by Eq. (5.1). Here, note that the strain fields ε_{ij} adopted by the periodic cell can vary based on the type of domain pattern imposed in the initial state. The volume average free energy $\tilde{\psi}$, average axial components of strain, $\tilde{\varepsilon}_{ij}$, and polarization, $\tilde{P}_i$, adopted by these domain patterns in their settled states are given in Table 5.2. Each pattern was simulated in a square region of side $L = 40\text{nm}$ using plane strain and electric field conditions.

The herringbone domain pattern “1234” shown in Fig. 5.16(a), is found to be stable at this scale. This domain pattern contains several domain walls in the periodic cell, which accounts for its relatively high free energy in comparison to the rank-1 domain patterns. Stresses in the herringbone domain pattern are developed at the $180°$ domain walls, while non-zero local electric fields are observed at the $90°$ domain walls.

During relaxation the domain walls drifted slightly, resulting in a small magnitude of net polarization ($\sim 0.05P_0$) due to the slightly unequal sizes of the $\pm P_2$ domains at equilibrium.The periodic domain pattern in Fig. 5.16(b) shows laminate "1323" which

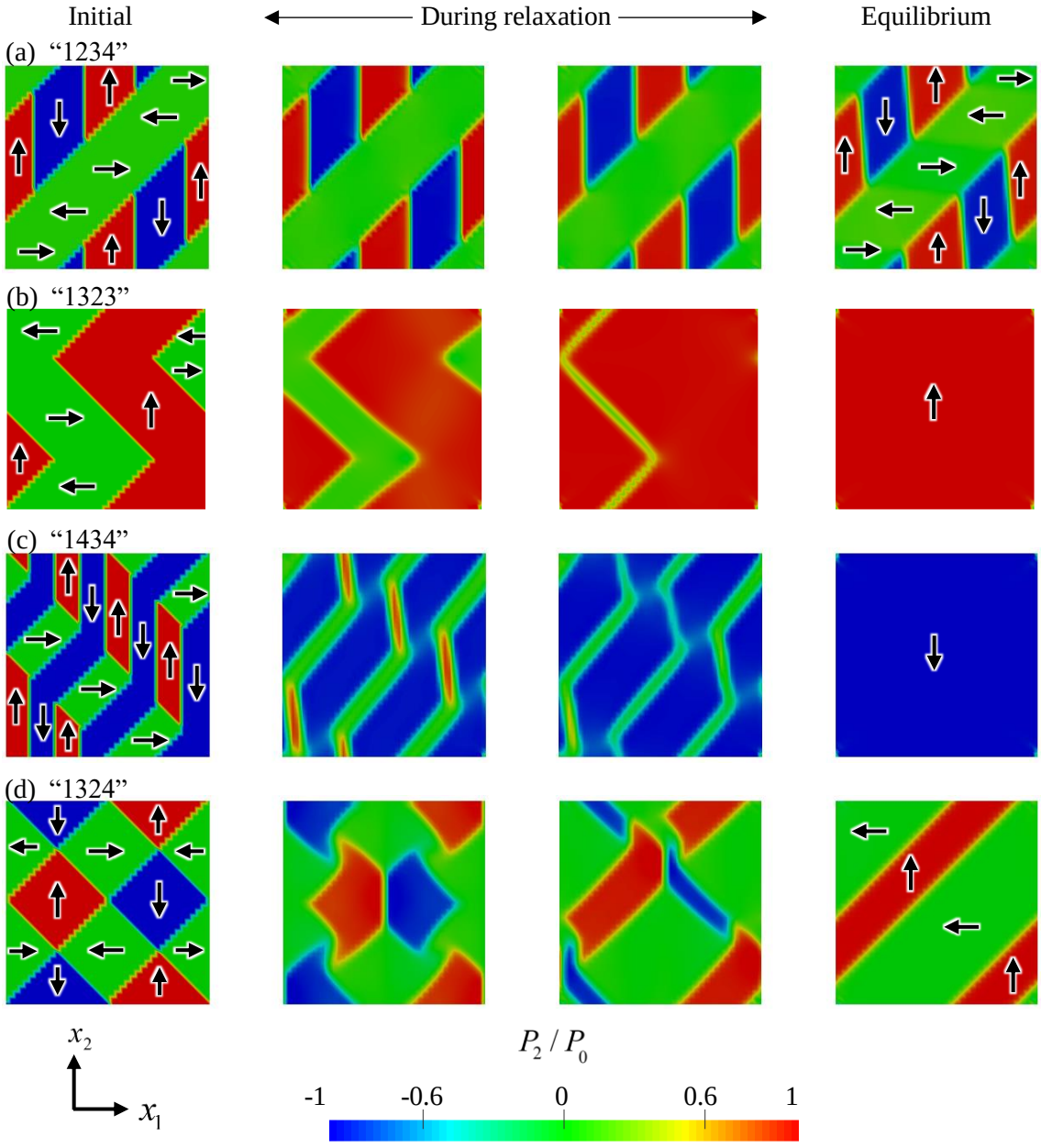

Figure 5.16: Testing the stability of rank-2 domain patterns with in-plane polarizations under zero external load conditions. Laminates: (a) "1234" (b) "1323" (c) "1434" and (d) "1324". Sub-figures map domain rearrangements during relaxation from the initial state (far left) to the final equilibrium state (far right).

contains alternating bands of $\pm P_1$ 180° domains interspersed with a zig-zag stripe which is a single $+P_2$ domain. This domain pattern was identified as a minimum energy state in the linear constrained theory [88] – that is, all domain walls satisfy compatibility conditions. However, at the nanoscale, the pattern is found to be unstable: during relaxation it dissolves to form a uniformly polarized $+P_2$ domain. At the settled state i.e., where domain walls are resolved but the polarization pattern is unchanged, the $\pm P_1$ domains experience a tensile stress σ_{22}, while the P_2 domains experience compressive stress σ_{22}. This is to be expected because the spontaneous strains component ε_{22} differs between the $\pm P_1$ domains (where it is ε_0^t) and the P_2 domains (where it is ε_0). Since these vertical zig-zag stripes are assumed to be perfectly adhered to each other, misfit stress arises from the difference in spontaneous strain. Fig. 5.17 shows the direct stresses σ_{11}, σ_{22} evaluated at a cross-section of the model where $x_2 = L/2$. It is clear that the herringbone pattern (label 'a') has relatively low values of stress throughout, while the tensile and compressive stresses in the alternating bands of the "1323" domain pattern (label 'b') are of order σ_0. This contribution of elastic energy due to misfit stress explains the lack of stability and accounts for the net energy of the domain pattern, see Table 5.2.

An additional factor contributing to the high energy of the "1323" domain pattern is the presence of disclinations at the junctions of domains. These arise because the unstressed condition of a 90° domain wall produces a slight rotation of about 0.63° in the barium titanate crystal lattice. Upon circulating a continuous junction of domains, no net rotation of the crystal lattice is permissible. Consequently the domains are stressed if the set of domain walls at a junction would otherwise produce a net rotation.

Rank – 2 periodic domain pattern	Average free energy	Average strain components $\tilde{\varepsilon}_{ij} = \langle \varepsilon_{ij} \rangle / \varepsilon_0$		Average polarization components $\tilde{P}_i = \langle P_i \rangle / P_0$	
	$\tilde{\psi}$	$\tilde{\varepsilon}_{11}$	$\tilde{\varepsilon}_{22}$	$\tilde{P}_1$	$\tilde{P}_2$
(a) Laminate "1234"	0.49	0.29	0.29	-0.05	0.05
(b) Laminate "1323"	0.48	0.32	0.29	0.47	0.00
(c) Laminate "1434"	0.77	0.06	0.54	0.24	-0.24
(d) Laminate "1324"	0.75	0.28	0.28	0.00	0.00

Table 5.2: The normalized volume average free energy $\tilde{\psi}$, average axial strains $\tilde{\varepsilon}_{ij}$, and polarization $\tilde{P}_i$ adopted by rank-2 periodic domain patterns with in-plane polarization in their settled state.

For example, the domains in the "1234" herringbone pattern are so arranged that there is no net lattice rotation upon circulating any junction: opposite rotations on passing $90°$ domain walls cancel. However, in the "1323" pattern, circulation of a domain junction implies two consecutive lattice rotations of $0.63°$, resulting in a disclination. The domain rearrangement process during relaxation in Fig. 5.16(b), indicates the growth of domains with a larger initial volume fraction, i.e., P_2 domains, in comparison to the $\pm P_1$ domains which reduce in size. The relaxation process eventually eliminates the misfit stresses of the "1323" domain pattern, resulting in a uniformly polarized, stress-free domain at equilibrium.

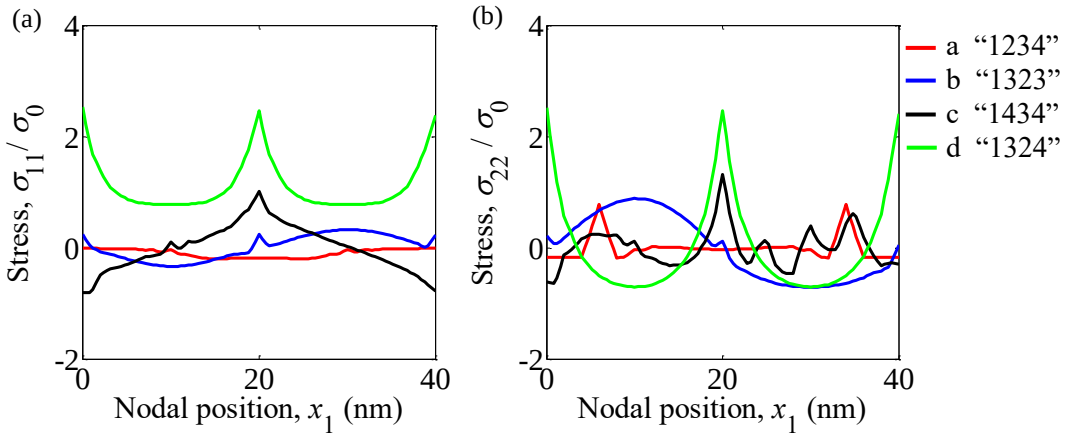

Figure 5.17: Stress distributions in the rank-2 periodic domain patterns with in-plane polarizations: (a) σ_{11} (b) σ_{22} at a cross-section $x_2 = L/2$, at varying x_1 positions.

The domain pattern "1434" shown in Fig. 5.16(c) contains stripe-like and herringbone-like domains. This domain pattern is unstable at the scale simulated $(L = 40\text{nm})$, dissolving into a monodomain. During relaxation, the $-P_2$ domains, which have the largest volume fraction, grow relative to neighbouring domains. Referring to Fig. 5.17, the "1434" pattern has stressed domains which contribute to an increased free energy.

The checkerboard domain pattern "1324" contains repeating groups of 90° domains forming closed polarization loops, or vortices, see Fig. 5.16(d). This pattern too is unstable: it dissolves into a rank-1 stripe domain pattern at equilibrium. As noted by Tsou et al. [88], the checkerboard pattern contains the strongest disclinations among the four in-plane rank-2 domain patterns of Fig. 5.16(a-d), leading to stresses of order $2\sigma_0$, and hence high energy. This can clearly be observed in the stress distributions of Fig. 5.17. During relaxation, the domain junctions dissolve by formation of 180° domain walls. Symmetry breaking occurs and the final state is a rank-1 domain pattern with non-zero average polarization at equilibrium.

Although the herringbone pattern "1234" is well known both at the nano- and micro-scales, the other patterns shown in Fig. 5.16(b-d) have relatively rarely been observed and reported [88], [179]. This is consistent with the phase-field simulations at the nanoscale that indicate instability of these patterns. However, it is of interest to consider how scaling affects the energy density of these patterns. Crudely estimating, the free energy $\int \psi \mathrm{d}V$ can be thought to include a contribution due to gradient energy $\int \psi_{\mathrm{w}} \mathrm{d}V$ and an elastic/dielectric energy part $\int \psi_{\mathrm{e}} \mathrm{d}V$. The gradient energy is mainly due to domain walls and scales with domain wall area. Meanwhile the contributions to the elastic/dielectric energy arise from misfit stress and disclinations, with disclinations being the main factor. For the ith disclination in a given pattern, the energy contribution scales with the square of its disclination angle, θ_i, the elastic modulus, $c \sim 67\mathrm{GPa}$ [180], and the volume V_i of material in proximity to the disclination (taken here to be the set of material points closest to the ith disclination). A rough estimate of the free energy can then be calculated using

$$\int \psi(\mathbf{x}) \mathrm{d}V \sim \int_{A_{90}} \gamma_{90} \mathrm{d}A_{90} + \int_{A_{180}} \gamma_{180} \mathrm{d}A_{180} + \sum_i c\theta_i^2 V_i \,. \tag{5.3}$$

Here $\gamma_{90} \sim 6\mathrm{mJ/m}^2$ and $\gamma_{180} \sim 13\mathrm{mJ/m}^2$ are the 90° and 180° domain wall energies respectively. A_{90} and A_{180} are the corresponding domain wall areas within the periodic cell. Dividing through by the periodic cell volume and using the normalization $\tilde{\psi} = (\psi_0 - \psi)/\psi_0$, the variation of the normalized free energy with scale can be compared for the different patterns, see Fig. 5.18.

At the nanoscale, with $L < 100\mathrm{nm}$, the contributions from gradient energy become significant, increasing the energy of each of the rank-1 and rank-2 domain

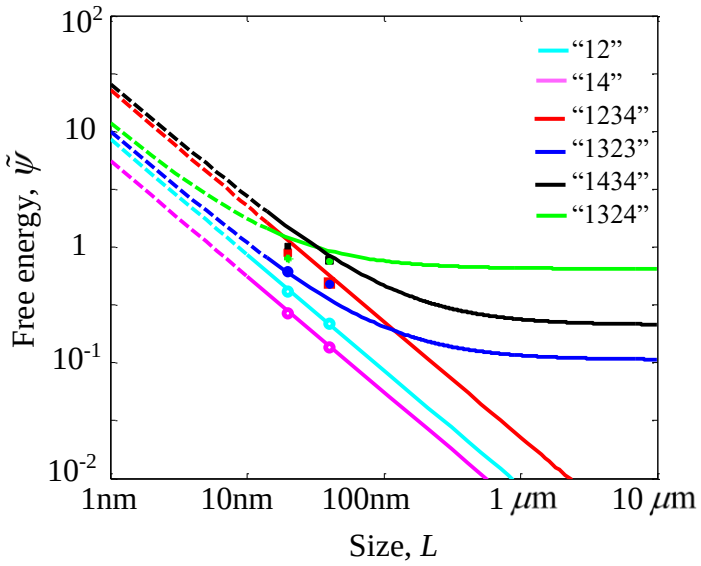

Figure 5.18: Estimates of the variation of free energy for rank-1 and rank-2 domain patterns as a function of periodic cell size, L. Markers indicate the energy calculated for domain patterns in Fig. 5.7(a-d) and Fig. 5.16(a-d) using phase-field simulations.

patterns. Conversely, at the micrometre scale the elastic energy contribution is dominant, and the energy density approaches a constant for the rank-2 domain patterns with non-zero elastic energy. For the herringbone pattern, "1234" and the rank-1 laminates, the domains are almost stress-free and so the gradient energy is the dominant contribution over a wide range of scale: then $\tilde{\psi} \propto L^{-1}$.

The phase field calculations of free energy, carried out at $L = 40\text{nm}$ and 20nm for various laminates are marked in Fig. 5.18. It was not practically feasible to carry out phase field simulations over a wide range of scales because of the computational cost, which increases approximately as L^4. Reducing the scale much below $L = 20\text{nm}$ is also problematic because the spacing between domain walls becomes comparable to the domain wall width – then the domains become unstable as was shown in Fig 5.9. This lower limit of stability is indicated by a transition to dashed lines in Fig. 5.18.

Since the area and volume contributions differ from pattern to pattern, some scale dependent cross-over in energies is expected, as seen in Fig 5.18. However, the energy estimates are not sufficiently precise to quantify the length scales at which cross-over occurs. In any case, it can be seen that the simpler, stress-free rank-1 laminates have lower energy than the rank-2 patterns at all scales. Stability of the laminates under zero external load conditions does not correspond to a global energy minimum, but rather a local minimum or neutral equilibrium state.

Fig. 5.18 provides a qualitative insight into the domain pattern energies. Rank-2 domain patterns which were unstable at the 40nm scale under zero external load conditions reduced their gradient energy and elastic energy contributions by evolving into simpler patterns such as rank-1 stripes, or forming a monodomain. By contrast, the herringbone domain pattern "1234" reached equilibrium although having substantial domain wall energy. Closer examination reveals that this domain pattern is easily dissolved: for example, application of external electric field $E_2 = -0.05E_0 \sim 1\text{MV/m}$ dissolves this domain pattern into a monodomain, see Fig. 5.19.

Next, the stability of three rank-2 domain patterns with out-of-plane polarizations is tested under zero external load conditions as described for a 3D model by Eq. (5.1). In each case the minimum periodic cell size that allows the pattern to be represented with sufficient elements to resolve the domain walls is used. Two of these domain patterns, namely "5556" and "5656", see Fig. 5.20(a, b), have a 2D arrangement of domain walls, but out-of-plane polarizations, parallel to x_3. For these patterns a prismatic plate- like periodic cell is used. The third pattern "1423", see Fig. 5.20(c), has a fully 3D domain wall arrangement, requiring a thicker periodic cell.

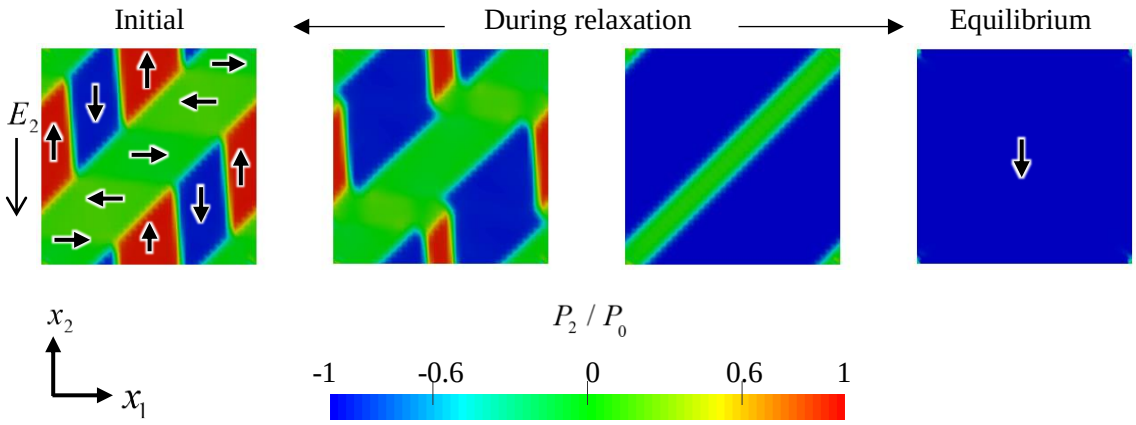

Figure 5.19: Effect of electric field, $E_2 = -1\text{MV/m}$ on the herringbone domain pattern "1234".

The laminate "5556" is initialized with its polarization values on a periodic cell of dimension $16\text{nm} \times 16\text{nm} \times 2\text{nm}$, see Fig. 5.20(a). During relaxation, the 180° domain walls curve to enclose a cylindrical P_3 domain. The radius of this cylindrical domain reduces to zero, leaving a monodomain at equilibrium. The volume average free energy and average axial components of strain and polarization adopted by this domain pattern in the settled state are given in Table 5.3. It is interesting to note that domain patterns similar to the "5556" laminate, though less regular, are observed experimentally [53], [105]. The current phase-field model lacks lattice friction, which is likely to be a factor in stabilising this domain pattern.

For interest, the ability of an external electric field E_3 to hold a cylindrical domain at the nanoscale is tested, such as that formed during the relaxation of pattern "5556", in equilibrium. The simulation is initialized with the "5556" pattern but subject to the boundary condition

$$\phi(x_1, x_2, D) = \phi(x_1, x_2, 0) - E_3 D \,. \tag{5.4}$$

Other boundary conditions are as in Eq. (5.1), giving zero average stress. Eq. (5.4) applies an electric field, E_3 across the thickness D of the 3D model. A cylindrical domain then reaches equilibrium with $E_3 = 4.3\text{MV/m}$ and a radius $r \sim 6\text{nm}$, see Fig. 5.21. The average axial strains in this case are $\tilde{\varepsilon}_{33} = 0.66$ and $\tilde{\varepsilon}_{11} = \tilde{\varepsilon}_{22} = -0.19$, which are of lesser magnitude than the field-free values of Table 5.3, reflecting the depolarizing effect of the electric field. On varying the applied electric field by $\Delta E_3 = \pm 0.20\text{MV/m}$, the pattern dissolves to a monodomain by unstable growth or shrinkage of the cylindrical domain.

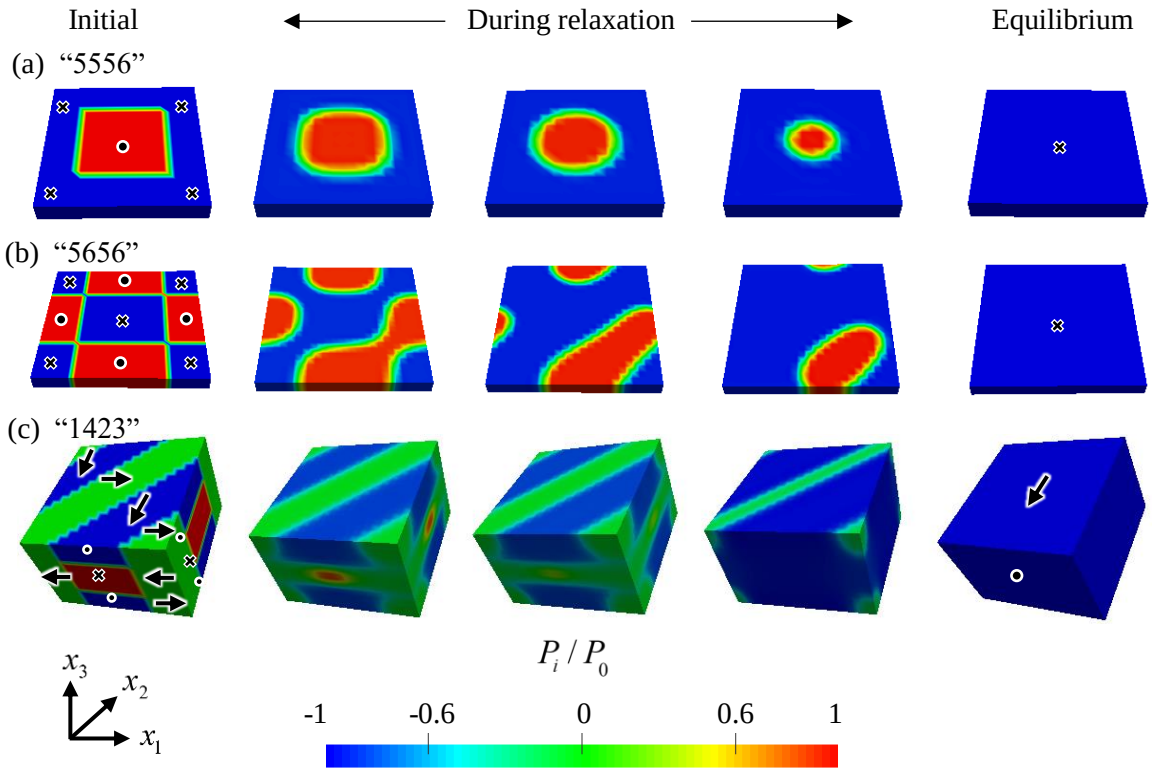

Figure 5.20: Testing the stability of rank-2 domain patterns with out-of-plane polarizations under zero external load conditions. P_3 / P_0 values in (a) laminate "5556" and (b) laminate "5656". P_2 / P_0 values in (c) laminate "1423".

Rank-2 periodic domain pattern	Average free energy	Average strain components $\tilde{\varepsilon}_{ij} = \langle \varepsilon_{ij} \rangle / \varepsilon_0$		Average polarization components $\tilde{P}_i = \langle P_i \rangle / P_0$	
	$\tilde{\psi}$	$\tilde{\varepsilon}_{11} = \tilde{\varepsilon}_{22}$	$\tilde{\varepsilon}_{33}$	$\tilde{P}_1 = \tilde{P}_2$	$\tilde{P}_3$
(a) Laminate "5556"	0.39	-0.26	0.82	0.00	-0.50
(b) Laminate "5656"	0.70	-0.27	0.86	0.00	0.00
(c) Laminate "1423"	0.74	0.24	-0.19	0.00	0.00

Table 5.3: The normalized volume average free energy $\tilde{\psi}$, average axial strains $\tilde{\varepsilon}_{ij}$, and polarization $\tilde{P}_i$ adopted by rank-2 periodic domain patterns with out-of-plane polarization in their settled states.

Attempts were made to find equilibrium states of this pattern at other electric field strengths. In most cases equilibrium could not be found, as expected given the instability of the pattern.

The periodic domain pattern "5656" shown in Fig. 5.20(b) is imposed on a periodic cell of size 24nm×24nm×2nm, with corresponding polarization values in the initial state. This domain pattern also dissolves into a monodomain under zero external load conditions. During relaxation, symmetry is broken and the $180°$ domain walls curve to form loops, each enclosing a P_3 domain. This reduces the domain wall area as discussed by Tagantsev et al. [179]. The eventual collapse to a monodomain is similar to that of the "5556" pattern. Patterns with intersecting $180°$ domain walls, like "5656" are rarely observed [179].

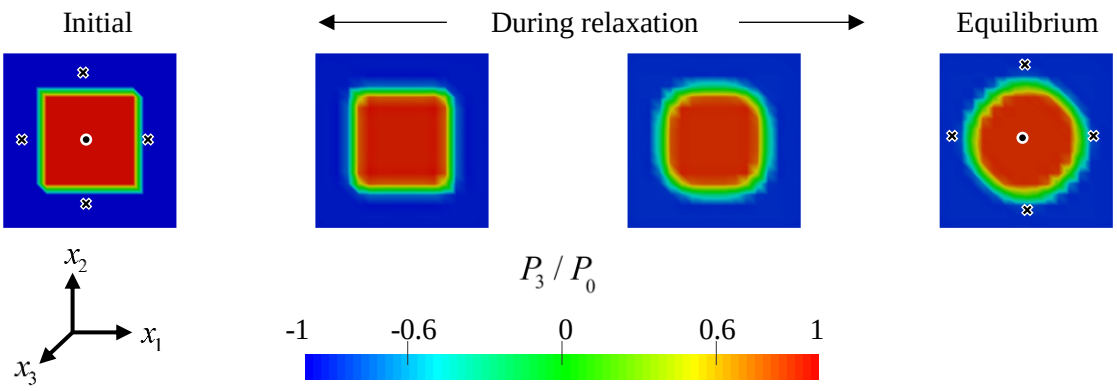

Figure 5.21: Evolution of laminate "5556" under an electric field, $E_3 = 4.3\text{MV/m}$.

The "1423" domain pattern comprises layers of rank-1 stripe domain pattern arranged in a three dimensional configuration as shown in Fig. 5.20(c). This domain pattern is initialized on a periodic cell of size $20\text{nm} \times 20\text{nm} \times 13\text{nm}$. At this scale, the gradient energy contribution is substantial, see Table 5.3; this destabilizes the domain pattern. However, the layered stripe domain pattern is disclination free. It has been observed in experiments [88], [179], and one can expect that this domain pattern could reach equilibrium at a larger length scale. In other work, the pattern was found stable with a 33nm cell size, whose boundaries were constrained to match a fixed strain field [181].

A fourth rank-2 laminate with out-of-plane polarization, "1325" [88] contains domains polarized along all three coordinate axes, and requires a minimum periodic cell size of about 60nm. This pattern is not tested here, due to greater computational power requirements as discussed in section 2.8 of chapter 2, and is the subject of future work.

5.6 Stabilization by external loading

The results in sections 5.3 and 5.5 suggest that, while simple rank-1 laminates are stable at the nanoscale, rank-2 laminates are typically unstable. The exception is the well-known herringbone domain pattern. Are there loading conditions that can stabilize the other patterns? To explore this question, the average of the spontaneous strain in each of the three laminates "1323", "1434" and "1324", found unstable under zero external load conditions is considered at first. Suppose a given pattern contains n domains, numbered $k = 1 \ldots n$, each having a volume fraction f_k and normalized spontaneous strain tensor ε_{ij}^k. Neglecting domain wall volume, the volume average of spontaneous strain in the periodic cell is

$$\bar{\varepsilon}_{ij} = \sum_{k=1}^{n} f_k \varepsilon_{ij}^k \qquad \left(0 \le f_k \le 1, \quad \sum f_k = 1\right). \tag{5.5}$$

In the simulations of section 5.3, the periodic cell under zero load conditions represented by Eq. (5.1), was allowed to adopt any value of average strain in order to minimize energy. The resulting equilibrium states have different domain volume fractions from the initial states and hence the average spontaneous strain changes during relaxation. Next, simulations in which the average strain is fixed at the $\bar{\varepsilon}_{ij}$ value of the initial state are conducted, using the boundary conditions

$$u_1(L, x_2)\big|_R = u_1(0, x_2)\big|_{R_m} + \bar{\varepsilon}_{11} L, \qquad u_2(x_1, L)\big|_S = u_2(x_1, 0)\big|_{S_m} + \bar{\varepsilon}_{22} L \tag{5.6}$$

in place of the corresponding displacement boundary conditions in Eq. (5.1). All other boundary conditions remain unchanged. Eq. (5.6) can be considered as a representation of residual stresses in the material. As before, plane simulations were conducted, enforcing $P_3 = 0$ and fixing $\varepsilon_{33} = \varepsilon_0^{\mathrm{t}}$. The resulting pattern evolution is shown in Fig. 5.22: fixing the average strain stabilizes the "1323" laminate, while "1434" and

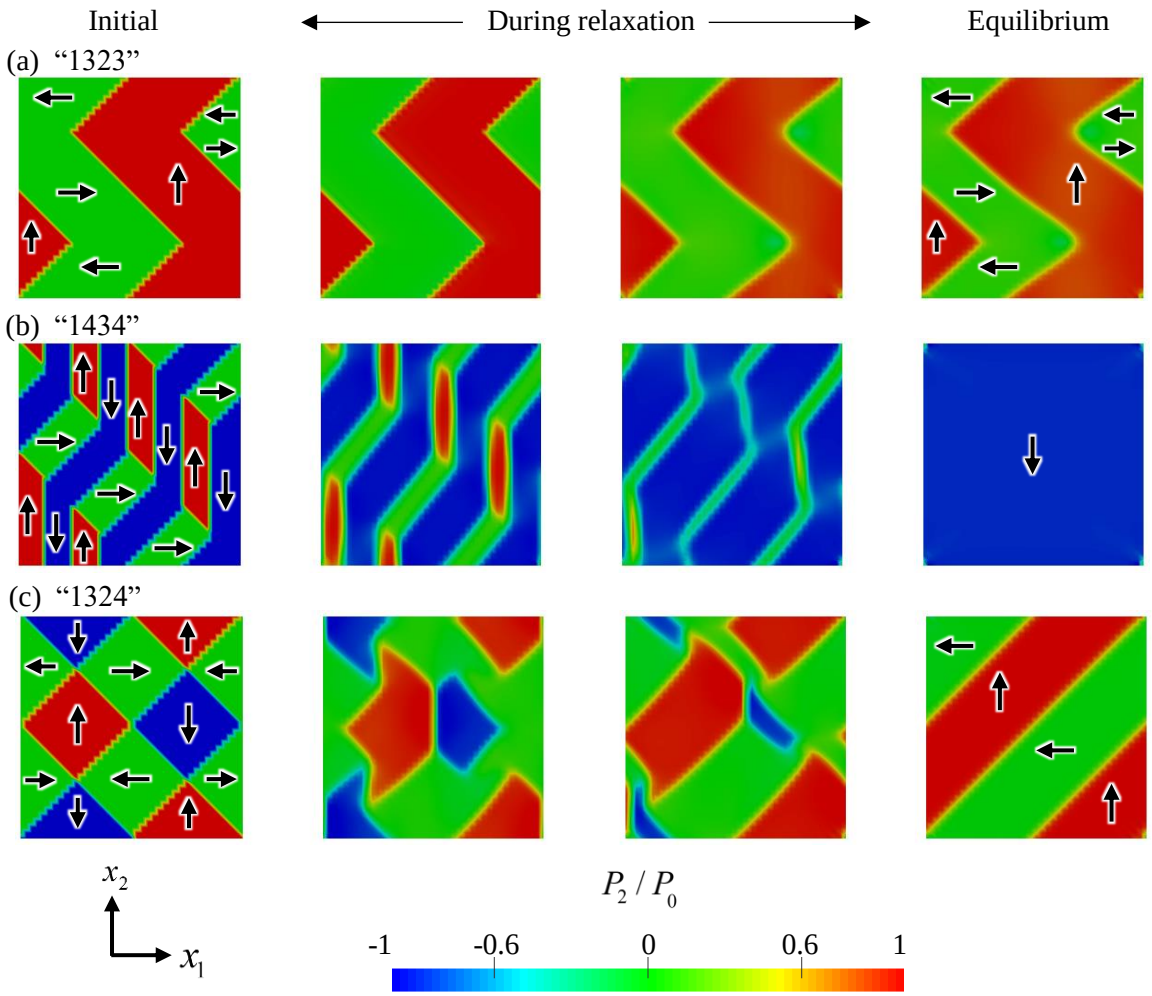

Figure 5.22: Evolution of rank-2 laminates (a) "1323" (b) "1434" (c) "1324", under fixed average strain boundary conditions.

"1324" still collapse into lower energy patterns. In the case of the "1324" pattern, the $90°$ stripe pattern that forms matches the imposed $\bar{\varepsilon}_{ij}$ without stress, while the "1434" collapses to a stressed monodomain.

A further attempt to stabilize the "1434" and "1324" patterns can be made by imposing a fixed average polarization state to match the average spontaneous polarization of the initial state. This discourages the formation of monodomain or simple stripe patterns because they do not match the initial average polarization.

Defining P_i^k as the normalized spontaneous polarization of the *k*th domain and neglecting domain wall volume, the volume average polarization in the periodic cell is

$$\bar{P}_i = \sum_{k=1}^{n} f_k P_i^k \qquad \left(0 \le f_k \le 1, \quad \sum f_k = 1\right). \tag{5.7}$$

This is applied to the periodic cell by replacing the zero average electric field condition in Eq. (5.1) with

$$\begin{aligned} \phi(L, x_2)\big|_R - \phi(L, 0)\big|_B &= \phi(0, x_2)\big|_{R_m} - \phi(0, 0)\big|_A \\ \phi(x_1, L)\big|_S - \phi(0, L)\big|_C &= \phi(x_1, 0)\big|_{S_m} - \phi(0, 0)\big|_A . \end{aligned} \tag{5.8}$$

These boundary conditions allow an arbitrary, but periodic, electric field to be set up in the periodic cell. The magnitude of the net electric field set up, is dependent on the uniform charge density $q = -\bar{P}_i n_i$ (where n_i is the outward surface normal) that is added on all boundary nodes of the periodic cell to enforce the average polarization. The other boundary conditions are as represented by Eq. (5.1). Note that Eq. (5.8) enforces *average polarization only* on the periodic cell, and *does not* bind the polarization values on individual boundary nodes. This allows for the evolution of a new domain pattern in the periodic cell, given its average polarization corresponds to the imposed boundary condition. For example, in the checkerboard pattern "1324", $\bar{P}_i = 0$, and the domain pattern undergoes some pattern change before stabilizing, see Fig. 5.23(a). During relaxation, $180°$ domain walls appear at the $90°$ domain junctions, forming a 'displaced' checkerboard pattern. Similar features at domain junctions have been imaged in $BaTiO_3$ lamellae by McGilly et al. [130]. The simulation in Fig. 5.23(b) indicates that the imposition of an average polarization does stabilize pattern "1434". The simulations with imposed average strain or polarization demonstrate that periodic laminations of domains can be stabilized by external loading:

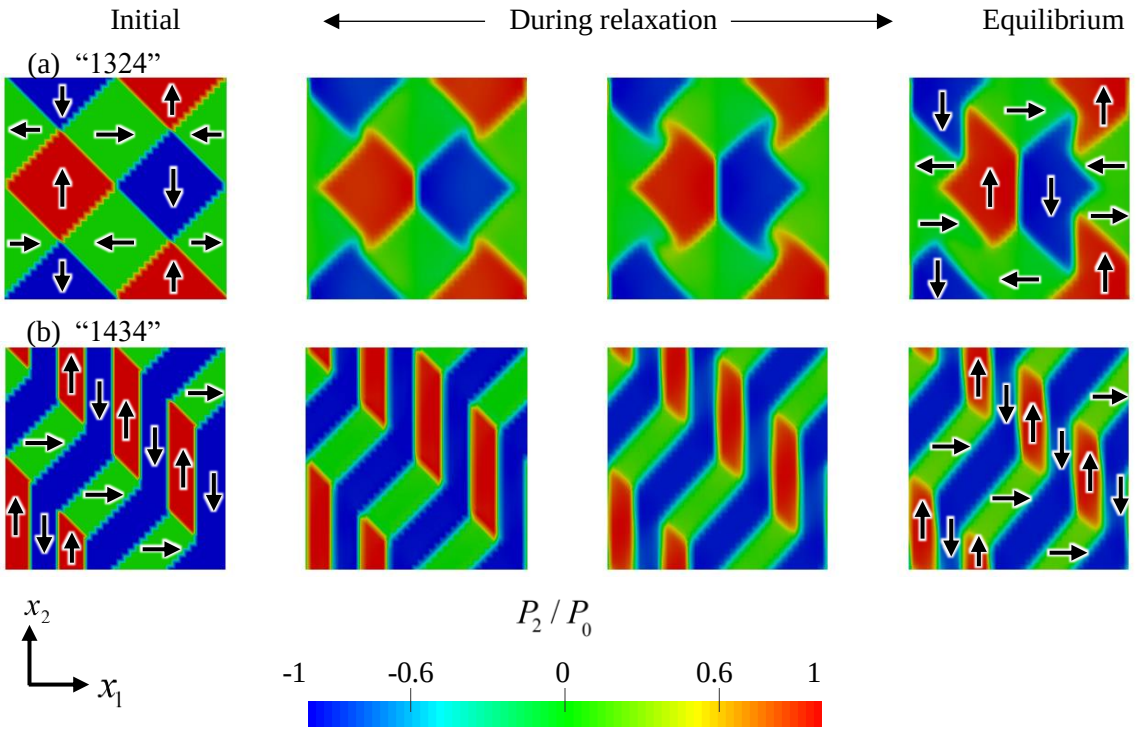

Figure 5.23: Evolution of the rank-2 domain patterns (a) "1324" (b) "1434", under fixed average polarization condition.

if domains form in a region of crystal that is mechanically constrained, or has charged surfaces, nanoscale patterns such as these could form.

It is also of interest to consider whether complicated patterns, such as the rank-2 laminates, could develop under some conditions, from simpler patterns, such as the rank-1 stripes. To explore this, the effect of imposing zero average polarization on rank-1 laminates "14" with $s = 14.1\text{nm}$ and $s = 7.1\text{nm}$ is studied, as shown in Fig. 5.24. The simulations are initialised with the $90°$ stripe domain patterns at equilibrium from Fig. 5.7(c-d). Note that these stripe patterns possess a net polarization field and only $90°$ domain walls. Next, if $\bar{P}_i = 0$ is imposed, some $180°$ domains are expected to form to accommodate the average polarization. In the simulations, during relaxation, the polarization in the domains reduces to near zero and rank-2 laminate patterns begin

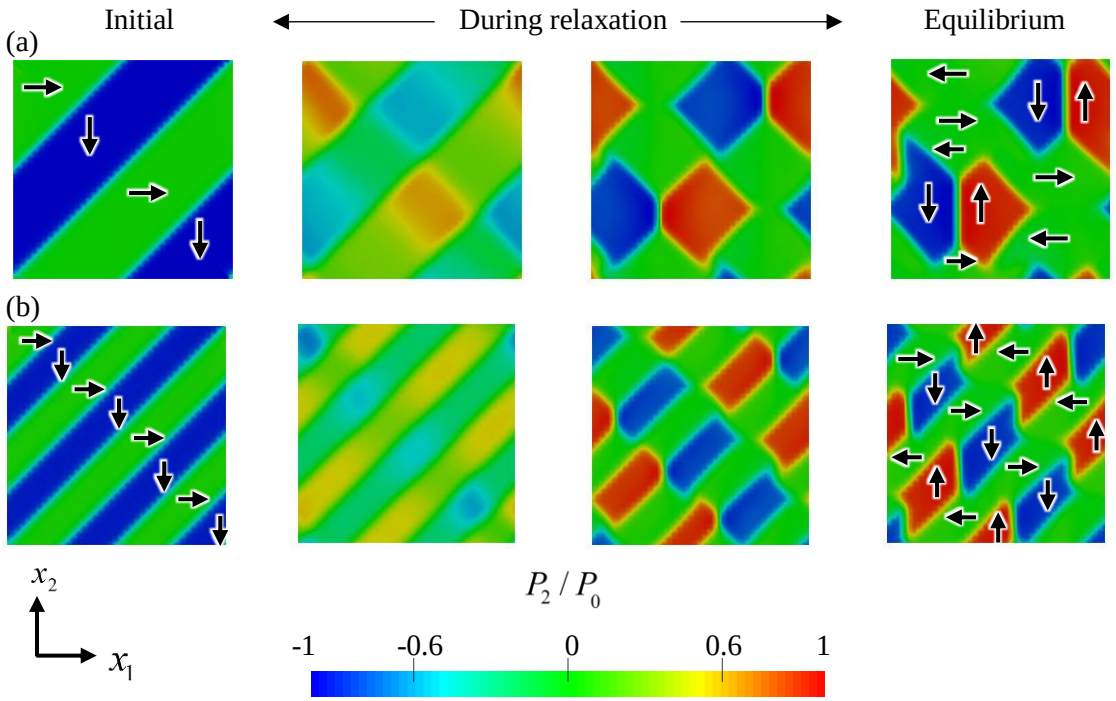

Figure 5.24: Evolution of the rank-1 90° stripe domain pattern under zero average polarization (a) $s = 14.1\text{nm}$ (b) $s = 7.1\text{nm}$.

to evolve. For $s = 14.1\text{nm}$, see Fig. 5.24(a) a 'displaced' checkerboard pattern as seen in Fig. 5.23(a) is found at equilibrium, while with $s = 7.1\text{nm}$, see Fig. 5.24(b) a herringbone domain pattern is stabilised. These simulations indicate potential mechanisms for the formation of rank-2 laminates from rank-1 laminates.

Finally, one example of the effect of electric field on a strain stabilized laminate is illustrated. Taking as initial state the stabilized "1323" laminate from Fig. 5.22(a), additional loading in the form of an electric field of magnitude $0.9E_0 = 20\text{MV/m}$ is applied, and the pattern is relaxed towards a new equilibrium state. Fig. 5.25(a-d) shows the resulting pattern evolution for electric field applied along the $+x_1$, $-x_1$, $+x_2$, and $-x_2$ axes respectively. In Fig. 5.25(a) and (b) the pattern collapses into 90° stripe domains by growing the domain aligned to the applied electric field. In Fig. 5.25(c) the

applied field in the $+x_2$ direction expands the domain polarized in this direction, but the pattern is otherwise unchanged. Fig. 5.25(d) is perhaps the most interesting case in that there is no domain in the initial state that is aligned with the applied electric field. The

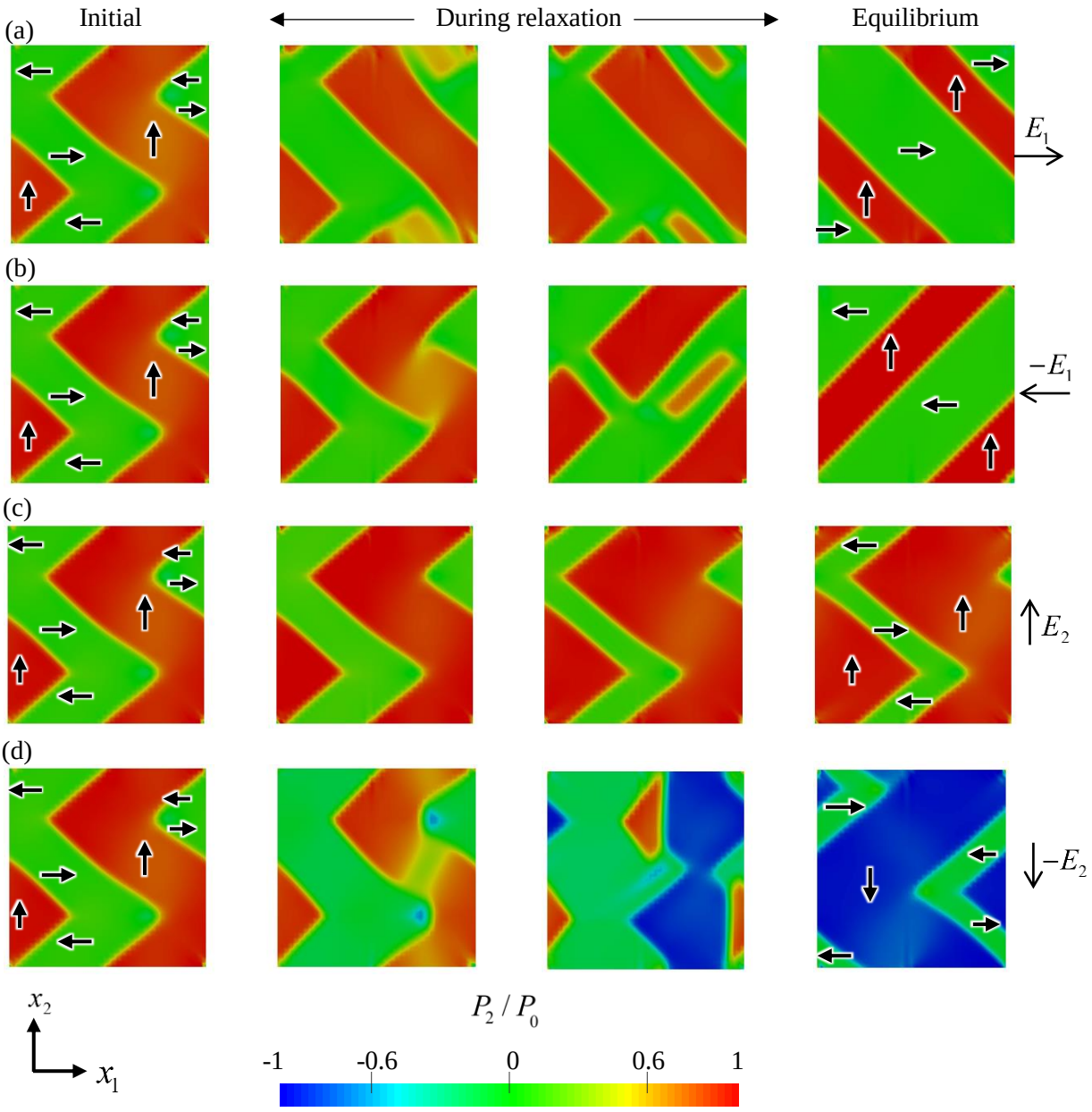

Figure 5.25: Evolution of rank-2 domain pattern "1323" stabilized by average strain and under electric fields (a) $E_1 = 20\text{MV/m}$ (b) $E_1 = -20\text{MV/m}$ (c) $E_2 = 20\text{MV/m}$ (d) $E_2 = -20\text{MV/m}$.

pattern undergoes a transition which produces laminate “1424”, a symmetry related pattern in the same family. From symmetry, the process can be reversed by subsequent application of electric field in the $+x_2$ direction, suggesting a mechanism for cyclic polarization switching at the nanoscale.

5.7 Conclusion

The stability of rank-1 and rank-2 laminates formed in tetragonal ferroelectrics was explored using a phase-field model, taking account of energy contributions from gradient energy and elastic strain energy due to misfit stresses. At the nanoscale and with zero external load conditions, the rank-1 laminates were found to be in neutral equilibrium and their application in a conceptual design of an energy harvester was explored. The more complex rank-2 laminates were on the whole unstable, with the exception of the herringbone domain pattern. Rank-2 domain patterns with multiple domain walls and disclinations were found to possess high energy density at the nanoscale, which destabilized them. The stability of rank-2 domain patterns with out-of-plane polarization was tested using the 3D phase-field model. The effect of scaling the rank-1 and rank-2 laminates was qualitatively discussed. It was found that the unstable rank-2 domain patterns could be equilibrated under external loads such as electric field, average strain or polarization, representative residual states of stresses and electric fields that are commonly present in ferroelectric crystals. Finally, the simulations indicated possible domain evolution paths, showing how rank-2 laminated domain patterns could form from simpler rank-1 domain patterns, and how polarization reversal could occur in nanoscale domain patterns.

6

Conclusions and future work

In this thesis, the Landis phase-field model was used to gain deeper understanding about the polarization patterns formed in nanoscale barium titanate and their behaviour under external loads. The model was also used as a design tool to develop nanoscale ferroelectric device concepts such as actuators and energy harvesters. The finite element code of the Landis phase-field model was extended to solve for three dimensional topologies, and the results provide insights on the formation of domain patterns with out-of-plane polarization. In this chapter, the key results from the current work are discussed and potential further work is explored.

6.1 Conclusions and discussion

The Landis phase-field model was used in chapter 3 as a design tool to develop nano-actuator concepts based on ferroelectric switching. The actuation cycle was demonstrated to be repeatable in three designs of nano-actuators namely the ‘clamped’, the ‘embedded’ and the ‘bending’. The design parameter space of the embedded and bending actuators that can be controlled through manufacturing processes, such as electrode coverage, aspect ratio and substrate strain, were explored to increase achievable displacements. A key result from this work is that actuation strains attained from ferroelectric switching (~0.4%) were several times greater than the actuation

strains offered by piezoceramics (~0.1%) in current market. Greater actuation strains of ~10% were attained in the bending actuator. This work is significant because the use of Landis phase-field model as a 'bottom-up' approach design tool was explored. That is, the model was employed to develop and optimize nano-actuator designs that could serve as an important initial step towards the development of a nano-actuator prototype. The results from this work might be of benefit for the industrial fabrication of nanoscale actuators.

Next, in chapter 4 the phase-field model was employed to explore the elusive nature of vortex polarization patterns in ferroelectrics. Generic configurations of nanowire sections were modelled with flux-closure polarization patterns. The effects of scaling, surface energy, surface conductivity and orientation of the nanowire section on the formation of a vortex polarization pattern were explored. A key result here is that the conditions under which the classic vortex polarization pattern is found to be favourable in barium titanate were identified: size < 35nm, surface energy < 4N/m, insulated boundaries and orientation of the nanowire section along a crystallographic axis. This explains the elusive nature of vortex patterns. The study provides insights on certain aspects of experimental observations in the literature, such as measured tetragonality in nano-particles and the appearance of stripe-like domain patterns. This work is important as the model demonstrates the effect of boundary conditions on the formation of polarization patterns, which could help to engineer domain configurations for device applications. The results serve as an initial step for nanoscale experiments which are driven to find classic vortex patterns in ferroelectrics.

In chapter 5, the Landis phase-field model was used to explore the stability of multi-rank laminates that are predicted to form in tetragonal ferroelectrics by the linear constrained theory. The stability of the rank-1 and rank-2 laminates formed in a

macroscopic crystal and comprising of nanoscale domains was tested by accounting for the energy contributions from polarization gradient and misfit strains. A unit cell of each multi-rank laminate was modelled with periodic boundary conditions and its stability was tested under zero external load conditions. The effects of external strain and electric fields on the behaviour of multi-rank laminates were explored. The study indicates that the simple rank-1 laminates with stripe-like features are stable; they have been widely observed in experiments. The less observed rank-2 laminates, for example patterns with checkerboard-like features, are typically unstable and dissolve into simpler patterns at the nanoscale. The study is significant because it provides useful insights on stabilizing the rank-2 periodic patterns with external loads; demonstrates the effects of scaling; and illustrates a mechanism to convert a simple rank-1 periodic pattern to a complex rank-2 pattern. The results are important to the design of ferroelectric thin films that are applied as energy harvesters.

In this work, the finite element code of the Landis phase-field model was extended to solve for three dimensional (3D) structures. This allowed for exploring the behaviour of domain patterns with out-of-plane polarizations. However, the 3D phase-field simulations were limited due to computational power requirements, as was discussed in section 2.8 of chapter 2. This limits a fair comparison between the phase-field simulations (<60nm) and experimental observations which are typically carried out at length scales of a few hundred nanometers in size. There is a need to adopt a faster approach, which could be based on mesh refining techniques, to reduce the computational time. This is discussed as a potential future work along with the possibility of improving the Landis phase-field model to account for temperature coefficients and surface energy in the next section.

6.2 Future work

The focus of the present work was to employ the Landis phase-field model to gain deeper understanding of nanoscale polarization patterns in barium titanate and their behaviour under external loads. While the model is well-established to describe the constitutive properties of barium titanate (symmetry, non-linear properties and domain wall energetics) at the nanoscale; it could be extended to account for the effects of temperature and surface energy to develop into a powerful and versatile design tool. In this work, the Landis phase-field model was solved using conventional finite element methods which could perhaps be improved using dynamic meshing techniques to reduce the overall computational power requirement. The well-established framework of the Landis phase-field model that solves for the interaction between the coupled fields could also be applied to explore the properties of other materials with similar behaviour (shape memory alloys, relaxors); and to study the phenomena of coupled fields, for example the electrochemical and mechanical properties in lithium ion batteries. This section explores some prospects of further work in developing the Landis phase-field model and considers how to apply these methods to solve critical problems in other materials with similar behaviour.

Design tool

In chapters 2-5, the Landis phase-field model was calibrated for $BaTiO_3$ at room temperature and predicted nanoscale ferroelectric behaviour under isothermal conditions. However, the model could not capture the effect of temperature changes on ferroelectric properties. In chapter 4, the surface energy was demonstrated to have dominant effects on nanoscale ferroelectric properties; but this effect was only crudely

approximated by modelling surface forces on the nanoscale region. Today, many phase-field models have been independently developed to describe the effects of temperature [22], [182], [183], surface energy [30], [143], [184], [185] and flexoelectricity [186]–[188] on polarization patterns in ferroelectrics. However, these models do not capture the anisotropic effects of barium titanate as accurately as the Landis phase-field model. Thus, there is no single phase-field model that is versatile in capturing a range of these effects on nanoscale ferroelectric properties. This is particularly beneficial if the phase-field model is used as a tool to develop 'realistic' nanoscale ferroelectric devices. For example, Whyte and Gregg [189] have developed a ferroelectric diode with saw tooth morphology that allows domain wall movement in only one direction, see Fig. 6.1(a). This device is an example of the recent advancement in 'domain wall electronics' [190], where a phase-field model can be employed as a tool to invent innovative ferroelectric device designs.

Temperature changes can induce partial/complete phase transformation and are typically associated with changes in ferroelectric properties. For example, L.Q. Chen and co-workers [22], [182] demonstrate enhancement in $BaTiO_3$ piezoelectric properties due to stabilization of the monoclinic phase at higher temperatures using phase-field methods [182], see Fig. 6.1(b). However, this phase-field model [182] does not accurately fit the polarization and strain values near the spontaneous states, that are accounted by the $\mathbf{f}$ and $\mathbf{g}$ tensors in Eq. (2.14) in the Landis phase-field model. Thus it is of interest to extend the Landis phase-field model to account for thermal effects. This can be done by the classical approximation [34], [191] of modelling the second order coefficient, $\bar{a}_{ij}$ in Eq. (2.14) as a linear function of temperature, $\bar{a}_{ij} = \bar{a}_{ij}^{0}(T - T_0)$. The linear variation with temperature is assumed because $\bar{a}_{ij}$ is dependent on the

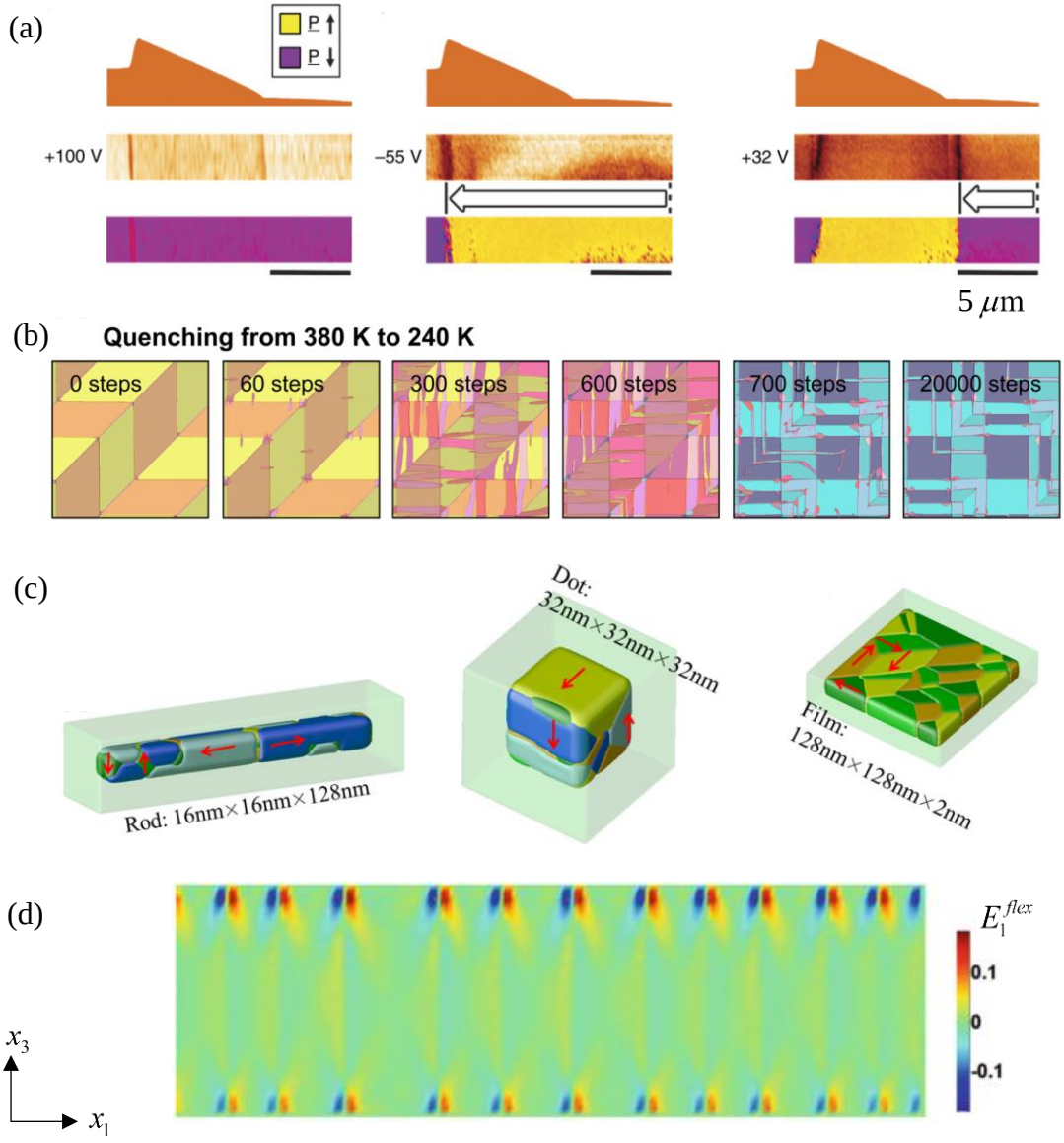

Figure 6.1: (a) The ferroelectric domain-wall diode, image modified from Whyte and Gregg [189] (b) Domain structure evolution between tetragonal to orthorhombic phase in $BaTiO_3$ during temperature cycling. Reprinted from Gu et al. [182]. Copyright 2014 by the American Physical Society. (c) Domain structures in $PbTiO_3$ nanoparticles with different shapes indicating the effects due to surface energy, images reprinted from Wang et al. [144], with permission from Elsevier. (d) Flexoelectric induced electric field in $BaTiO_3$ thin film, image modified from Chen et al. [186]. With permission of Springer.

susceptibility of the material, κ which is experimentally observed to vary linearly with temperature [34]. Alternatively, $\overline{a}_{ij}$ can also be modelled as a hyperbolic cotangent function of temperature [192] to include certain quantum mechanical effects that arise at low temperature ranges [193]. Overall, this task would extend our understanding of the domain structures as a function of temperature, and assist in designing devices such as ultrasound transducers that operate under a wide range of temperatures [194].

Surface energy is known to affect the phase transition temperatures [30], [185], the formation of polarization patterns [143], [144] (see Fig. 6.1(c)), and the tetragonality of ferroelectric crystals at the nanoscale [184], [195]. In the phase-field simulations by Glinchuk et al. [185], surface energy is shown to cause a shift in transition temperature of ferroelectric and ferromagnetic nanoparticles. Likewise, Wang et al. [144] employ a phase-field model to provide useful insights on the effect of surface energy on a temperature-shape phase diagram and domain switching in $PbTiO_3$ nanoparticles. However, these phase-field models [185], [144] are not well calibrated to capture the anisotropic effects in a ferroelectric region, for example the energy contribution from eighth order polarization terms has not been included. Thus, it would be an interesting challenge to extend the Landis phase-field model to account for surface energy effects. Following Wang et al. [144] a compressive stress proportional to the curvature of the nanoparticle surface, ($\sigma \propto -\mu / R$, $\mu =$ surface tension, $R =$ nanoparticle radius) can be introduced in Eq. (2.14). This is similar to modelling the effect of hydrostatic pressure on a sphere. This task could enable the phase-field model to provide useful insights on domain evolution in ferroelectric particles at the nanoscale.

Next, the flexoelectric effect on nanoscale domain patterns in ferroelectrics is discussed. Flexoelectricity is the effect of strain gradients on spontaneous polarization

in a ferroelectric crystal and becomes dominant at the nanoscale ($\sim 10^8 \mathrm{m}^{-1}$) [187], see Fig. 6.1(d). Gu et al. [187] introduce the contribution from the flexoelectric field [186] in the phase-field model and demonstrate its effects on domain wall behaviour, such as polarization rotation at the wall. Introducing this term in the Landis phase-field model could help to engineer domain walls and manipulate their density to tune piezoelectric properties [188].

These tasks of introducing thermal effects, surface energy effects and flexoelectricity in the Landis phase-field model, would enrich the model to develop towards a more powerful and versatile design tool. The model could then be used to explore a wide range of effects on nanoscale ferroelectric behaviour.

Reducing computational time

In the current work, the Landis phase-field model was solved using conventional methods based on finite element simulations. This approach was computationally intensive and simulations of ferroelectric regions with large length scales (>100nm) were limited. Thus, the theoretical simulations and experimental observations (which are typically carried out at large length scales) could not be directly compared. Thus, it is important to reduce the computational time for simulating large ferroelectric regions by phase-field methods. Here, the ideas of adopting dynamic meshing and meshless techniques are discussed; an ‘integrated approach’ where a phase-field model and a micromechanics based model can be used together to describe macroscopic ferroelectric behaviour is explored.

Conventional computational methods based on finite elements are inefficient to deal with large mesh sizes or complex geometries. Alternative methodologies of computing based on meshless techniques have been developed [196], [197] where the

nodes are scattered in the model and are free to move. Here, the nodes typically track the focus of the problem for example in Fig. 6.2(a), the nodes are shown to track the crack growth. Mesh refinement technique is another method where the solver traverses through the grid and estimates the errors due to adding or deleting elements [198], [199]. This technique results in a fine mesh near material inhomogeneities (e.g., in Fig. 6.2(b) mesh with small element sizes is observed closer to the dendrite surface) and in a relatively coarse mesh where the material properties are homogeneous. The use of the meshless or mesh refinement techniques is typically assessed based on the model length scale and has been employed in phase-field modeling of thin shells [197], [198]. Solving the Landis phase-field model using the meshless or mesh refinement techniques could potentially expedite the computations and enable to simulate large length scales of a ferroelectric region. However, care is to be taken in choosing the element size so as to capture the fine domain walls (~2nm) in ferroelectric materials.

The configuration of domains at the microscopic scale is important to the macroscopic behaviour (such as domain switching, hysteresis) in ferroelectrics [159], [160], [200]. However, modelling the effects of domain arrangement on macroscopic ferroelectric behaviour (length scales >100nm) using a phase-field model is a cumbersome process. Here, an idea is to develop an ‘integrated’ approach, which uses a

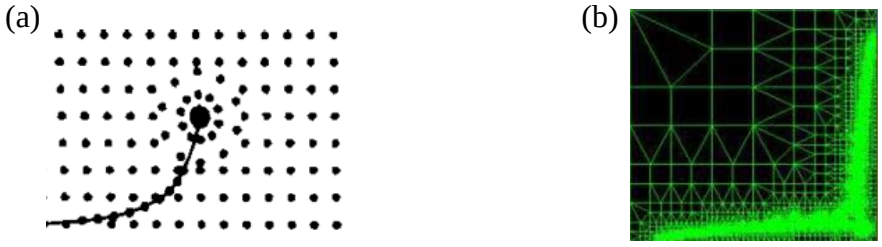

Figure 6.2: (a) Progression of fatigue crack growth modelled using meshless methods, reprinted from Belytschko et al. [196], with permission from Elsevier (b) Dynamic mesh refinement technique around the surface of a dendrite, image from [198].

combination of both the Landis phase-field model and a micromechanics based model (e.g., switching model [66]). That is, the Landis phase-field model could be 'switched on' near material inhomogeneities such as defects/surfaces to accurately solve for stress/electric fields; while ferroelectric regions with homogeneous properties are solved using the micromechanics approach. A challenge here is to model the ferroelectric region where the two theoretical approaches meet. This can be resolved by adopting methods similar to the scale bridging techniques used in the multi-scale modelling approach (a method which predicts material behaviour at different length scales by combining two or more theoretical models). For example, Uetsuji et al. [201] use homogenization theory to describe macroscopic properties such as domain switching in ferroelectrics based on the polarization orientation at the microscopic level. Here, a periodic cell is modelled using phase-field methods to capture the polarization orientation at the microscale. The resulting elastic, electric and electromechanical behaviour is transformed (using an asymptotic homogenization theory) to serve as input parameters for the macroscopic model. This multi-scale modelling method is well established for ferroelectrics [201], [202], and can be used to develop the integrated approach proposed for ferroelectrics. The integrated approach could potentially reduce the computational time required to simulate large ferroelectric regions as the phase-field simulations are carried out only at selected regions in the material and enable a pragmatic material design approach to develop devices at the microscale.

Phase-field model for relaxors and other related applications

The Landis phase-field model serves as a well-established framework that describes the interaction between the electro-mechanical fields in a ferroelectric material. For example, the model relates higher order strain and polarization terms and

accounts for energy contributions from these coupled fields, see Eq. (2.14). This encourages the application of the phase-field method, to explore other materials with similar behaviour such as the relaxors. The method could also be employed to study phenomena such as the coupling between electrochemical and mechanical stress generation in Lithium ion batteries. These potential future works are next discussed.

Relaxors are known to exhibit electromechanical properties that are superior to a ferroelectric crystal [203] resulting in applications in medical ultrasonic transducers [204], [205] and energy harvesters [206], [207]. These materials are similar to ferroelectrics but are characterised by a complex ‘glassy behaviour’ that is known to enhance its dielectric and piezoelectric properties [208]. The glassy behaviour is not completely understood and is associated with the appearance of polar nanoregions in the relaxors. Several atomistic models are developed to study the interaction between individual atoms in a relaxor ferroelectric [209], [210]; however, at present there are very few continuum models [72], [211] that describe the elementary relaxor behaviour. This presents an opportunity to apply the Landis phase-field methods to describe relaxor behaviour. The challenge here is to model the evolution of polar nanoregions as a function of temperature using phase-field methods. The appearance of polar nanoregions could then contribute to understanding the interaction between polarized domains and phase boundary motion in relaxors. The phase-field model could also be used as a design tool to engineer relaxor-ferroelectric composites.

Next, the use of phase-field methods to describe the coupling between electrochemical processes and mechanical properties of electrodes in Lithium ion batteries are discussed. That is, insertion of Lithium into the electrode material induces stresses, which leads to crack growth and an eventual breakdown of the battery [212], [213]. These batteries are important for portable energy storage due to compact design

and light-weight. Thus it is important to study the interaction between the lithium diffusion process and the stress generation in electrodes to design long-life batteries. Phase-field methods have been applied to describe the interaction between the electrochemical processes and the mechanical properties [214], [215], however the models do not capture the coupling fields effectively. For example, Huttin and Kamlah [214] describe the effect of interface energy and elastic energy on the stress generation in electrodes, but the effect of stressed electrodes on lithium diffusion is not captured by the model. Di Leo et al. [215] apply a Cahn-Hilliard-type phase-field theory to phase-separating Li-ion electrode materials, however the coefficients are derived for an isotropic system while several electrode materials used in the current market are highly anisotropic. Developing a phase-field model based on the Landis methods could possibly address the anisotropic issues.

The present work applies the Landis phase-field model to gain deeper understanding on nanoscale ferroelectric properties. The work explores the relatively new concept of designing ferroelectric devices (nano-actuators) based on a ‘bottom-up’ modelling approach. The results from the current work provide interesting insights on the formation of nanoscale polarization patterns such as vortices that helps in developing nanoscale ferroelectric memory devices. The study on periodic polarization patterns explains certain experimental observations of stripe-like patterns in nanoscale ferroelectrics that could be potentially used to develop energy harvester devices. These results could serve as an important initial step for nanoscale experimentation or in the development of a prototype for the proposed device concepts. The present work might benefit the industrial application of ferroelectrics and could encourage research on other active materials. The potential directions of further work are discussed and indicate prospective applications of the Landis phase-field model.

A

Appendix

The phase-field model employed in this thesis has been developed by Landis and co-workers and the details of the model and material properties are found in Refs. [29] and [68] respectively. For the benefit of the readers, a brief description on the Landis phase-field theory and the barium titanate material properties employed in the model are reproduced in the appendix.

A.1 Landis phase-field theory

In this section, the governing equations solved in the Landis phase-field model are listed from Ref. [29]. The mechanical equilibrium equations used are the balances of linear and angular momentum in an arbitrary volume V and the bounding surface S:

$$\begin{aligned} &\sigma_{ji,j} + b_i = \rho \ddot{u}_i && \text{in} && V, \\ &\sigma_{ij} = \sigma_{ji} && \text{in} && V, \\ &\sigma_{ji} n_j = t_i && \text{on} && S, \end{aligned} \tag{A.1.1}$$

where the indicial notations with summation over repeated indices are used to represent the Cartesian components of Cauchy stress σ_{ji}, body force per unit volume b_i, mechanical displacements u_i (note: the double overdot represents a second derivative with respect to time), unit vector normal to a surface element n_j, tractions applied to the

surface t_i. ρ is the mass density and assuming linear kinematics in the model, the strain components ε_{ij} are described in terms of the displacements as:

$$\varepsilon_{ij} = \frac{1}{2}(u_{i,j} + u_{j,i}) \qquad \text{in} \qquad V. \tag{A.1.2}$$

Electrical equilibrium in the model is governed by the quasi-static forms of Maxwell's equations:

$$\begin{aligned} &D_{i,i} - q = 0 && \text{in} && V, \\ &D_i n_i = -\omega && \text{on} && S, \\ &E_i = -\phi_{,i} && \text{in} && V, \end{aligned} \tag{A.1.3}$$

where V is any arbitrary volume and S the bounding surface. D_i is the electric displacement; q and ω are the volume and surface charge densities; E_i is the electric field; and ϕ is the electric potential.

In addition to the electro-mechanical equilibrium equations, Su and Landis [29] introduce a new system of micro-force tensors ($\xi_{ji}, \pi_i, \gamma_i$), which are work conjugates of polarization P_i. For example $\xi_{ji} n_j \dot{P}_i$ represents the power density spent across surfaces by neighboring polarization configurations. While $\pi_i \dot{P}_i$ and $\gamma_i \dot{P}_i$ are the power densities spent internally by the material (e.g., arrangement of atoms in unit cells) and by external sources respectively. Further details on the micro-forces and the derivation of the balance law can be found in Ref. [29]. For equilibrium of the ferroelectric system, the micro-forces lead to a balance law:

$$\xi_{ji} + \pi_i + \gamma_i = 0 \qquad \text{in} \qquad V. \tag{A.1.4}$$

The above equilibrium equations along with the time-dependent Ginzburg Landau equation described in chapter 2, Eq. (2.13) are the governing equations that are solved

in the Landis phase-field model. In the Landis phase-field model the variational statement or the principle of virtual work is given by:

$$\begin{aligned}&\int_V \beta_{ij}\dot{P}_j\delta P_i \ \mathrm{d}V + \int_V \rho\ddot{u}_i\delta u_i \ \mathrm{d}V + \int_V \sigma_{ji}\delta\varepsilon_{ij} - D_i\delta E_i + \eta_i\delta P_i + \xi_{ji}\dot{P}_{i,j} \ \mathrm{d}V \\ &= \int_V b_i\delta u_i - q\delta\phi + \gamma_i\delta P_i \ \mathrm{d}V + \int_S t_i\delta u_i - \omega\delta\phi + \xi_{ji}n_j\delta P_i \ \mathrm{d}S.\end{aligned} \tag{A.1.5}$$

Eq. (A.1.5) serves as a base from which the finite element equations for the model are derived. Further details on the derivation of Eq. (A.1.5) can be found in Ref. [29].

A.2 Material properties

In this section, the co-efficient values of the Helmholtz free energy function, see Eq. (2.14), used in the Landis phase-field model are listed here. The Cartesian form of the Helmholtz free energy expression in Eq. (2.14), is given by Eq. (A.2.1):

$$\begin{aligned}\psi = {} & \frac{a_0}{2}\left(P_{1,1}^2 + P_{2,2}^2 + P_{3,3}^2 + P_{1,2}^2 + P_{2,1}^2 + P_{1,3}^2 + P_{3,1}^2 + P_{2,3}^2 + P_{3,2}^2\right) + \frac{a_1}{2}(P_1^2 + P_2^2 + P_3^2) \\ & + \frac{a_2}{4}(P_1^4 + P_2^4 + P_3^4) + \frac{a_3}{2}(P_1^2P_2^2 + P_2^2P_3^2 + P_1^2P_3^2) + \frac{a_4}{6}(P_1^6 + P_2^6 + P_3^6) + a_6(P_1^4(P_2^2 + P_3^2) \\ & + P_2^4(P_1^2 + P_3^2) + P_3^4(P_1^2 + P_2^2)) + \frac{a_5}{4}(P_1^4P_2^4 + P_2^4P_3^4 + P_1^4P_3^4) - \frac{b_1}{2}(\varepsilon_{11}P_1^2 + \varepsilon_{22}P_2^2 + \varepsilon_{33}P_3^2) \\ & - \frac{b_2}{2}((\varepsilon_{22} + \varepsilon_{33})P_1^2 + (\varepsilon_{11} + \varepsilon_{33})P_2^2 + (\varepsilon_{11} + \varepsilon_{22})P_3^2) - b_3((\varepsilon_{12} + \varepsilon_{21})P_1P_2 + (\varepsilon_{13} + \varepsilon_{31})P_1P_3 \\ & + (\varepsilon_{23} + \varepsilon_{32})P_2P_3) + \frac{c_1}{2}(\varepsilon_{11}^2 + \varepsilon_{22}^2 + \varepsilon_{33}^2) + c_2(\varepsilon_{11}\varepsilon_{22} + \varepsilon_{11}\varepsilon_{33} + \varepsilon_{22}\varepsilon_{33}) + \frac{c_3}{2}(\varepsilon_{12}^2 + \varepsilon_{21}^2 + \varepsilon_{13}^2 \\ & + \varepsilon_{31}^2 + \varepsilon_{23}^2 + \varepsilon_{32}^2) + (\frac{f_1}{2}\varepsilon_{11}^2 + \frac{f_2}{2}(\varepsilon_{22}^2 + \varepsilon_{33}^2) + f_3(\varepsilon_{11}\varepsilon_{22} + \varepsilon_{11}\varepsilon_{33}) + f_4\varepsilon_{22}\varepsilon_{33} + \frac{f_5}{2}(\varepsilon_{12}^2 + \varepsilon_{21}^2 \\ & + \varepsilon_{13}^2 + \varepsilon_{31}^2) + \frac{f_6}{2}(\varepsilon_{23}^2 + \varepsilon_{32}^2))P_1^2 + (\frac{f_1}{2}\varepsilon_{22}^2 + \frac{f_2}{2}(\varepsilon_{11}^2 + \varepsilon_{33}^2) + f_3(\varepsilon_{11}\varepsilon_{22} + \varepsilon_{22}\varepsilon_{33}) + f_4\varepsilon_{11}\varepsilon_{33} \\ & + \frac{f_5}{2}(\varepsilon_{12}^2 + \varepsilon_{21}^2 + \varepsilon_{23}^2 + \varepsilon_{32}^2) + \frac{f_6}{2}(\varepsilon_{13}^2 + \varepsilon_{31}^2))P_2^2 + (\frac{f_1}{2}\varepsilon_{33}^2 + \frac{f_2}{2}(\varepsilon_{11}^2 + \varepsilon_{22}^2) + f_3(\varepsilon_{11}\varepsilon_{33} \\ & + \varepsilon_{22}\varepsilon_{33}) + f_4\varepsilon_{11}\varepsilon_{22} + \frac{f_5}{2}(\varepsilon_{13}^2 + \varepsilon_{31}^2 + \varepsilon_{23}^2 + \varepsilon_{32}^2) + \frac{f_6}{2}(\varepsilon_{12}^2 + \varepsilon_{21}^2))P_3^2 + (\frac{g_1}{4}\varepsilon_{11} + \frac{g_2}{4}(\varepsilon_{22} \\ & + \varepsilon_{33}))P_1^4 + (\frac{g_1}{4}\varepsilon_{22} + \frac{g_2}{4}(\varepsilon_{11} + \varepsilon_{33}))P_2^4 + (\frac{g_1}{4}\varepsilon_{33} + \frac{g_2}{4}(\varepsilon_{11} + \varepsilon_{22}))P_3^4 + \frac{g_3}{4}(\varepsilon_{12} + \varepsilon_{21})(P_1P_2^3 \\ & + P_2P_1^3) + \frac{g_3}{4}(\varepsilon_{13} + \varepsilon_{31})(P_1P_3^3 + P_3P_1^3) + \frac{g_3}{4}(\varepsilon_{23} + \varepsilon_{32})(P_2P_3^3 + P_3P_2^3) + \frac{1}{2\kappa_0}((D_1 - P_1)^2 \\ & + (D_2 - P_2)^2 + (D_3 - P_3)^2)\end{aligned} \tag{A.2.1}$$

The co-efficients in Eq. (A.2.1) are chosen to fit the properties of a mono-domain single crystal $BaTiO_3$, measured by Li et al. [58] at room temperature ($\sim 22°C$). Further details on the experiments conducted by Li et al. can be found in Ref. [58]. In brief, the spontaneous polarization and strains of $BaTiO_3$ polarized along the x_3-axis measured by Li et al. [58] is:

$$\begin{aligned} &P_3^s = 0.26\ \text{C/m}^2,\ P_1^s = P_2^s = 0,\ \varepsilon_{33}^s = 0.0082, \\ &\varepsilon_{11}^s = \varepsilon_{22}^s = -0.0027,\ \varepsilon_{12}^s = \varepsilon_{13}^s = \varepsilon_{23}^s = 0, \end{aligned} \tag{A.2.2}$$

and the elastic, piezoelectric and dielectric properties measured in the same coordinate system are:

$$\begin{aligned} &s_{11}^E = 8.01\times10^{-12}\,\text{m}^2/\text{N},\quad s_{12}^E = -1.57\times10^{-12}\,\text{m}^2/\text{N},\quad s_{13}^E = -4.6\times10^{-12}\,\text{m}^2/\text{N}, \\ &s_{33}^E = 12.8\times10^{-12}\,\text{m}^2/\text{N},\quad s_{44}^E = 17.8\times10^{-12}\,\text{m}^2/\text{N},\quad s_{66}^E = 7.91\times10^{-12}\,\text{m}^2/\text{N}, \\ &d_{33} = 106\times10^{-12}\,\text{C/N},\quad d_{31} = -50\times10^{-12}\,\text{C/N},\quad d_{15} = 580\times10^{-12}\,\text{C/N}, \\ &\kappa_{11}^\sigma = 4100\kappa_0 = 36.3\times10^{-9}\,\text{F/m},\quad \kappa_{33}^\sigma = 160\kappa_0 = 1.42\times10^{-9}\,\text{F/m}, \\ &\kappa_0 = 8.854\times10^{-12}\,\text{F/m},\quad \text{(dielectric permittivity of free space).} \end{aligned} \tag{A.2.3}$$

In order to fit the measured properties of $BaTiO_3$ in Eq. (A.2.2) and Eq. (A.2.3), the co-efficients in Eq. (A.2.1) are chosen as follows:

$$\begin{aligned} &a_1 = -0.668325E_0/P_0,\quad a_2 = -3.80653E_0/P_0^3,\quad a_3 = 0.78922E_0/P_0^3, \\ &a_4 = 12.4421E_0/P_0^5,\quad a_6 = 0.134226E_0/P_0^5, \\ &b_1 = 2.54138E_0/\varepsilon_0P_0,\quad b_2 = 1.74267E_0/\varepsilon_0P_0,\quad b_3 = 0.399353E_0/\varepsilon_0P_0, \\ &c_1 = 2.04999\varepsilon_0/\sigma_0,\quad c_2 = 0.971673\varepsilon_0/\sigma_0,\quad c_3 = 1.27976\varepsilon_0/\sigma_0, \\ &f_1 = 0.663581E_0/\varepsilon_0^2P_0,\ f_2 = 0.841326E_0/\varepsilon_0^2P_0,\ f_3 = -0.170635E_0/\varepsilon_0^2P_0, \\ &f_4 = 0.687281E_0/\varepsilon_0^2P_0,\ f_5 = 0.106647E_0/\varepsilon_0^2P_0,\ f_6 = 0.213294E_0/\varepsilon_0^2P_0, \\ &g_1 = -3.66149E_0/\varepsilon_0^2P_0^3,\ g_2 = 6.27423E_0/\varepsilon_0^2P_0^3,\ g_3 = -1.21644E_0/\varepsilon_0^2P_0^3, \end{aligned} \tag{A.2.4}$$

Where, $P_0 = 0.26\text{C/m}^2$, $\varepsilon_0 = 0.0082$, $E_0 = 2.18247\times10^7\,\text{V/m}$ and $\sigma_0 = 692\times10^6\,\text{N/m}^2$.

Additional details on the co-efficients can be found in Ref. [29] and [68].

References

[1] J. F. Scott, “Applications of modern ferroelectrics,” *Science (80-.).*, vol. 315, pp. 954–9, Feb. 2007.

[2] S. Zhang, F. Li, X. Jiang, J. Kim, and J. Luo, “Advantages and challenges of relaxor-$PbTiO_3$ ferroelectric crystals for electroacoustic transducers – A review,” *Prog. Mater. Sci.*, vol. 68, pp. 1–66, 2015.

[3] C. R. Bowen, H. A. Kim, P. M. Weaver, and S. Dunn, “Piezoelectric and ferroelectric materials and structures for energy harvesting applications,” *Energy Environ. Sci.*, vol. 7, no. 320963, p. 25, 2014.

[4] X. Chen, X. Tang, X. Chen, Y. Chen, X. Guo, H. Ge, and Q. Shen, “Nonvolatile data storage using mechanical force-induced polarization switching in ferroelectric polymer,” *Appl. Phys. Lett.*, vol. 042903, pp. 0–4, 2015.

[5] www.cypress.com, “Datasheet on FM25W256 256Kb SPI F-RAM,” *Cypress Semiconductor Corporation*, 2013.

[6] www.digitimes.com/photogallery, “Ramtron announces 8Mb FeRAM,” *Ramtron International corporation*, 2009.

[7] K. Uchino, “Glory of piezoelectric perovskites,” *Sci. Technol. Adv. Mater.*, vol. 16, no. 4, p. 046001, 2015.

[8] H. D. Espinosa, R. A. Bernal, and M. Minary-Jolandan, “A Review of Mechanical and Electromechanical Properties of Piezoelectric Nanowires,” *Adv. Mater.*, vol. 24, pp. 4656–4675, 2012.

[9] J. Zhang, C. Wang, and C. Bowen, “Piezoelectric effects and electromechanical theories at the nanoscale.,” *Nanoscale*, vol. 6, pp. 13314–27, 2014.

[10] J. Briscoe and S. Dunn, “Piezoelectric nanogenerators – a review of nanostructured piezoelectric energy harvesters,” *Nano Energy*, vol. 14, pp. 15–29, 2015.

[11] A. Koka, Z. Zhou, H. Tang, and H. A. Sodano, “Controlled synthesis of ultra-long vertically aligned $BaTiO_3$ nanowire arrays for sensing and energy harvesting applications,” *Nanotechnology*, vol. 25, p. 375603, 2014.

[12] J. Ryu, A. V. Carazo, K. Uchino, and H. E. Kim, “Magnetoelectric properties in piezoelectric and magnetostrictive laminate composites,” *Jpn. J. Appl. Phys.*, vol. 40, pp. 4948–4951, 2001.

[13] Y. Wang, W. Chen, B. Wang, and Y. Zheng, “Ultrathin Ferroelectric Films: Growth, Characterization, Physics and Applications,” *Materials (Basel).*, vol. 7, pp. 6377–6485, 2014.

[14] www.itrs.net, “Chapter summaries 2013,” *Int. Technol. Roadmap Semicond.*, 2013.

[15] A. Gruverman and A. Kholkin, “Nanoscale ferroelectrics: processing, characterization and future trends,” *Reports Prog. Phys.*, vol. 69, pp. 2443–2474, 2006.

[16] S.-J. Chiu, Y.-T. Liu, H.-Y. Lee, G.-P. Yu, and J.-H. Huang, “Strain enhanced ferroelectric properties of multiferroic $BiFeO_3/SrTiO_3$ superlattice structure prepared by radio frequency magnetron sputtering,” *Thin Solid Films*, vol. 539, pp. 75–80, 2013.

[17] J. Seidel, L. W. Martin, Q. He, Q. Zhan, Y.-H. Chu, A. Rother, M. E. Hawkridge, P. Maksymovych, P. Yu, M. Gajek, N. Balke, S. V Kalinin, S. Gemming, F. Wang, G. Catalan, J. F. Scott, N. A. Spaldin, J. Orenstein, and R. Ramesh, “Conduction at domain walls in oxide multiferroics.,” *Nat. Mater.*, vol. 8, pp. 229–234, 2009.

[18] G. J. Weng and D. T. Wong, “Thermodynamic driving force in ferroelectric crystals with a rank-2 laminated domain pattern, and a study of enhanced electrostriction,” *J. Mech. Phys. Solids*, vol. 57, pp. 571–597, 2009.

[19] L. Van Lich, T. Shimada, K. Nagano, Y. Hongjun, J. Wang, K. Huang, and T. Kitamura, “Anomalous toughening in nanoscale ferroelectrics with polarization vortices,” *Acta Mater.*, vol. 88, pp. 147–155, 2015.

[20] I. I. Naumov, L. Bellaiche, and H. Fu, “Unusual phase transitions in ferroelectric nanodisks and nanorods.,” *Nature*, vol. 432, no. 7018, pp. 737–40, Dec. 2004.

[21] G. J. Weng, “The Prager Medal Lecture: micromechanics and some aspects of phase fields in ferroelectric crystals,” *Acta Mech.*, vol. 225, pp. 979–998, 2014.

[22] L.-Q. Chen, “Phase-Field Method of Phase Transitions/Domain Structures in Ferroelectric Thin Films: A Review,” *J. Am. Ceram. Soc.*, vol. 91, no. 6, pp. 1835–1844, Jun. 2008.

[23] I. Steinbach, “Phase-field models in materials science,” *Model. Simul. Mater. Sci. Eng.*, vol. 17, p. 073001, 2009.

[24] S. C. Hwang and R. M. McMeeking, “A finite element model of ferroelectric polycrystals,” *Ferroelectrics*, vol. 211, pp. 177–194, 1998.

[25] J. E. Huber and N. A. Fleck, “Ferroelectric switching: A micromechanics model versus measured behaviour,” *Eur. J. Mech. A/Solids*, vol. 23, pp. 203–217, 2004.

[26] I. Münch, M. Krauß, C. M. Landis, and J. E. Huber, “Domain engineered ferroelectric energy harvesters on a substrate,” *J. Appl. Phys.*, vol. 109, no. 10, p. 104106, 2011.

[27] I. Münch, M. Krauß, W. Wagner, and M. Kamlah, “Ferroelectric nanogenerators coupled to an electric circuit for energy harvesting,” *Smart Mater. Struct.*, vol. 21, no. 11, p. 115026, Nov. 2012.

[28] W. J. Chen, Y. Zheng, B. Wang, D. C. Ma, and C. M. Wu, “Misfit strain-temperature phase diagrams and domain stability of asymmetric ferroelectric capacitors: Thermodynamic calculation and phase-field simulation,” *J. Appl. Phys.*, vol. 115, p. 094101, 2014.

[29] Y. Su and C. M. Landis, “Continuum thermodynamics of ferroelectric domain evolution: Theory, finite element implementation, and application to domain wall pinning,” *J. Mech. Phys. Solids*, vol. 55, pp. 280–305, Feb. 2007.

[30] A. N. Morozovska, M. D. Glinchuk, and E. A. Eliseev, “Phase transitions induced by confinement of ferroic nanoparticles,” *Phys. Rev. B - Condens. Matter Mater. Phys.*, vol. 76, 2007.

[31] Z. Sun, T. Chen, J. Luo, and M. Hong, “Bis(imidazolium) L-Tartrate: A Hydrogen-Bonded Displacive-Type Molecular Ferroelectric Material,” *Angew. Chemie Int. Ed.*, vol. 51, pp. 3871–3876, 2012.

[32] I. Grinberg, D. V. West, M. Torres, G. Gou, D. M. Stein, L. Wu, G. Chen, E. M. Gallo, A. R. Akbashev, P. K. Davies, J. E. Spanier, and A. M. Rappe, “Perovskite oxides for visible-light-absorbing ferroelectric and photovoltaic materials.,” *Nature*, vol. 503, pp. 509–12, 2013.

[33] J. L. Hutchinson, J. S. Anderson, and C. N. R. Rao, “Electron microscopy of ferroelectric bismuth oxides containing perovskite layers,” *Proc. R. Soc. A Math. Phys. Eng. Sci.*, vol. 355, pp. 301–312, 1977.

[34] A. F. Devonshire, “Theory of barium titanate - Part 1,” *Philos. Mag. J. Sci.*, vol. 40:309, pp. 1040–1063, 1949.

[35] A. F. Devonshire, “Theory of barium titanate - Part II,” *London, Edinburgh, Dublin Philos. Mag. J. Sci.*, vol. 42:333, pp. 1065–1079, 1951.

[36] T. Ogawa and T. Ikegaya, “Elastic constants measured from acoustic wave velocities in barium titanate piezoelectric ceramics,” *Jpn. J. Appl. Phys.*, vol. 54, p. 011501, 2014.

[37] M. Zhang, Z. Guo, R. Tai, H. Luo, K. Namikawa, and J. Cao, “Observation of dual relaxation dynamics of polarization clusters in barium titanate by photon

correlation spectroscopy," *Jpn. J. Appl. Phys.*, vol. 042401, no. 54, p. 042401, 2015.

[38] W. Zhang, Y. Gao, L. Kang, M. Yuan, Q. Yang, H. Cheng, W. Pan, and J. Ouyang, "Space-charge domination epitaxial $BaTiO_3$ heterostructures," *Acta Mater.*, vol. 85, pp. 207–215, 2015.

[39] Y. Tian, Y. Gong, Z. Zhang, and D. Meng, "Phase evolutions and electric properties of $BaTiO_3$ ceramics by a low-temperature sintering process," *J. Mater. Sci. Mater. Electron.*, vol. 25, pp. 5467–5474, 2014.

[40] M. Sendova, B. D. Hosterman, R. Raud, T. Hartmann, and D. Koury, "Temperature-dependent, micro-Raman spectroscopic study of barium titanate nanoparticles," *J. Raman Spectrosc.*, vol. 46, no. August 2014, pp. 25–31, 2015.

[41] J. Hlinka and P. Márton, "Phenomenological model of a 90° domain wall in $BaTiO_3$-type ferroelectrics," *Phys. Rev. B*, vol. 74, pp. 104104–1–12, 2006.

[42] K. Dayal and K. Bhattacharya, "A real-space non-local phase-field model of ferroelectric domain patterns in complex geometries," *Acta Mater.*, vol. 55, pp. 1907–1917, 2007.

[43] I. Münch and J. E. Huber, "A hexadomain vortex in tetragonal ferroelectrics," *Appl. Phys. Lett.*, vol. 95, p. 022913, 2009.

[44] A. Koka and H. A. Sodano, "Energy harvesting from arrays of long barium titanate nanowires," in *Proceedings of the ASME SMASIS 2013 conference*, 2013.

[45] E. Burcsu, G. Ravichandran, and K. Bhattacharya, "Large electrostrictive actuation of barium titanate single crystals," *J. Mech. Phys. Solids*, vol. 52, no. 4, pp. 823–846, Apr. 2004.

[46] Y. H. Hu, H. M. Chan, Z. X. Wen, and M. P. Harmer, "Scanning electron microscopy and transmission electron microscopy study of ferroelectric domains in doped $BaTiO_3$," *J. Am. Ceram. Soc.*, vol. 69, no. 8, pp. 594–602, 1986.

[47] S. Y. Cheng, N. J. Ho, and H. Y. Lu, "Transformation-induced twinning: The 90° and 180° ferroelectric domains in tetragonal barium titanate," *J. Am. Ceram. Soc.*, vol. 89, no. 7, pp. 2177–2187, 2006.

[48] Y. W. Li and F. X. Li, "The effect of multi-rank domain pattern on the polarization response of $BaTiO_3$ crystal during electric field loading," *J. Appl. Phys.*, vol. 117, p. 244101, 2015.

[49] J. Wang, W. Shu, T. Shimada, T. Kitamura, and T. Y. Zhang, "Role of grain orientation distribution in the ferroelectric and ferroelastic domain switching of ferroelectric polycrystals," *Acta Mater.*, vol. 61, no. 16, pp. 6037–6049, 2013.

[50] N. Liu, Y. Su, and G. J. Weng, “A phase-field study on the hysteresis behaviors and domain patterns of nanocrystalline ferroelectric polycrystals,” *J. Appl. Phys.*, vol. 113, no. 2013, 2013.

[51] J. Li, C. Lei, L. Li, Y. Shu, and Y. Liu, “Unconventional phase field simulations of transforming materials with evolving microstructures,” *Acta Mech. Sin.*, vol. 28, pp. 915–927, 2012.

[52] G. Arlt and P. Sasko, “Domain configuration and equilibrium size of domains in $BaTiO_3$ ceramics,” *J. Appl. Phys.*, vol. 51, pp. 4956–4960, 1980.

[53] J. A. Hooton and W. J. Merz, “Etch patterns and ferroelectric domains in $BaTiO_3$ single crystals,” *Phys. Rev.*, vol. 98, no. 2, pp. 409–413, 1955.

[54] M. E. Lines and A. M. Glass, *Principles and applications of ferroelectrics and related materials*, pp. 59–81, 1977

[55] H. Koike, T. Otsuki, T. Kimura, M. Fukuma, Y. Hayashi, Y. Maejima, K. Amantuma, N. Tanabe, T. Masuki, S. Saito, T. Takeuchi, S. Kobayashi, T. Kunio, T. Hase, Y. Miyasaka, N. Shohata, and M. Takada, “A 60-ns 1-Mb nonvolatile ferroelectric memory with a nondriven cell plate line write/read scheme,” *IEEE J. Solid-State Circuits*, vol. 31, pp. 1625–1634, 1996.

[56] P. Chandra and P. B. Littlewood, “A Landau primer for ferroelectrics,” in *Physics of ferroelectrics*, pp. 69–116, 2007.

[57] D. Ter Haar, *Collected papers of LD Landau*. 2013.

[58] Z. Li, S. Chan, M. H. Grimsditch, and E. S. Zouboulisa, “The elastic and electromechanical single crystals properties of tetragonal $BaTiO_3$ single crystals,” *J. Appl. Phys.*, vol. 70, pp. 7327–7332, 1991.

[59] A. F. Devonshire, “Theory of ferroelectrics,” *Adv. Phys.*, vol. 3, pp. 85–130, 1954.

[60] S. C. Hwang and R. M. Mcmeeking, “The prediction of switching in polycrystalline ferroelectric ceramics,” *Ferroelectrics*, vol. 207, pp. 465–495, 1998.

[61] J. E. Huber, N. A. Fleck, C. M. Landis, and R. M. Mcmeeking, “A constitutive model for ferroelectric polycrystals,” *1Journal Mech. Phys. Solids*, vol. 47, pp. 1663–1697, 1999.

[62] C. Miehe, D. Rosato, and B. Kiefer, “Variational Principles in Dissipative Electro-Magneto-Mechanics: A Framework for the Macro-Modeling of Functional Materials,” *Intl. J. Numerical Methods in Engineering*, vol. 86, no. 10, pp. 1225–1276, 2011.

[63] S. C. Hwang, C. S. Lynch, and R. M. McMeeking, “Ferro Electric/Ferroelastic Interactions and a Polarization Switching Model,” *Acta Metall. Mater.*, vol. 43, no. 5, pp. 2073–2084, 1995.

[64] J. E. Huber and N. A. Fleck, “Multi-axial electrical switching of a ferroelectric: theory versus experiment,” *J. Mech. Phys. Solids*, vol. 49, pp. 785–811, 2001.

[65] J. Y. Li and D. Liu, “On ferroelectric crystals with engineered domain configurations,” *J. Mech. Phys. Solids*, vol. 52, pp. 1719–1742, 2004.

[66] J. E. Huber, “Micromechanical modelling of ferroelectrics,” *Curr. Opin. Solid State Mater. Sci.*, vol. 9, no. 3, pp. 100–106, Jun. 2005.

[67] C. M. Landis, “Non-linear constitutive modeling of ferroelectrics,” *Curr. Opin. Solid State Mater. Sci.*, vol. 8, no. 1, pp. 59–69, Jan. 2004.

[68] A. Kontsos and C. M. Landis, “Phase-Field Modeling of Domain Structure Energetics and Evolution in Ferroelectric Thin Films,” *J. Appl. Mech.*, vol. 77, p. 041014, 2010.

[69] R. Ahluwalia, A. K. Tagantsev, P. Yudin, N. Setter, N. Ng, and D. J. Srolovitz, “Influence of flexoelectric coupling on domain patterns in ferroelectrics,” *Phys. Rev. B*, vol. 89, p. 174105, 2014.

[70] Y. C. Shu and K. Bhattacharya, “Domain patterns and macroscopic behaviour of ferroelectric materials,” *Phil. Mag. B* vol. 81, no. 12. 2001, pp. 2021–2054.

[71] C. M. Wu, W. J. Chen, Y. Zheng, D. C. Ma, B. Wang, J. Y. Liu, and C. H. Woo, “Controllability of vortex domain structure in ferroelectric nanodot: fruitful domain patterns and transformation paths.,” *Sci. Rep.*, vol. 4, p. 3946, Jan. 2014.

[72] Y.-B. Ma, K. Albe, and B.-X. Xu, “Lattice-based Monte Carlo simulations of the electrocaloric effect in ferroelectrics and relaxor ferroelectrics,” *Phys. Rev. B*, vol. 91, pp. 1–13, 2015.

[73] B. Li, X. Liu, F. Fang, J. Zhu, and J.-M. Liu, “Monte Carlo simulation of ferroelectric domain growth,” *Phys. Rev. B*, vol. 73, pp. 1–7, 2006.

[74] F. Xue, X. S. Gao, and J.-M. Liu, “Monte Carlo simulation on the size effect in ferroelectric nanostructures,” *J. Appl. Phys.*, vol. 106, no. 11, p. 114103, 2009.

[75] A. Kontsos and C. M. Landis, “Computational modeling of domain wall interactions with dislocations in ferroelectric crystals,” *Int. J. Solids Struct.*, vol. 46, pp. 1491–1498, Mar. 2009.

[76] S. Prosandeev, D. Wang, A. R. Akbarzadeh, and L. Bellaiche, “First-principles-based effective Hamiltonian simulations of bulks and films made of lead-free $Ba(Zr,Ti)O_3$ relaxor ferroelectrics,” *J. Phys. Condens. Matter*, vol. 27, p. 223202, 2015.

[77] U. V Waghmare, “First-principles theory, coarse-grained models, and simulations of ferroelectrics.,” *Acc. Chem. Res.*, vol. 47, pp. 3242–9, 2014.

[78] R. P. Feynman, “Forces in molecules,” *Phys. Rev.*, vol. 56, pp. 340–343, 1939.

[79] P. Umari and A. Pasquarello, “Ab initio molecular dynamics in a finite homogeneous electric field.,” *Phys. Rev. Lett.*, vol. 89, no. 2, p. 157602, 2002.

[80] B. B. Van Aken, T. T. M. Palstra, A. Filippetti, and N. A. Spaldin, “The origin of ferroelectricity in magnetoelectric $YMnO_3$.,” *Nat. Mater.*, vol. 3, no. March, pp. 164–170, 2004.

[81] A. Renuka Balakrishna and J. E. Huber, “Working principle of a nano-actuator based on ferroelectric switching,” in *ECCOMAS Conference on Smart Structures and Materials*, pp. 24–26, 2013.

[82] A. Renuka Balakrishna and J. E. Huber, “Design Optimization of a Ferroelectric Nano-Actuator Using Phase-Field Modeling,” *MRS Proc.*, vol. 1674, 2014.

[83] A. Renuka Balakrishna, J. E. Huber, and C. M. Landis, “Nano-actuator concepts based on ferroelectric switching,” *Smart Mater. Struct.*, vol. 23, no. 8, p. 085016, Aug. 2014.

[84] A. Renuka Balakrishna and J. E. Huber, “Scale effects and the formation of polarization vortices in tetragonal ferroelectrics,” *Appl. Phys. Lett.*, vol. 106, p. 092906, 2015.

[85] A. Renuka Balakrishna, I. Muench, and J. E. Huber, “Study of periodic domain patterns in tetragonal ferroelectrics using phase-field methods,” in *Proceedings of the ASME SMASIS 2015 conference*, pp. 1–6, 2015.

[86] A. Renuka Balakrishna, J. E. Huber, and I. Muench, “Periodic domain patterns in tetragonal ferroelectrics at the nanoscale - a phase-field study,” *Phys. Rev. B*, under review, 2016.

[87] A. Renuka Balakrishna and J. E. Huber, “Nanoscale domain patterns and a concept for an energy harvester,” *Smart Mater. Struct.*, under review, 2016.

[88] N. T. Tsou, P. R. Potnis, and J. E. Huber, “Classification of laminate domain patterns in ferroelectrics,” *Phys. Rev. B - Condens. Matter Mater. Phys.*, vol. 83, no. 184120, pp. 1–6, 2011.

[89] D. Schrade, R. Mueller, B.X. Xu, and D. Gross, “Domain Evolution in Ferroelectric Materials: A Continuum Phase Field Model and Finite Element Implementation,” *Comp. Methods in Appl. Mech. Engn.*, vol. 196, pp. 4365–437, 2007.

[90] W. Cao and L. E. Cross, “Theory of tetragonal twin structures in ferroelctric perovskites with a first-order phase transition,” *Phys. Rev. B*, vol. 44, no. 1, pp. 5–12, 1991.

[91] W. Li and C.M. Landis, “Nucleation and growth of domains near crack tips in single crystal ferroeelctrics,” *Engineering Frac. Mech.*, vol. 78, pp. 1505–1513, 2011.

[92] A. Abdollahi and I. Arias, “Phase-field modeling of the coupled microstructure and fracture evolution in ferroelectric single crystals,” *Acta Mat.*, vol. 59, pp. 4733–4746, 2011.

[93] B. Völker, P. Marton, C. Elsässer, and M. Kamlah, “Multiscale modeling for ferroelectric materials: a transition from the atomic level to phase-field modeling,” *Continuum Mech. Thermodyn.*, vol. 23, pp. 435–451, 2011.

[94] W. Zhang and K. Bhattacharya, “A computational model of ferroelectric domains. Part I: Model formulation and domain switching,” *Acta Mater.*, vol. 53, pp. 185–198, 2005.

[95] Z. Li, S. K. Chan, M. H. Grimsditch, and E. S. Zouboulis, “The elastic and electromechanical properties of tetragonal $BaTiO_3$ single crystals,” *J. Appl. Phys.*, vol. 70, pp. 7327–7332, 1991.

[96] R. Ahluwalia and W. Cao, “Influence of dipolar defects on switching behavior in ferroelectrics,” *Phys. Rev. B*, vol. 63, p. 012103, 2000.

[97] C. S. Ganpule, V. Nagarajan, S. B. Ogale, A. L. Roytburd, E. D. Williams, and R. Ramesh, “Domain nucleation and relaxation kinetics in ferroelectric thin films,” *Appl. Phys. Lett.*, vol. 77, p. 3275, 2000.

[98] D. Berlincourt and H. Jaffe, “Elastic and Piezoelectric Coefficients of Single-Crystal Barium Titanate,” *Phys. Rev.*, vol. 111, no. 1, pp. 143–148, 1958.

[99] C. H. Ahn, K. M. Rabe, and J.-M. Triscone, “Ferroelectricity at the nanoscale: local polarization in oxide thin films and heterostructures,” *Science*, vol. 303, pp. 488–491, 2004.

[100] M. Dawber, P. Chandra, P. B. Littlewood, and J. F. Scott, “Depolarization corrections to the coercive field in thin-film ferroelectrics,” *J. Phys. Condens. Matter*, vol. 15, pp. L393–L398, 2003.

[101] J. Padilla, W. Zhong, and D. Vanderbilt, “First-principles investigation of 180° domain walls in $BaTiO_3$,” *Phys. Rev. B*, vol. 53, no. 10, pp. 5969–5973, 1996.

[102] J. M. Gregg, “Exotic Domain States in Ferroelectrics: Searching for Vortices and Skyrmions,” *Ferroelectrics*, vol. 433, no. 1, pp. 74–87, Jan. 2012.

[103] T. Shinjo, T. Okuno, R. Hassdorf, K. Shigeto, and T. Ono, "Magnetic Vortex Core Observation in Circular Dots of Permalloy," *Science (80-.).*, vol. 289, no. 5481, pp. 930–932, Aug. 2000.

[104] J. Raabe, R. Pulwey, R. Sattler, T. Schweinböck, J. Zweck, and D. Weiss, "Magnetization pattern of ferromagnetic nanodisks," *J. Appl. Phys.*, vol. 88, no. 7, p. 4437, 2000.

[105] V. Grubsky, S. MacCormack, and J. Feinberg, "All-optical three-dimensional mapping of 180° domains hidden in a $BaTiO_3$ crystal," *Opt. Lett.*, vol. 21, no. 1, pp. 6–8, 1996.

[106] O. C. Zeinkiewicz and R. L. Taylor, "The finite element method," *London: McGraw-Hill*, vol. 3, 1977.

[107] A. Richards, "University of Oxford Advanced Research Computing," *Zenodo.10.5281/zenodo.22558*, 2015.

[108] N. J. Conway, Z. J. Traina, and S.-G. Kim, "A strain amplifying piezoelectric MEMS actuator," *J. Micromechanics Microengineering*, vol. 17, no. 4, pp. 781–787, Apr. 2007.

[109] M. Pozzi and T. King, "Piezoelectric actuators in micropositioning," *Eng. Sci. Educ. J.*, no. February, pp. 31–36, 2001.

[110] H. Iwai, "Roadmap for 22nm and beyond," *Microelectron. Eng.*, vol. 86, no. 7–9, pp. 1520–1528, Jul. 2009.

[111] J. Wang, "Switching mechanism of polarization vortex in single-crystal ferroelectric nanodots," *Appl. Phys. Lett.*, vol. 97, no. 19, p. 192901, 2010.

[112] W. J. Chen, Y. Zheng, and B. Wang, "Phase field simulations of stress controlling the vortex domain structures in ferroelectric nanosheets," *Appl. Phys. Lett.*, vol. 100, no. 6, p. 062901, 2012.

[113] L. Mazet, S. M. Yang, S. V Kalinin, S. Schamm-Chardon, and C. Dubourdieu, "A review of molecular beam epitaxy of ferroelectric $BaTiO_3$ films on Si, Ge and GaAs substrates and their applications," *Sci. Technol. Adv. Mater.*, vol. 16, no. 3, p. 036005, 2015.

[114] J. F. Scott, "Dimensional Effects on Ferroelectrics: Ultra-Thin Single Crystals, Nanotubes, Nano-Rods, and Nano-Ribbons," *Ferroelectrics*, vol. 316, pp. 13–21, 2005.

[115] K.-I. Park, S. Xu, Y. Liu, G.-T. Hwang, S.-J.L. Kang, Z. L. Wang, and K. J. Lee, "Piezoelectric $BaTiO_3$ Thin Film Nanogenerator on Plastic Substrates," *Nano Lett.* vol. 10, pp. 4939–4943, 2010.

[116] B. E. Volland, H. Heerlein, and I. W. Rangelow, “Electrostatically driven microgripper,” *Microelectron. Eng.*, vol. 61–62, pp. 1015–1023, Jul. 2002.

[117] J. E. Huber, N. A. Fleck, and M. F. Ashby, “The selection of mechanical actuators,” *Proc. R. Soc. A*, vol. 453, pp. 2185–2205, 1997.

[118] C. A. Satkoski, N. S. Ruikar, S. D. Biggs, and G. M. Shaver, “Piezoelectric fuel injection: Cycle-to-cycle control of tightly spaced injections,” *Control Eng. Pract.*, vol. 20, no. 11, pp. 1175–1182, 2012.

[119] A. Kamantsev, A. Mashirov, P. Mazaev, V. Koledov, and V. Shavrov, “Manipulations of Submicro-fibers of Culex Pipiens with the Help of Nano-tweezers with Shape Memory Effect into Vacuum Chamber of FIB,” in *Microscopy and Microanalysis conference*, vol. 21, no. 0998, pp. 5–6, 2015.

[120] T. Bartel, T. Röglin, T. Bartel, S. Breda, S. Gaisbauer, D. Mayer, and J. Millitzer, “Development of Piezoelectric Inertial Actuators for the Reduction of Vibrations in a Car Body,” in *Proc. AIA-DAGA 2013 Conference on Acoustics*, 2013.

[121] B. Huang, J. Tseng, C. Chang, and C. Li, “Using Finite Element Analysis and Experimental Analysis on Vibration of a Piezoelectric Micro Pump,” *J. Appl. Math. Phys.*, vol. 3, pp. 1038–1043, 2015.

[122] Y. Tian, B. Shirinzadeh, and D. Zhang, “A flexure-based five-bar mechanism for micro/nano manipulation,” *Sensors Actuators A Phys.*, vol. 153, pp. 96–104, 2009.

[123] S. Tsukahara, J. Torres, D. Neal, and H. H. Asada, “Design method for buckling amplified piezoelectric actuator using flexure,” in *JSME 2012 11th Motion and Vibration Conference*, 2012.

[124] B. Mosadegh, A. D. Mazzeo, R. F. Shepherd, S. A. Morin, U. Gupta, I. Z. Sani, D. Lai, S. Takayama, and G. M. Whitesides, “Control of soft machines using actuators operated by a Braille display,” *Lab Chip*, vol. 14, pp. 189–199, 2014.

[125] X. J. Mu, G. Zhou, H. B. Yu, Y. Du, H. H. Feng, J. M. L. Tsai, and F. S. Chau, “A Compact circumferential scanned endoscopic imaging probe using a MEMS-driven pyramidal polygon reflector,” *Opt. Express*, vol. 20, pp. 902–905, 2012.

[126] M. R. Motamedi, D. Florant, and V. Duchaine, “A Wearable Haptic Device Based on Twisting Wire Actuators for Feedback of Tactile Pressure Information,” *J. ref J. Robot. Mechatronics*, vol. 27, no. 4, pp. 419–429, 2015.

[127] C. Kittel, “Theory of the Structure of Ferromagnetic Domains in Films and Small Particles,” *Phys. Rev.*, vol. 70, no. 11, pp. 965–971, 1946.

[128] I. Naumov and H. Fu, “Vortex-to-Polarization Phase Transformation Path in Ferroelectric $Pb(ZrTi)O_3$ Nanoparticles,” *Phys. Rev. Lett.*, vol. 98, no. 7, p. 077603, Feb. 2007.

[129] L. Hong and A. K. Soh, "Unique vortex and stripe domain structures in $PbTiO_3$ epitaxial nanodots," *Mech. Mater.*, vol. 43, no. 6, pp. 342–347, Jun. 2011.

[130] L. J. McGilly, A. Schilling, and J. M. Gregg, "Domain bundle boundaries in single crystal $BaTiO_3$ lamellae: searching for naturally forming dipole flux-closure/quadrupole chains.," *Nano Lett.*, vol. 10, pp. 4200–5, 2010.

[131] R. G. P. McQuaid, A. Gruverman, J. F. Scott, and J. M. Gregg, "Exploring vertex interactions in ferroelectric flux-closure domains.," *Nano Lett.*, vol. 14, no. 8, pp. 4230–7, 2014.

[132] L.-W. Chang, V. Nagarajan, J. F. Scott, and J. M. Gregg, "Self-similar nested flux closure structures in a tetragonal ferroelectric.," *Nano Lett.*, vol. 13, no. 6, pp. 2553–7, Jun. 2013.

[133] Y. Ivry, D. P. Chu, J. F. Scott, and C. Durkan, "Flux Closure Vortexlike Domain Structures in Ferroelectric Thin Films," *Phys. Rev. Lett.*, vol. 104, no. 20, p. 207602, May 2010.

[134] C.-L. Jia, K. W. Urban, M. Alexe, D. Hesse, and I. Vrejoiu, "Direct observation of continuous electric dipole rotation in flux-closure domains in ferroelectric $Pb(Zr,Ti)O_3$," *Science*, vol. 331, no. 6023, pp. 1420–3, Mar. 2011.

[135] R. G. P. McQuaid, L. J. McGilly, P. Sharma, A. Gruverman, and J. M. Gregg, "Mesoscale flux-closure domain formation in single-crystal $BaTiO_3$," *Nat. Commun.*, vol. 2, no. May, p. 404, Jan. 2011.

[136] L. J. McGilly and J. M. Gregg, "Polarization Closure in $PbZr_{(0.42)}Ti_{(0.58)}O_3$ Nanodots," *Nano Lett.*, vol. 11, pp. 4490–4495, 2011.

[137] R. Skomski, "Nanomagnetics," *J. Phys. Condens. Matter*, vol. 15, pp. R841 – R896, 2003.

[138] C.-L. Jia, K. W. Urban, M. Alexe, D. Hesse, and I. Vrejoiu, "Direct observation of continuous electric dipole rotation in flux-closure domains in ferroelectric $Pb(Zr,Ti)O_3$," *Science*, vol. 331, no. 6023, pp. 1420–3, Mar. 2011.

[139] T. Hoshina, H. Kakemoto, T. Tsurumi, S. Wada, and M. Yashima, "Size and temperature induced phase transition behaviors of barium titanate nanoparticles," *J. Appl. Phys.*, vol. 99, no. 5, p. 054311, 2006.

[140] J. E. Spanier, A. M. Kolpak, J. J. Urban, I. Grinberg, L. Ouyang, W. S. Yun, A. M. Rappe, and H. Park, "Ferroelectric phase transition in individual single-crystalline $BaTiO_3$ nanowires.," *Nano Lett.*, vol. 6, no. 4, pp. 735–9, Apr. 2006.

[141] D. J. Srolovitz and J. F. Scott, "clock-model description of incommensurate ferroelectric films and of nematic-liquid-crystal films," *Phys. Rev. B*, vol. 34, no. 3, p. 1815, 1986.

[142] K. Uchino, E. Sadanaga, and T. Hirose, “Dependence of the Crystal Structure on Particle Size in Barium Titanate,” *J. Am. Ceram. Soc.*, vol. 72, pp. 1–4, 1989.

[143] Y. Su, H. Chen, J. J. Li, A. K. Soh, and G. J. Weng, “Effects of surface tension on the size-dependent ferroelectric characteristics of free-standing $BaTiO_3$ nano-thin films,” *J. Appl. Phys.*, vol. 110, no. 8, p. 084108, 2011.

[144] J. J. Wang, X. Q. Ma, Q. Li, J. Britson, and L.-Q. Chen, “Phase transitions and domain structures of ferroelectric nanoparticles: Phase field model incorporating strong elastic and dielectric inhomogeneity,” *Acta Mater.*, vol. 61, no. 20, pp. 7591–7603, Dec. 2013.

[145] W. Ma, “Surface tension and Curie temperature in ferroelectric nanowires and nanodots,” *Appl. Phys. A*, vol. 96, no. 4, pp. 915–920, May 2009.

[146] A. Marchand, J. H. Weijs, J. H. Snoeijer, and B. Andreotti, “Why is surface tension a force parallel to the interface?,” *Am. J. Phys.*, vol. 79, p. 999, 2011.

[147] A. Schilling, D. Byrne, G. Catalan, K. G. Webber, Y. A. Genenko, G. S. Wu, J. F. Scott, and J. M. Gregg, “Domains in ferroelectric nanodots.,” *Nano Lett.*, vol. 9, no. 9, pp. 3359–64, Sep. 2009.

[148] L. J. McGilly and J. M. Gregg, “Scaling of superdomain bands in ferroelectric dots,” *Appl. Phys. Lett.*, vol. 98, no. 13, p. 132902, 2011.

[149] R. Ahluwalia, N. Ng, A. Schilling, R. G. P. McQuaid, D. M. Evans, J. M. Gregg, D. J. Srolovitz, and J. F. Scott, “Manipulating Ferroelectric Domains in Nanostructures Under Electron Beams,” *Phys. Rev. Lett.*, vol. 111, no. 16, p. 165702, Oct. 2013.

[150] A. Schilling, S. Prosandeev, R. G. P. McQuaid, L. Bellaiche, J. F. Scott, and J. M. Gregg, “Shape-induced phase transition of domain patterns in ferroelectric platelets,” *Phys. Rev. B*, vol. 84, no. 6, p. 064110, Aug. 2011.

[151] W. S. Yun, J. J. Urban, Q. Gu, and H. Park, “Ferroelectric Properties of Individual Barium Titanate Nanowires Investigated by Scanned Probe Microscopy,” *Nano Lett.*, vol. 2, no. 5, pp. 447–450, May 2002.

[152] J. J. Urban, J. E. Spanier, L. Ouyang, W. S. Yun, and H. Park, “Single-Crystalline Barium Titanate Nanowires,” *Adv. Mater.*, vol. 15, no. 5, pp. 423–426, Mar. 2003.

[153] J. Hong and D. Fang, “Size-dependent ferroelectric behaviors of $BaTiO_3$ nanowires,” *Appl. Phys. Lett.*, vol. 92, no. 1, p. 012906, 2008.

[154] A. Hubert and R. Schafer, *Magnetic domains: The analsysis of magnetic microstructures*, 2008.

[155] D. Ter Haar, *Collected papers of L.D.Landau*. 2013.

[156] A. Wachowiak, J. Wiebe, M. Bode, O. Pietzsch, M. Morgenstern, and R. Wiesendanger, "Direct observation of internal spin structure of magnetic vortex cores.," *Science*, vol. 298, no. 5593, pp. 577–80, Oct. 2002.

[157] Y. Wen, Z. Feng, B. F. Miao, R. X. Cao, L. Sun, B. You, D. Wu, W. Zhang, Z. S. Jiang, R. Cheng, and H. F. Ding, "Fast and controllable switching the circulation and polarity of magnetic vortices," *J. Magn. Magn. Mater.*, vol. 370, pp. 68–75, Dec. 2014.

[158] R. D. Gomez, T. V. Luu, A. O. Pak, K. J. Kirk, and J. N. Chapman, "Domain configurations of nanostructured permalloy elements," *J. Appl. Phys.*, vol. 85, p. 6163, 1999.

[159] G. Arlt, "The role of domain walls on the dielectric, elastic and piezoelectric properties of ferroelectric ceramics," *Ferroelectrics*, vol. 76:1, pp. 451–458, 1987.

[160] G. Arlt, "The influence of microstructure on the properties of ferroelectric ceramics," *Ferroelectrics*, vol. 104:1, pp. 217–227, 1990.

[161] J. Rödel, "Effective intrinsic linear properties of laminar piezoelectric composites and simple ferroelectric domain structures," *Mech. Mater.*, vol. 39, pp. 302–325, 2007.

[162] W. Y. Kim and H. C. Lee, "Low-voltage nonvolatile multi-bit memory fabricated by the patterning and transferring of ferroelectric polymer film," *Org. Electron.*, vol. 19, pp. 1–6, 2015.

[163] J. M. Ball and R. D. James, "Fine phase mixtures as minimizers of energy," *Arch. Ration. Mech. Anal.*, vol. 100, pp. 13–52, 1987.

[164] K. Bhattacharya, "Comparison of the geometrically nonlinear and linear theories of martensitic transformation," *Contin. Mech. Thermodyn.*, vol. 5, pp. 205–242, 1993.

[165] N. Tsou, *Compatible domain structures in ferroelectric single crystals*. 2011.

[166] A. DeSimone and R. D. James, "A constrained theory of magnetoelasticity," *J. Mech. Phys. Solids*, vol. 50, pp. 283–320, 2002.

[167] C. M. Dudhe, S. B. Nagdeote, S. J. Khambadkar, P. R. Arjunwadkar, and R. R. Patil, "Study of 90° and 180° Nanodomains in $BaTiO_3$ Nanoparticles Using Transmission Electron Microscopy," *Ferroelectrics*, vol. 471, no. June, pp. 148–155, 2014.

[168] J. F. Scott, "Nanoferroelectrics: statics and dynamics.," *J. Phys. Condens. Matter*, vol. 18, pp. R361–R386, 2006.

[169] O. Kolosov, A. Gruverman, J. Hatano, K. Takahashi, and H. Tokumoto, "Nanoscale visualization and control of ferroelectric domains by atomic force microscopy," *Phys. Rev. Lett.*, vol. 74, no. 21, p. 4309, 1995.

[170] V. Gopalan, V. Dierolf, and D. A. Scrymgeour, "Defect–Domain Wall Interactions in Trigonal Ferroelectrics," *Annu. Rev. Mater. Res.*, vol. 37, pp. 449–489, 2007.

[171] X. Tan and J. K. Shang, "Partial dislocations at domain intersections in a tetragonal ferroelectric crystal," *J. Phys. Condens. Matter*, vol. 16, pp. 1455–1466, 2004.

[172] E. Soergel, "Visualization of ferroelectric domains in bulk single crystals," *Appl. Phys. B Lasers Opt.*, vol. 81, pp. 729–752, 2005.

[173] N. T. Tsou, J. E. Huber, and A. C. F. Cocks, "Evolution of compatible laminate domain structures in ferroelectric single crystals," *Acta Mater.*, vol. 61, no. 2, pp. 670–682, 2013.

[174] G. Goldsztein, "The effective energy and laminated microstructures in martensitic phase transformations," *J. Mech. Phys. Solids*, vol. 49, pp. 899–925, 2001.

[175] P. R. Potnis, N. T. Tsou, and J. E. Huber, "A review of domain modelling and domain imaging techniques in ferroelectric crystals," *Materials (Basel).*, vol. 4, pp. 417–447, 2010.

[176] R. Ramesh, *Thin film ferroelectric materials and devices*. Springer Science and Business Media, 2013.

[177] D. Guyomar, A. Badel, E. Lefeuvre, and C. Richard, "Toward energy harvesting using active materials and conversion improvement by nonlinear processing," *IEEE Trans. Ultrason. Ferroelectr. Freq. Control*, vol. 52, no. 4, pp. 584–594, 2005.

[178] H. K. H. Kim, S. Priya, H. Stephanou, and K. Uchino, "Consideration of Impedance Matching Techniques for Efficient Piezoelectric Energy Harvesting," *IEEE Trans. Ultrason. Ferroelectr. Freq. Control*, vol. 54, no. 9, pp. 1851–1859, 2007.

[179] A. K. Tagantsev, L. E. Cross, and J. Fousek, *Domains in ferroic crystals and thin films*. 2009.

[180] B. L. Cheng, M. Gabbay, W. Duffy, and G. Fantozzi, "Mechanical loss and Young's modulus associated with phase transitions in barium titanate based ceramics," *J. Mater. Sci.*, vol. 31, pp. 4951–4955, 1996.

[181] I. Muench, A. Renuka Balakrishna, and J. E. Huber, "Spatial periodic ferroelectric structures on the nanoscale," *Manuscr. Prep.*

[182] Y. Gu, F. Xue, S. Lei, T. T. A. Lummen, J. Wang, V. Gopalan, and L. Q. Chen, "Monoclinic phases arising across thermal inter-ferroelectric phase transitions," *Phys. Rev. B - Condens. Matter Mater. Phys.*, vol. 90, p. 024104, 2014.

[183] X. Zhang, J. B. Wang, B. Li, X. L. Zhong, X. J. Lou, and Y. C. Zhou, "Sizable electrocaloric effect in a wide temperature range tuned by tensile misfit strain in $BaTiO_3$ thin films," *J. Appl. Phys.*, vol. 109, p. 126102, 2011.

[184] A. N. Morozovska, E. A. Eliseev, and M. D. Glinchuk, "Ferroelectricity enhancement in confined nanorods: Direct variational method," *Phys. Rev. B - Condens. Matter Mater. Phys.*, vol. 73, pp. 1–13, 2006.

[185] M. D. Glinchuk, E. A. Eliseev, A. N. Morozovska, and R. Blinc, "Giant magnetoelectric effect induced by intrinsic surface stress in ferroic nanorods," *Phys. Rev. B - Condens. Matter Mater. Phys.*, vol. 77, pp. 1–11, 2008.

[186] H. T. Chen, A. K. Soh, and Y. Ni, "Phase field modeling of flexoelectric effects in ferroelectric epitaxial thin films," *Acta Mech.*, vol. 225, no. 4–5, pp. 1323–1333, Jan. 2014.

[187] Y. Gu, M. Li, A. N. Morozovska, Y. Wang, E. A. Eliseev, V. Gopalan, and L.-Q. Chen, "Flexoelectricity and ferroelectric domain wall structures: Phase-field modeling and DFT calculations," *Phys. Rev. B*, vol. 89, p. 174111, 2014.

[188] L. Jiang, J. Tang, Y. Zhou, Q. Yang, Y. Zhang, L. Guo, and X. Zhong, "Simulations of local-mechanical-stress-induced ferroelectric polarization switching by a multi-field coupling model of flexoelectric effect," *Comput. Mater. Sci.*, vol. 108, pp. 1–7, 2015.

[189] J. R. Whyte and J. M. Gregg, "A diode for ferroelectric domain-wall motion.," *Nat. Commun.*, vol. 6, p. 7361, 2015.

[190] G. Catalan, J. Seidel, R. Ramesh, and J. F. Scott, "Domain wall nanoelectronics," *Rev. Mod. Phys.*, vol. 84, no. 1, pp. 119–156, Feb. 2012.

[191] A. J. Bell and L. E. Cross, "A phenomenological gibbs function for $BaTiO_3$ giving correct E field dependence of all ferroelectric phase changes," *Ferroelectrics*, vol. 59, no. November, pp. 197–203, 1984.

[192] J. J. Wang, P. P. Wu, X. Q. Ma, and L. Q. Chen, "Temperature-pressure phase diagram and ferroelectric properties of $BaTiO_3$ single crystal based on a modified Landau potential," *J. Appl. Phys.*, vol. 108, no. 2010, pp. 0–8, 2010.

[193] E. K. H. Salje, B. Wruck, and H. Thomas, "Order-parameter saturation and low-temperature extension of Landau theory," *Zeitschrift für Phys. B Condens. Matter*, vol. 404, pp. 399–404, 1991.

[194] D. Pang, X. Long, and H. Tailor, “A lead-reduced ferrolectric solid solution with high curie temperature: $BiScO_3$–$Pb(Zn_{1/3}Nb_{2/3})O_3$–$PbTiO_3$,” *Ceram. Int.*, vol. 40, pp. 12953–12959, 2014.

[195] T. Hoshina, S. Wada, Y. Kuroiwa, and T. Tsurumi, “Composite structure and size effect of barium titanate nanoparticles,” *Appl. Phys. Lett.*, vol. 93, no. 19, p. 192914, 2008.

[196] T. Belytschko, Y. Krongauz, D. Organ, M. Fleming, and P. Krysl, “Meshless methods: An overview and recent developments,” *Comput. Methods Appl. Mech. Eng.*, vol. 139, no. 96, pp. 3–47, 1996.

[197] F. Amiri, D. Millán, Y. Shen, T. Rabczuk, and M. Arroyo, “Phase-field modeling of fracture in linear thin shells,” *Theor. Appl. Fract. Mech.*, vol. 69, pp. 102–109, 2014.

[198] N. Provatas, M. Greenwood, B. Athreya, N. Goldenfeld, and J. Dantzig, “Multiscale Modeling of Solidification: Phase-Field Methods To Adaptive Mesh Refinement,” *Int. J. Mod. Phys. B*, vol. 19, no. 31, pp. 4525–4565, 2005.

[199] N. Provatas, N. Goldenfeld, and J. Dantzig, “Adaptive Mesh Refinement Computation of Solidification Microstructures using Dynamic Data Structures,” vol. 290, pp. 265–290, 1998.

[200] Y. W. Li and F. X. Li, “The effect of multi-rank domain pattern on the polarization response of $BaTiO_3$ crystal during electric field loading,” *J. Appl. Phys.*, vol. 117, p. 244101, 2015.

[201] Y. Uetsuji, T. Hata, H. Kuramae, and K. Tsuchiya, “Homogenization modeling of domain switching in ferroelectric materials,” *Acta Mech.*, vol. 225, pp. 2969–2986, 2014.

[202] B. Völker, P. Marton, C. Elsässer, and M. Kamlah, “Multiscale modeling for ferroelectric materials: A transition from the atomic level to phase-field modeling,” *Contin. Mech. Thermodyn.*, vol. 23, pp. 435–451, 2011.

[203] R. A. Cowley, S. N. Gvasaliya, S. G. Lushnikov, B. Roessli, and G. M. Rotaru, “Relaxing with relaxors: a review of relaxor ferroelectrics,” *Adv. Phys.*, vol. 60, no. November, pp. 229–327, 2011.

[204] Y. Chen, K.-H. Lam, D. Zhou, Q. Yue, Y. Yu, J. Wu, W. Qiu, L. Sun, C. Zhang, H. Luo, H. Chan, and J. Dai, “High Performance Relaxor-Based Ferroelectric Single Crystals for Ultrasonic Transducer Applications,” *Sensors*, vol. 14, no. July, pp. 13730–13758, 2014.

[205] S. E. Park and T. R. Shrout, “Characteristics of relaxor-based piezoelectric single crystals for ultrasonic transducers,” *IEEE Trans. Ultrason. Ferroelectr. Freq. Control*, vol. 44, no. 5, pp. 1140–1147, 1997.

[206] Z. Xie, B. Peng, J. Zhang, X. Zhang, Z. Yue, and L. Li, “Highly (100)-Oriented $Bi(Ni_{1/2}Hf_{1/2})O_3$-$PbTiO_3$ Relaxor-Ferroelectric Films for Integrated Piezoelectric Energy Harvesting and Storage System,” *J. Am. Ceram. Soc.*, vol. 98, pp. 2968–2971, 2015.

[207] Z. Xie, Z. Yue, G. Ruehl, B. Peng, J. Zhang, Q. Yu, X. Zhang, and L. Li, “$Bi(Ni_{1/2}Zr_{1/2})O_3$-$PbTiO_3$ relaxor-ferroelectric films for piezoelectric energy harvesting and electrostatic storage,” *Appl. Phys. Lett.*, vol. 104, p. 243902, 2014.

[208] A. Bosak, D. Chernyshov, and S. Vakhrushev, “Glass-like structure of a lead-based relaxor ferroelectric,” *J. Appl. Crystallogr.*, vol. 45, pp. 1309–1313, 2012.

[209] M. Sepliarsky and R. E. Cohen, “First-principles based atomistic modeling of phase stability in PMN-*x*PT.,” *J. Phys. Condens. Matter*, vol. 23, p. 435902, 2011.

[210] A. Al-Barakaty, S. Prosandeev, D. Wang, B. Dkhil, and L. Bellaiche, “Finite-temperature properties of the relaxor $PbMg_{1/3}Nb_{2/3}O_3$ from atomistic simulations,” *Phys. Rev. B*, vol. 91, p. 214117, 2015.

[211] J. A. Gallagher and C. S. Lynch, “Combining experiments and modeling to characterize field driven phase transformations in relaxor ferroelectric single crystals,” *Acta Mater.*, vol. 89, pp. 41–49, 2015.

[212] H. Gabrisch, J. Wilcox, and M. M. Doeff, “TEM Study of Fracturing in Spherical and Plate-like $LiFePO_4$ Particles,” *Electrochem. Solid-State Lett.*, vol. 11, p. A25, 2008.

[213] S. W. Lee, M. T. McDowell, L. A. Berla, W. D. Nix, and Y. Cui, “Fracture of crystalline Germanium during electrochemical lithium insertion,” *Proc. Natl. Acad. Sci.*, vol. 2, pp. 15–19, 2012.

[214] M. Huttin and M. Kamlah, “Phase-field modeling of stress generation in electrode particles of lithium ion batteries,” *Appl. Phys. Lett.*, vol. 101, no. 2012, p. 133902, 2012.

[215] C. V. Di Leo, E. Rejovitzky, and L. Anand, “A Cahn–Hilliard-type phase-field theory for species diffusion coupled with large elastic deformations: Application to phase-separating Li-ion electrode materials,” *J. Mech. Phys. Solids*, vol. 70, pp. 1–29, 2014.